NLTE accretion disc models for the AM Canum Venaticorum systems

A theoretical contribution leading into a new phase of understanding to such systems

A dissertation for the degree doctor scientiarum

by

Mosab R. Nasser

September, 1998 - November, 2001

University of Tromsø
Faculty of Science - Department of Physics
Astrophysics Group

Preface

This thesis is a product of the burst of the scientific activity which started at the University of Tromsø in 1982 by Jan-Erik Solheim and his students. Most of their work has been done using photometric techniques, to study the AM CVn systems. Later on spectroscopy was introduced to the group to answer some of their curious questions about such systems. J.-E. Solheim, K. Massacand, S. Bard, T. Nymark and D. Semionoff have all contributed with their investigations to a better understanding of the AM CVn spectra. Not all - nor even most - of the basic questions concerning the structure and evolution of the AM CVn systems are fully resolved. My part in this project came as a continuation to the work done by D. Semionoff during his Master thesis. However, in this work we concentrate all our investigations on the accretion disc of the AM CVn systems by analyzing and modeling the optical spectra of most of the AM CVn family members. Parameters such as the mass accretion rate, the angle of inclination, the inner and outer radii of the disc, the abundance of elements, the LTE/NLTE treatment of the model, the distance to the systems and their evolutionary track are all of our concern.

This work came to complete a small part of the AM CVn family picture, which has been drawn long time ago by many scientists in many different institutions. The material in this thesis is presented in its natural order to make it easier for the reader to follow our work.

Not surprisingly, a great many people at numerous institutions indirectly contributed to the preparation of this work. Indeed, it is virtually impossible for me to recall all their names, however, I am particularly grateful to the Norwegian department of education, the State Loan Fund and the World Laboratory in Geneva - Switzerland, for financing my three years of study at the University of Tromsø as an English taught quota student. I am very grateful to my supervisor Jan-Erik Solheim who introduced me to the AM CVn systems in particular, and to the interacting binary white dwarfs in general. I also thank him for carefully reading portions of an earlier draft of this thesis, and providing me with crucial feedback. A great many thanks to

Ivan Hubeny at GSFC, NASA, the author of our main modeling tools. I also express my gratitude to him for his extremely useful comments to us while publishing this work, and also for his willingness to participate in the final discussion of this thesis.

I would like to thank Tim Abbot, Roy Østensen and Anlaug Amanda Kaas for their cooperation with me during my observations at the Nordic Optical Telescope (NOT) in Spain. I would also like to thank Leif Hansen at Niels Bohr Institute for Astronomy in Copenhagen for his collaboration with me in finding a good way to reduce the spectroscopic data taken with the NOT.

I wish to thank my colleagues here in Tromsø, Jose, Frank, Robert and Synnøve for their support and willingness to attend and listen to my seminars during my Ph.D. work. I also thank the staff here at the Physics Department and especially Per-Ivar Emmanuelsen, who was always there, whenever I needed his advise and help in software problems during my three years of research.

Finally, I will forever be grateful to my parents and my wife for supporting me all the time, specially in my dark moments, and who contributed much more than they will ever know to the completion of this work.

Therefore, I dedicate this work to my parents, my wife and my son *'Elias'.*

"The universe, we have built it with power, verily, we are expanding it, (The holy Qur'an, Ch51, Verse 47)."

Contents

Chapter 1

Accretion in binary systems

Most of this chapter has been written based on the book by Frank et al. (1992), with the title 'Accretion power in astrophysics'. All the physical quantities, which will be used throughout the text of the chapters in this thesis are in cgs units and defined in the Appendix.

1.1 Introduction

Since the early 1970s, when accretion discs were first postulated, they have been discovered observationally in many types of systems e.g. cataclysmic variables, low mass X-ray binaries, young stellar objects and even a few Algols. Saturn's ring system was first astrophysical disc to be discovered. When Galileo observed the rings in 1610, he believed them to be two giant moons in orbit about the planet. However, these moons appeared fixed in position, unlike the four satellites of Jupiter which he had previously observed. Moreover, Saturn's "moons" had disappeared completely by the time Galileo resumed his observations of the planet in 1612. Many explanations were put forth to explain Saturn's "strange appendages", which grew, shrank and disappeared every 15 years. In 1655, Huygens finally deduced the correct explanation, that Saturn's strange appendages are a flattened disc of material in Saturn's equatorial plane, which appear to vanish when the earth passes through the plane of the disc. The greatest difficulty of that time was recognition of the possibility and plausibility of astrophysical disc systems. Contrast this to the situation today, when almost any flattened object observed in the heavens is initially suspected of being a disc. The discovery of Saturn's rings shifted the attention gradually into the possibility of other astrophysical discs (e.g. spiral galaxies). With the advanced technology of today and with the existence of the ground and space

telescopes, we are able to discover observationally many accretion discs in many types of systems e.g. cataclysmic variables, low mass X-ray binaries and young stellar objects. Systems containing discs around compact objects are some of the most important astrophysical phenomena. A great deal of energy is released in such systems. The release of gravitational potential energy as mass falls onto a black hole is the most efficient energy generation mechanism known.

Most stars are members of binary systems and most of them end their lives as white dwarfs, so it is not surprising that binary stars composed of a white dwarf and a main sequence star are a common product of stellar evolution. Many of these binary stars are sufficiently close for mass transfer to occur and the cataclysmic variable stars (CVs) have long been recognized as such systems. CVs are fascinating both for evolutionary properties as binary stars and because they are in many ways ideally set up for the study of accretion. In such systems, the main sequence star fills its Roche lobe, and a thin stream of matter overflows at the inner Lagrangian point. The matter in the stream has considerable angular momentum and cannot go straight to the white dwarf. Instead it collides with itself and form a disc around the accreting white dwarf. Within the disc, viscous interaction transports angular momentum from small to large radii (where it is removed by tidal interaction with the donor star), allowing the matter to accrete onto the compact star. Dynamical stability of mass transfer (allowing CVs to be long lived) demands that the donor main sequence star be less massive than its companion white dwarf. The white dwarfs are dim because of their size, thus in CVs it is often the disc that dominates the spectrum over a wide range of wavelength.

In this chapter, we will focus on the theory of accretion in binary systems, where a low mass star fills its Roche lobe and transfers matter on to its compact companion. We will define and classify the binary systems and present the basic equations which governs them, and also describe the requirements for the mass transfer which can form the accretion disc in such systems.

1.2 Definition and classification of binary systems

A *binary system* can be simply defined as one containing two stars that describe close orbits around their common center of gravity, under the influence of their mutual gravitation. No restriction has been placed in this definition on the separation of the two components. They can be in contact, or separated by thousands of astronomical units, or even more. The definition would have to be stretched a little to include common-proper-motion pairs, so many of which have been discovered by Luyten (1933), since it must for a long time remain an open question whether such pairs

are moving in very long-period orbits, or simply traveling together.

A class of objects in which one basic parameter is allowed to vary over such a wide range will contain many dissimilar individuals, and it is natural to look for some form of classification that will divide the whole group into nearly more homogeneous sub-classes. An obvious classification is proved by the method of observation. Very wide pairs can be resolved by the telescope and recognized visually as double stars, if they are near enough to us. These are the *visual binary systems*. It is convenient to include in this class pairs that are not actually resolved, but which are discovered by careful measurements of the position of the star relative to background stars in the same field. These systems are usually termed *astrometric binaries*. However, Many binary systems contain stars that are so close together that they can never be resolved in a telescope, or be discovered from their transverse motions. They can be discovered spectroscopically from the variations in their radial velocities, and are therefore called *spectroscopic binaries*. The orbital planes of some of these are oriented so that the two components eclipse each other as seen from the Earth, and these are called *eclipsing binaries*. There are two other groups of objects whose binary nature is less directly inferred. The *spectrum binaries* are stars that show composite spectra, but whose components are too widely separated from each other to show observable velocity changes; some of these might be visual binaries if they were nearer to the Sun. Some, at least, of the *ellipsoidal variables* are binaries that just fail to be eclipsing, but show periodic light variations because of the distortion of their components.

The techniques used to observe these different kinds of binaries are very different, and a classification based on them is very useful for distinguishing the astronomers who study binary systems. It has few other merits, however. Recognition of a visual binary depends not only on the true separation of its components, but also on its distance from the Sun. Visual binaries, at least those for which orbits may be determined, are relatively near neighbors. Spectroscopic binaries can be recognized at much greater distances, since it is only necessary for their discovery, that the system be bright enough to be observed. Eclipsing binaries can be recognized at even greater distances if the eclipses are fairly deep. Such binaries have been recognized in another galaxy. About 50 percent of all stars are assumed to be in binary systems. Generally, there are three kinds of binary systems:

Contact binaries, which are systems where the two stars share a common envelop. From a distance such systems look much like a single star. About 50 percent of all binary systems are contact binaries.

Semi-detached binaries, where the two stars do not share a common envelope, but

exchange mass through Roche lobe overflow. In a system like this the star which fills its Roche lobe is gradually being devoured by its companion, its outer layers being peeled off first, enabling us to study its inner layers directly. These systems thus represent a unique possibility to look into the heart of a star, which in a normal star is obscured by the outer layers.

Detached binaries, where the two stars, albeit affecting each other gravitationally, are too distant to exchange mass except by stellar winds.

1.2.1 Orbital elements

The term *orbital elements* originated in the study of planetary motions. Six quantities are needed to define the motion of a planet in its elliptical orbit, and those usually chosen are;

• Two angles i and Ω which define the position of the orbital plane in space with respect to a reference plane. The choice of the plane is arbitrary; for planetary orbits it can be that of the Earth's orbit, or the invariable plane of the Solar System.
• A third angle ω, defining the orientation of the longest axis of the elliptical orbit within the orbital plane. In many dynamical studies of the solar system, it has been found convenient to use another angle ϖ, defined as $\omega + \Omega$. This composite angle is called the *longitude of perihelion*: note that it is composed of two angles in different planes.
• Two quantities a (the major semi-axis) and e (the eccentricity) that define the size and the shape of the ellipse.
• A time t corresponding to a given position of the planet in its orbit (usually the time of perihelion passage). The period, P_{orb}, is not a necessary separate element, since within the Solar System all periods are given by Kepler's third law

$$\frac{a^3}{P_{orb}^2} = constant \tag{1.1}$$

The orbit of a binary system may be similarly defined although a different reference plane is chosen, and the period is related to the major semi-axis by the generalized form of Kepler's law

$$\frac{a^3}{P_{orb}^2} = \frac{G(M_1 + M_2)M_\odot}{4\pi^2} \tag{1.2}$$

where M_1 and M_2 are the masses of the two stars in solar mass. A complete dynamical description of the system, therefore, requires a knowledge of the period P_{orb}, which has come to be regarded as an extra orbital element. For more illustration see Fig. 1.1.

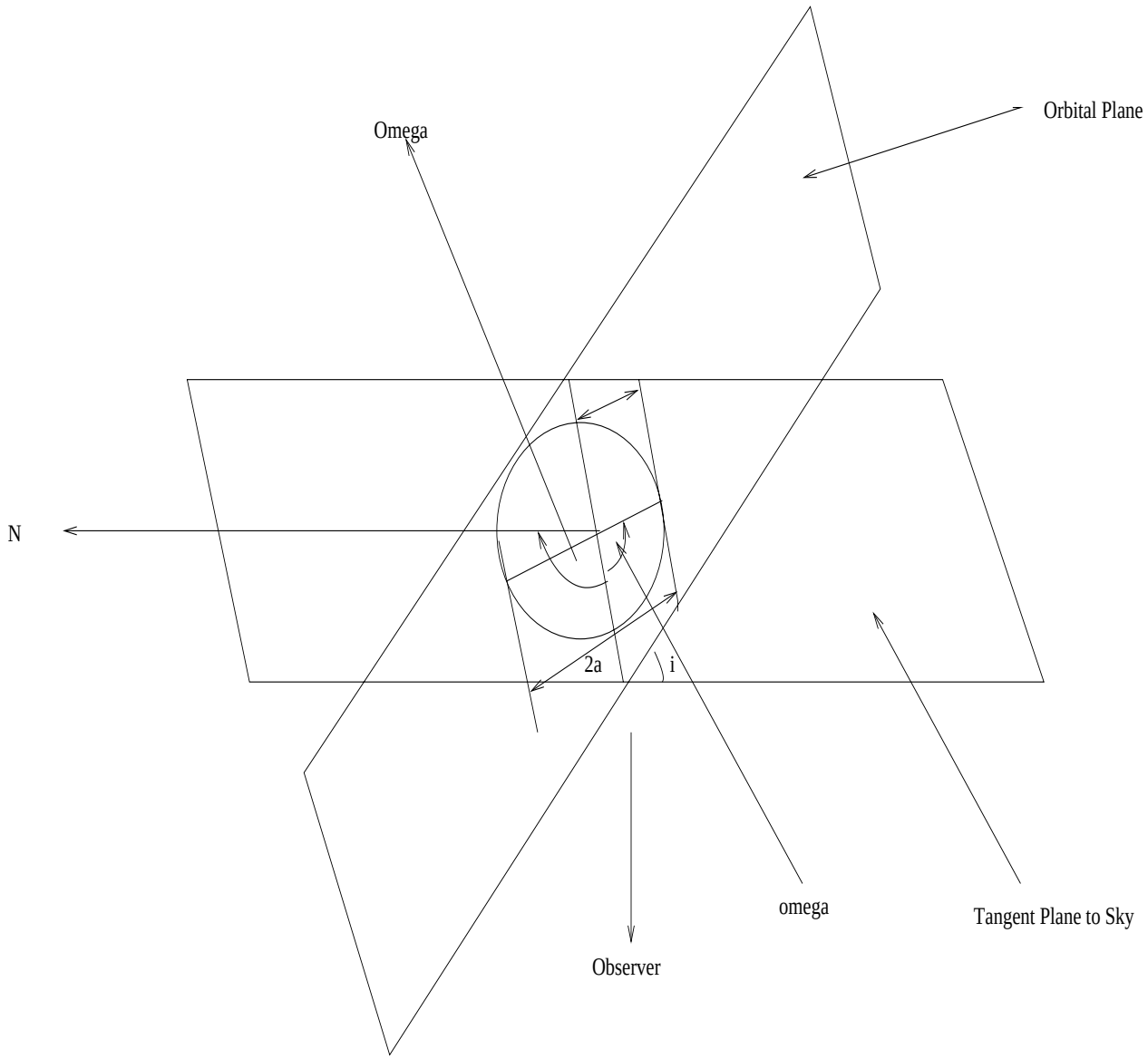

Figure 1.1: Orbital plane and the tangent plane to the sky illustrating the significance of the orbital elements. Omega in the figure means Ω while omega means ω.

The following quantities are used to define the binary orbit:
$P_{orb} \rightarrow$ the orbital period, usually expressed in days (spectroscopic or eclipsing binaries) or years (visual binaries).

$i \rightarrow$ the inclination of the orbital plane to the tangent plane of the celestial sphere at the star.

$\Omega \rightarrow$ the position angle (measured from North through East) of the line of nodes joining the intersections of the orbital and tangent planes, and measured in the latter.

$\omega \rightarrow$ the angle between the direction to the ascending node (at which the star crosses the tangent plane while receding from the observer) and that to the point of the closest approach of the two stars (periastron). This angle is measured in the orbital plane, in the direction of orbital motion. By convention observers always give the value of ω appropriate to the secondary (fainter) component of a system, while observers of eclipsing and spectroscopic systems usually quote the value of the orbit of the primary component.

$a \rightarrow$ the major semi-axis of the orbit, usually expressed in kilometers or astronomical units.

$e \rightarrow$ the eccentricity of the orbit, a dimensionless number between zero and unity.

$t \rightarrow$ the time at which the two stars pass through periastron.

1.2.2 Interacting binary systems

There are two main reasons why many binary systems transfer matter at some stage of their evolutionary lifetimes:

(i) In the course of its evolution, one of the stars in a binary system may increase in radius filling its Roche lobe, or the binary separation may shrink due to the gravitational radiation from the system, to the point where the gravitational pull of the companion can remove the outer layers of its envelope. This process is called Roche lobe overflow.

(ii) One of the stars may, at some evolutionary phase, eject much of its mass in the form of a stellar wind; some of this material will be captured gravitationally by the companion (stellar wind accretion).

The situation described in (i) is highly expected during the system evolution; for example, the binary separation my shrink because of orbital angular momentum is being lost from the system as a consequence of stellar wind mass loss, or gravitational radiation, where the rate of energy loss by means of gravitational radiation is given

by the formula

$$\frac{dE}{dt} = -\frac{32G}{5c^5}\left(\frac{M_1 M_2}{M_2 + M_2}\right)^2 a^4\omega^6 \tag{1.3}$$

where ω is the angular velocity ($=2\pi/P_{orb}$) different from ω mentioned as an angle in sec. 1.2.1. For the purpose of studying the accretion process, the distinction between these two alternatives are unimportant, although crucial to the study of the binary evolution. In our discussion of binary accretion we shall have much to say about the first case and very little and maybe nothing about (ii) because it is not applied to the AM CVn systems. On the other hand we will use case (i) to apply it on the case of the AM CVn systems.

1.3 Roche lobe overflow

The problem of two closely placed masses, orbiting each other and described above in the case (i) in which one star of a lower mass fills its Roche lobe and its outer layers are disrupted by the companion. This phenomena was first studied in the 19th century by the French mathematician Edouard Roche and its solution bears his name. The problem is formulated as follows: consider the orbit of a test particle in the gravitational potential due to two massive bodies orbiting each other under the influence of their mutual gravitational interactions. The two bodies (primary and secondary stars in a binary system) as seen in fig 1.2 are assumed to be massive, and that the third body (test particle) does not perturb their Keplerian orbits. Roche treatment additionally introduces two simplifications: that those orbits are circular and that the two main bodies are "centrally condensed", that is, they can be viewed as point masses. This is usually a good approximation for binary systems, since tidal effects tends to circulize originally eccentric orbits in time-scales short compared to the time over which mass transfer occurs. It is convenient to write the masses of the two stars in solar mass since M_1 and M_2 lies in the range (0.05-100)$M_\odot$ for all types of stars. The binary separation, a, is then given in term of the fundamental observational quantity, the binary period, P_{orb} through Kepler's law given in equation(1.2).

For binary periods of order of years , days, or hours, a can be conveniently expressed in the alternative form:

$$a = 1.5 \times 10^{13} M_1^{1/3}(1+q)^{1/3} P_{yr}^{2/3} cm, \tag{1.4}$$

$$= 2.9 \times 10^{11} M_1^{1/3}(1+q)^{1/3} P_{day}^{2/3} cm, \tag{1.5}$$

$$= 3.5 \times 10^{10} M_1^{1/3}(1+q)^{1/3} P_{hr}^{2/3} cm, \tag{1.6}$$

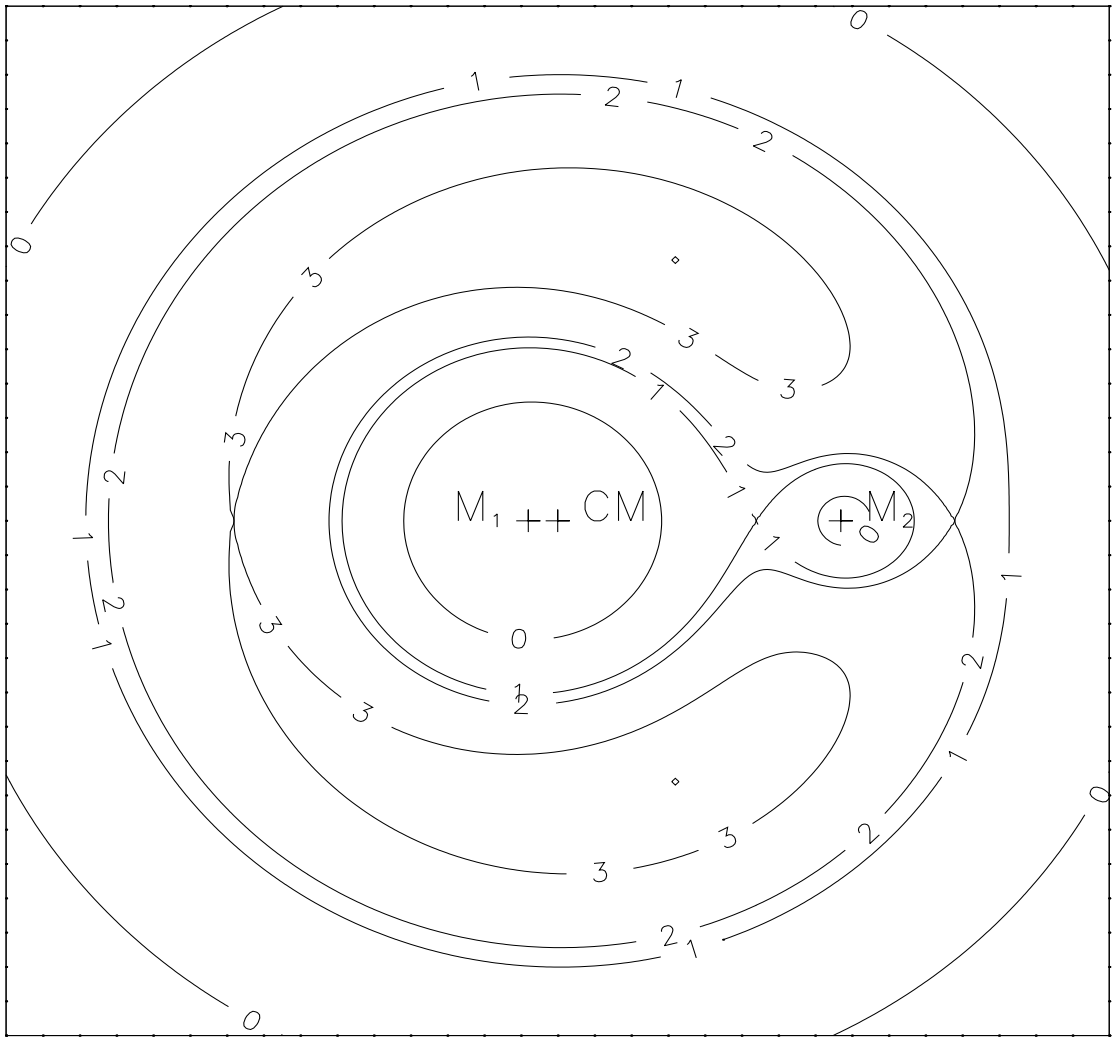

Figure 1.2: The Roche lobe equipotential surfaces. M_1, M_2, CM, 1, 2 and 3 shown in the figure represents the mass of the primary, the mass of the secondary, the system's center of mass, L_1, L_2 and L_3, respectively.

giving the typical sizes of systems in terms of periods ($P_{yr} = P$ in years, etc.) and the mass ratio

$$q = \frac{M_2}{M_1} \tag{1.7}$$

where M_1 and M_2 are the masses of the primary and the secondary (which fills its Roch lobe) star respectively. Any gas flow between the two stars is governed by the Euler equation

$$\rho \frac{\partial \mathbf{v}}{\partial t} + \rho \mathbf{v}.\nabla \mathbf{v} = -\nabla P + f. \tag{1.8}$$

Where $\rho, \mathbf{v}$ and P are the density, velocity and the pressure of the gas respectively, while f is the force per unit volume. This equation has the form of (mass density) $\times$ (acceleration) = (force density) and it is simply an expression of Newton's second law for a continuous fluid. The gas pressure can be expressed using the equation of state of the perfect gas given using the perfect gas law:

$$P = \rho kT/\mu m_H \tag{1.9}$$

where $m_H \approx m_p$ is the mass of the hydrogen atom and μ is the mean molecular weight, which is the mean mass per particle of gas measured in units of m_H. k and T are Boltzmann constant and the temperature of the gas, respectively.

For convenience we will choose to work in the coordinate system, co-rotating with the binary, with angular velocity ω relatively to the inertial frame. We then have to introduce extra terms to include inertia and Coriolis forces. With the above assumptions, the Euler equation for the Roche problem is

$$\frac{\partial \mathbf{v}}{\partial t} + (\mathbf{v} \cdot \nabla)\mathbf{v} = -\nabla \mathbf{\Phi_R} - 2\omega \wedge \mathbf{v} - \frac{1}{\rho}\nabla P \tag{1.10}$$

with the angular velocity of the binary, ω, given in terms of a unit vector, $\mathbf{e}$, normal to the orbital plane by

$$\omega = \left(\frac{G(M_1 + M_2)M_\odot}{a^3} \right)^{1/2} \mathbf{e}$$

On the right hand side of equation (1.10) the term $-2\omega \wedge \mathbf{v}$ represents the Coriolis force per unit mass and the $-\nabla \mathbf{\Phi_R}$ term corresponds to the gravitational and centrifugal forces. The quantity $\mathbf{\Phi_R}$ is called Roche potential and is given by

$$\mathbf{\Phi_R}(r) = -\frac{GM_1M_\odot}{|r - r_1|} - \frac{GM_2M_\odot}{|r - r_2|} - \frac{1}{2}(\omega \wedge r)^2 \tag{1.11}$$

Here $\mathbf{r}_1$ and $\mathbf{r}_2$ are the positional vectors for the two dominant masses.

Let us now examine the form of the equipotential surfaces of $\mathbf{\Phi}_R(r)$. By moving the test particle relatively to the two major masses we see in Fig 1.2, that while our test particle stays close to the center of mass of one of the stars, it feels only minor perturbations, caused by the other star and the Roche equipotential appears as two closely spherical separated surfaces. As we move the test particle away from the star, the equipotential surfaces depart from spherical shape and finally interconnect in L_1, known as a primary Lagrangian point. A test particle, placed at this equipotential surface, belongs equally to each star since their gravitational forces balance each other exactly. The two parts of this dumbbell-shaped surface, passing through L_1 are known as Roche lobes. Continuing to move outward, we see that Roche potential continue to increase, making the L_1 point a *saddle point*. This means that any material particle in the vicinity of the L_1 will find it easier to escape to the other Roche lobe than to escape the system altogether. Further out we meet equipotential surfaces, intersecting in L_2 and L_3 (the secondary and tertiary Lagrangian points), and, finally, at larger distance from the system's center of mass (CM) the potential surface again becomes spherical, so the gravitational field of the system becomes indistinguishable from that of a single mass, located at the center of mass. It should be stressed again, that the Roche potential does not include the Coriolis force, affecting the flow of the matter in the system.

Returning to the definition of a close binary system, we may now refine it. A detached binary is a system where both stars are within their Roche lobes. If in the process of the evolution, one star fills its lobe, so its outer layers will pass through the inner Lagrangian point into the other lobe, and eventually be captured by another star. As will be shown later, unless the other star is too large, the accretion will proceed through an accretion disc. Such mass transfer will continue as long as the mass-losing star fills its Roche lobe. Such system is called a semi-detached binary. However, if the flow of the matter is so strong, that it allows the escape beyond the L_3 equipotential surface, both stars will be enveloped by the ejected gas, forming a contact binary. A single stellar system may go through all those stages as its components evolve. This type of mass transfer is called Roche lobe overflow.

1.4 The geometry of a binary system

To treat Roche lobe overflow in a quantitative manner, we need to establish a set of parameters which can give an idea of the geometry of the critical surface. Those should include both geometrical parameters of the systems and physical parameters of its components, in particular, its dependence on the mass ratio q and the binary separation a. The main quantitatives we shall need are measures of the sizes of

the Roche lobe and of the distances of L_1 point from either star. One of the most important geometric parameters is the secondary lobe radius. Since the critical surface is of a peculiar shape, it has to be described by some mean value. Reasonable substitute seems to be a volume averaged Roche lobe radius, which is the radius of a sphere, having the same volume as lobe as seen in Fig. 1.3. The good fit for all values of q is given by the approximate analytic formula Eggleton (1983)

$$\frac{R_{L_2}}{a} = \frac{0.49q^{2/3}}{0.6q^{2/3} + \ln(1+q^{1/3})} \tag{1.12}$$

Clearly, we can find the lobe radius R_{L_1} of the primary by replacing q by q^{-1}. Due to Paczynski, it is often convenient to use a simple form of equation(1.12) for system with q ranges between $0.1 - 0.8$ given as follows

$$\frac{R_{L_2}}{a} = \frac{2}{3^{4/3}}\left(\frac{q}{1+q}\right)^{1/3} = 0.462\left(\frac{M_2}{M_1+M_2}\right)^{1/3} \tag{1.13}$$

The values of R_{L_1} and R_{L_2} can be calculated if we know the values of both a and q, where a can be calculated as a function of M_1 and M_2 using Fig. 1.3 and rewriting equation(1.2) as

$$a = \left(\frac{G}{4\pi^2}(M_1+M_2)M_\odot P_{orb}^2\right)^{1/3}$$

or as a function of q using any of the equations (1.4 - 1.6). In some cases it is difficult to calculate R_{L_1} or R_{L_2} as a function of M_1 and M_2 due to the lack of information about the system, while it can be easier to calculate it as a function of q if we can calculate q from the observable quantities if they are available. It can be found by using the system's *superhump period*, P_s, which can be observed in light-curves of certain binary systems as a photometric modulation with a period few percent longer or shorter than the orbital. As numerical disc dynamics simulations suggests, it might reflect disc precession, which produces additional shear and thus variation in dissipated energy, emitted from the disc surface Frank et al. (1992), Warner (1995b). The *beat period* then is given by

$$\frac{1}{P_b} = \mid \frac{1}{P_s} - \frac{1}{P_{orb}} \mid \tag{1.14}$$

For mass ratios smaller than $q = 0.22$ the beat period can be expressed as: (Warner 1995a)

$$\frac{P_b}{P_{orb}} = A\frac{1+q}{q}, \tag{1.15}$$

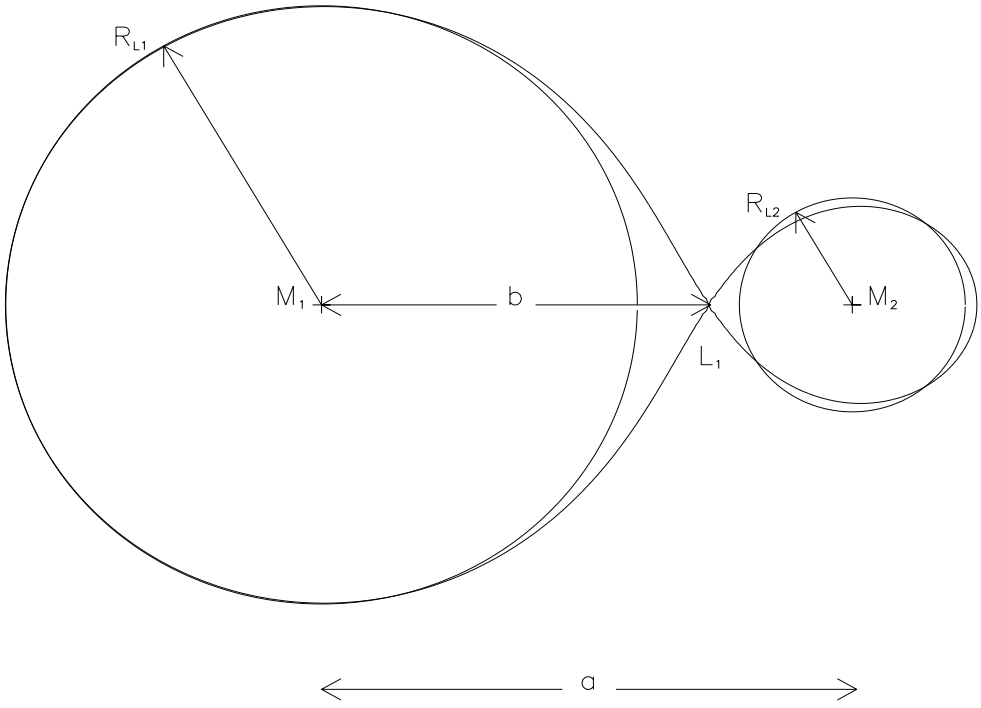

Figure 1.3: This figure shows a binary system components, the primary and the secondary stars with their Roch lobes.

where

$$A \approx \begin{cases} 3.85 & \text{for } 0.1 \leq q \leq 0.22; \\ 3.73 & \text{for } q \leq 0.1. \end{cases}$$

By substituting P_{orb} from (1.14) into (1.15), q will have the following form:

$$q = \frac{A}{\frac{P_s}{|P_{orb} - P_s|}} - A \tag{1.16}$$

Another important parameter is the distance from the primary Lagrangian point L_1 to the center of a primary, b_1. It can be approximated by the Plavec and Kratochvil formula (Frank et al. (1992))

$$\frac{b_1}{a} = 0.500 - 0.227 \log q \tag{1.17}$$

The mean density $\bar{\rho}$ of a lobe-filling star can be determined by the binary period P_{orb}:

$$\bar{\rho} = \frac{3 M_2 M_\odot}{4\pi R_2^3} \cong 115 P_{orb_{(hr)}}^{-2} \text{g cm}^{-3} \tag{1.18}$$

If one assumes a structure for the lobe-filling star, and thus relation $R_2(M_2)$, then equation (1.18) fixes its properties uniquely for a given period. For example, if we assume that the lobe-filling star is close to the lower main sequence we know that its radius and mass are approximately in solar units, i.e $M_2 \cong R_2/R_\odot$ thus (1.18) can be written as follows

$$\bar{\rho} = \frac{3 M_2 M_\odot}{4\pi R_2^3} = \frac{3 M_\odot}{4\pi R_\odot^3} \frac{1}{M_2^2} = \frac{1.4}{M_2^2} \text{g cm}^{-3}$$

This relation and (1.18) now give a *period* $-$ *mass* relation

$$M_2 \cong 0.11 P_{orb_{(hr)}} \tag{1.19}$$

and a *period* $-$ *radius* relation

$$R_2 \cong 7.9 \times 10^9 P_{orb_{(hr)}} \text{cm} \tag{1.20}$$

Note that these relations come about because we assumed that the secondary star was close to the lower main sequence. At the same time we cannot assume a main-sequence star structure or any other type without checking carefully the conditions for this to hold. For example the previous relation will be different if the mass loosing star is a white dwarf. An important consequence of the mass transfer in a binary system is that it will change its mass ratio q, not only that but the orbital

period P_{orb} and the separation a by the same process, because of the redistribution of angular momentum within the system. Since the Roche geometry is determined by a and q, it is important to know whether the effect of these changes will shrink or swell the Roche lobe of the mass-loosing star and the whole system. We will briefly investigate this effect to determine the rate of expansion or contraction of the Roche lobe. For the mass transfer to be self-sustaining the mass-losing star lobe should either contract, or a star should expand faster than the lobe due to some process. Roche geometry changes are governed by the angular momentum of the system J. We will describe it as the sum of the components angular momentum

$$J = (M_1 a_1^2 + M_2 a_2^2) M_\odot \omega$$

where

$$a_1 = \frac{M_2}{M_1 + M_2} \text{ and } a_2 = \frac{M_1}{M_1 + M_2}$$

are the distances of the two stars from the centre of mass. Using the value of $\omega = 2\pi/P_{orb}$ and substituting for P_{orb} from (1.2) gives

$$J = M_1 M_2 \sqrt{\frac{Ga}{M_1 + M_2}} M_\odot^{3/2} \tag{1.21}$$

Usually it is a good approximation to assume that all the mass lost by the mass loosing star is accreted by the primary, so the total angular momentum and the accreted mass will remain conserved within the system, so that $\dot{M}_1 + \dot{M}_2 = 0, \dot{M}_2 < 0$. Logarithmic differentiation of (1.21) with respect to time gives

$$\frac{\dot{a}}{a} = \frac{2\dot{J}}{J} + \frac{2(-\dot{M}_2)}{M_2}\left(1 - \frac{M_2}{M_1}\right) \tag{1.22}$$

Conservative mass transfer is characterized by constant binary mass and angular momentum; setting $\dot{J} = 0$ in (1.22) and using $\dot{M} < 0$, we see that the binary separation expands ($\dot{a} > 0$) if conservative mass transfer takes place from the less massive to the more massive star, this means more mass is placed near the center of mass, so the remaining mass of the secondary M_2 must move in a wider orbit to conserve angular momentum and the orbital period of the system will increase. One good application of such phenomena is the AM CVn stars where the mass-losing star is the one with a lower mass. Conversely, if the mass transfer occur from the more massive to the less massive star, the binary orbit will shrink and the binary separation and the orbital period of the system will decrease. The Roche lobe size is affected by the change in the mass ratio as well as separation. Logarithmic

differentiation of (1.13) gives

$$\frac{\dot{R_{L_2}}}{R_{L_2}} = \frac{\dot{a}}{a} + \frac{\dot{M_2}}{3M_2} \tag{1.23}$$

combining with (1.22) yields

$$\frac{\dot{R_{L_2}}}{R_{L_2}} = \frac{2\dot{J}}{J} + \frac{2(-\dot{M_2})}{M_2}\left(\frac{5}{6} - q\right) \tag{1.24}$$

Clearly there are two cases which controls such equation, depending on whether q is larger or smaller than 5/6. In the case of $q > 5/6$ conservative mass transfer shrinks the Roche lobe down on the mass-losing star, and any angular momentum loss ($\dot{J} < 0$) will accentuate this. Mass transfer continues only if either (i) the secondary star expands, or (ii) the binary loses angular momentum. Case (i) occurs when the secondary star evolves off the main sequence. Then its radius will expand on a nuclear time-scale t_{nuc} determined by hydrogen shell burning and as a result the lobe too will expand on the time-scale t_{nuc}. Case (i) describes mass transfer driven by evolutionary expansion of the secondary star. Many systems and cataclysmic variables are a best example where the secondary star has such a low mass that the main-sequence lifetime exceeds the Hubble time, and this mechanism will never occur. In such case mass transfer must be driven by angular momentum loss case (ii). Different mechanisms can remove angular momentum specially from systems with short-period, gravitational radiation is quiet efficient. Another possibility is the loss of angular momentum to the mass loss by the wind, any mechanism which spins down the secondary star will ultimately remove angular momentum from the binary, as tides force the secondary to corotate.

1.5 Disc formation

The consideration of the last two sections have shown how mass transfer in close binary systems can occur via Roche lobe overflow. The result of this is that an element of mass, passing through the inner Lagrangian point L_1 from one of the Roche lobes to another as in fig(1.2) has rather high specific angular momentum in many cases, so that it cannot accrete and settle directly on the mass-capturing star. Due to the high specific angular momentum of the matter, it will form a ring around the mass-capturing star as will be soon explained in detail. A cross-section of a mass transfer channel around L_1 depends on the overflow of the secondary Roche lobe. For our purpose it is sufficient to visualize this channel as a point source of particles,

injected into the primary Roche lobe with certain velocity, which we will divide into parallel and perpendicular velocities $v_{\parallel}$ and $v_{\perp}$ with respect to the line, connecting the centers of the components in a *non*-rotating frame.

We have $v_{\perp} \sim b_1\omega$, while $v_{\parallel} \leq c_s$, where the c_s is the sound speed in the envelope of the secondary, since we expect the gas to be pushed through L_1 by pressure. According to our initial definitions the distance from L_1 to the center of a primary b_1 is less than a half of binary separation. Using $\omega = 2\pi/P_{orb}$ and expressing a through

$$a = 2.9 \times 10^{11} M_1^{1/3} (1+q)^{1/3} P_{orb_{(day)}}^{2/3}$$

we obtain

$$v_{\perp} \sim 100 M_1^{1/3} (1+q)^{1/3} P_{orb_{(day)}}^{-1/3} \text{ km s}^{-1}$$

In such case $v_{\perp} \ll v_{\parallel}$ and it cannot be higher than 10 km/s for the temperature $< 10^5$K and since $v_{\parallel} \approx c_s$ the stream will follow a ballistic trajectory determined by the Roche lobe potential, as though it consisted of a set of test particles. To a good approximation we can take the stream trajectory as the orbit of a test particle released from rest at L_1 and falling in the gravitational field of the primary alone. Its orbit can be assumed to be elliptical and precessing due to the perturbations caused by the secondary. This elliptical orbit will be lying in the primary plane. A continuous stream trying to follow this orbit will therefore intersect itself, resulting in dissipation of energy via shocks which eventually will be radiated away. However, the stream of particles have no easy way to get rid of the angular momentum, therefore they will settle at the lowest energy (circular) orbit for a given angular momentum. In such case we expect the gas initially to orbit the primary in the binary plane at a radius R_{circ} such that the Kepler orbit at R_{circ} has the same specific angular momentum as the transferring gas had on passing through L_1. The gas in such case will have circular velocity

$$v_{\phi}(R_{circ}) = \left(\frac{G M_1 M_{\odot}}{R_{circ}} \right)^{1/2}$$

By equating the angular momentum of such circular Keplerian orbit L_{circ} and the initial momentum at the primary Lagrangian point L_{L_1} we get

$$L_{circ} = R_{circ} . \left(\frac{G M_1 M_{\odot}}{R_{circ}} \right)^{1/2} = b_1^2 . \omega = L_{L_1}$$

Using $\omega = 2\pi/P_{orb}$ where P_{orb} is the binary orbital period and rearranging the result to include a we get

$$\frac{R_{circ}}{a} = \left(\frac{4\pi^2}{G M_1 M_{\odot} P_{orb}^2} \right) a^3 \left[\frac{b_1}{a} \right]^4$$

Substitute for b_1 from (1.17) and for P_{orb} from (1.2) yields

$$\frac{R_{cric}}{a} = (1+q).(0.500 - 0.227 \log q)^4 \tag{1.25}$$

If you compare this result with (1.17), you will find that R_{circ} lies within the Roche lobe of the primary. It is also easy to show that the circularization radius R_{circ} is always smaller than the lobe radius R_L of the primary. Typically it is a factor 2-3 smaller, except for very small q. The captures material will orbit within the Roche lobe of the primary unless the primary already occupies this space, i.e. if $R_\star > R_{circ}$. Using equations (1.4 - 1.6) we can rewrite (1.25) as

$$R_{circ} \cong 4(1+q)^{4/3}[0.500 - 0.227 \log q]^4 P^{2/3}_{orb_{(day)}} R_\odot \tag{1.26}$$

Since the gas flow from the mass loosing to the primary stars, the gas has to meet this drain of energy, the only way to achieve this is by sinking deeper into the gravitational potential of the primary, by orbiting it more and more closely, this in turn requires it to lose angular momentum. Since a circular orbit has the least energy for a given angular momentum, we might expect most of the gas to spiral slowly inwards towards the primary, through a series of approximately circular orbits in the binary orbital plane. This spiraling-in process entails a loss of angular momentum. With the absence of the external torques, this can only occur by transfer of angular momentum outwards through the disc by the internal torques. Thus the most famous phenomena of the disc will occur in this case, and that is, the outer parts of the disc will gain angular momentum and will spiral outwards. The original ring of matter at $R = R_{circ}$ will spread to both smaller and larger radii by this process and form the accretion disc.

1.6 Disc basics

One of the basic assumptions is that the disc is geometrically thin, which means $H \ll R$, where H is the thickness of the disc and R is the radial distance. The consequence of this assumption is that $dP/dR \simeq 0$, this has another important consequence, because the equation of motion then in the radial direction may be written according to the hydrostatic equilibrium as:

$$\frac{1}{\rho}\frac{dP}{dR} = \frac{d\phi}{dR} + \frac{v^2}{R} \tag{1.27}$$

where (dP/dR) is the pressure force, $(d\phi/dR)$ is the gravitational force, $(\phi = -GM/R)$ and (v^2/R) is the centrifugal force. As mentioned before that if $H \ll R$ then $(dP/dR = 0)$, and equation (1.27) becomes:

$$\frac{d\phi}{dR} = -\frac{v^2}{R} \tag{1.28}$$

This result means that:

The gravitational force = - The centrifugal force

This means that the gas around the compact object is moving as free particles. Finally we are going to write the basic relations for a standard accretion disc model, with $H \ll R$, which moves in Keplerian orbits around the central star, starting with the angular velocity $\Omega_K = (\frac{GM}{R^3})^{1/2}$, the angular momentum $\ell = (GMR)^{1/2}$ and finally the orbital Keplerian velocity $v_K = (GM/R)^{1/2}$.

1.7 Viscosity

What causes the transport of matter and angular momentum in accretion disc? This question is the subject of a longstanding debate, but most of those working in this field tend now to agree that it has been answered, since even a very weak magnetic field leads to a linear instability (Chandrasekhar 1961) which, in its fully developed regime, is able to provide necessary stresses (Balbus & Hawley 1991; Hawley & Balbus 1991). However, it is unlikely that this mechanism operates in cold neutral discs (e.g Gammie & Menou 1998). Besides, this issue which has not been settled yet is whether this magnetic instability is the only instability responsible for the "anomalous viscosity", or whether a purely hydrodynamic instability, generated by shear in differentially rotating discs, may not be of comparable or even higher efficiency. Since a non-magnetic Keplerian disc is linearly stable, this hydrodynamic instability needs a finite amplitude perturbation to be triggered. It is important to note that the widely used α-prescription for turbulent viscosity (Shakura & Sunyaev 1973) does not invoke any particular mechanism at the origin of turbulence: it is a simple parameterization which is tailored to yield turbulent velocities that remain subsonic. It is often asserted that the main success of the α-prescription is the prediction of recurrent outburst of dwarf novae (e.g. Cannizzo 1993). However, if such eruptive phenomena are indeed of thermal origin, as is commonly thought, it is likely that many ad-hoc viscosities, not only α-prescription, could work as well. The machinery part of viscosity that it is slowly lowering material in the gravitational

potential of an accreting object and extracting the energy as radiation. A vital part of this machinery is the dissipation process which converts the orbital kinetic energy into heat. One of the main unsolved problems of disc structure is the precise nature of this dissipation. The material at the neighboring radii moves with different angular velocity Ω_K, but whenever the rotation law departs from $\Omega_K = const$ or solid body rotation, fluid elements on neighboring streamlines will slide past each other. Because of the ever present chaotic thermal motions of fluid molecules or turbulent motions of fluid elements, viscous stresses are generated. In this case the angular momentum is transported orthogonally to the gas motion.

1.7.1 Two rings exchange mass and angular momentum

In this subsection we will study the behavior of the accretion disc orbits. This can be done by assuming two neighboring streamlines (rings) moving with Keplerian rotation around the primary star. The two orbits matter will have the following parameters:

(i) (m_1, m_2) the test particles masses.

(ii) (e_1, e_2) the specific energy.

(iii) (ℓ_1, ℓ_2) the specific angular momentum.

(iv) (j_1, j_2) the total angular momentum.

In this case the time-scale on which the orbiting gas can redistribute its angular momentum, is normally lower than the time-scale, over which it loses energy by radiative cooling t_{rad} and dynamical (orbital) time-scale t_{dyn}. Therefore, the gas will lose as much as it can for a given angular momentum, which itself decreases more slowly. Since a circular orbit has the least energy for a given angular momentum, we must expect most of the gas to spiral inwards towards the primary through the series of approximately circular orbits in the binary orbital plane. This spiraling in process entails a loss of angular momentum, in the absence of the external torques, this only occurs by transfer of angular momentum outwards through the disc by the internal torques, thus the outerparts of the disc will gain angular momentum and will spiral outwards and the innerparts of the disc will gain mass and spiral inwards.

Let us check what would be the behavior of the radii of the two orbits with the change of ℓ and m.

$$\ell = \frac{j}{m}, \ell = \ell_K(R)$$

where ℓ is the specific angular momentum and K stands for Keplerian. In such case the increase of the matter's angular momentum will make it to spiral inwards and

the angular momentum will spiral outwards, i.e. the radius of the orbit will increase and that means

$$\ell_1' = \ell_1 + d\ell = \frac{j_1'}{m_1'} = \frac{j_1 - dj}{m_1 + dm} \tag{1.29}$$

$$\ell_1' = \ell + d\ell = (\frac{j_1}{m_1})\Big(\frac{1 - dj/j_1}{1 + dm/m_1}\Big) \tag{1.30}$$

but

$$\frac{1}{1 + dm/m_1} = 1 - (\frac{dm}{m_1}) + (\frac{dm}{m_1})^2 + ...$$

Take the first two terms of the last expansion, and then substitute in (1.30) we get

$$\ell_1' = \ell_1 \times (1 - \frac{dj}{j_1} - \frac{dm}{m_1}) \tag{1.31}$$

This relation means that $\ell_1' < \ell_1$, which also means that the mass in the accretion disc accretes inwards while the angular momentum accretes outwards.

1.8 AM Herculis stars

Many accretion discs and probably the AM CVn discs are part of them, have been formed around the central star which has a magnetic field. The strength of this magnetic filed can vary from system to system and cause some kind of instability, such as the linear instability of Chandrasekhar (1961) and Balbus & Hawley (1991), which we talked about in the previous section. Magnetic fields can also push the disc away from the surface of the central star, forming a hole in the disc or a boundary layer. In some other systems the magnetic field can be very strong (several tens of millions of Gauss) and in such case the matter in the accretion stream is partially ionized, it can't form a disc (because charged particles can not cross the magnetic field lines, only spiral around them). Instead, the gas is threaded onto the magnetic field lines and plunges straight down onto magnetic poles of the white dwarf, generating X-ray emission at the poles. AM Herculis stars are the best example of the magnetic systems. The magnetic field in these stars is so strong (it is a bout fifty million times the strength of the Earth's magnetic field) that no accretion disc can form. During secular evolution the secondary star loses mass to the primary. The matter flow is channeled by the magnetic field and accretes via accretion columns near the magnetic poles. In such systems the magnetic field of the white dwarf is strong enough to synchronize the rotation of the white dwarf with that of the binary, the red star secondary and the white dwarf rotate essentially as rigid bodies.

Chapter 2

Accretion disc theory

2.1 Introduction

Accretion discs are important ingredients in our current understanding of many astrophysical systems on all scales. Examples of presumed disc accretors include young stars, compact objects in close binary systems, active galactic nuclei (AGN) and quasars (QSQs). The basic philosophy behind the accretion disc model is the following: The matter first forms a disc shaped annular structure around the accreting object, at the circularization radii appropriate to the specific angular momentum of the incoming matter. The thickness of the disc H is very small compared to the radius R. The material in the disc rotates at near Keplerian velocities, and hence there is shear between two adjacent layers. One of the main long-standing problems of accretion discs, is their angular momentum transport mechanism. In order to sustain the observed mass transfer rate, and the size of the disc, highly efficient viscous process must be available to transport the angular momentum outwards. Viscosity, the exact nature which still is under discussion, operates in the disc, transports angular momentum outwards, and leads to small flux of matter in the radial direction. The viscosity generates heat, which is assumed to be radiated in the perpendicular direction to the surface of the disc. The famous α prescription (Shakura & Sunyaev 1973), which scales the effective viscosity by a dimensionless parameter α, has been very successful. It also shows how poorly their processes are understood. All the information about a distant accretion disc, comes from studying its electromagnetic radiation. However, it is very important to realize that unlike most laboratory situations, radiation is not only the probe of the medium, but also one of the most important energy balance agents. In other words, radiation not only reveals the structure of the disc, but in fact determines it. All diagnostic approaches that treat

disc radiation only as a probe, are therefore, at least in principle, uncertain. Several papers have already been published on the computations of the accretion disc spectra, applying different assumptions about the nature of the system, and considering system parameters in various ranges. One of the most important papers in this field is the one by La Dous (1989), which focused on applying as wide range of parameters as possible. All the computations which has been done in the past, focused mostly on the solar composition stationary accretion disc. The purpose of this project, is to investigate the physics of the pure helium discs, and to discuss the influence of different physical parameters, on the integrated radiation in the optical region of the spectra (where the accretion disc dominates) in both LTE and NLTE cases.

Discs in different types of systems are governed by different boundary conditions which will affect their structure. For example, tidal forces and the impact of the gas stream at the edge of the disc are important in close binaries but do not occur in active galactic nuclei discs. A boundary layer forms between the accretion disc and the accreting white dwarf or neutron star, but will be absent if the compact object is a black hole. The observed differences between these systems should shed light on the boundary layer physics. Relativistic effects must be included when calculating accretion onto a black hole.

Many investigations about the wind itself has been done so far, but we always look for a better understanding to this phenomena. For example, how is it driven, where does it leave the disc, what energy does it remove and what effect does this have on the temperature profile in the disc and on the boundary layer? With the space telescope high speed observations of the UV resonance lines produced in the wind has been obtained. Perhaps observations such as these in eclipsing systems, when combined with the spatial distributions of the line emissivity and continuum from the disc itself, will give answer to these questions.

The physics of all types of disc are interrelated, therefore studying one type of disc can help explain them all. For example, one particular theory, the thermal limit cycle, was first developed to explain the outburst mechanism of dwarf novae, though it is not the only possible explanation. This limit cycle has since been applied to low mass X-ray binaries and active galactic nuclei to explain various phenomena such as soft X-ray transients and variability in quasars.

In the previous chapter we have seen that in many binary systems undergoing mass transfer, the accreting material will have sufficient angular momentum to form an accretion disc, and we have discussed the basics of the such disc. We have also discussed briefly another type of systems where the central star has a very strong magnetic field, which prevents such disc to form. In this chapter we will study the accretion discs in detail starting with α-disc, and then derive all the equations of

the thin disc approximation, where the disc flow is confined so closely to the orbital plane that to the first approximation one can regard the disc as a two-dimensional gas flow.

2.2 α-Disc

α - discs are the standard model which have been studied in detail by Shakura and Sunyaev (1973). The mass in α - disc sustains Keplerian orbits, and thus the orbital speeds vary with radius producing shear stress. Viscosity therefore causes the mass of the disc to accrete towards successively inner orbits about the primary star. As the orbits of the mass of the disc move closer towards the primary, gravitational energy is lost and converted into radiation, producing a luminous disc.

The accretion disc would have an inner radius equal to the radius of the white dwarf or more and the outer radius reaching approximately the inner Lagrangian point (see figure 1.1 and 1.2). In this section we are going to discuss the radial temperature and the radiation emission distribution in α - disc. Taking two arbitrary radii R_1 and R_2 within the disc, assuming that the disc is in a steady state (stationary), the sum of the torques due to shear stresses in the section of disc between R_1 and R_2 plus the transport in and out of angular momentum in the same section must be zero, see Fig. 2.1 for illustration. Consider ω to be the angular speed (which is radially dependent, corresponding to Keplerian orbits). W_1 and W_2 are the shear stresses between R_1 and R_2 respectively. This will lead us to the following relation:

$$0 = W_1 2\pi R_1^2 - W_2 2\pi R_2^2 + \dot{M}\omega_2 R_2^2 - \dot{M}\omega_1 R_1^2 \tag{2.1}$$

where W_1 and W_2 are the shear stresses at R_1 and R_2 respectively, and ω_1 and ω_2 are the corresponding angular velocities. Therefore

$$W_1 2\pi R_1^2 + \dot{M}\omega_1 R_1^2 = W_2 2\pi R_2^2 + \dot{M}\omega_2 R_2^2 \tag{2.2}$$

Since R_1 and R_2 are arbitrary radii, we have that:

$$W 2\pi R^2 + \dot{M}\omega R^2 = C(constant) \tag{2.3}$$

Assuming that the shear stress at the inner radius of the disc is negligible (Shakura & Sunyaev 1973), we have

$$W 2\pi R^2 + \dot{M}\omega R^2 = \dot{M}\omega_{in} R_{in} \tag{2.4}$$

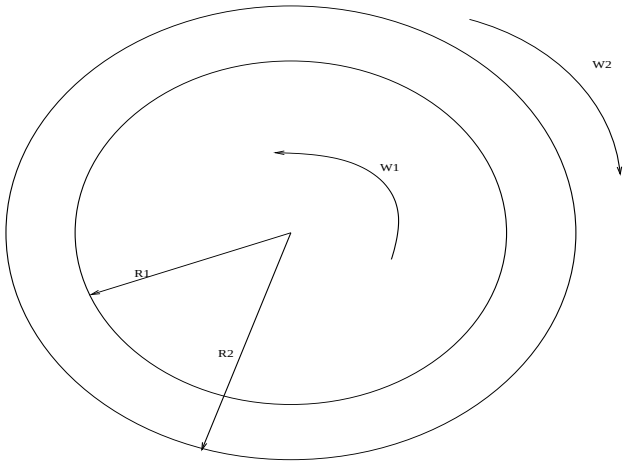

Figure 2.1: Section of accretion disc between radii R_1 and R_2. W_1 and W_2 are the shear stresses at R_1 and R_2 respectively.

where R_{in} is the inner radius of the disc and ω_{in} is the angular speed at the inner radius. Thus,

$$W = \frac{\dot{M}}{2\pi R^2}(\omega R^2 - \omega_{in} R_{in}^2) \tag{2.5}$$

The amount of energy being emitted from the disc in the section between radii R_1 and R_2 is equal to the work due to shear stresses in R_1 and R_2 plus the transport in and out of energy in the same section. Therefore

$$\dot{E_{12}} = W_1 2\pi R_1 v_{\phi_1} - W_2 2\pi R_2 v_{\phi_2} - \dot{M}\left(\frac{v_{\phi_1}^2}{2} - \frac{GM_\star}{R_1}\right) + \dot{M}\left(\frac{v_{\phi_2}^2}{2} - \frac{GM_\star}{R_2}\right) \tag{2.6}$$

where $M_\star$ is the mass of the central star, $\dot{E_{12}}$ is the energy emitted in the corresponding section of the disc and v_{ϕ_1} and v_{ϕ_2} are the orbital speeds at R_1 and R_2 respectively. The energy emitted per unit area Q at radius R_1 would be:

$$Q(R_1) = \lim_{R_2 \to R_1} \frac{\dot{E_{12}}}{2\pi(R_2^2 - R_1^2)} \tag{2.7}$$

Substituting in (2.7), we have:

$Q(R_1) = \lim_{R_2 \to R_1} \frac{1}{2\pi(R_2+R_1)} \frac{1}{R_2-R_1} \times \left(\left[\dot{M} \left[\frac{v_{\phi 2}^2}{2} - \frac{GM_\star}{R_2} \right] - W_2 2\pi R_2 v_{\phi_2} \right] - \left[\dot{M} \left[\frac{v_{\phi 1}^2}{2} - \frac{GM_\star}{R_1} \right] - W_1 2\pi R_1 v_{\phi_1} \right] \right)$

Since R_1 and R_2 are arbitrary radii within the disc, we have that in general for a radius R:

$$Q = \frac{1}{4\pi R} \frac{d}{dR} \left[\dot{M} \left(\frac{v_\phi^2}{2} - \frac{GM_\star}{R} \right) - W 2\pi R v_\phi \right] \tag{2.8}$$

Considering that the mass of the disc are following the Keplerian orbits ($v_\phi^2 = GM_\star/R$) and $\omega^2 = GM_\star/R^3$, substituting equation (2.5) in equation (2.8) and evaluating the corresponding derivative, we have:

$$Q = \frac{3\dot{M}GM_\star}{8\pi R^3} \left[1 - (\frac{R_{in}}{R})^{1/2} \right] \tag{2.9}$$

The luminosity of the disc L_{disc} may be obtained by integrating the energy emission per area Q over the surface of the disc

$$L_{disc} = \int_{R_{in}}^{R_{out}} 4\pi R Q dR \tag{2.10}$$

where R_{in} and R_{out} are the inner and outer radii of the disc respectively. Substituting equation (2.9) in equation (2.10) and evaluating the corresponding integral we obtain:

$$L_{disc} = \frac{\dot{M}GM_\star}{2R_{in}} \left[1 - \frac{3R_{in}}{R_{out}} \left(1 - \frac{2}{3} (\frac{R_{in}}{R_{out}})^{1/2} \right) \right] \tag{2.11}$$

assuming that $R_{in} \ll R_{out}$ we obtain:

$$L_{disc} = \frac{\dot{M}GM_\star}{2R_{in}} \tag{2.12}$$

which is the energy equation. Assuming that the disc emitting locally as a blackbody, and considering equation (2.9), the following is the radial effective temperature distribution of the disc

$$T_{eff}(R) = \left[\frac{3G\dot{M}M_\star}{8\pi R^3 \sigma_s} \left(1 - (\frac{R_{in}}{R})^{1/2} \right) \right]^{1/4} \tag{2.13}$$

where σ_s is the Stefan-Boltzmann constant

2.3 Stationary thin accretion disc

In this section we will discuss the basics of a stationary thin accretion disc around a compact object. The task will be to derive and solve the basic equations involved in such theory. Some of the equations which will be used in this section are taken from Frank et al. (1992).

Basic assumptions:

• The disc is geometrically thin in the z direction i.e. $H \ll R$ and the matter moves with Keplerian rotation

• The disc is stationary and assumed to be optically thick.

• Pressure is given as: $P = P_{rad} + P_{gas}$.

• The mass of the central star M and the mass accretion rate $\dot{M}$ are known quantities.

We consider first the structure of the disc in the z-(vertical) direction and since there is essentially no flow in this direction, hydrostatic equilibrium must hold:

$$\frac{1}{\rho}\frac{dP}{dz} = \frac{d\phi}{dz} = \frac{GM}{R^2}\frac{z}{R} \tag{2.14}$$

If the typical scale-height of the disc in the z-direction is H, then we may set $dP/dz \sim P/H$ and $z \sim H$ then equation (2.14) becomes

$$\frac{1}{\rho}\frac{P}{H} = \frac{GM}{R^2}\frac{H}{R} \tag{2.15}$$

but $c_s^2 = P/\rho$ where c_s is the speed of sound and $\rho = \Sigma/H$ where Σ is the surface density. Substitute the value of c_s in equation (2.15) to get

$$c_s^2 = \left(\frac{GM}{R}\right)\left(\frac{H^2}{R^2}\right) \longrightarrow c_s^2 = v_k^2\left(\frac{H}{R}\right)^2 \tag{2.16}$$

From this result we can write the first disc equation as

$$\frac{c_s}{v_k} = \frac{H}{R} \longrightarrow H \cong c_s(\frac{R}{GM})^{1/2}R \tag{2.17}$$

In this case we demand $c_s \ll (GM/R)^{1/2}$ which means for a thin disc we require that the local Kepler velocity should be highly supersonic. This condition has its effect on the temperature of the disc and on the cooling mechanism.

Next we write conservation equations for the mass and angular momentum transport in the disc due to the radial drift motions. An annulus of the disc material laying between R and $R + \Delta R$ has total mass $2\pi R\Delta R\Sigma$ and total angular momentum $2\pi R\Delta R\Sigma R^2\Omega$. The rate of change of both quantities is given by the net flow from the neighboring annuli. For the mass of the annulus $\frac{\partial}{\partial t}(2\pi R\Delta R\Sigma) = v_R(R,t)2\pi R\Sigma(R,t) - v_R(R+\Delta R,t)\times 2\pi(R+\Delta R)\Sigma(R+\Delta R,t) \cong -2\pi\Delta R\frac{\partial}{\partial R}(R\Sigma v_R)$. Thus, in the limit $\Delta R \to 0$ we get the mass conservation equation

$$R\frac{\partial\Sigma}{\partial t} + \frac{\partial}{\partial R}(R\Sigma v_R) = 0 \tag{2.18}$$

In this case of stationary accretion disc, nothing depends on time so $\frac{\partial}{\partial R}(R\Sigma v_R) = 0 \to R\Sigma v_R =$ constant. This represents the constant inflow of mass through each point of the disc and since $v_R < 0$ we write

$$\dot{M} = 2\pi R\Sigma(-v_R) \tag{2.19}$$

The conservation of angular momentum equation is given as:

$$R\frac{\partial}{\partial t}(\Sigma R^2\Omega) + \frac{\partial}{\partial R}(R\Sigma v_R R^2\Omega) = \frac{1}{2\pi}\frac{\partial G}{\partial R} \tag{2.20}$$

where $G(R,t)$ represents the viscous torques given as $G(R,t) = 2\pi R\nu\Sigma R^2 d\Omega/dR$. where $\nu \sim \lambda\bar{v}$ defined as the coefficient of kinematic viscosity. Assuming $\partial/\partial t = 0$ then equation (2.20) becomes

$$R\Sigma v_R R^2\Omega = \frac{G}{2\pi} + \frac{C}{2\pi}$$

where C is a constant. Substituting the value of $G(R,t)$ we get

$$-\nu\Sigma d\Omega/dR = \Sigma(-v_R)\Omega + C/(2\pi R^3) \tag{2.21}$$

The constant C is related to the rate at which angular momentum flows into the compact star, or equivalently, the coupling exerted by the star on the inner edge of the disc. Let us suppose that the disc extends all the way down to the surface $R = R_\star$ of the central star. In realistic situation, the star must rotate more slowly than break-up speed at its equator, i.e with angular velocity $\Omega_\star < \Omega_k(R_\star)$. In this

case the angular velocity of the disc material remains Keplerian and thus increases inwards, until it begin to decrease to the value $\Omega_\star$ in a boundary layer of a radial extent t_b. Hence there exists a radius $R = R_\star + t_b$ at which $\Omega' = d\Omega/dR = 0$. In such case $t_b \ll R_\star$, and thus Ω is very close to its Keplerian value at the point where $\Omega' = 0$ which means

$$\Omega(R_\star + t_b) = \left(\frac{GM}{R_\star^3}\right)^{1/2}[1 + (b/R_\star)] \tag{2.22}$$

If t_b instead is comparable to $R_\star$, the thin disc approximations all break down at $R = R_\star + t_b$, this is no longer a boundary layer, but some kind of thick disc. At $R = R_\star + t_b$, (2.21) becomes

$$C = 2\pi R_\star^3 \Sigma v_R \Omega(R_\star + t_b)|_{R_{\star+t_b}} \tag{2.23}$$

which by using (2.22) and (2.19) implies

$$C = -\dot{M}(GMR_\star)^{1/2} \tag{2.24}$$

to terms of order $a/R_\star$. Substituting this into (2.21) and setting $\Omega = \Omega_k = (GM/R^3)^{1/2}$, we will find another basic disc equation

$$\nu\Sigma = \frac{\dot{M}}{3\pi}\left[1 - \left(\frac{R_\star}{R}\right)^{1/2}\right] \tag{2.25}$$

Next we will try to find the equation which represents the total flux emitted from the disc where

$$2F = Q^+ \longrightarrow F = \frac{1}{2}Q^+$$

where

$$Q^+ = \frac{3\dot{M}GM_\star}{4\pi R^3}\left[1 - \left(\frac{R_{in}}{R}\right)^{1/2}\right]$$

is the energy emitted from one side of the disc while the total flux represented by the total energy emitted from the two sides of the disc are given as:

$$F(R) = \frac{3\dot{M}GM_\star}{8\pi R^3}\left[1 - \left(\frac{R_{in}}{R}\right)^{1/2}\right] \tag{2.26}$$

As we see here that the energy flux through the faces of a steady thin disc is independent of viscosity, which is an important result. $F(R)$ is a quantity of prime observational significance, and (2.26) shows that its dependence on $\dot{M}, R, etc.$ is

known. The result relies on the implicit assumption that ν can adjust itself to give the required $\dot{M}$. The independence of $F(R)$ from ν has come about because we were able to use conservation laws to eliminate ν; clearly the other disc properties (e.g. $\Sigma, v_R, etc.$) do depend on the viscosity ν.

The remaining set of equations represents the local structure of thin discs. In such case both the pressure and the temperature gradients are essentially vertical. Thus we can treat the vertical disc structure at a given radius as if it were a one-dimensional version of stellar structure. In such case we have the equations of hydrostatic equilibrium and energy transport to solve, with the radial disc structure only entering the calculations in the fixing of the local energy generation rate $F(R)$. For isothermal z-structure, the hydrostatic equation (2.14) would give

$$\rho(R,z) = \rho_c(R) exp(-z^2/2H^2) \tag{2.27}$$

Where H is the disc thickness given by (2.17), here $\rho_c(R)$ is the density on the central plane $z = 0$. Thus in general we can define a central disc density approximately by

$$\rho = \Sigma/H \tag{2.28}$$

$$H = Rc_s/v_\phi \tag{2.29}$$

The sound speed c_s is given by

$$c_s^2 = P/\rho \tag{2.30}$$

where in general the pressure P is the sum of gas and radiation pressures:

$$P = \frac{\rho\kappa T_c}{\mu m_p} + \frac{4\sigma}{3c}T_c^4 \tag{2.31}$$

Here σ is the Stefan-Boltzmann constant, and we have assumed that the temperature $T(R,z)$ is close to the central temperature $T_c(R) = T(R,0)$.

The temperature T_c must be given by an energy equation relating the energy flux in the vertical direction to the rate of generation of energy by viscous dissipation, this can be described such that the viscous heating equal to the radiative cooling. The case can be different in the stars because the vertical energy transport mechanism may be either radiative or convective, depending on whether or not the temperature gradient required for radiative transport is smaller or greater than the gradient given by the adiabatic assumption $P\rho^{-\gamma}$ =constant, where γ is known as the adiabatic index, or the ratio of specific heats. In the thin disc approximation the assumption

of radiative transport is valid because in such case the disc medium is essentially "plane parallel" at each radius, so that the temperature gradient is effectively in the z-direction, as we pointed out above. Under these circumstances, the flux of radiant energy through a surface z-constant is given by

$$F(z) = \frac{-16\sigma T^3}{3\kappa_R \rho}\frac{\partial T}{\partial z} \tag{2.32}$$

where κ is the Rosseland mean opacity. It is implicitly assuming in writing (2.32) that the disc is optically thick in the sense that

$$\tau = \rho H \kappa_R(\rho, T_c) = \Sigma \kappa_R \gg 1 \tag{2.33}$$

so that the radiation field is locally very close to the blackbody value: once τ given by (2.33) becomes ≤ 1, the expression (2.32) breaks down as the radiation can escape directly. The energy balance equation is

$$\partial F/\partial z = Q^+$$

where Q^+ defined as the volume rate of energy production by viscous dissipation, by integration we have

$$F(H) - F(0) = \int_0^H Q^+(z)dz \tag{2.34}$$

Since the total dissipation rate through one half of the vertical structure must give the dissipation rate per unit face area (2.26) and using (2.32) we have

$$F(z) \sim (4\sigma/3\tau)T^4(z) \tag{2.35}$$

using (2.33), so that provide the central temperature greatly exceeds the surface temperature ($T_c^4 >> T^4(H)$), then the total flux (2.34) becomes approximately

$$\frac{4\sigma}{3\tau}T_c^4 = F(R) \tag{2.36}$$

which is our required energy equation.

Next, we shall solve the steady disc equations derived before for a simple case. This will allow us to check if the blackbody and thin approximations are valid for this particular case, in addition to that we will try to illustrate the general procedure for solving these equations. We will solve such equations for the standard disc

model (Shakura & Sunyaev 1973), and to do that we need to give only a viscosity prescription and a relation for the opacity. The α-prescription is given as

$$\nu = \alpha c_s H \tag{2.37}$$

and assume that ρ and T_c are such that the Rosseland mean opacity is well approximated by Kramer's law:

$$\kappa_R = 6.6 \times 10^{22} \rho T_c^{-7/2} cm^2 g^{-1} \tag{2.38}$$

In addition to that, equation (2.31) includes both terms for the gas and the radiation pressure. In our solution we shall drop the radiation pressure term $(4\sigma/3c)T_c^4$ assuming gas pressure domination. With these consideration we have completed the set of disc equations which are:

$$\begin{aligned}
1).\ \rho &= \Sigma/H; \\
2).\ H &= c_s R^{3/2}/(GM)^{1/2}; \\
3).\ c_s^2 &= P/\rho; \\
4).\ P &= \frac{\rho \kappa T_c}{\mu m_p} + \frac{4\sigma}{3c} T_c^4; \\
5).\ \nu &= \alpha c_s H \\
6).\ \tau &= \Sigma \kappa_R(\rho, T_c) = \tau(\Sigma, \rho, T_c); \\
7).\ \nu\Sigma &= \frac{\dot{M}}{3\pi}\left[1 - \left(\frac{R_\star}{R}\right)^{1/2}\right]; \\
8).\ \frac{4\sigma T_c^4}{3\tau} &= \frac{3GM\dot{M}}{8\pi R^3}\left[1 - \left(\frac{R_\star}{R}\right)^{1/2}\right]
\end{aligned} \tag{2.39}$$

These eight equations can be solved for eight unknowns $H, c_s, T_c, \rho, \Sigma, \tau$ and ν as a function of $\dot{M}, M, R$ and any parameter appearing in the viscosity prescription $\nu = \nu(\rho, T_c, \Sigma, \alpha, ...)$. The final solution of such equations will have the following form:

$$X = X_0 \alpha^{p_1} \dot{M}_{16}^{p_2} M_1^{p_3} R_{10}^{p_4} f^{p_5} \tag{2.40}$$

where X is the physical parameter like Σ, P, T_c, etc., X_0 is a dimensionless numerical constant and p_1, p_2, p_3, p_4 and p_5 are constants. We omit numerical factors to avoid the complications in the final solution, so in (2.40) we put $\dot{M}_{16} = \dot{M}/10^{16}\mathrm{g\ s^{-1}}$, $M_1 = M/M_\odot$, $R_{10} = R/10^{10}\mathrm{cm}$ and $f^4 = 1 - (R_\star/R)^{1/2}$ and take $\mu = 0.615$,

appropriate to a fully ionized cosmic mixture of gases. With such simplifications we can start explaining the procedure of how to solve such equations.
First, substitute (5) into (7) we get

$$\alpha c_s H\Sigma = R(7) \tag{2.41}$$

where the $R(7)$ means the right hand side of equation (7). In equation (4) and in the gas pressure term we assume that $\kappa/\mu m_p = h$ for simplification and then from both (3) and (4) we get

$$c_s = (hT)^{1/2} \tag{2.42}$$

Substitute the value of c_s in (2.41) we get

$$\alpha(hT)^{1/2} H\Sigma = R(7) \tag{2.43}$$

From equation (2) and (3) using (4) we get

$$(hT)^{1/2} = \frac{H v_k}{R} \tag{2.44}$$

Substitute (2.44) into (2.43) we get

$$\alpha \frac{v_k}{R} H^2\Sigma = R(7) \tag{2.45}$$

In equation (8) substitute $\Sigma = \rho H$ which exist implicitly in τ we get

$$\frac{4\sigma T_c^4}{3\Sigma\kappa} = R(8) \tag{2.46}$$

where R(8) means the right hand side of equation (8). From (2.44) we get

$$T^4 = \frac{1}{h^4}(\frac{H v_k}{R})^8$$

Substitute this value in (2.46) to get

$$\frac{4\sigma}{3\Sigma\kappa}\frac{1}{h^2}(\frac{v_k}{R})^8 H^8 = R(8) \tag{2.47}$$

From equation (2.45) we can get:

$$H^2 = \frac{1}{\Sigma}\frac{1}{\alpha}\frac{R}{v_k}R(7) \tag{2.48}$$

Substitute (2.48) in (2.47) to get

$$\frac{4\sigma}{3\Sigma\kappa}\frac{1}{h^2}(\frac{v_k}{R})^8\left[\frac{1}{\Sigma}\frac{1}{\alpha}\frac{R}{v_k}R(7)\right]^4 = R(8) \tag{2.49}$$

With more simplifications we will end up with the following formula for Σ

$$\Sigma^5 = \frac{4\sigma}{3\kappa}\frac{1}{h^2}(\frac{v_k}{R})^8\left[\frac{1}{\alpha}\frac{R}{v_k}R(7)\right]^4\frac{1}{R(8)} \tag{2.50}$$

With even more simplifications we can get the following results for Σ and the rest of the parameters (Frank et. al. 1992):

$$\begin{aligned}
\Sigma &= 5.2\alpha^{-4/5}\dot{M}_{16}^{7/10}M_1^{1/4}R_{10}^{-3/4}f^{14/5}\text{g cm}^{-2},\\
H &= 1.7\times10^8\alpha^{-1/10}\dot{M}_{16}^{3/20}M_1^{-3/8}R_{10}^{-9/8}f^{3/5}\text{cm},\\
\rho &= 3.1\times10^{-8}\alpha^{-7/10}\dot{M}_{16}^{11/20}M_1^{5/8}R_{10}^{--15/8}f^{11/5}\text{g cm}^{-3},\\
T_c &= 1.4\times10^4\alpha^{-1/5}\dot{M}_{16}^{3/10}M_1^{1/4}R_{10}^{-3/4}f^{5/6}\text{K},\\
\nu &= 1.8\times10^{14}\alpha^{4/5}\dot{M}_{16}^{3/10}M_1^{-1/4}R_{10}^{3/4}f^{6/5}\text{cm}^{-2}s^{-1},\\
v_R &= 2.7\times10^4\alpha^{4/5}\dot{M}_{16}^{3/10}M_1^{-1/4}R_{10}^{-1/4}f^{-14/5}\text{cm s}^{-1},\\
\tau &= 33\alpha^{-4/5}\dot{M}_{16}^{1/5}f^{4/5}
\end{aligned} \tag{2.51}$$

From such results we note that the unknown α-parameter does not enter any of the expressions for the disc quantities with a high power. This means that the very reasonable looking orders of magnitudes of these quantities are not particularly sensitive to the actual value of α, which is encouraging.

By the same way we can find the values of these physical parameters (2.51) for the case of radiation pressure domination.

2.4 Thermal stability of accretion discs

In the standard approach to stationary accretion disc models (Shakura & Sunyaev 1973) the energy equation takes into account only local, usually radiative, cooling that balances the viscous heating. In most cases global heat transport is neglected.

This approach is justified as long as the disc is geometrically thin, because the ratio of the advection term representing the global entropy transport to the viscous heating term is of the second order in the relative disc thickness H/R, where H and R are the semi-thickness of the disc and the distance from the central object, respectively. In some time dependent calculations of thin models (e.g., Taam & Lin 1984; Lasota & and Pelat 1991) the advective heat transport is taken into account, but it represents only a small contribution to the total energy balance. In slim disc approach (Abramowicz, Lasota, & Xu 1986; Abramowicz et al. 1988; Chen & Taam 1993) terms up to the second order in H/R are taken into account, so that advection is part of the scheme together with the $(H/R)^2$-order terms in the radial Euler equation. In the high accretion rate regime, when H/R is not negligibly small, the cooling of optically thick slim discs is always dominated by advection. In the radiation-pressure-dominated slim disc models, the advective cooling rate per unit surface Q_{adv} satisfies the relation (Abramowicz et al. 1986)

$$Q_{adv} \geq (H/R)^2 Q_+, \tag{2.52}$$

where Q_+ is the viscous heating rate per unit area. The relation between optically thick and thin discs has bees studied by Wandel & Liang (1991) and Luo & Liang (1994) with purely phenomenological 'bridging formulas' for the case of effective optical depth around unity. The latter authors have concluded that optically thick and thin sequences of solutions are always connected in the $\dot{M}$ (mass accretion rate) versus Σ (surface density) plane. In all those models the hot inner regions of the accretion disc are not geometrically thin, because of the relative inefficiency of the optically thin cooling that makes $H/R = c_s/v_k$ close to unity (c_s is the adiabatic speed of sound and v_k is the Keplerian speed). Advection is neglected. Furthermore, they are all thermally unstable. This is not just a technical difficulty that could be repaired without modifying the basic properties of the proposed models. In most cases, the a posteriori calculated advective heat transport is found to be dominant cooling mechanism at high accretion rates. The advection is connected with the radial flow of the matter. It is a way in which different parts of a disc communicate with each other. If the radial velocity is high enough, then, this advective cooling term is relevant, otherwise is not. The advection cooling effects will be prominent for the case which close to or exceeding the Eddington limit accretion rate, but it can be neglected in the standard disc model since the accretion rate is much lower than the Eddington limit. The Eddington limit accretion rate can be written as a function of Eddington luminosity as follows:

$$\dot{M}_{Edd} = \frac{L_{Edd}}{c^2} \tag{2.53}$$

where c is the speed of light and L_{Edd} is the Eddington luminosity given as

$$L_{Edd} = 1.3 \times 10^{38} \left(\frac{M}{M_{\odot}} \right) \; ergs \; s^{-1}$$

and defined as the maximum luminosity emitted from a non-rotating star, where at the same time the star remains in hydrostatic equilibrium. If the luminosity exceeds L_{Edd}, mass loss must be driven by the radiation pressure. Eddington limit appears in a number of areas in astrophysics including the late stages of stellar evolution, novae and accretion discs.

To solve the equations for both the advectively dominated accretion disc flow (ADAF) and slim discs, which have the same equations as the stationary thin disc, except the energy equation, which has the following from

$$Q_{+} = Q_{adv} + Q_{rad} \tag{2.54}$$

where the radiative cooling assumed to be provided by optically thin thermal bremsstrahlung with emissitivity per unit area.

$$Q_{brem} = 1.24 \times 10^{21} H \rho^2 T^{1/2} ergs \; s^{-1} cm^{-2} \tag{2.55}$$

The advection cooling rate is taken in the form (see, e.g.,Chen & Taam 1993):

$$Q^{-}_{adv} = \Sigma v_r T \frac{dS}{dR} = -\frac{\dot{M}}{2\pi r} T \frac{dS}{dr} = \frac{\dot{M}}{2\pi r^2} \frac{P}{\rho} \xi \tag{2.56}$$

where Σ is the surface density of the disc as defined before, S is the specific entropy and ξ assumed to be unity which is given in this form ($\xi = -[(4-3\beta)/(\Gamma_3 - 1)](d\ln T/d\ln r) + (4-3\beta)(d\ln\Sigma/d\ln R)$). Here $\beta = \frac{P_g}{P}$, $\Gamma_3 = 1 + (4-3\beta)(\gamma - 1)/[\beta + 12(\gamma-1)(\beta-1)]$, γ is the ratio of specific heats. For optically thin discs $\beta = 1$.

We solved the disc equations for both types assuming gas pressure domination in the ADAF case, while radiation pressure domination in the slim disc case with Q_{adv} dominates in (2.54). The solution of such equations for both cases showed that both the ADAF and the slim discs are having the same values for their physical parameters such as Σ, H, ρ, etc., except only one parameter which is the temperature. For the detailed calculations and solutions, see Nasser (1998).

2.5 Cataclysmic Variables

For writing this section, the book of B. Warner with the title 'Cataclysmic Variable Stars' (Warner 1995) has been used as a main reference for this task. Of the

(approximately) four hundred thousand million stars in our Galaxy, more than half are not single stars like our Sun, but occur in binary or multiple systems. Binary star systems come in many flavors: red stars orbiting blue stars, huge stars orbiting tiny stars, black holes orbiting blue giants, red stars orbiting neutron stars, and so on. We are mainly studying a particular interesting group of binary stars: the Cataclysmic Variables (or CV for short). In a CV binary, one star is a white dwarf: a collapsed star with the mass of the Sun in the volume of the Earth. The other star is a red dwarf rather like our Sun, but redder and less massive. The red dwarf and the white dwarf orbit each other once every few hours: they are so close together that the average CV system would fit comfortably into our Sun. When we observe CVs, we can not resolve the two stars: they appear on the sky as a point source.

The red star in a CV is also so close to the white dwarf that it becomes tidally distorted. The gas is stripped off the red star and falls towards the white dwarf. Due to the conservation of angular momentum, the infalling gas can not plunge directly onto the surface of the white dwarf. In systems where the white dwarf does not have an appreciable magnetic field, the infalling gas forms a disc – an accretion disc – with the white dwarf at its centre. The gas in the disc spirals down towards the white dwarf, radiating its gravitational potential energy away as it goes. The accretion disc usually outshines both the red star and the white dwarf in visible light. If the white dwarf is strongly magnetic, other interesting things happen as discussed in the previous chapter.

The CV with accretion disc come in several flavors. The first to be discovered were the *novae*. They draw attention to themselves by their amplitude variations 6 to 19 magnitudes, and a period of months or years. Two kinds of novae have been classified, the first kind, called fast novae, are novae that increase to a maximum brightness in a matter of hours, then fade back to their original brightness in a few days or weeks. The second kind, called slow novae, are a novae that increase in brightness over a few days, and then stay bright for a few months or even years. Novae outbursts are thermonuclear runaways of hydrogen-rich material that has accreted onto the white dwarf. Most novae known have only been observed to undergo one novae outburst, but several are *recurrent novae*.

Another group of non-magnetic CVs is the *dwarf novae*. Their outbursts are not quite as spectacular as those of novae, but the outbursts occur more often. An interesting subset of the dwarf novae are the *SU Ursa Majoris Stars*. They show two distinct kinds of outburst: normal dwarf nova outburst, and *superoutburst*, which last 5-10 times longer and slightly brighter than the usual dwarf novae outbursts. During the superoutburst, SU UMa stars shows an additional modulation of the light curve, a *superhump*, which is caused by precession of the accretion disc. A superhumps shows up in the light curve as a modulation with a period slightly

longer (a few percent) than the orbital period.

Another group of CVs with accretion discs are the *novae-like variables*. The difference between the novae-like variables and dwarf novae is that novae-like variables do not undergo dwarf novae outbursts. This is because the rate of transfer of matter in their discs is stable, and the overall brightness varies only slightly about its mean level. Some novae-like variables show superhumps, like those of SU UMa stars in superoutburst. Unlike the superoutbursting systems, however, these novae-likes have supehumps in their light curves all the time. They are the *permanent superhumpers* (Solheim 2001, private communication). An interesting group of CV systems of this type is the AM Canum Venaticorum systems. They are *helium-rich* CVs: no hydrogen has ever been detected in any of them. They have much shorter orbital periods than the hydrogen-rich systems: the two stars of the AM CVn itself whizz around each other almost every a quarter of an hour. The reason for the permanent superhump in the AM CVn systems must be due to the shape 'eccentricity' of the discs; and the mass-donating red star must be much less massive than the accreting white dwarf. In the following chapters we are going to discuss the properties of the AM CVn systems in detail, and model their optical spectra. This might lead us to a better understanding to such systems especially the physics of the primary and secondary stars, the mass transfer rate, the accretion disc, the superhump phenomena, the geometry of the systems, the distance and finally the evolutionary track, where do they come from and where will they evolve?

Chapter 3

AM Canum Venaticorum systems

3.1 Introduction

AM CVn systems are very particular type of cataclysmic variables, they are called helium cataclysmic. At the moment we know eight such systems: AM CVn, CR Boo, HP Lib, V803 Cen, CP Eri , GP Com, RX J1914.4+245, and KL Dra (Nelemans et al. 2001a). It is currently believed that they are interacting binary white dwarf systems (Faulkner et al. 1972) with a degenerate C-O primary, and in which the secondary low mass object $M_2 \leq 0.084 M_\odot$ is slowly loosing its mass as it is layer by layer wrapped off in a process transferring almost a pure helium gas to the white dwarf primary, most likely in the equatorial region, in which almost a pure helium accretion disc is formed.

The secondary itself is most probably a sub-luminous object, highly irradiated, because of its close distance to the primary object, since we see no traces of it in the combined spectrum (Nymark & Solheim 1995).

The AM CVn family members have in common a He-rich composition (no hydrogen lines seen). They are analogous of the H-rich cataclysmic variables, showing wide absorption lines and ultra-short photometric variability. Photometric observed periods are between 17 and 45 minutes. If the periods observed are the binary periods or the superhump periods, then the only solution for such systems is that both objects are degenerate or semi-degenerate.

The optical spectra of the AM CVn stars have shallow, symmetric He I absorption lines of variable depth profile, suggestive of variable filling by emission contributions, while the UV spectra of AM CVn and the other objects in their high states show absorption lines of He II, C IV, N IV, N V, Si III and Si IV (Wood et al. 1987). Some of the group members have distinct high and low states depending on the

mass transfer rate. Thus AM CVn and HP Lib of a permanent high state have broad line absorption spectra like those of UX UMa subclass of CVs, with high mass transfer rate $\dot{M}$ through their discs, GP Com has strong emission lines typical of low $\dot{M}$ system, and the others change from predominantly absorption line spectra in their high states to weak emission lines spectra in their low states, as in the VY Scl subclass of the H-rich CVs.

The short-period photometric variations of AM CVn stars are interpreted in this model to be the same 'superhump' phenomenon observed in superoutbursts of SU UMa stars (Patterson et al. 1993; Warner 1995a). It is now well accepted that the superhump phenomenon in SU UMa stars can be explained by the precessing eccentric disc model (Whitehurst 1988; Hiros & Osaki 1990; Lubow 1994). In this model, an accretion disc becomes tidally unstable by the so called 3:1 resonance between the disc matter and the orbiting secondary, and develops a precessing eccentric disc. A periodic tidal stress of the disc by the orbital secondary star gives rise to periodic photometric light variations with the synodic period between the orbiting secondary star and the precessing eccentric disc. It is also known that a tidal instability occurs only in systems with mass ratio $q = (M_2/M_1) < 0.25$, where M_1 and M_2 are the masses of the primary and the secondary stars, respectively (Whithurst 1988). The AM CVn systems are found to satisfy this condition because their secondary stars are very low-mass white dwarfs.

In addition to these characteristics, very large amplitude photometric variations have been observed in some AM CVn systems. The time scales of this type of variations are of days and their amplitudes reach 3-4 mag. The light curves of large amplitude photometric variations are very similar to those of dwarf nova outbursts. This type of variation has not been observed in all AM CVn systems, but so far only in three systems (CR Boo, V803 Cen, and CP Eri), which have similar 'superhump' periods.

Although the cause of these phenomena has not yet been clarified, they are thought to be a similar phenomenon to the dwarf nova outburst. Three models have been discussed in the past for this phenomenon, just in parallel to the hydrogen rich accretion disc systems of the dwarf novae. One is the disc instability model discussed by Smak (1983) and Cannizzo (1984). Smak (1983) has pointed out that the thermal limit cycle instability of accretion discs, which is thought to be responsible for the ordinary dwarf nova outburst, should also be applicable to the helium disc systems. Cannizzo (1984) calculated light curves based on this model. The other model is the mass-transfer burst model in which the mass-transfer rate from the secondary star is variable. Warner (1995) proposed the latter model based on the irradiation-induced mass-transfer instability in the secondary star. Osaki (1989) extended the disc-instability model which was discovered by Whitehurst (1988). The new model now is called thermal-tidal-instability model. The unified model for dwarf-nova outburst

based on a disc instability that takes into account these two-types of instabilities was proposed by Osaki (1996).

In this chapter I am going to use such long history of the AM CVn systems in addition to the use of the previous two chapters, to be able to build the basics of my research work. Based on the spectroscopic and photometric properties and the thermal-tidal-instability model for each system, I am going to calculate analytically the basic parameters for each system. Such parameters will be used later on as input parameters for my modeling work, using the disc atmosphere code TLUSDISK, as we will see in chapter(5). First, in the next subsections, I will present shortly the properties of each system separately, and then calculate the values of the physical parameters based on such properties, in addition to the evolutionary models. These values will be used later on as input parameters for the disc models.

3.2 Photometric and spectroscopic properties

In most cases if not all of them, the theory is always proposed after the existence of an observational phenomena. In astrophysics, photometry and spectroscopy are the main tools which astronomers use to build the basics of their scientific theories. This is what we will do in the case of the AM CVn systems. We will set the input parameters for our theoretical models based on the observed photometric and spectroscopic quantities. With this method we will be able to determine the unknown quantities of the systems based on the known ones.

3.2.1 High state objects, AM CVn & HP Lib

AM CVn was found to have broad, shallow absorption He I lines and no traces of hydrogen, and first classified as a DB white dwarf (Greenstein & Matthews 1957). Five years later photometric variability with a period of 17.5 min was discovered by Smak (1967) and Paczyński suggested that it could be a semi-detached pair of degenerate objects, in which mass transfer is driven by loss of angular momentum due to gravitational wave radiation. Flickering, which is typical for cataclysmic variables was found by Warner & Robinson (1972), and this inspired Faulkner, Flannery & Warner (1972) to propose the double-degenerate white dwarf model, which has been the main accepted explanation for the AM Cvn systems since then. The dominant photometric period is 525 s, which is a first harmonic of the fundamental period of 1051 s (Solheim et al. 1998). A precession period of 13.38 hr is detected by Patterson et al. (1993). Doppler tomography has established 1028.73 s as the binary period (Nelemans, Steeghs & Groot 2001b).

Spectroscopic data for AM CVn can be described as roughly blackbody with an effective temperature of 20000 K spectra (Wampler 1967; Oke 1974). Line spectra, featuring very broad asymmetric lines with emission cores were found to comply with accretion disc theoretical spectra. In the optical region most of the lines belong to the He I, while UV spectra show the presence of heavier elements as Si, C, N and maybe Mg and Fe. Additional puzzling feature is the He II emission line, seen at λ 4686 Å (Patterson et al. 1992).

So far most of the UV spectra of AM CVn were obtained with IUE (Greenstein 1979; Patterson et al. 1992). They show deep absorption lines of highly ionized metals, and are similar to the spectra of a nova-like variable RW Sex. Their profiles can be attributed to the hot expanding gas cloud, ejected from the system.

The IUE spectra (Solheim 1992), extended to the optical and infrared regions by U, B, V, R and I photometric points (Massacand & Solheim 1995), represents the most complete wavelength coverage, published up to date. Spectrum, composed of those two datasets is displayed in Fig. 3.1.

AM CVn is the most thoroughly observed object of its group, during the past few years a wealth of information was also obtained for the rest of the family members, where HP Lib found to be similar to AM CVn system. This star was identified as an AM CVn star by O'Donoghue et al (1994). Its fundamental period of 1119 s is close to the fundamental period of AM CVn itself, and its lack of change, indicate that this is also an object stuck in its high state. A superhump period is not yet detected (Aminzade et al 1999).

3.2.2 Intermediate state objects, V803 Cen, CR Boo & CP Eri

V803 Cen was discovered by Elvius (1975) to be an unusually blue object in which its spectrum shows only broad, shallow absorption lines of He I with complete absence of H lines. The He I features were found to vary strongly, fading to invisibility at times. It was classified as a rapid variable with a dominating period of 1611 s with a complex harmonic structure and a member of the AM CVn family by O'Dononghue, Menzies & Hill (1987). CR Boo (= PG 1346-082) is a blue star classified as an AM CVn object by Wood et al. (1987), who presented spectroscopy and high-speed photometry and demonstrated that the star is a short-period cataclysmic binary, in which the mass transfered through the accretion disc was predominantly helium rather than hydrogen. A WET campaign identified a coherent period of 1471 s, which is likely the orbital period (Provencal et al. 1997) and most likely the superhump period. CP Eri qualifies as an interacting binary white dwarf system by

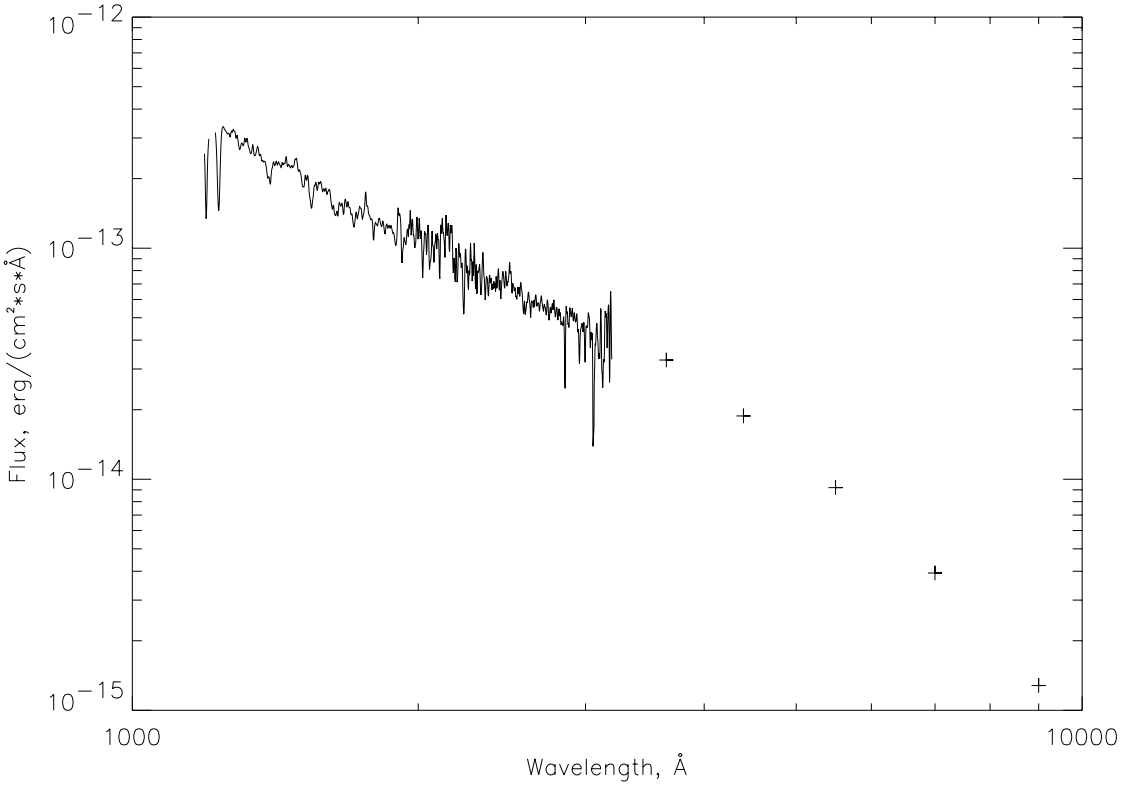

Figure 3.1: The observed spectrum of AM CVn, consisting of a continuous part and some photometric points (crosses). The continuous part of the spectrum was obtained by IUE (Solheim, 1992). The U, B, V, R and I data were obtained at the Nordic Optical Telescope (Massacand & Solheim, 1995), while the J and K data were a part of a study of more than one hundred faint objects (Probst 1983).

demonstrating a complete lack of hydrogen lines in its spectrum. The object is both spectroscopic and photometric variable (Abbott 1992). In the manner of V803 Cen and CR Boo, CP Eri undergoes large magnitude outburst, from $\approx$ 19.7 - 16.5, on a timescale of about one day (Szkody 1989), although our knowledge of the object's outburst is not as comprehensive as CR Boo and V803 Cen. The features of neutral helium detected in the spectrum vary from emission to absorption depending on the magnitude of the system. Absorption features are seen during high state, and emission features are seen in low state, exactly as observed for CR Boo and V803 Cen. The spectral features are shallow, characteristic of Doppler broadening and pressure broadening in the atmosphere of a compact object. As with all members of the AM CVn family, no hydrogen is detected.

V803 Cen, CR Boo & CP Eri are known to show large-amplitude variations up to five magnitudes, on a time scale less than a day to several months. The origin of such large-amplitude variations is still poorly understood. Warner (1995a) proposed the similarity to VY Scl-type cataclysmic variables, whose 'low states' are generally believed to result from reduced mass-transfer. Tsugawa and Osaki (1997) applied the dwarf nova-type thermal and tidal instability model to the helium disc systems, including V803 Cen and CR Boo. They succeeded in understanding the behavior of these systems by considering the stability of the accretion disc depending on the mass transfer. Tsugawa and Osaki (1997) expected that intermediate mass-transfer systems, such as V803 Cen and CR Boo, will undergo dwarf nova-type disc instability, analogous to SU UMa-type dwarf novae in hydrogen-rich systems. They suggested higher mass-transfer systems would resemble ER UMa stars, which are a sub-group of SU UMa-type dwarf novae having extremely short supercycle length (Kato et al. 1999). Subsequent observation indeed confirmed the presence of 46.3-d supercycle in CR Boo (Kato et al. 2000), whose behavior is extremely analogous to ER UMa stars.

3.2.3 Low state object, GP Com

GP Com is a blue, high proper motion star (Giclas, Burnham & Thomas 1961), found by Burbidge & Strittmatter (1971) to have an optical spectrum dominated by He I emission lines. The emission lines similar to those seen in cataclysmic variables stars (CVs) and rapid photometric variability led to the suggestion that GP Com is a binary star. This was finally confirmed by Nather, Robinson & Stover's (1981) detection of a 46-min period in emission lines. The orbital period is too short to allow a hydrogen-rich donor star, consistent with the absence of hydrogen emission in GP Com. It shows only strong He I emission lines with a very flat continuum. GP Com shows the binary nature most clearly of all AM CVn type stars, while

being in a constant low state. This is the only object in the group in addition to the AM CVn, for which orbital period was directly observed as a spectral line shift, indicating the movement of its components. Marsh et al. (1991) attempted to model the optical lines with LTE model, obtaining a reasonable fit, but only with peculiar abundances. In application to GP Com, the LTE model is crude, and cannot explain the presence of high excitation lines like N IV and He II (Marsh et al. 1995). The rest of the objects will not be discussed in this work because very little is known about them so far.

3.3 Evolutionary models of AM CVn systems

There are four evolutionary models which describe the AM CVn systems, two of them describe the systems as a C-O degenerate primary and a semi-degenerate secondary by Savonije et al. (1986) and Tutukov & Federova (1989). The other two describe the systems as double degenerate by Savonije et al. (1986) and Zapolsky & Salpeter (1969). The difference between these models is due to the difference in the mass-radius relation, which describes the secondary star in such systems. In our calculations we focus on the evolutionary models of both Savonije et al. (1986) and Tutukov & Federova (1989) which describe the systems as a C-O degenerate primary and a semi-degenerate secondary, and then find out with which model will our calculations agree. This is because as we will see later in this work that our calculations agree with the model for a semi-degenerate secondary, and disagree with the models which describe the secondary as a degenerate object.

In this section we will derive the relation between the mass of the secondary star and the orbital period of the system, using the mass radius relation of Savonije et al. (1986), which we used in our work to investigate the systems. By the same way we can apply the derivation method for the other mass radius relations of the other evolutionary models.

The mass-radius relation derived by Savonije et al. (1986) for a semi-degenerate secondary is

$$\left(\frac{R_2}{R_\odot}\right) = 0.029\left(\frac{M_2}{M_\odot}\right)^{-0.19} \tag{3.1}$$

The radius of the secondary star in this case is assumed to be the Roche lobe radius given as:

$$R_2^3 = \frac{(0.462)^3}{4\pi^2} G M_2 P_{orb}^2 \tag{3.2}$$

We can rewrite equation (3.1) as:

$$R_2^3 = (0.029R_\odot)^3 \left(\frac{M_2}{M_\odot}\right)^{-0.57} \tag{3.3}$$

By equating both equation (3.2) with equation (3.3) we get,

$$\left(\frac{M_2}{M_\odot}\right)^{-1.57} = \frac{(0.462)^3 G M_\odot P_{orb}^2}{4\pi^2 (0.029R_\odot)^3} \tag{3.4}$$

which can be rewritten as

$$\left(\frac{M_2}{M_\odot}\right) = \left[\frac{(0.462)^3 M_\odot}{(0.029R_\odot)^3}\left(\frac{GP_{orb}^2}{4\pi^2}\right)\right]^{-0.637}$$

which can be again rearranged to look like the following

$$\left(\frac{M_2}{M_\odot}\right) = \left(\frac{0.029R_\odot}{0.462M_\odot^{1/3}}\right)^{1.91}\left(\frac{4\pi^2}{GP_{orb}^2}\right)^{0.637} \tag{3.5}$$

If we substitute the values of all the constants in equation (3.5), the following will be the final mass-P_{orb} relation for a semi-degenerate secondary in the AM CVn systems

$$\left(\frac{M_2}{M_\odot}\right) = 633.8 \times P_{orb(s)}^{-1.27} \tag{3.6}$$

If we repeat the same steps done to find the mass-P_{orb} relation of Savonije et al. (1986) to the mass radius relation of Tutukove & Federova (1989) of the following form:

$$\left(\frac{R_2}{R_\odot}\right) = 0.043\left(\frac{M_2}{M_\odot}\right)^{-0.062}$$

we will get the following relation for the mass of the secondary star as a function of the orbital period

$$\left(\frac{M_2}{M_\odot}\right) = (1.37 \times 10^4) P_{orb(s)}^{-1.686} \tag{3.7}$$

We repeated the same steps using the following mass-radius relation derived by Savonije et al. (1986) for the fully degenerate secondary

$$\left(\frac{R_2}{R_\odot}\right) = 0.013\left(\frac{M_2}{M_\odot}\right)^{-0.333} \tag{3.8}$$

and we found the following mass-P_{orb} relation for the fully degenerate secondary

$$\frac{M_2}{M_\odot} = 44.64 \times P_{orb}^{-1}(s) \tag{3.9}$$

Finally, the following mass-radius relation of Zapolsky & Salpeter (1969) was taken from Nelemans et al. (2001a)

$$R_{ZS} \approx 0.0106 - 0.0064 \ln M_{WD} + 0.0015 M_{WD}^2 \tag{3.10}$$

In the next section we will use the relations we derived so far, to calculate the values for the physical parameters in the AM CVn systems.

3.4 Estimates for the systems parameters

Before proceeding to the model spectra calculations, we must establish a set of parameters characterizing the disc in our target systems. The data available as we will see in the next chapters are only for four of the family members which are: AM CVn, HP Lib, V803 Cen and CR Boo, because these are the objects which we were able to observe in the northern hemisphere and we already have some data available for them. This means that the modeling attempts will be focused on these four systems. To be able to build good models, we have to set the values of the known parameters as an input for such models. We will use the observed quantities of the AM CVn systems in addition to the values predicted by the other evolutionary and instability models, to calculate the values of such input parameters with some accuracy. Using the observed quantity like the orbital period P_{orb} or the superhump period, and the predicted value of q, in addition to the mass of the secondary star M_2 from the mass-radius relation used in the evolutionary models, we are going to develop our calculations. From such values and using the thermal-tidal-instability model of Tsugawa & Osaki (1997), we are going to estimate the size of the disc for each system, in addition to the rest of known parameters, to determine both the mass accretion rate in the disc $\dot{M}$ and the angle of inclination i, as we will see in chapter (5).

In this section we will write the basic equations, which will be used to calculate the systems parameters, starting with the ratio between the masses of the two stars to be given as $q = M_2/M_1$.

The distance a between the primary M_1 and the secondary star M_2 can be calculated as:

$$a = 3.5 \times 10^{10} M_1^{1/3} (1+q)^{1/3} P_{orb}^{2/3}(h) \tag{3.11}$$

or

$$a = \left(\frac{G}{4\pi^2} (M_1 + M_2) M_\odot P_{orb}^2 \right)^{1/3} \tag{3.12}$$

The Roche lobe of the primary is found by:

$$R_{L_1} = \frac{0.49 q^{-2/3}}{0.6 q^{-2/3} + \ln(1 + q^{-1/3})} a \tag{3.13}$$

The mass-radius relation is given by (Hansen & Kawaler 1994) for electron degenerate star as follows:

$$M \approx 10^{-6} R^{-3} \left(\frac{2}{\mu_e} \right)^5 \tag{3.14}$$

If electrons are non-relativistic, application of equation (3.14) to the mean density of the white dwarfs ($M \approx 0.6$) yields a radii of $R \approx 0.01$ for $\mu_e = 2$ (completely ionized ^{4}He, ^{12}C, ^{16}O etc.). If relativistic effects cannot be neglected, the following approximate relation (Nauenberg 1972) can be used instead:

$$R_1(1) = 7.79 \times 10^8 \left[(\frac{M_1}{M_{ch}})^{-2/3} - (\frac{M_1}{M_{ch}})^{2/3} \right]^{1/2} \tag{3.15}$$

This will provide us with main geometrical scale later in the course of this work, when we will estimate the size of the components of our binary systems.

The mass transfer rate can be given according to Warner (1995a) as :

$$\dot{M} = \frac{4.4 \times 10^{-12} M_1^{2/3}}{(1+q)^{1/3} (\frac{5}{6} + \xi_{ad} - q)} \times P_{orb}^{-5.21}(h) \tag{3.16}$$

where $\xi_{ad} = \partial \ln R_2 / \partial \ln M_2$ is the adiabatic response of the secondary. In thermal equilibrium $\xi_{ad} = -1/3$, but in the case of non-equilibrium $\xi_{ad} = -0.19$. The non-equilibrium models were found more appropriate to the AM CVn systems. By using the mass-radius relation for a semi-degenerate secondary (3.6), equation (3.16) can be rewritten as:

$$\dot{M} = 2.06 \times 10^{-27} M_1^{2/3} (1+q)^{-1/3} (2(\frac{5}{6} + \xi - q))^{-1} (\frac{P_{orb(h)}}{1000})^{-5.21} \tag{3.17}$$

We will discuss our results for $\dot{M}$ with respect to this equation in chapter 7. From this relation for $\dot{M}$ and with equation (3.11) we can deduce a new relation between a and $\dot{M}$, which can be used to find the size of the disc as a function of $\dot{M}$, using the thermal-tidal-instability models of Tsugawa & Osaki (1997). To achieve this goal, first we have to rewrite equation (3.17) as follows:

$$P_{orb}^{2/3} = 10^2 \Big[\frac{\dot{M}}{2.06 \times 10^{-27} M_1^{2/3} (1+q)^{-1/3} (2(\frac{5}{6} + \xi - q))^{-1}} \Big]^{-0.128} \tag{3.18}$$

Substitute equation (3.18) into equation (3.11) we obtain the final $a - \dot{M}$ relation:

$$a = 3.5 \times 10^{12} M_1^{1/3} (1+q)^{1/3} \Big[\frac{\dot{M}}{2.06 \times 10^{-27} M_1^{2/3} (1+q)^{-1/3} (2(\frac{5}{6} + \xi - q))^{-1}} \Big]^{-0.128} \tag{3.19}$$

By applying this equation for each system and using the estimated disc radius from the photometric observations or from the tidal instability models of Tsugawa & Osaki (1997), we can find the rest of parameters for each systems. For example the disc size which we can use is $R_{disc} = (0.4 - 0.5)a$ (where a is the distance between the two stars) which is about $15R_1$, as a reference radius for both AM CVn and HP Lib. This is the disc size found for AM CVn (Solheim et al. 1998). For the unstable systems like V803 Cen and CR Boo, the disc size according to the thermal-tidal-instability model of Tsugawa & Osaki (1997) can oscillate within the three possibilities, the circularization radius (or the Lubow-Shu radius $R_{LS} = 0.29a$), the critical radius for the tidal instability $R_{cr} = 0.46a$ and the terminal disc radius $R_d = 0.36a$ at the end of a superoutburst, which represents the strength of the tidal torques during the superoutburst, which is in the average $15R_1$. This gives us the possibility to assume that the disc size in the AM CVn systems is about $15R_1$. A hole of $1.4R_1$ is assumed to be in the center of the disc of the AM CVn systems, to make a room for a boundary layer, since almost all the AM CVn systems are X-ray sources (Warner 1995b). The He II line in emission at λ 4686 Å in the AM CVn systems is expected to appear due to the effect of the boundary layer in such systems (Robinson et al. 1993; Warner 1995b), or due to an optically thin layer of gas at the top of the disc (Marsh et al. 1991). By this way we have set the boundary conditions for our calculations, which will be discussed in more detail in chapter(5).

Finally we will write the estimated parameters for each system, based on the mass-radius relation for the secondary star derived by Savonije et al. (1986), Tutukov & Federova et al. (1989) and Zapolsky & Salpeter (1969). These parameters will describe both cases, the semi-degenerate and fully-degenerate secondary. Most of

Table 3.1: Estimated parameters for the AM CVn system, the values of $P_{orb} = 1028.27s$ and $q = 0.084$ were taken from Warner (1995a).

Parameter	SSD	SD	$TFSD$	ZSD
$M_2/M_\odot$	0.094	0.046	0.114	0.033
$M_1/M_\odot$	1.1	0.547	1.36	0.39
R_1(cm)	4.4×10^8	9×10^8	1.5×10^8	1.12×10^9
a(cm)	1.6×10^{10}	1.27×10^{10}	1.7×10^{10}	1.14×10^{10}
R_{L_1}(cm)	9.4×10^9	7.5×10^9	1.0×10^{10}	6.7×10^9
R_d(cm)	$17.5R_1$	$7R_1$	$55R_1$	$4.8R_1$

the equations in this chapter, in addition to the thermal-tidal-instability model of Tsugawa & Osaki (1997) are involved in the calculations.

In the tables (3.1 - 3.4), SSD coresspond's to Savonije-semi-degenerate, SD coresspond's to Savonije-degenerate, TFSD coresspond's to Tutukov and Federova-semi-degenerate and ZSD coresspond's to Zapolsky & Salpeter-degenerate. The estimated parameters are shown in table (3.1 - 3.4).

3.5 Modeling the AM CVn systems

Each system in the AM CVn family is understood to contain a primary star (accretor) and a secondary star (donor), the accretion disc and the wind. Each component has a certain temperature which make such component dominates a certain region in the system's spectra, but with some overlap with the other components. For example, in the case of the AM CVn, the primary star and the wind dominate the UV part of the spectrum, while the accretion disc and the secondary star dominate the optical and the IR regions, respectively. We are not the first to model the optical spectra of the AM CVn systems, Kepler (1989) used blackbody calculations to model the optical spectra of V803 Cen, to find the temperature of the disc, which corresponded to a certain magnitude of the system. He found that, at a high state around B≈13.5, a fit of a Planck function from 3900 Å to 7100 Å gives $T_{eff} = 25776 \pm 682$K. The intermediate state spectra around B≈14, gives an effective temperature of $T_{eff} = 17106 \pm 275$ while the low state spectra at B≈17.2 gives a fit with $T_{eff} = 7315 \pm 73$k.

Table 3.2: Estimated parameters for CR Boo, the values of $P_{orb} = 1471s$ and $q = 0.057$ were taken from Provencal (1997).

Parameter	SSD	SD	$TFSD$	ZSD
$M_2/M_\odot$	0.059	0.029	0.062	0.021
$M_1/M_\odot$	1.035	0.524	1.07	0.37
R_1(cm)	5.4×10^8	9.23×10^8	5.12×10^8	1.15×10^9
a(cm)	2×10^{10}	1.59×10^{10}	2.0×10^{10}	1.4×10^{10}
R_{L_1}(cm)	1.49×10^{10}	1.19×10^{10}	1.5×10^{10}	1.06×10^{10}
R_d(cm)	$13.0R_1$	$6.2R_1$	$14R_1$	$4.45R_1$

Table 3.3: Estimated parameters for V803 Cen, the values of $P_{orb} = 1611s$ and $q \leq 0.043$ were taken from Warner (1995a).

Parameter	SSD	SD	$TFSD$	ZSD
$M_2/M_\odot$	0.053	0.027	0.054	0.019
$M_1/M_\odot >$	1.23	0.63	1.25	0.44
R_1(cm) $<$	3.78×10^8	8.87×10^8	3.59×10^8	1.06×10^9
a(cm) $>$	2.22×10^{10}	1.78×10^{10}	2.23×10^{10}	1.58×10^{10}
R_{L_1}(cm) $>$	1.42×10^{10}	1.14×10^{10}	1.42×10^{10}	1.01×10^{10}
R_d(cm) $>$	$21R_1$	$7R_1$	$22R_1$	$5.4R_1$

Table 3.4: Estimated parameters for HP Lib, the values of $P_{orb} = 1119s$ and $q \geq 0.07$ were taken from Nasser et al. (2001).

Parameter	SSD	SD	$TFSD$	ZSD
$M_2/M_\odot$	0.085	0.039	0.099	0.030
$M_1/M_\odot <$	1.13	0.557	1.32	0.43
R_1(cm) $>$	4.6×10^8	8.9×10^8	2.87×10^8	1.07×10^9
a(cm) $<$	1.7×10^{10}	1.35×10^{10}	1.8×10^{10}	1.24×10^{10}
R_{L_1}(cm) $<$	1.029×10^{10}	8.17×10^9	1.09×10^{10}	7.5×10^9
R_d(cm) $<$	$(15-18)R_1$	$(7-9)R_1$	$(25-30)R_1$	$(4-6)R_1$

Patterson et al. (1993) studied the AM CVn system itself, by creating a model which can find the relation between the mass of the central (primary) star with mass M_1 and the system's angle of inclination, as seen in Fig. 3.2 taken form Patterson et al. (1993). In this figure they assumed that the troughs signify the projected velocity at the outer edge of the disc, which is assumed to occur at a radius 85% of the primary's Roche lobe radius. This generates the constraints shown by the dotted curve in Fig. 3.2, which requires $i > 32°$ if $M_1 < 1.4M_\odot$. The other constraint arises from the line wings, which extend to 2340 $\pm$ 200 km s^{-1} from line center, which is interpreted as the maximum projected velocity. The two versions of this constraint is shown as the cross-hatched curves in Fig. 3.2. With the natural (but unprovable) assumption that the line-forming region extends to the white dwarf surface, they have a constraint defined by the intersection of the two curves: $M_1 = 0.65 \pm 0.05 M_\odot$, $i = 48° \pm 4°$. If the line-forming region extends only down to $R_{inner} = 3R_*$, then the star must lie in the other intersection of curves in Fig. 3.2. Since the actual location of R_{inner} is not known, the firm constraint is $M_1 > 0.6M_\odot$, $i < 51°$.

El-Khoury & Wickramasinghe (2000) made LTE models for the optical spectra of both AM CVn and CR Boo. More about the method they used and the discussion of their results will be in more details in both Chapter 6 and 7.

Here in Tromsø, many have participated in modeling the spectra of the AM CVn systems, and for all the systems components except the wind. In 1995 S. Bard modeled the AM CVn accretion disc using the FORTRAN code ATLAS (Kurucz 1970). He found that the stellar model synthetic spectrum provides a better fit to the observed spectrum than the Planckian disc spectrum. Also, for a given accretion

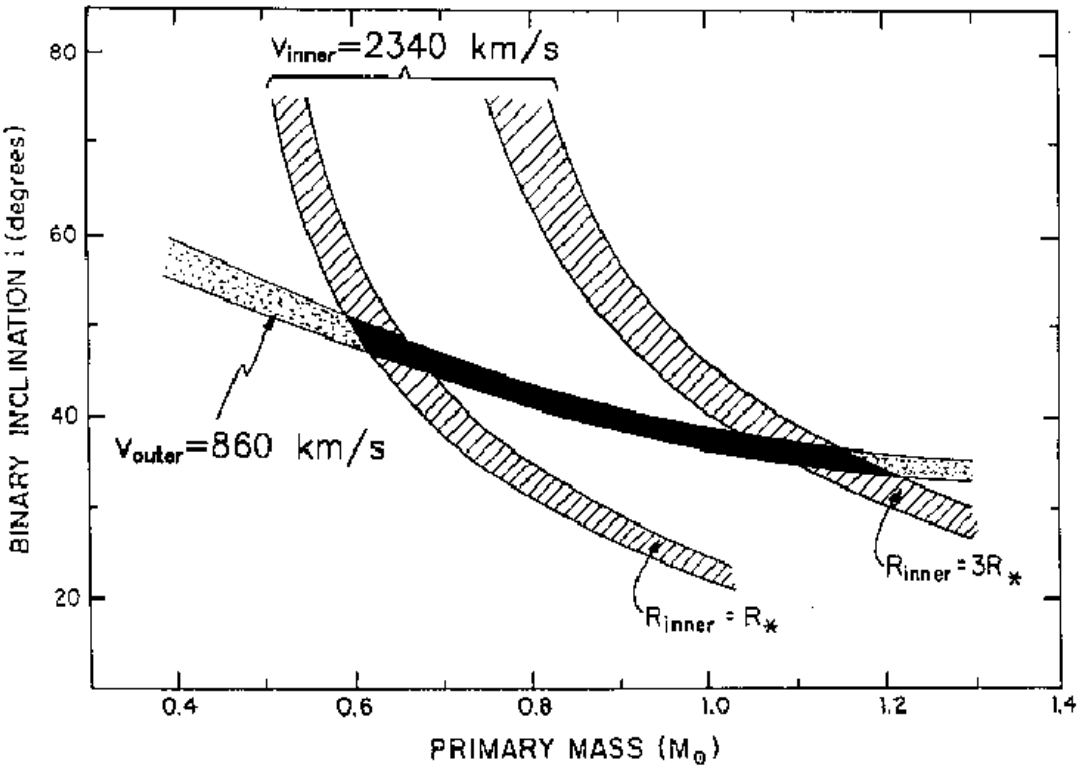

Figure 3.2: Constraints on M_1 and i. Dotted shading indicates the region allowed by a projected $v_{outer} = 860 \pm 20$ km s^{-1}, assuming R_{outer} is 85% of the Roche lobe radius. Cross-hatched shading indicates regions allowed by a projected $v_{inner} = 2340 \pm 200$ km s^{-1}, with two alternate assumptions about the inner edge of the disc $R_{inner} = R_*$ ("full disc"), or $R_{inner} = 3R_*$ ("ring"). For this assumed range, the star must reside in the region shown in black. This figure is taken from Patterson et al. (1993).

rate, the synthetic spectrum composed of the sum of a series of stellar atmospheres is flatter than that of the corresponding blackbody sum. In 1995, T. Nymark & J.-E. Solheim also focused all their investigations on the secondary star irradiated by both the disc and the primary star, using the TLUSTY code (Hubeny 1988; 1990). They have also studied the accretion disc, the primary and secondary stars using blackbody approximations. their results will also be discussed in chapter 6 and 7.

This work came as a continuation to the work done by D. Semionoff for the AM CVn accretion discs, during his Master thesis work in 1998. Semionoff was able to fit part of the spectra (approximately 250 Å) and determine the mass accretion rate and the angle of inclination for AM CVn, CR Boo and V803 Cen. In his calculations he faced two main problems: the outer rings in the disc model did not converge due to their low effective temperatures, and the other one is the appearance of some lines in his model spectra which do not exist in the observed ones, because he used the mass ratio of He/H= 100. In the next chapters we will present and discuss our modeling work and describe our solution to such problems, and in the end compare our results with the ones from the previous works.

Chapter 4

Observations and data reduction techniques

4.1 Introduction

Spectroscopy is one of the fundamental tools of the astronomer, which can increase the astronomer's ability to perform quantitative analysis for the astronomical data. However, with this increased ability has come increased demands upon the tools used for reducing such data. This chapter is intended to discuss the basic steps of reducing the CCD images, extracting and calibrating the slit spectra using IRAF. All the data are assumed to be taken with the Nordic Optical Telescope and our main goal is to absolute flux calibrate this spectroscopic data. All the basic steps which are required to achieve this goal, such as the removal of the instrumental signature after which we will be able to extract our spectra will be discussed. Additional resources the reader may wish to review are 'A Beginner's Guide to Using IRAF by Jeannette Barnes' and 'A User's Guide to Reducing Slit Spectra with IRAF by Phil Massey, Frank Valdes, and Jeannette Barnes'. Also a user's guide 'The Reduction steps of Long Slit Spectra by M. Nasser (2000)' can be very useful, if all the reduction steps mentioned in the guide are followed exactly as it should be, which can lead to the absolute flux calibration of the spectroscopic data.

In this chapter we will *briefly* go through all the reduction steps from the CCD reduction to the long slit spectra extraction and flux calibration. During the discussion of the reduction steps we will 'not' follow the same reduction steps as described in IRAF user guides, but will do those which we find adequate for our data. We will leave the detailed steps as an exercise to the interested reader.

4.2 Run preparation for the data acquisition

The spectra presented in this work were obtained in three different runs (1997, 1999 and 2001) at the Nordic Optical Telescope by three different observers. According to our observational experience, we found that there are two very important factors which can determine the quality of the reduced spectra. The first one is the proper preparation for the run which mainly depends on the observer himself. The second factor is the weather conditions which mainly depend on God and the observer can do nothing about it, except praying for God to clear up the sky! The run preparation also depends on many factors, such as the correct choice of grisms and slits, which also depends on whether the observer needs absolute or relative flux calibrated spectra, and whether the fine details of the lines are very important for his scientific problem or not. The second factor is the visibility of the science objects and the standard stars. The observer must choose standards which have the same altitude and in the same region of the sky as his targets at the time of observations. This can help to avoid having problems with the extinction correction later on. To do that, the observer can plot the so called 'visibility plot' which shows the visibility of each object at different hours of the night. The standard stars must be chosen bright enough to avoid having problems with the final flux calibration, due the lake of light from the standard star. The lake of light can also occur if the standard star is not properly aligned in the slit during the observation even if it is very bright. In addition to that, the observer must plot the field (chart) of his science objects and standards before starting the run, to help him recognize the objects in the field during the observations, which can make the observations go faster. The quality of the data also depends on how the observations were done. Many different factors control that, such as the experience of the observer, the willingness of the support astronomer to help, the quality of the telescope instruments, the weather conditions, the visibility of the objects and the most important of all is the conditions of the observer, which determine whether he was sleeping during the observations or not!!

4.3 (1997-2001) observations

By taking into account all what has been discussed in the previous section, we have conducted three campaigns (1997, 1999 and 2001) at the Nordic Optical Telescope. The 1997 observations were done by both J.-E. Solheim & D. Semionoff for three successive nights. The weather conditions were good enough to obtain the good data listed in table (4.1). The data were successfully reduced using IRAF routines. In 1999, J.-E. Solheim and me observed at the NOT for three successive nights.

The weather conditions were very bad 'snowing' in the first night and cloudy in the second night while in the last night we had a clear sky. Unfortunately, our preparation for the run was not sufficient to obtain the flux calibrated spectra we wanted, which made us also lose the observations of the third night. As a result of our reduction process using IRAF, we managed to get only a relatively flux calibrated spectra. Only one spectrum of 1999 observations is presented in this work while the rest were found not useful for our modeling work. Our major mistake in this run was the wrong choice of grisms, slits and filters. Much of an effort has been done but the achievements were very little, but as a result we have learnt a good lesson in observational techniques and strategy. In 2001 we were given another chance for four nights at the NOT to correct our 1999 mistake. At this time I went alone to the telescope with a good run preparation and crossing my fingers for the weather. My run preparation was very good and the weather conditions were even better. The observations went very fine and most of the reduced spectra came to be even better than what I expected. The observed data is listed in table (4.2). The data were reduced and absolute flux calibrated using IRAF routines. Finally, I can say that I had a great satisfaction about the run preparation, the weather conditions, the observations and the data reduction. We also include in table (4.3) and table (4.4) the U, B and V magnitudes of the systems during the observations.

4.4 The data

To be able to obtain an absolute flux calibration for any data, we must perform a good observations with a correct combinations of frames taken with certain slits and grisms. First, we need flat field images, lamps and spectra for both the science objects and the standard stars, and all has to be taken with the same slit and grism. For the standard star we can obtain its data with a wider slit than the slit used for the other frames. We should also take into account that our standard must be chosen in such away that, it has the same visibility and located in the same area of the sky as our targets at the time of observation. This will certainly assign almost the same air mass for both the standard stars and the science objects, which can be very useful when we apply the extinction correction for our science objects. To start the reduction steps, first we make a directory call it iraf, inside iraf type **mkiraf**. This will create a login.cl file where all the reduction steps are saved. In the logfile we can describe every step we make, and we can also write the parameters used in the tasks into the logfile. Finally, preferably if we save every relevant table or figure we obtain.

The first thing to do is to change the data file into *file.imh*, so it can match IRAF

format, then we should check all the existed files to be sure that we have all the required frames for the reduction process. This can be done using the command **display file.imh**. Fig. 4.1, Fig. 4.2, Fig. 4.3 and Fig. 4.4 are the raw images of the flat field, the lamp and the science object which are the required frames for the reduction process.

4.5 CCD reduction steps

In this section we will briefly outline how and why the CCD images need work. Most of the calibration data is intended to remove additive effects: the electronic pedestal level (measured from the overscan region on each of the images), the pre-flash level and/or underlying bias structure, and if necessary, the dark current. The flat-field data (dome or projector flats exposures) will remove the multiplicative gain and illumination variations across the chip. Frings are an additive effect that must be removed at last. When we obtained our frames at the telescope, the output signal was '**biased**' by adding a pedestal level of several hundred ADU's. We need to determine this bias level for each frame individually. This can be done by displaying the frames one by one to determine the bias of each frame. The bias level is usually a slight function of position on the chip, varying primarily along columns. We can remove this bias level to first order by using the data in the *overscan region*, which is almost 40 columns at the right edge of the frames, obtained with the Nordic Optical Telescope.

The data has to be averaged over all the columns in the overscan region, and fit these values as a function of line-number. This fit will be subtracted from each column in the frame. At this point we will chop off the overscan region, and keep only the part of the image containing useful data. This later step usually trims off not only the overscan region but the first and last few rows and columns of the data. these steps can be done using the task **ccdproc** which is under the package **noao**, **imred**, **ccdred**. First, set up the translation table for the image headers by running **setinstrument**; this will also set various defaults within the **ccdred** package. Enter the proper **biassec** and **trimsec** into **ccdproc** at this time. Substantiate that the header translations are valid by running **ccdlist**. Process all the frames to remove the overscan and average bias, and to trim the images (first pass through **ccdproc**). The output of this processing will look like Fig. 4.5 for each image. After this step our frames will be bias subtracted and only the useful part of the data is present, the output frames as a result of this step are shown in Fig. 4.6 and Fig. 4.7 for both the lamp and the science frames, and the same is applied on the flat-field frames.
The next step in removing the instrumental signature is to flat-field the data. The

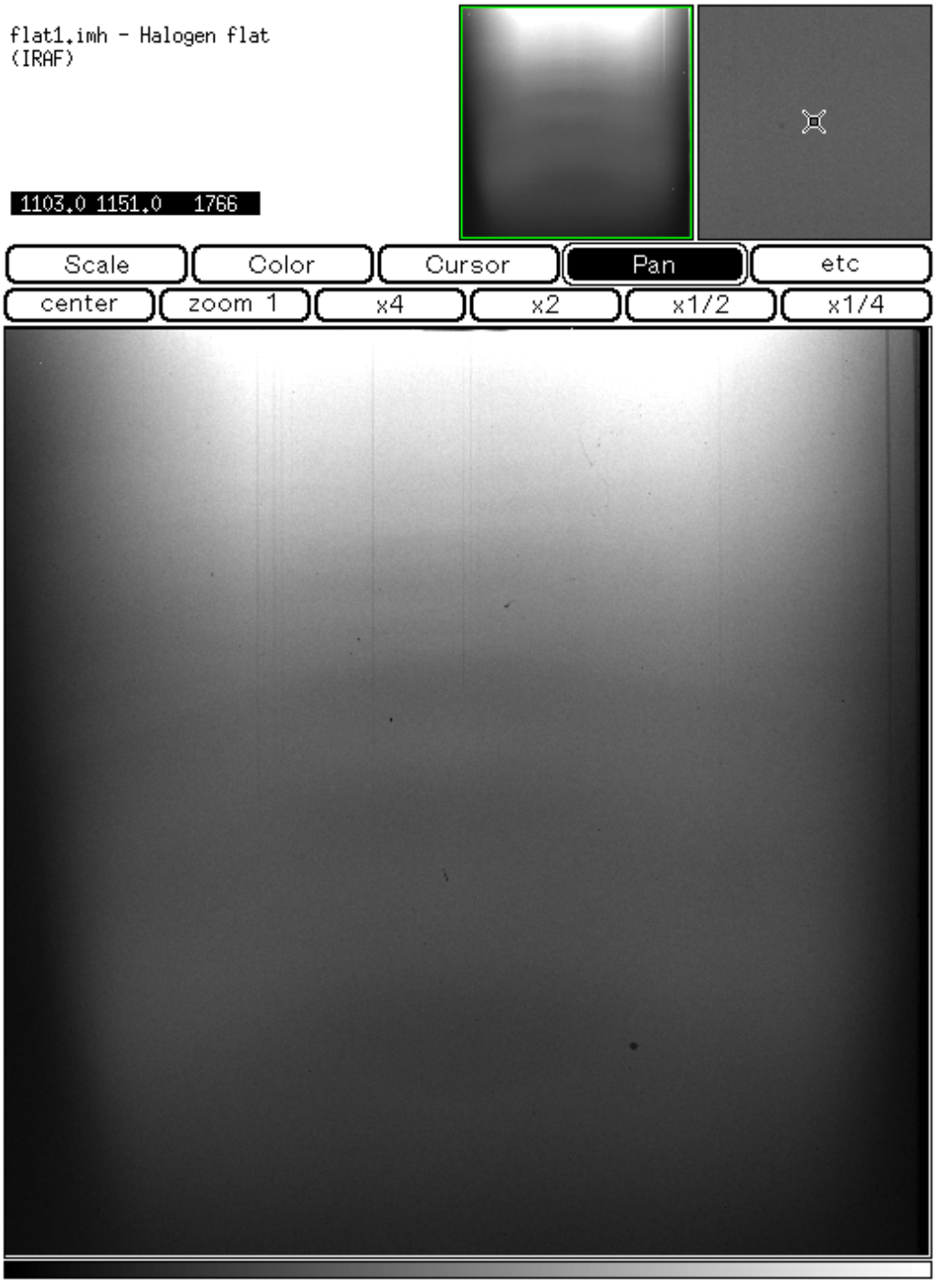

Figure 4.1: A halogen flat-field image taken with 2048 × 2048 CCD camera at the Nordic Optical Telescope in April 2001. No reduction steps have been performed on such image yet.

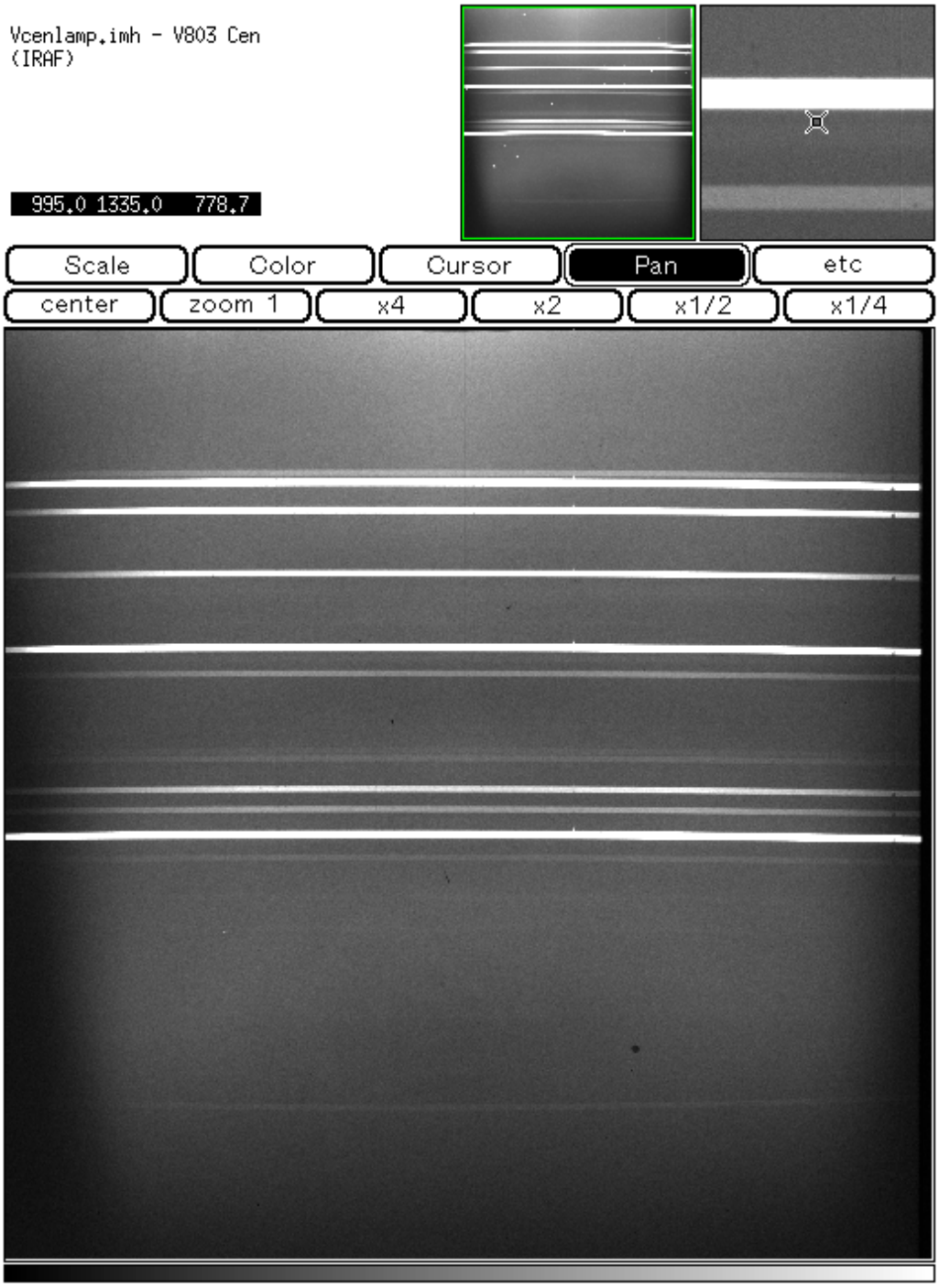

Figure 4.2: An image of a helium lamp taken with 2048 × 2048 CCD camera at the Nordic Optical Telescope in April 2001. No reduction steps have been performed on such image yet.

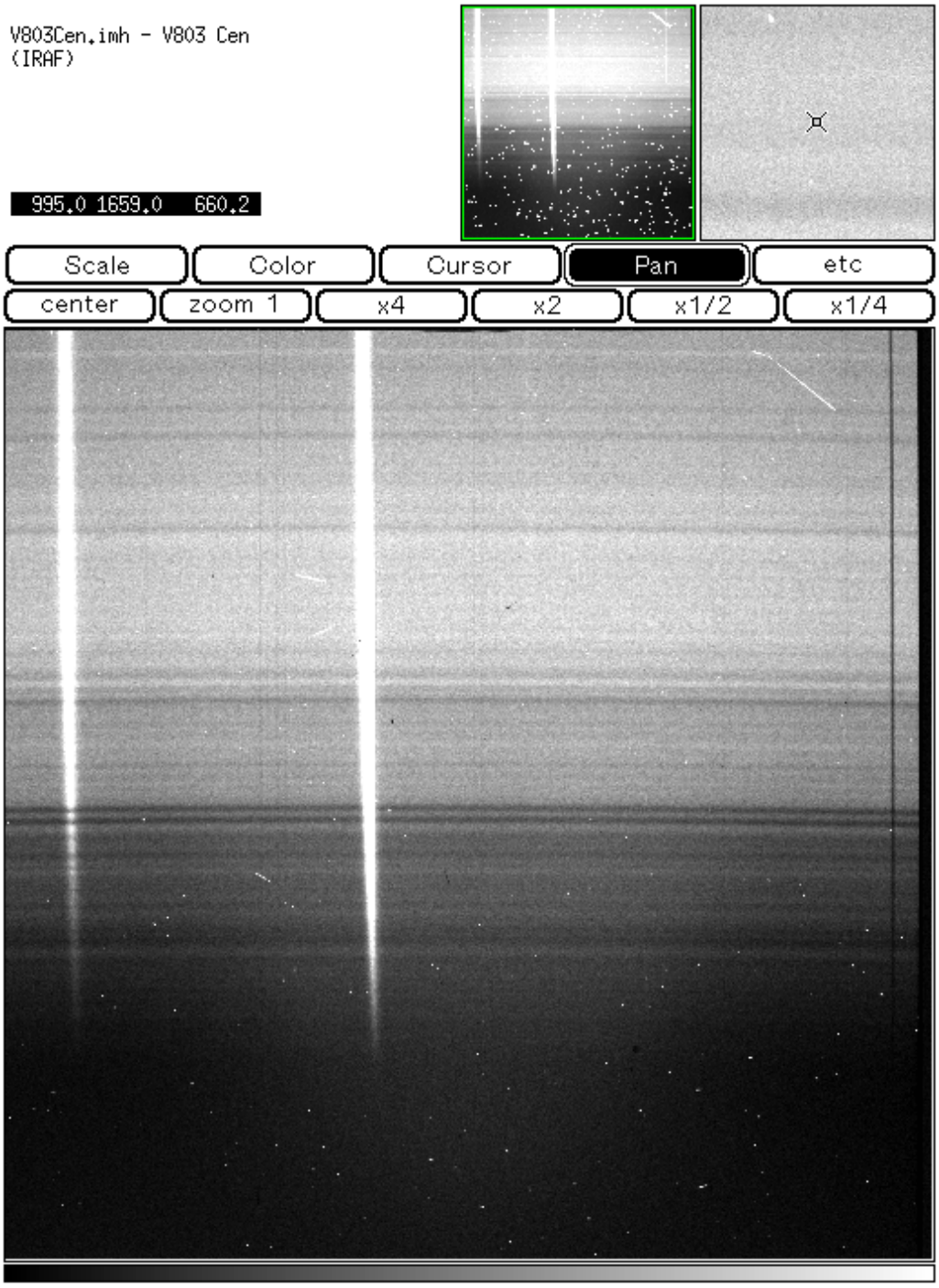

Figure 4.3: An image of V803 Cen taken with 2048 × 2048 CCD camera at the Nordic Optical Telescope in April 2001. No reduction steps have been performed on such image yet. The sharp line close to the middle of the image is the spectrum of V803 Cen, while the line to the left is a spectrum of anonymous star in the same field as V803 Cen.

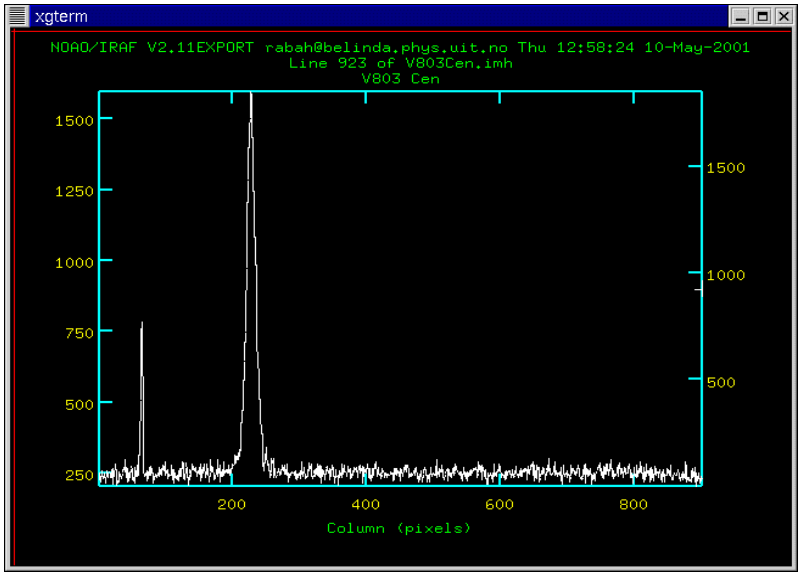

Figure 4.4: The aperture of both V803 Cen and the anonymous star in the field are shown in this figure. This is another way of testing the frames of our data.

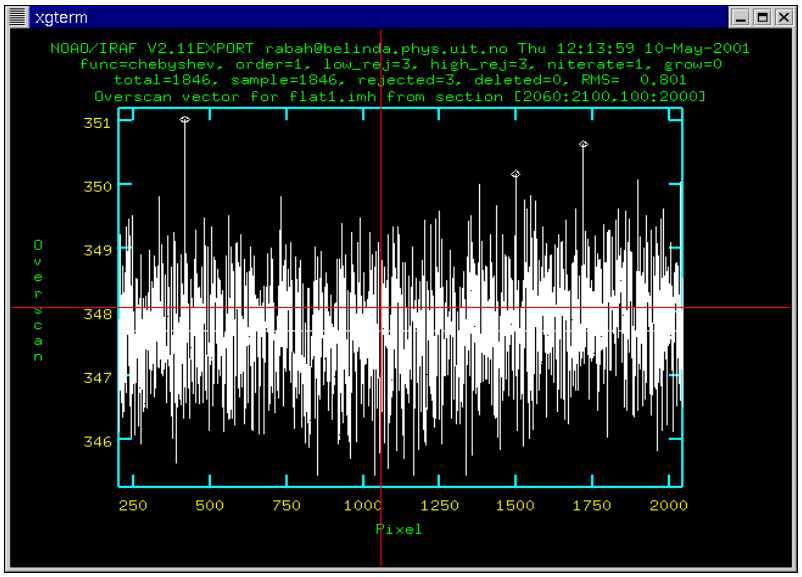

Figure 4.5: This is a sample plot which we get as a result of running **ccdproc** task to subtract the bias level and to chop the overscan region.

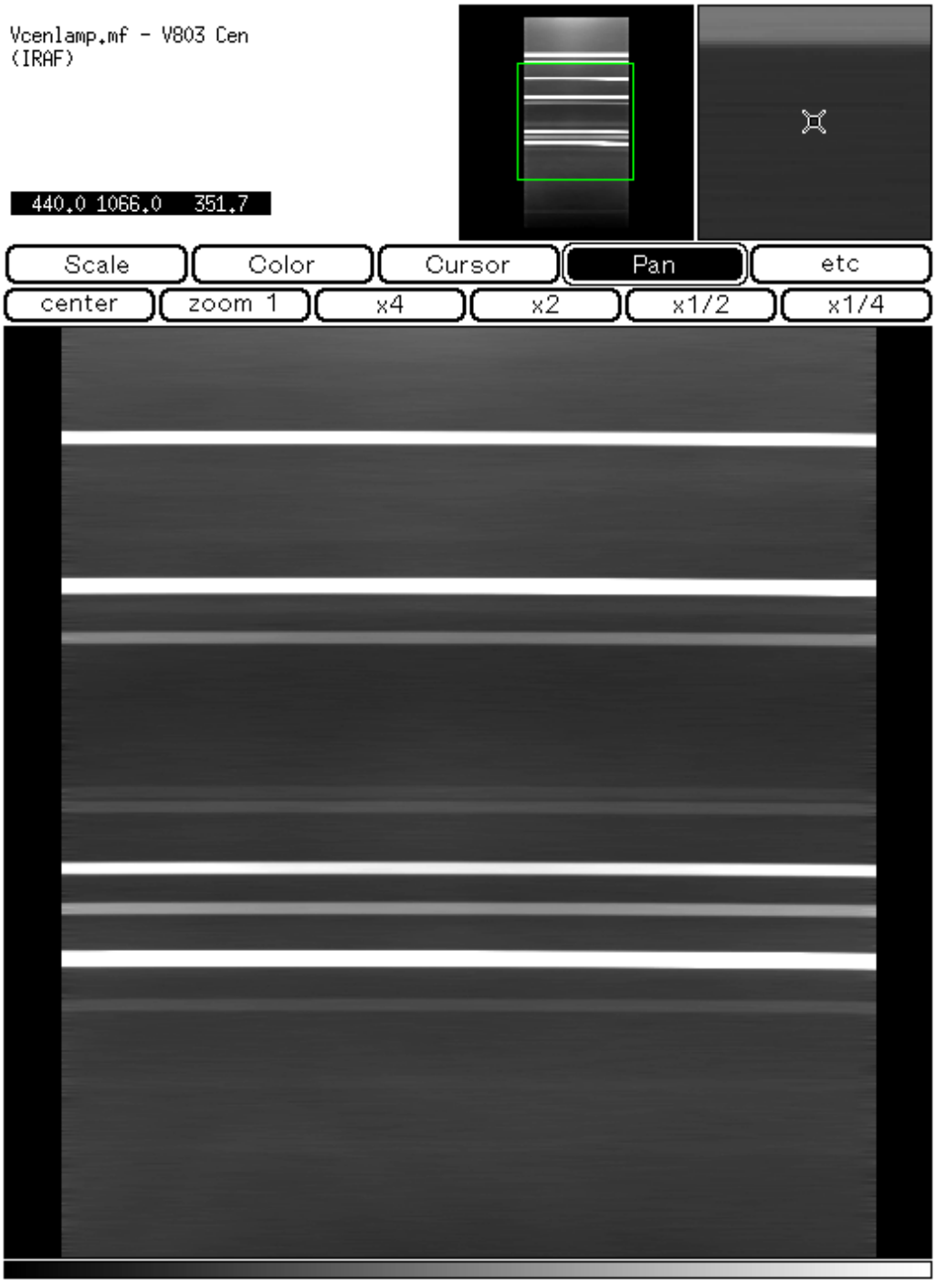

Figure 4.6: The frame of a helium lamp after running the **ccdproc** task on it, which subtracts the bias level and chops the overscan region.

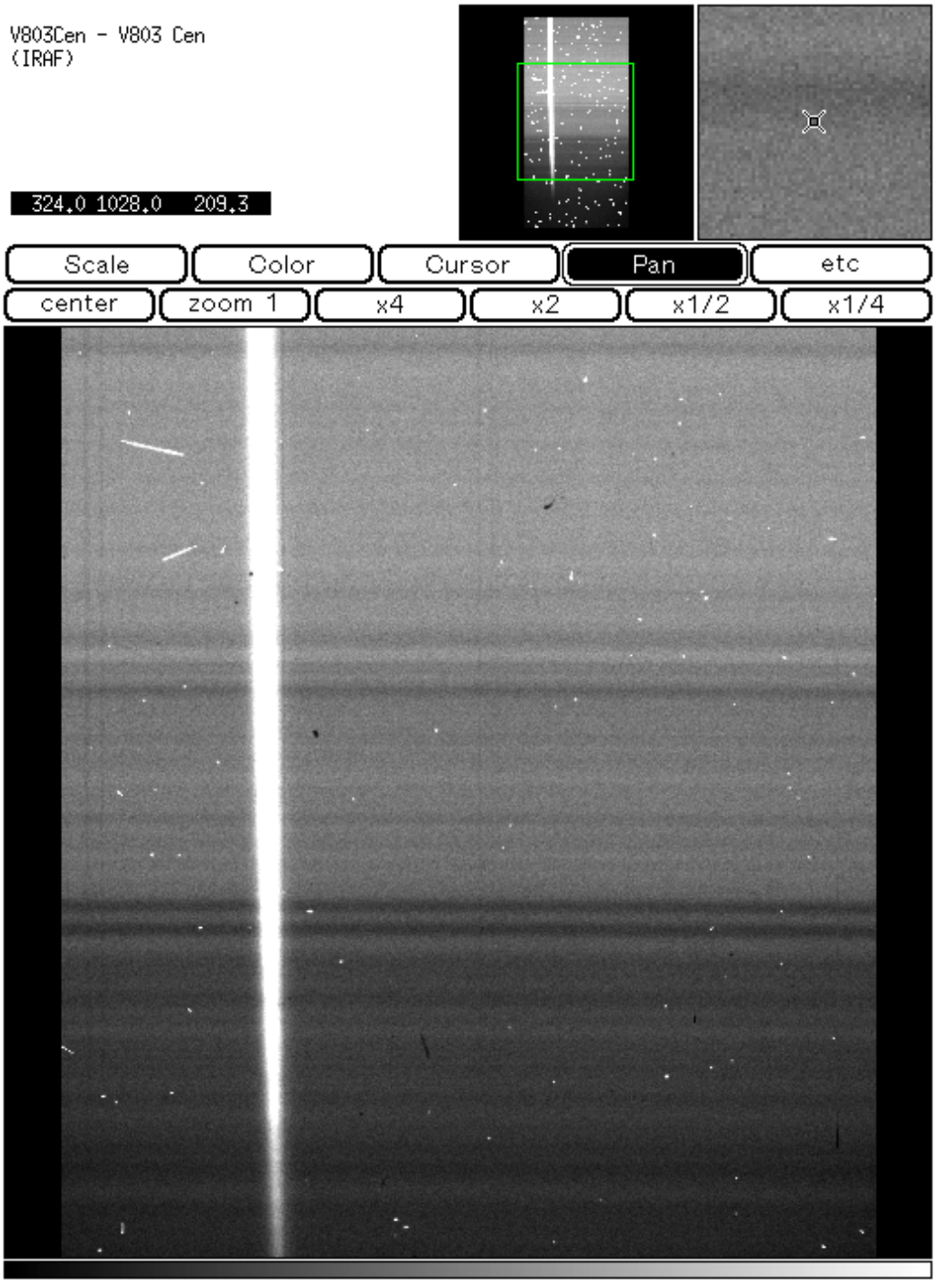

Figure 4.7: The frame of the science object V803 Cen after running the **ccdproc** task on it, which subtracts the bias level and chops the overscan region. In this figure we see that the anonymous star which was in the field has been canceled out of the image, because it is not part of our concern.

variations in sensitivity are multiplicative, and we need to divide the data by the flat-field to remove the pixel-to-pixel gain variations. To do such step, first we want to combine the flat-field exposures. This can be done using the task **flatcombine** which is under the **noao, imred** and **ccdred** packages. The reasonable values for the parameters which can be applied on data taken with the NOT can be found in the user's guide by Nasser (2000). It is preferable if we combine at least five frames to get a super-flat "**Sflat**" as seen in Fig. 4.8. This is still not enough to divide our data 'Science objects' by the flat field. One step is left and that is to normalize the super-flat-field into a value ≈ 1 using the response task which is under **noao, twodspec** and **longslit** packages. The reason for doing this step is to divide the **Sflat** by the average value before flat-field division so that we roughly preserve the correct counts in our objects frames. The output from the response task is a normalized super flat-field '**NSflat**' seen in Fig. 4.9. Finally we divide our science objects by the normalized flat-field. Fig. 4.10 shows the raw spectrum of our science object after the flat-field division. After this step let us call our science frames as "*science.flat*"

4.6 Wavelength calibration

Our first step is to do wavelength calibration for which we apply the He-frames. When the first He-frames are displayed some obvious defects are visible such as a few bad columns. The emission lines follow the rows with good accuracy. We therefore use the task **median** to filter the He-images with median filter 50×1 pixels. The result is clearly much nicer to look at.

Next we want to identify the He-lines in the two-dimensional images. To do that we run the task **identify** which can be found under the **noao, twodspec** and **longslit** package. After choosing the best value for each parameter in the task, the fit has to be made to the middle column of the image.

The main problem is to identify a few lines in the He-spectrum. This is a very difficult and critical task, and the best thing to do is to get help for identifying such lines. This help can be obtained from http://www.noao.edu/kpno/specatlas/index.html, by choosing the type of lamp and the wavelength range where the lines has to be identified. Finally, after identifying at least three lines, the rest of the job can be done automatically by IRAF commands, see the user's guide for the details. The final fit will look like Fig. 4.11. We should cover all the spectral intervals with fitting points as far as possible, and we should not use a too high order in the fit. When we have found what we consider the optimum fit, we use this as reference when we in the next step apply the **reidentify** task to make fits along other columns of

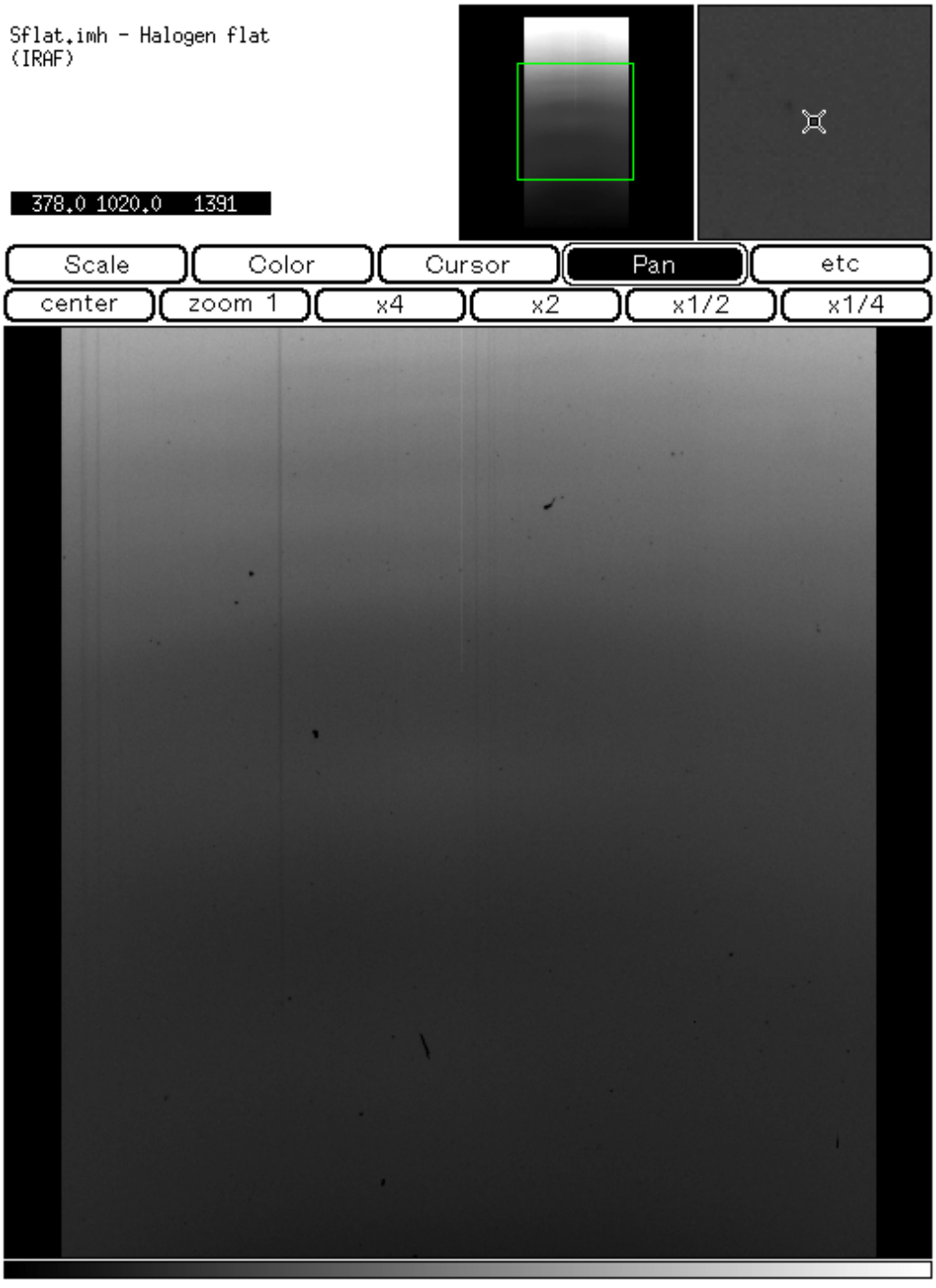

Figure 4.8: The super-flat **'Sflat'** frame which is produced as a result of running the **flatcombine** task.

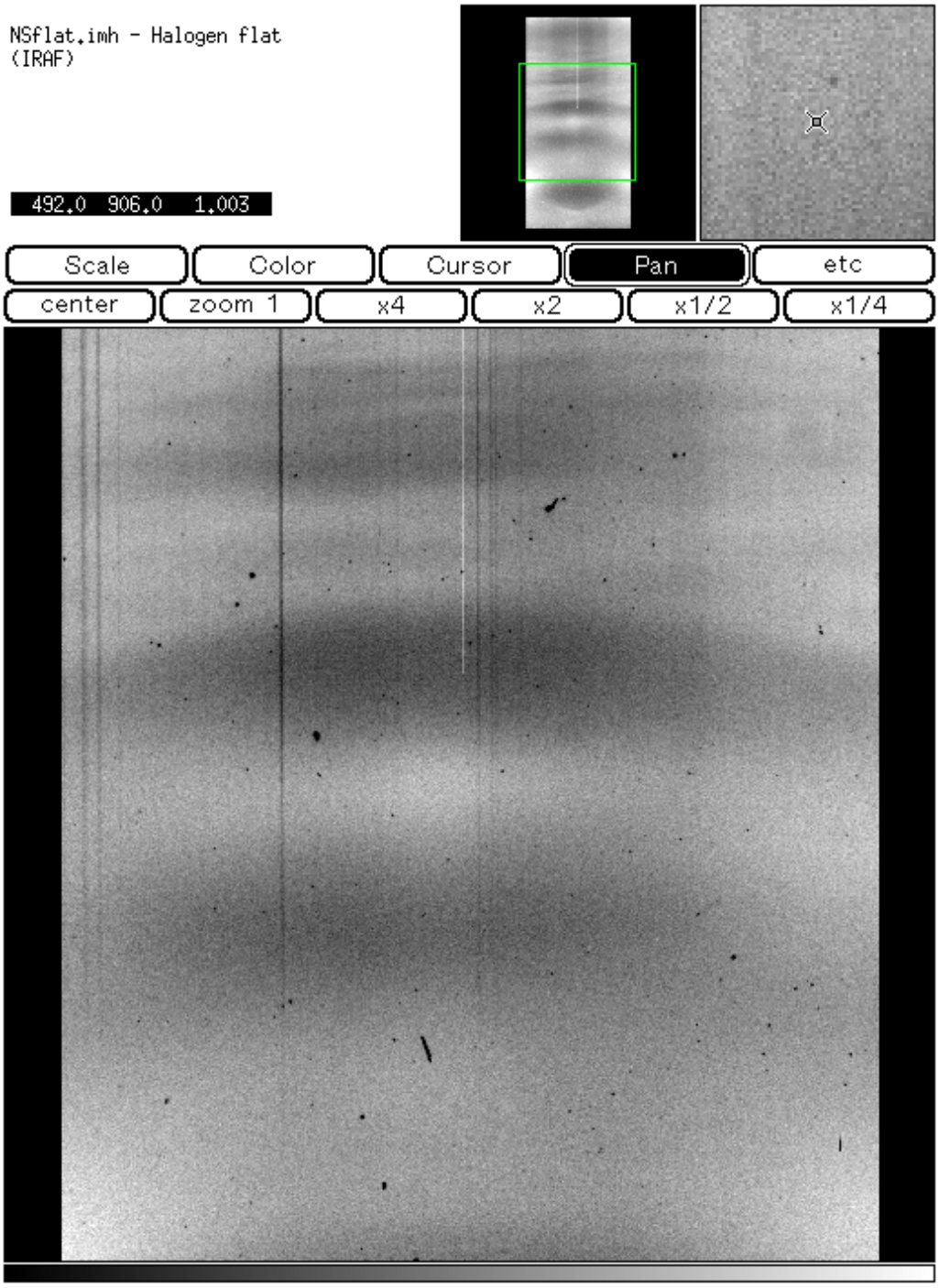

Figure 4.9: The normalized super-flat **'NSflat'** frame which is produced as a result of running the **response** task. On the upper left side of the image we can see the number "1.003" which represents the number of counts at a random position in the frame. This indicates that the super flat-field has been averaged into unity.

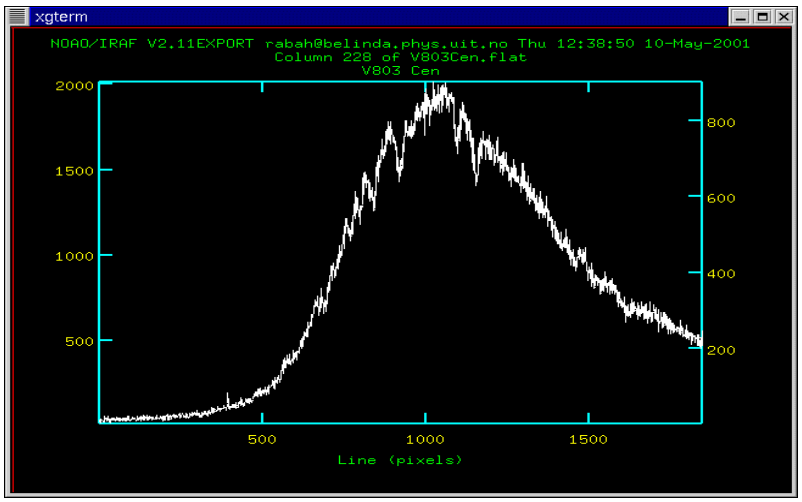

Figure 4.10: This plot shows the raw spectrum of V803 Cen after the flat field division. We see that almost all the cosmic emission lines have canceled out. We can also see the helium absorption lines in this non-flux-calibrated spectrum, which indicate that the system may have been in the high state during the observations.

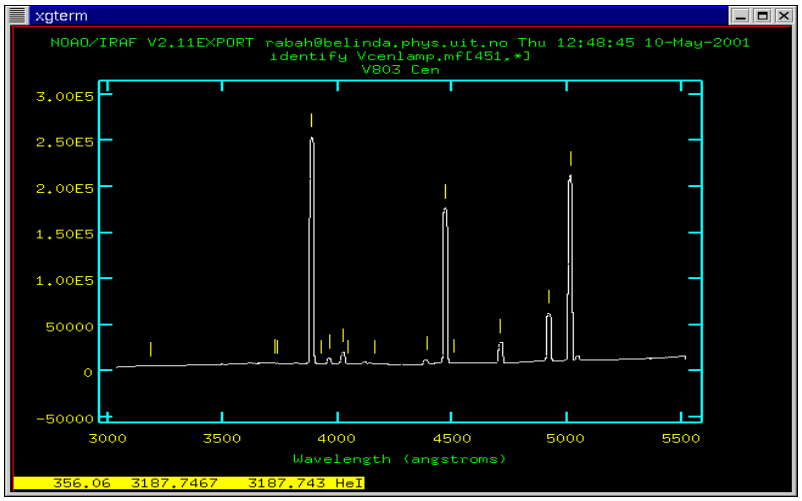

Figure 4.11: The figure shows how the lamp frame will look like after identifying all the emission lines in the helium lamp.

the He-frames. We used **reidentify** in the interactive mode to be able to follow each step separately. By these steps we have mapped the wavelength along several columns in the He-frames. We should apply the task **reidentify** on all the lamps which are of our concern. Next, we fit these maps with **fitcoords**, which has to be done interactively, and then study the residuals carefully by displaying them in various possible ways.

Finally, we transform the images of the spectra of our science objects and the standard star using the task **transform**. The resulting frames are given the names "*science.flat.trans*". In these frames the Y-axis will be linear in wavelength. Let us agree to put the parameter *dy*= 0.1. That will make a step of 1 pixel in Y equal to 1Å.

4.7 Background subtraction and extinction correction

The first thing to do before we start the background subtraction is to display the *science.flat.trans* with its strong emission lines. The sky background is a function of the wavelength. It is conveniently determined and subtracted as seen in Fig. 4.12 by the task **background** in an interactive mode. Uncontaminated areas of sky background are specified by the parameter *sample*, but it is recommended to set these intervals in an interactive mode. It is often an advantage to set the parameter *naverage* to a negative value. Make test fits for some y-coordinate values, you choose after inspection of the displayed image. The background has to be fitted with a low order function. The detailed process is described in Nasser (2000) with the reasonable values chosen for the parameters. If the process was successful, you can enjoy how nice even the strong sky emission lines have canceled out. The science frames are then called "*science.flat.trans.back*". The task **extinction** is used to correct for atmospheric extinction. First, we must check that the airmass and the exposure time are given in the image header. For the extinction table, we must use the one which is specially made for the region where the observations were taken. After the extinction correction is done, the frames will be named as "*science.flat.trans.back.extinc*"

4.8 Flux calibration

Observing spectrophotometric standards is the tool which we use to calibrate our science objects. The idea in flux calibration is to measure the instrumental sensi-

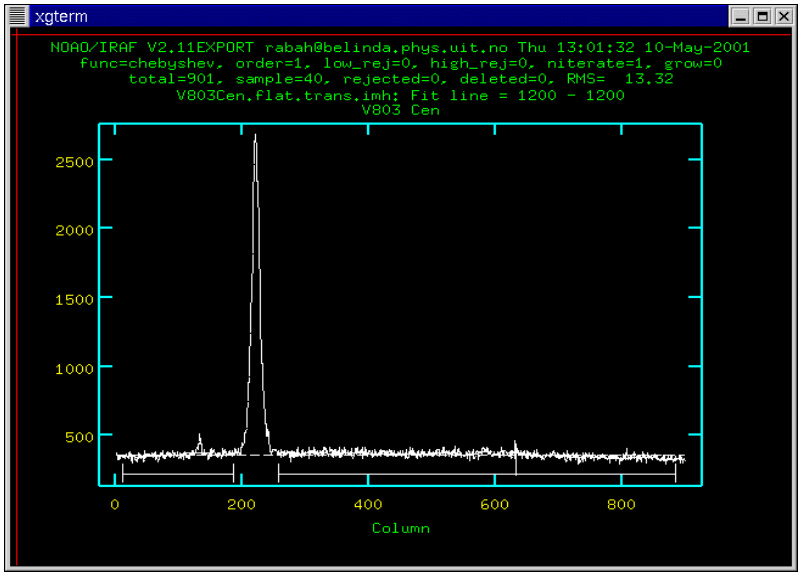

Figure 4.12: In this figure we show how to choose the sky background.

tivity by observing a star which its spectral flux is known in absolute units. The directory **onedstds**$ in IRAF houses several sub-directories containing the standard star calibrations. The file **onedstds$README** explains where these calibrations come from. Each star has its own individual file within a given sub-directory, which specifies the wavelength, width of the pass-band, and the magnitude of the standard star. The first step in the flux calibration process is to extract the spectrum of our standard star from the reduced frame *standard.flat.trans.back.extinc*. For this purpose we use the task **apall** which is under **noao, twodspec, apextract** package in interactive mode. We should answer 'yes' when **apall** ask for permission to make a trace, this will make us be able to determine how well the star spectrum follows the direction along column. Next step is to extract the spectrum. For each step in wavelength, all counts from the star is sampled, and a one-dimensional spectrum results. The output spectrum of this step will produce a frame with *.ms.imh* extension, which we can plot using the task **splot**. It is possible to see some cosmic emission lines in the spectrum which must be removed. The spectrum might become very noisy below λ3000 which has to be corrected, see Nasser (2000) for the detailed steps. After all, we can give the spectrum a new name such as *std-spec*. We continue with the task **standard** which is under **noao, onedspec** package. The task compares the observed and standard fluxes. The later as mentioned before are present in an IRAF directory **onedstds**$ with a file named after the star. Before

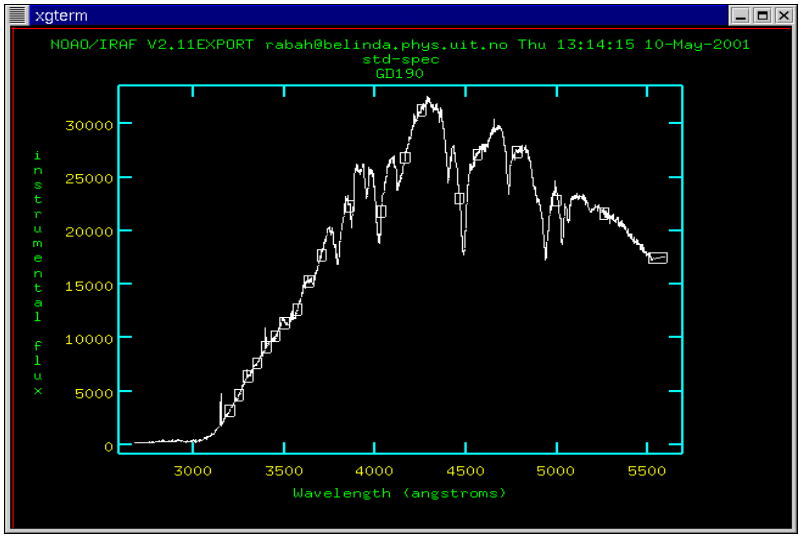

Figure 4.13: The spectrum of the standard star GD190 is shown with small boxes where the observed pass-band are placed. The reason for running this task is to compare the observed and the standard fluxes, and the task will then interpolate 'observed' values for these bands.

we call **standard** we must find the calibration data directory and name of the star spelled in the directory. In the same task we should also name the extinction file. The output figure after running such task is seen in Fig. 4.13. The stellar spectrum is shown with small boxes where the observed pass-bands are placed. It is possible to make some artificial pass-bands with the cursor (a-option). The task will then interpolate 'observed' values for these bands. The output - let us call it *std* - is a file which we can read. It contains three columns, the wavelength, the flux and the pass-band as the first, second and the third column respectively. The calibration measurements in *std* is used by the task **sensfunc** to calculate the spectral sensitivity. While running this task we should determine the best fit interactively as seen in Fig. 4.14. The final sensitivity function is output into a one-dimensional image which we can call it *sens*. The sensitivity function file may be displayed by **splot** as seen in Fig. 4.15.

We are now ready to flux calibrate our science frames *science.flat.trans.back.extinc* by extracting the spectrum using the task **apall**, which as a result gives an output spectrum with *science.flat.trans.back.extinc.flux*. The final flux calibration step can be done by means of **fluxcalib** in the **twodspec** and **longslit**. The calibrated image can be given the name *science.flat.trans.back.extinc.flux.ms.imh*. In case we have

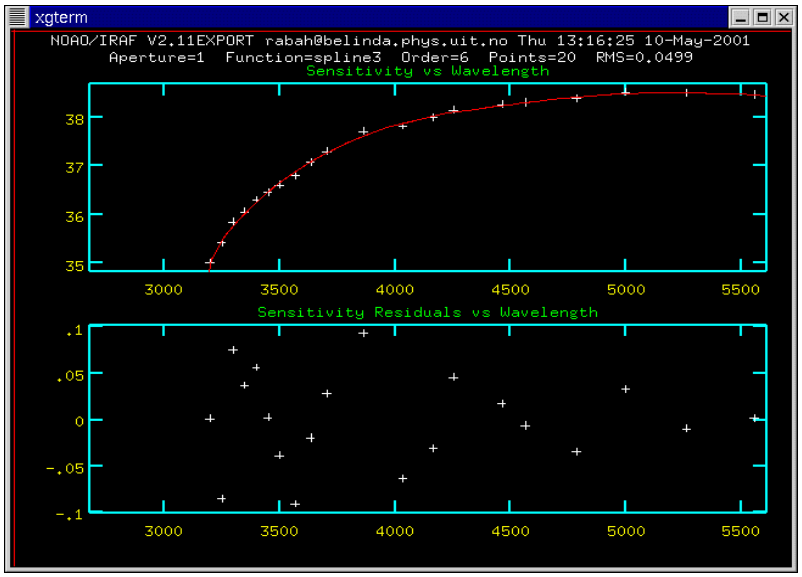

Figure 4.14: Making a good fit with **sensfunc** to be able to calculate the spectral sensitivity.

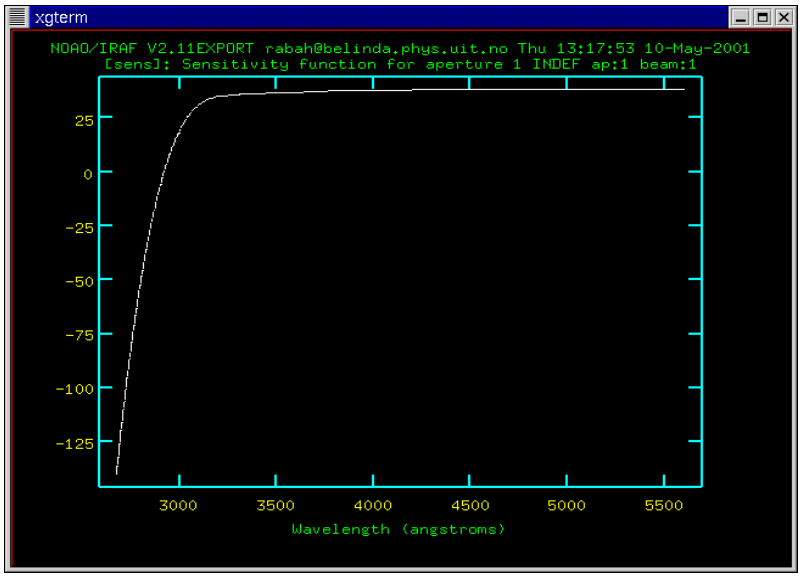

Figure 4.15: The output of the sensitivity function fit called 'sens'. It is a one-dimensional image which can be displayed using **splot**. This is the output file which will be used to flux-calibrate the frames of the science objects.

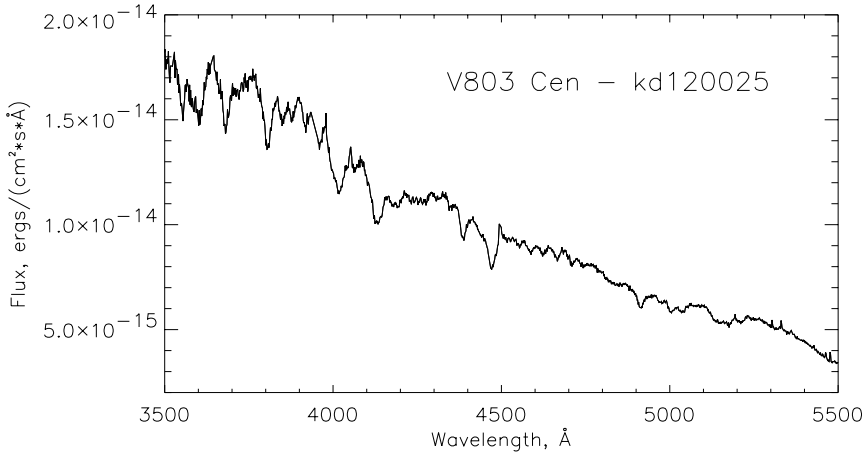

Figure 4.16: The final flux-calibrated spectrum of V803 Cen, which clearly shows that our reduction steps are correct, because we succeeded to obtain an absolute flux calibration for our science objects.

done everything right the flux unit should be ergs $s^{-1}cm^{-2}$Å^{-1}. The final absolute flux-calibrated spectrum is shown in Fig. 4.16.

4.9 Analysis and discussion

In the previous sections we have gone briefly through all the reduction steps which led us to the absolute flux calibration of our spectroscopic data. During the reduction process, minor common problems appeared such as determining the bias level and choosing the proper overscan region for each frame, in addition to choosing the right value for each parameter in all the tasks. In general, all the reduction steps went smoothly as expected and we did not face any serious problems. That is mainly because we followed all the required reduction steps mentioned in detail in the user's guide by Nasser (2000). In this section we discuss the reduced flux-calibrated spectra taken with the Nordic Optical Telescope, for three nights from the 12th -15th of April 2001. The reason for doing such observations is because the objects which we are observing are unstable. V803 Cen and CR Boo are both members of the AM CVn family, which change from high, intermediate and low state within a very short time. We decided to observe such systems for four nights continuously to detect such systems in all of their states if possible, which can give us a better idea

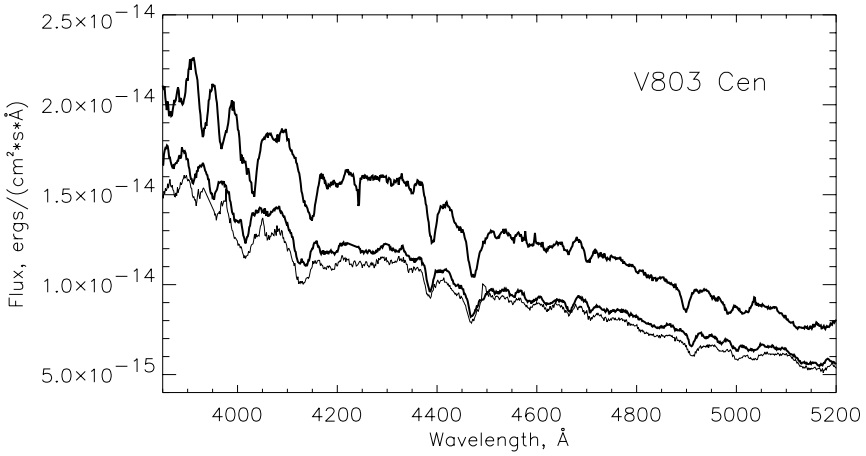

Figure 4.17: A comparison between the flux calibrated spectra of V803 Cen taken on April 12th (kd120025) 'thin line' and on April 13th from the top (kd130039) and (kd130019) 'thick lines'.

about their mass accretion rate in each state. The systems show deep absorption He I lines in their high state while such lines become almost in emission in the low state. During the four nights of observations, apparently the systems were stuck in the high state and we were not able to detect them in any other state. In Fig. 4.17 we compare the calibrated spectra of V803 Cen taken on April 12th 'thin line' with the spectra of the same object taken on April 13th 'thick lines'. From this figure we can easily see that the system was in a rising state on April 13th when compared to the state of April 12th. The system went down into a lower state on April 14th described by the thick lines as seen in Fig. 4.18. From aperture photometry analysis, we were able to determine the magnitude of V803 Cen in the three nights which varied between (14.3 - 14.8), which indicates that the system was in the oscillating or a high state during the observations.

The same comparation has been done for the spectra of CR Boo as seen in Fig. 4.19. The spectra of CR Boo taken on April 13th were not well flux calibrated, so we avoid presenting it in this work. We found that the system was down on April 14th, when compared to the system status of April 12th. From the aperture photometry, the B-magnitude found for CR Boo during the three nights varied between 13.9 - 14.7, which also indicates that the system was in the high state during the observations. In chapter 6, we will show theoretical models fitted to the same spectra presented in the last three figures of this chapter for both V803 Cen and CR Boo.

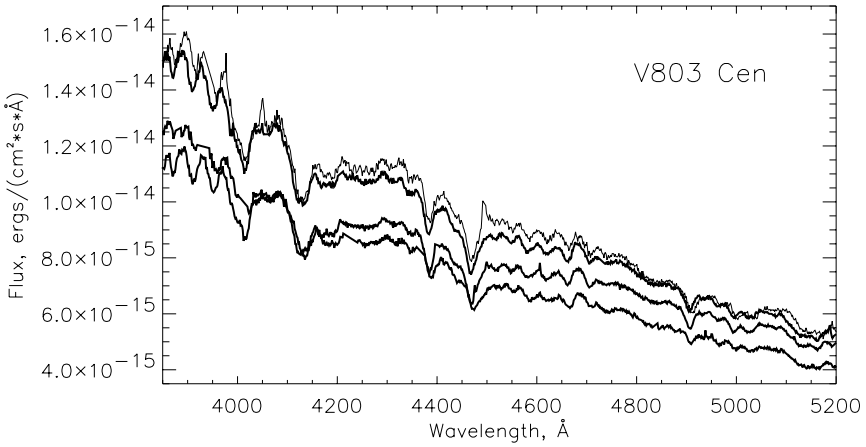

Figure 4.18: A comparison between the flux calibrated spectra of V803 Cen taken on April 12th (kd120025) 'thin line' and on April 14th from the top (kd140095), (kd140098) and (kd140083) 'thick lines'.

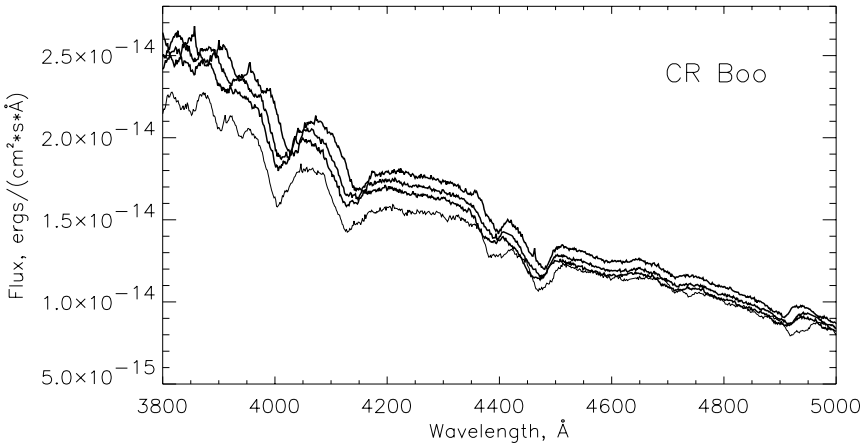

Figure 4.19: A comparison between the flux calibrated spectra of CR Boo taken on April 12th (kd120040) 'thin line' and on April 14th from the top (kd140068) ,(kd140071) and (kd140127) 'thick lines'.

Table 4.1: List of spectra, obtained with the Nordic Optical Telescope in March 1997.

File	Object	grism	slit	Ex.T.
Name	Name	#	arcsec	Sec.
gc010007	GD 71	6	2.5	500
gc010011	PG 0943+441	4	2.5	200
gc010015	PG 1022+050	4	2.5	300
gc010041	AM CVn	4	2.5	400
gc010043	AM CVn	6	2.5	600
gc010051	GP Com	4	2.5	600
gc010052	GP Com	6	2.5	1200
gc010056	V803 Cen	4	2.5	800
gc010067	CR Boo	4	2.5	600
gc010068	CR Boo	6	2.5	1200
gc010076	HP Lib	4	2.5	400
gc010080	PG 1606+422	4	2.5	200
gc010081	PG 1606+422	6	2.5	400
gc020051	GD 71	6	0.7	1200
gc020065	PG 0943+441	6	0.7	1200
gc020068	AM CVn	6	0.7	2400
gc030014	V803 Cen	6	2.5	1600
gc030015	V803 Cen	4	2.5	800
gc030024	HP Lib	6	2.5	800
gc030025	HP Lib	4	2.5	800
gc030028	PG 1606+422	6	2.5	800
gc030029	PG 1606+422	6	0.7	1200
gc030084	PG 0943+441	4	2.5	200
gc030084	PG 0943+441	4	2.5	200
gc030085	PG 0943+441	6	2.5	800
gc030091	AM CVn	6	2.5	1200
gc030092	AM CVn	4	2.5	800
gc030094	PG 1314+293	6	2.5	400
gc030095	PG 1314+293	6	0.7	1800
gc030099	GP Com	4	2.5	800
gc030100	GP Com	6	2.5	1800
gc030102	CR Boo	4	2.5	1200
gc030108	V803 Cen	4	2.5	800
gc040007	V803 Cen	6	2.5	1600
gc040018	HP Lib	6	2.5	800
gc040020	CR Boo	6	2.5	2400
gc040023	HP Lib	4	2.5	1400

Table 4.2: List of spectra, obtained with the Nordic Optical Telescope on the 12th - 15th of April 2001, with the same grism, number 6.

File	Object	slit	t(exp)
Name	Name	arcsec	s
kd120025	V803 Cen	2.5	1800
kd120027	V803 Cen	2.5	1800
kd120029	V803 Cen	2.5	1800
kd120040	CR Boo	2.5	1800
kd120052	HZ 43	5	1000
kd120057	GD 190	5	1000
kd130010	CR Boo	2.5	1800
kd130019	V803 Cen	2.5	1800
kd130036	GD 140	5	400
kd130039	V803 Cen	2.5	1200
kd130042	CR Boo	2.5	1800
kd130045	GD 190	5	1000
kd130058	CR Boo	2.5	1800
kd130061	CR Boo	2.5	1800
kd130064	HZ 43	5	600
kd140061	HZ 43	5	600
kd140068	CR Boo	2.5	1800
kd140071	CR Boo	2.5	1800
kd140083	V803 Cen	2.5	1800
kd140095	V803 Cen	2.5	1800
kd140098	V803 Cen	2.5	1800
kd140118	CR Boo	2.5	1800
kd140121	HZ 43	5	1800
kd140124	GD 190	5	1800
kd140127	CR Boo	2.5	1500

Table 4.3: The U,B and V magnitudes of V803 Cen with error 0.02 for the three nights of 2001 observations.

V803 Cen	U	B	V
April 12th	13.69	14.55	14.65
April 13th	13.30	14.30	14.41
April 14th	14.01	14.80	14.90

Table 4.4: The U,B and V magnitudes of CR Boo with error 0.02 for the two nights of 2001 observations.

V803 Cen	U	B	V
April 12th	13.79	14.70	14.88
April 14th	13.01	13.90	14.10

Chapter 5

Model atmosphere calculations

5.1 Introduction

One of many ways to prove the interpretation of the AM CVn stars as an IBWD, is to create a synthetic spectrum or a light curve of a model system and compare them with the observations. To construct such spectra we need the tool which is a program package, developed by Ivan Hubeny at the Goddard Space Flight Center of NASA. The package includes several programs, most important of which are program for calculating vertical structure of accretion disc TLUSDISK and program for calculating an emergent spectra from stellar or disc atmosphere SYNSPEC. The program TLUSDISK is based on the stellar atmosphere model calculations program TLUSTY (Hubeny 1988; 1990). It is designed to calculate a vertical structure of a steady state equilibrium accretion disc. Its output model atmosphere can be directed to SYNSPEC (Hubeny & Lanz 1990a), which evaluates atmospheric opacity and emissivity and produces a synthetic spectrum. Those two programs are accompanied with a set of utility and shell programs, which simplify the process of preparing the initial input and processing the output. In this chapter we will describe the most important properties of TLUSDISK, leaving the rest of the description to the respective program guides. The good model atmosphere will be used as a basic tool for our modeling process, to investigate the output spectra expected as a result from using TLUSDISK code. In addition to that, we will discuss the effect of explicit consideration of certain atoms like helium and hydrogen. The influence of some of the disc parameters on the output disc spectra such as the mass accretion rate $\dot{M}$, the angle of inclination i, the inner and outer radii of the disc $R_{in}\&R_{out}$ and the abundance of elements will be part of our major investigations. We will also study the effects of departures from LTE in order to assess the necessity of

computing more complicated and more time-consuming NLTE models. Finally, all these investigations will be used as our main tool to build the model, which can produce the spectra, that best fit the observed spectra of the AM CVn systems. Before proceeding into all these investigations, it is more wise to discuss in short the theory of stellar atmospheres, which our modeling attempts are based on.

5.2 Stellar atmospheres

Stellar atmospheres are the basis of our work, so in this section we will review the basic formulae which determine the conditions in stellar atmospheres, based on the stellar atmospheres book by Mihalas (1978), and the lecture notes 'Radiative transfer in stellar atmospheres' by Rutten (1999). Although disc atmospheres have some distinctive differences from stellar atmospheres, which we will discuss later in this section, the theories describing them are similar in principle. In stellar atmosphere all the energy generated in the interior has to traverse the atmosphere before emerging at the surface of the star. The energy released by a star is either created by nuclear reactions deep inside its interior or, as is the case with white dwarfs, is caused by the slow leakage of remaining energy after all nuclear reactions have stopped, causing a cooling of the star. In both cases the energy comes from the interior of the star. Energy, passing through the medium, will undergo changes in spectral distribution, dependent on the state of the atoms it interacts with, as well as it will change the state and in turn will encounter different surroundings. Thus it is impossible to separate their influence on each other and the problem needs to be solved as a whole. Interaction with the material in the atmosphere may, however, alter the frequency distribution of the energy, or convert it to kinetic or other forms of energy. Thus the radiative flux at a given frequency may vary greatly through the atmosphere, and depends strongly on the physical state of the atmosphere at all depths. On the other hand, the state of the stellar materials influenced by the amount and the strength of the energy which is transported through it. The two problems of finding the flux and establishing the structure of the atmosphere are therefore linked, and cannot be easily solved. In most cases this must be solved numerically, and this fact has given rise to the large fields of stellar atmosphere modeling. In this section we will briefly explain the main equations, governing the interaction between radiation and matter and the steps leading to the creation of a model atmospheres.

5.2.1 Intensity

The specific intensity I(**r**,**n**,ν,t) of radiation at position **r**, traveling in direction **n**, with frequency ν at time t is defined such that the amount of energy transported by radiation of frequencies $(\nu, \nu + d\nu)$ across an element of area dS into a solid angle $d\omega$ in a time interval dt is

$$dE = I(\mathbf{r}, \mathbf{n},\ \nu, t)\ dS\ cos\theta\ d\omega\ d\nu\ dt \tag{5.1}$$

where θ is the angle between the direction of the beam and the normal to the surface. The dimensions of I are ergs cm^{-2} sec^{-1} hz^{-1} sr^{-1}. The specific intensity is independent of the distance between the radiation source and the observer if the amount of energy, contained in the ray, is preserved.

5.2.2 Mean intensity

In both the physical and the mathematical description of a radiation field it is useful to employ various angular averages or moments. Thus we define the *mean intensity* to be the straight average of the specific intensity over all solid angles *i.e*

$$J(\mathbf{r},\ \nu, t) = (4\pi)^{-1} \oint I(\mathbf{r}, \mathbf{n},\ \nu, t)\ d\omega \tag{5.2}$$

The mean intensity has dimensions ergs cm^{-2} sec^{-1} hz^{-1}. The element of solid angle $d\omega$ is given by $d\omega = sin\theta\ d\theta\ d\phi = -d\mu\ d\phi$. If we consider one dimensional atmospheres, I is independent of ϕ, hence

$$J(z,\ \nu, t) = (4\pi)^{-1} \int_0^{2\pi} d\phi\ \int_{-1}^{1} d\mu\ I(z,\ \mu,\ \nu, t) = \frac{1}{2} \int_{-1}^{1} I(z,\ \mu,\ \nu, t)\ d\mu \tag{5.3}$$

The same result applies in spherical geometry with z replaced by r.

5.2.3 The flux

We define the flux of radiation $F(\mathbf{r},\ \nu, t)$ as a vector quantity such that $F.dS$ gives the net rate of radiant energy flow across the arbitrarily oriented surface dS per unit time and frequency interval. The flux can be derived from the specific intensity which is considered as a sum of the specific intensities over all solid angles and obtain

$$F(\mathbf{r},\ \nu, t) = \oint I(\mathbf{r}, \mathbf{n},\ \nu, t)\ \mathbf{n}\ d\omega \tag{5.4}$$

The flux dimensions : ergs cm^{-2} sec^{-1} hz^{-1}

5.3 The transfer equation

As radiation passes through the gas composing a stellar atmosphere, it interacts with the material and is absorbed, emitted, and scattered repeatedly. These phenomena determine how radiative transfer occurs in the atmosphere. It is very important in stellar atmospheres to make a distinction between true absorption and emission on one hand and the process of scattering on the other. This is because the physical nature of the interaction between the atmospheric material and radiation is quite different in these two cases. However, it is also important to realize that in the spectral lines the dichometry between these processes can be established uniquely only when we consider a transition between two specified atomic states, with no coupling to any other states allowed. As soon as sequence of transitions among several interacting states are considered, fundamental ambiguities arise, and it is no longer possible to describe a given line as an absorption or a scattering line in a rigorous way; nor would it be important or useful to do so. Nevertheless, it is fruitful to have at least an intuitive notion of the contrast between these two basic processes. For more detail Mihalas (1979) is one of the best references explaining such processes with good examples.

5.3.1 Derivation

To derive the transfer equation, we need to understand the behavior of the energy carried by the radiation field. First, to describe the removal of energy from the radiation field by matter let us introduce a macroscopic coefficient $\chi(\mathbf{r},\, \nu, t)$ called the *extinction coefficient*, or *opacity*, or sometimes the *total absorption coefficient*. This coefficient is defined such that an element of material, of cross-section dS and length ds, removes from a beam with specific intensity $I(\mathbf{r}, \mathbf{n},\, \nu, t)$, incident normal to dS and propagating into a solid angle $d\omega$, an amount of energy

$$dE = \chi(\mathbf{r}, \mathbf{n},\, \nu, t)\; I(\mathbf{r}, \mathbf{n},\, \nu, t)\; dS\; ds\; d\omega\; d\nu\; dt \tag{5.5}$$

within a frequency band $d\nu$ in a time dt. The extinction coefficient is the product of an atomic absorption cross-section and the number density of absorpers summed over all states that can interact with photons of frequency ν. The frequency variation of χ may be extremely complicated, and may include thousands or millions of transitions (bound-bound, bound-free, and free-free). It is sometimes useful to distinguish between 'absorption' and 'scattering'; hence we introduce volume coefficients $\kappa(\mathbf{r},\nu, t)$ and $\sigma(\mathbf{r},\nu, t)$ that describe the rate at which energy is removed from the beam by true absorption and scattering respectively. The total extinction is

given by

$$\chi(\mathbf{r},\,\nu,t) = \kappa(\mathbf{r},\,\nu,t) + \sigma(\mathbf{r},\,\nu,t) \tag{5.6}$$

That is, both processes are assumed to occur independently and to add linearly. In actual practice χ is sufficient to describe energy removed from the beam; the distinction between κ and σ is useful mainly in defining the emission coefficient.

Second, we need to describe the emission of radiation from the stellar material. This can be done if we introduce the macroscopic *emission coefficient* or *emissivity* $\eta(\mathbf{r},\mathbf{n},\,\nu,t)$ defined such that the amount of energy released from an element of material of cross section dS and length ds, into a solid angle $d\omega$, within a frequency band $d\nu$, in direction $\mathbf{n}$ in a time interval dt, is

$$dE = \eta(\mathbf{r},\mathbf{n},\,\nu,t)\;dS\;ds\;d\omega\;d\nu\;dt \tag{5.7}$$

The dimensions of η are ergs cm^{-3} sec^{-1} hz^{-1} sr^{-1}. As was true for the opacity, *thermal* emissivity is *isotropic* for *static* media (without imposed preferred directions) but is *angle dependent* for *moving* material owing to Doppler-shift effects. For radiation emitted in scattering processes, there is normally an explicit angle -dependence, even for static media. The emissivity is calculated by summing products of upper-state populations and transition probabilities over all relevant processes that release a photon at frequency ν. In writing the transfer equation, we shall usually use the symbol η to denote the total emissivity.

Let us now consider the problem of radiative transport. Choose an internal coordinate system and examine the flow of energy through a fixed volume element in a definite time interval. Let us assume that the radiation field is, in general, time-dependent. If we suppose that the material is at rest, then both χ and η will be isotropic (unless we consider anisotropic scattering). In moving material one must account for changes in photon frequency and direction (Doppler shift and aberration) resulting from the transformation between the laboratory frame and the fluid frame. Now calculate the energy in a frequency interval $d\nu$, passing in a time dt through a volume element of length ds and cross-section dS oriented normal to a ray traveling in direction $\mathbf{n}$ into solid angle $d\omega$. The difference between the amount of energy that emerges (at position $\mathbf{r}+\triangle\mathbf{r}$ at time $t+dt$) and that incident (at $\mathbf{r}$ and $\mathbf{t}$) must equal the amount created by emission from the material in the volume minus the amount absorbed. That is

$$[I(\mathbf{r}+\triangle\mathbf{r},\mathbf{n},\,\nu,t+\triangle t) - I(\mathbf{r},\mathbf{n},\,\nu,t)]dS\;d\omega\;d\nu\;dt$$

$$= [\eta(\mathbf{r},\mathbf{n},\,\nu,t) - \chi(\mathbf{r},\mathbf{n},\,\nu,t)I(\mathbf{r},\mathbf{n},\,\nu,t)]ds\;dS\;d\omega\;d\nu\;dt \tag{5.8}$$

Let s denote the path-length along the ray; then $\triangle t = \triangle s/c$ and

$$I(\mathbf{r} + \triangle\mathbf{r}, \mathbf{n}, \nu, t + \triangle t) = I(\mathbf{r}, \mathbf{n}, \nu, t) + [c^{-1}(\partial I/\partial t) + (\partial I/\partial s)]ds \tag{5.9}$$

Substituting equation (5.9) into equation (5.8) we have the transfer equation

$$[c^{-1}(\partial/\partial t) + (\partial/\partial s)]I(\mathbf{r}, \mathbf{n}, \nu, t) = [\eta(\mathbf{r}, \mathbf{n}, \nu, t) - \chi(\mathbf{r}, \mathbf{n}, \nu, t)I(\mathbf{r}, \mathbf{n}, \nu, t)] \tag{5.10}$$

The derivative along the ray may be re-expressed in terms of an orthogonal coordinate system:

$$\frac{\partial I}{\partial s} = \left(\frac{\partial x}{\partial s}\right)\left(\frac{\partial I}{\partial x}\right) + \left(\frac{\partial y}{\partial s}\right)\left(\frac{\partial I}{\partial y}\right) + \left(\frac{\partial z}{\partial s}\right)\left(\frac{\partial I}{\partial z}\right) = n_x\frac{\partial I}{\partial x} + n_y\frac{\partial I}{\partial y} + n_z\frac{\partial I}{\partial z}$$

where (n_x, n_y, n_z) are the components of the unit vector $\mathbf{n}$. We may thus write equation(5.10) as

$$[c^{-1}(\partial/\partial t) + (\mathbf{n}.\bigtriangledown)]I(\mathbf{r}, \mathbf{n}, \nu, t) = \eta(\mathbf{r}, \mathbf{n}, \nu, t) - \chi(\mathbf{r}, \mathbf{n}, \nu, t)I(\mathbf{r}, \mathbf{n}, \nu, t) \tag{5.11}$$

For a *one dimensional planar atmosphere* $n_z = (dz/ds) = cos\theta = \mu$; further, the derivatives $(\partial/\partial x)$ and $(\partial/\partial y)$ are identically zero, and we obtain

$$[c^{-1}(\partial/\partial t) + \mu(\partial/\partial z)]I(\mathbf{r}, \mathbf{n}, \nu, t) = \eta(\mathbf{r}, \mathbf{n}, \nu, t) - \chi(\mathbf{r}, \mathbf{n}, \nu, t)I(\mathbf{r}, \mathbf{n}, \nu, t) \tag{5.12}$$

or, for the *time-dependent* case,

$$\mu[\partial I(z, \mathbf{n}, \nu)/\partial z] = \eta(z, \mathbf{n}, \nu) - \chi(z, \mathbf{n}, \nu)I(z, \mathbf{n}, \nu) \tag{5.13}$$

Equation(5.13) is the *standard transfer equation* for plane-parallel model atmospheres calculations.

Writing $d\tau(z, \nu) = -\chi(z, \nu)dz$, we define an *optical depth scale* $\tau(z, \nu)$ which gives the integrated absorptivity of the material along the line of sight. The negative sign is introduced so that the optical depth increases inward into the atmosphere from zero at the surface, and thus provides a measure of how deeply an outside observer can see into the material. In addition we define the *source function* to be the ratio of the total emissivity to the total opacity,

$$S(z, \nu) = \eta(z, \nu)/\chi(z, \nu) \tag{5.14}$$

Using both the relation for the optical depth and equation (5.14), we can rewrite equation (5.13) as follows

$$\mu(\partial I_\nu/\partial\tau_\nu) = I_\nu - S_\nu \tag{5.15}$$

5.3.2 Boundary conditions

Solution of the transfer equation requires the specification of boundary conditions. There are two fundamental cases, the planar and a spherical atmospheres. For a finite plane-parallel atmosphere of the optical depth τ_ν we must specify the boundary conditions on both faces of the slab or shell as incoming and outgoing radiation relatively to the observer. At the upper boundary we will have

$$I(\tau_\nu = 0,\ \mu,\ \nu) = I^-(\mu,\ \nu), \qquad (-1 \leq \mu \leq 0) \tag{5.16}$$

and

$$I(\tau_\nu = T_\nu,\ \mu,\ \nu) = I^+(\mu,\ \nu), \qquad (0 \leq \mu \leq 1) \tag{5.17}$$

at the lower boundary. Most of the time the external irradiation, represents I^+ can be ignored and set to zero. For a lower boundary condition one may replace equation (5.17) by a *boundedness condition* in analytical work where the limit $\tau_\nu \to \infty$ is taken, specifically we impose the requirement that

$$\lim_{\tau_\nu \to \infty} I(\tau_\nu,\ \mu,\ \nu) e^{-\tau_\nu/\mu} = 0 \tag{5.18}$$

5.3.3 Formal solution

Let us now obtain a formal solution of the equation of transfer. If the source function S_ν is given, then equation (5.15) can be solved as first-order linear differential equation. Integration factor can be found as $exp(-\tau_\nu/\mu)$, so we have to integrate the equation

$$\frac{\partial[I_\nu \exp(\tau_\nu/\mu)]}{\partial \tau_\nu} = -\mu^{-1} S_\nu \exp(-\tau_\nu/\mu) \tag{5.19}$$

Integration of equation (5.19) yields

$$I(\tau_1,\ \mu,\ \nu) = I(\tau_2,\ \mu,\ \nu) e^{-(\tau_2 - \tau_1)/\mu} + \mu^{-1} \int_{\tau_1}^{\tau_2} S_\nu(t) e^{-(t-\tau_1)/\mu} dt \tag{5.20}$$

This result can be used to find an outgoing radiation ($\mu \geq 0$) at the arbitrary point in semi-infinite atmosphere. Setting $\tau_1 = \tau_\nu$ and $\tau_2 = \infty$ and imposing the boundedness condition of equation (5.18) gives

$$I(\tau_\nu,\ \mu,\ \nu) = \int_{\tau_\nu}^{\infty} S_\nu(t) e^{-(t-\tau_\nu)/\mu} dt/\mu, \qquad (0 \leq \mu \leq 1) \tag{5.21}$$

For incoming radiation, $(-1 \leq \mu \leq 0)$, set $\tau_2 = 0$ and apply the upper boundary condition $I^- = 0$; we then obtain

$$I(\tau_\nu,\ \mu,\ \nu) = \int_0^{\tau_\nu} S_\nu(t) e^{-(\tau_\nu - t)/(-\mu)} dt/(-\mu), \qquad (-1 \leq \mu \leq 0) \tag{5.22}$$

One of the most important applications of equation (5.21) is the expression for the emergent intensity seen by an external observer ($\tau = 0$),

$$I(0,\ \mu,\ \nu) = \int_0^\infty S_\nu(t) e^{-t/\mu} dt/\mu \tag{5.23}$$

The physical significance of equation (5.23) is that the emergent intensity is a weighted average of the source function along the line of sight; the weighting function is the fraction of the energy emitted at the depth that penetrates to the surface along a ray whose optical depth slant-length is (τ/μ).

5.4 Equation of state

The equations of state appropriate to the interiors of most stars are simple in one major respect: they may be derived using the assumption that the radiation, gas, fluid, or even solid, is in the state of *local thermodynamic equilibrium* or LTE. By this we mean that at a particular position in the atmosphere complete thermodynamic equilibrium is as very nearly true as we could wish. it is only near stellar surfaces or in highly dynamic events, such as in supernovae, where this assumption may no longer be valid. The reason why LTE works straightforward: particle-particle and photon-photon mean free paths are short and collision rates are rapid compared to other stellar length or time scales. A major exception to this rule involves nuclear reactions, which are usually slow. Thus, to a high degree of approximation, two widely separated regions in the atmosphere are effectively isolated from one another as far as the thermodynamics are concerned and, for any one region, the Boltzmann populations of ion energy levels are consistent with local electron kinetic temperature. In order to investigate the interaction between the medium of the stellar atmosphere and the radiation field, we must find a way to describe the properties of the matter. The high temperature and low densities of stellar atmospheres allow their treatment as a perfect gas. The state of such systems is specified by the distribution of its particles over all possible energy levels, bound and free. This means knowing the *occupation numbers* of those levels. To specify them we need to find the appropriate probabilities of transition between the levels for the components of gas. In this part of the chapter we will discuss both cases, LTE and NLTE which will be used as a reference to explain our future tests using TLUSDISK code.

5.4.1 Matter in LTE

In thermodynamic equilibrium every process being considered is expected to be in exact balance with its inverse process. From this point of view all processes can be

divided into two groups: radiative and collisional. Collisional processes are expected to be in detailed balance as long as the particle velocity distribution of the colliding particles remains an equilibrium distribution. This group include also emission and absorption processes such as free-bound recombination and free-free emission. Radiative processes are those dependent only on the nature of the radiation field, like photoionisation and photoexcitation. They will be in detailed balance only if the radiation field is in equilibrium, that it is isotropic and has Planckian energy distribution. If only some processes are in detailed balance, then the final state of the atmosphere will depend on whenever those processes prevail over non balanced. In LTE all material energy partitioning, *i.e*, all atomic, ionic and molecular level populations, is given by Maxwellian-like Saha-Boltzmann $N_i/N \sim exp(-E_i/KT)$ statistics as defined by the local temperature, just as if the location sits within a thermodynamic equilibrium enclosure as seen by the matter component of the ensemble (but not by photons). Thus, the definition of LTE is to assume the validity of all TE material distribution laws at the local temperature. The equality $S_{\nu_0} = B_{\nu_0}$ then follows by entering the Boltzmann distribution

$$S_{\nu_0} = \frac{2h\nu_0^3}{c^2} \frac{1}{\frac{g_u n_l}{g_l n_u} - 1} \tag{5.24}$$

The index 0 to S_{ν_0} signifies that the complete-redistribution version of the line source function is frequency dependent. The essential premise of LTE is that collisions control the energy partitioning of the matter in the medium more strictly than that they control the energy partitioning of the radiation. All material energy distribution (velocity, ionisation, excitation and dissociation) are then fixed by the local kinetic temperature (Maxwell, Saha, Boltzmann), while the radiative energy distributions may depart slightly from the local TE values:

$$S_\nu = B_\nu$$

where

$$B_\nu(T) = \frac{2h\nu^3}{c^2} \frac{1}{e^{h\nu/kT} - 1}$$

The LTE equality $S_\nu = B_\nu$ holds when the source function is dominated by collisions and/or when the frequency and angle-averaged radiation field is Planckian. Deep within the atmosphere both conditions are fulfilled. There, the photons are 'honoray particles' that fully participate in the thermodynamics of the gas. Their mean free paths are much smaller than the scales over which state parameters vary appreciably. However, even there I_ν is not exactly isotropic; therefore, (or rather, because) the net flux $F_\nu \neq 0$ and transports energy outwards, a leak that inhibits strict TE even for the very close confinement within the atmosphere - strict TE doesn't exist in nature.

5.4.2 Departures from LTE

Non-local thermodynamical equilibrium (NLTE or non-LTE) is a loose term which implies that the assumption of LTE fails. Often one then assumes statistical equilibrium implicitly, usually with the Maxwell distribution and complete redistribution in frequency and angle. However, the populations are now permitted to differ from the local Saha-Boltzmann equilibrium values. Also, the temperature T loses the universal meaning it had in the LTE description and denotes now only the kinetic temperature of the gas and $S_\nu \neq B_\nu$. NLTE population departure coefficients b_i are defined as:

$$b_l = n_l/n_l^{(LTE)} \qquad b_u = n_u/n_u^{(LTE)}$$

with n is the actual population and $n^{(LTE)}$ is the Saha-Boltzmann values for the lower and upper level, respectively. These formal expressions do not specify what part of the source function is controlled by B_ν or by J_ν (at this frequency or other frequencies); they only express the overall result in term of population departures relative to the LTE equilibrium values. The actual values of n_l and n_u may depend on B_ν and J_ν at widely different frequencies through other transitions that may feed excess population into these levels or deplete them excessively. Bound-free transitions contain at least partial thermalization, since part of the photon energy produces kinetic energy (ionisation) or uses kinetic energy (recombination), but they may also depend on J_ν or at other frequencies. This partial thermalization and sensitivity to radiation is also hidden in the resulting population departures. Only free-free photon emission and extinction are strictly kinetic, respectively creating and destroying photons in every interaction.

5.5 Modeling tools

The main goal of the theory of stellar atmospheres is to describe the flow of energy through the outermost layers of a star or a accretion disc, and to predict the observational characteristics of the emergent radiation. However, this involves solving a number of highly coupled, non-linear equations, a task that can only be done numerically. The model atmosphere problem refers to the construction of mathematical models that provide a description of the physical structure of a stellar atmosphere and of its emergent spectrum. In its greatest generality, the problem is one of enormous complexity, and presents both physical and mathematical difficulties that are beyond solution at the present time. It is therefore necessary to make a number of simplifications, and to deal with idealized models that are rather high-order abstractions from reality. These simplifications can be achieved from the theoretical

point of view such as:

(a) *Geometry.* In this case the atmosphere is composed of *homogeneous plane-parallel layers* where the thickness of the atmosphere is small compared to the radius of the star, which is also widely applied in the accretion disc atmosphere modeling, or *homogeneous spherical shells* when the thickness is an appreciable fraction of the radius. The assumption of homogeneity makes the problem one-dimensional and thus greatly simplifies the analysis.

(b) *Steady state.* Stationary atmosphere *'steady state'* is assumed which means avoid the discussion of all time-dependent phenomena, such as stellar pulsations, shocks, transient expanding envelopes (novae and supernovae), heating by a binary companion, variable magnetic field, *etc.*

(c) *Momentum balance.* Having specified a steady state, we shall consider either *hydrostatic equilibrium* in which the static gas pressure distribution just balances gravitational forces, or one-dimensional, laminar, steady flows. With this assumption we ignore the possible large effects of magnetic forces: both large-scale and small-scale. We also ignore the effects of small-scale motions such as waves, and larger scales such as super-granulation flows, convective cells, *etc.* as well as major tidal distortions in close binaries.

(d) *Energy balance.* In such case we assume that the atmosphere is in *radiative equilibrium*, which again implies that it is static. This means ignoring the effects of magnetic field.

5.5.1 Complete linearization 'CL'

From a physical point of view, the solution of the NLTE stellar atmospheres problem entails the specification, at each point in the medium, of the distribution of the radiation field as a function of frequency, temperature and density of the material, and the distribution of the atoms and ions over all bound states. These distribution functions are to be determined in such away that the constraints of energy balance, momentum balance (hydrostatic equilibrium), steady-state statistical equilibrium, and charge and number conservation are all satisfied rigorously. To achieve that two basic physical points has to be considered. First, *no one variable is more fundamental than any other, for they all interact.* Thus we must regard the solution at a given depth-point m_d to consist of the vector

$$\Psi_d = (J_1, ..., J_K, N, T, n_e, n_1, ..., n_L)^T, \qquad (d = 1, ..., D) \tag{5.25}$$

Where D is the number of depth-points, K is the number of frequencies, and L is the total number of bound levels considered.

Second, *the variables interact globally throughout the atmosphere, and a change in any variable at a given point implies changes in all other variables at all other points.* Thus, if we alter occupation numbers locally, this changes the emissivity and opacity of the material, and hence, via the transfer equation, the radiation field throughout the atmosphere. We suppose that our desired solution Ψ_d can be written in terms of the current solution Ψ_d^0 as $\Psi_d = \Psi_d^0 + \delta\Psi_d$. We then choose $\delta\Psi_d$ so as to satisfy all constraints more closely; i.e if $f_d(\Psi_d) = 0$ represents the entire system of constraints, we demand that $f_d(\Psi_d^0 + \delta\Psi_d) = 0$ and

$$f_d(\Psi_d^0) + \sum_j \frac{\partial f_d}{\partial \psi_{d,j}} \delta\Psi_{d,j} = 0 \tag{5.26}$$

The complete system may be presented in the general form as:

$$-\mathbf{A_d}\delta\Psi_{d-1} + \mathbf{B_d}\delta\Psi_d - \mathbf{C_d}\delta\Psi_{d+1} = \mathbf{L_d}, \tag{5.27}$$

suitable for Feautrier elimination scheme. Here $\mathbf{A_d}, \mathbf{B_d}$ and $\mathbf{C_d}$ are $NN \times NN$ matrices, and $\mathbf{L_d}$ is the residuum vector (of dimension NN) at depth d. As $\mathbf{L_d} \to 0$, the corrections $\delta\Psi_d \to 0$.

5.5.2 Accelerated lambda iteration 'ALI'

In the classical lambda iteration method the mean intensity is expressed by the source function, for which we have an initial guess, and then the lambda operator given as

$$\Lambda_\tau(f(t)) = \frac{1}{2}\int_0^\infty f(t)E_1|t-\tau|dt \tag{5.28}$$

is applied to the source function. The new expression for the mean intensity is then

$$J_\nu = \Lambda_\nu S_\nu$$

Application of the lambda operator to the source function gives more accurate value for the source function near the upper boundary while leaving it unaltered at infinity (Mihalas, 1978). This operation is repeated until the change in J_ν from one iteration to the next is below a certain value. This simplified scheme has some severe disadvantages, the most important being that instead of converging the solution it tends to stabilize it. This implies that even if the difference between the solution of successive iterations is small, an impractically great number of iterations may be needed to reach a final solution. Another problem is that the iteration correspond

to the following successive scatterings, and when large number of scatterings is involved, a great number of iterations is needed. Consequently the convergence is slow and the procedure fail in most cases of interest for stellar atmospheres.

On the other hand, the principal difficulty in applying the CL method for the sophisticated model atmospheres is the cubic increase of the computing time with the increase of the total number of variables. Further progress can be achieved, if all considered frequencies could be grouped into relatively few essential blocks. This method is named multifrequency or multigray algorithm. The other possible alternative is a so called *Accelerated Lambda Iteration* (ALI), for a detailed review see (Hubeny, 92). The essence of it is to express the radiation intensity through the approximated lambda operator, acting on the source function, plus a correction term, obtained from the previous iteration. As in the classical lambda iteration method, ALI method results in a short iteration time, but suffers from the slow convergence near the exact value. Nevertheless, as long as all energy levels were considered separately, all the above methods could not be used for the iron-peak element rich atmospheres. To solve this problem, a statistical method of grouping many energy levels into the "superlevels" was introduced. This method, incorporating the best of both the CL and ALI, would be a benefit, when calculating a spectra with thousands to millions of lines (the so called *line-blanketed* models). Such hybrid CL/ALI method, will be discussed in detail in the next section.

5.5.3 Hybrid CL/ALI method

This method was developed by Hubeny & Lanz (1995b). This is a more significantly improved method, which combines advantages of both its constituents. Its rate of convergence is virtually as high as for the standard CL method, while the computer time per iteration is almost as low as for the standard ALI method (Cannon 1973, Hubeny 1992).

As discussed in detail by Hubeny & Lanz (1992), one may reduce the total time either by reducing the time per iteration, or by reducing the number of iterations needed to achieve a certain accuracy, or both. They have suggested two methods for such solution. The first is the so-called Kantorovich method (keeping the Jacobian fixed after few iterations), so that the costly matrix inversion are calculated only a few times. The second is an application of the so-called Ng acceleration, which reduces the number of iterations by using information not only from the previous iteration step, but also from several previous iteration.

Another approach of reducing the time per iteration (Hubeny & Lanz 95b), namely by reducing the size of the matrices to be inverted. This can be done for example, by

linearizing only those quantities which are 'essential', while keeping the others fixed during linearization and updating them during a subsequent formal solution. This approach consists of keeping selected radiative transitions rates 'fixed'. These fixed rates are calculated exactly in the formal solution step and are then held fixed during linearization. Subsequently, these rates are updated in the next formal solution step, 'formal solution' means a solution of one equation at a time, using current values of all other state parameters (for instance, solving the radiative transfer equation for given frequency for current values of the level populations, temperature and electron density). The drawback of too many transitions taken in this mode, is basically recovering a lambda-iteration type of behavior (stabilization of the solution rather than convergence). A much more sophisticated way of reducing the size of matrices to be inverted is the multifrequency/multigray method. Basically one substitute

$$\{J_1, \ldots, J_{NF}\} \rightarrow \{\bar{J}_1, \ldots, \bar{J}_{NB}\},$$

where $\bar{J}_i$ represents a mean intensity characteristic of ith frequency block, and NB is the number of blocks. We must have NB$\ll$NF in order to achieve a substantial reduction of time. The essence of the method consists of selecting appropriate frequency bands and the individual frequency points belonging to them, which is also the drawback of the method.

Finally, the ALI method itself can reduce the number of unknowns (and thus a number of equations to be linearized) by expressing the mean intensity at the wavelength ν through

$$J_\nu^{(i)} = \Lambda_\nu^* S_\nu^{(i)} + (\Lambda_\nu - \Lambda_\nu^*) S_\nu^{(i-1)} \tag{5.29}$$

Here Λ_ν and Λ_ν^* are the exact and approximate lambda operators, J_ν is the mean intensity of radiation, and S_ν is the source function, all at frequency ν. Superscripts i indicates the iteration number. The second term on the right hand side of equation (5.29) represents the correction, known from the previous iteration, while the first one represents an action of an approximate operator,Λ^*, on the source function, which is expressed as a function of temperature, density and atomic level populations. This eliminates radiative transfer equation from the coupled system of structural equations. In the case of a diagonal (local) Λ^*, the first term of (5.29) is particularly simple, it is just a multiplication of the local source function by a real number. However, the basic problem is that when (5.29) is substituted into the statistical equilibrium, hydrostatic equilibrium and radiative equilibrium equations, one still obtains a non-linear system. This can be dealt with by dividing all frequency points in the model into two groups. The first contain the 'crucial' frequency points (typically, a few frequencies near the important continuum edges, and the centers of the strongest lines) to be treated exciplicitly, i.e., to be fully linearized. The rest

of frequency points comprise the so-called ALI points and are treated by means of the ALI formalism.

With the above mentioned methods, the time for the formal solution increases with the number of frequency points considered, but the basic point is that since only one transfer equation is solved at a time, the increase of computer time is linear in the number of frequency points and not cubic as in the original CL.

5.6 TLUSDISK & SYNSPEC

The program TLUSDISK is based on the model stellar atmosphere code TLUSTY (Hubeny 1988,1990a,b). It is designed to calculate the vertical structure of a steady state equilibrium accretion disc and its atmospheres, under the assumptions stated in the next section using the CL/ALI (Complete Linearization/Accelerated Lambda Iteration) method (Hubeny & Lanz 1995b). The user is given much freedom in choosing parameters for the calculation. This includes the possibility to calculate LTE and NLTE models of different levels of sophistication, of atmospheres consisting of elements from hydrogen to zinc. Heavier elements can also be included in the model if that is necessary. The program solves the basic equations (radiative transfer, hydrostatic equilibrium, energy balance, statistical equilibrium, charge and particle conservation) by the so-called hybrid CL/ALI method discussed in the previous section. This method combines advantages of its two basic constituents, a high convergence rate of the method of complete linearization, first introduced by Auer and Mihalas (1969), and a low computer time per iteration as the Accelerated Lambda Iteration (ALI) method, introduced by Cannon (1973) and Hubeny (1992).

The user has the freedom to calculate the so-called semi-empirical models, which means that not all the basic equations have to be actually solved. The program has options for omitting some of the equations, keeping the corresponding quantities fixed. For instance, one may keep the temperature fixed and skip the energy balance equations (all the other equations being solved exactly). The program is fully data oriented as far as the choice of the atomic species, ions, energy levels, transitions, and opacity sources is concerned.

The first run of TLUSDISK produces a LTE model starting from an LTE-grey model. If further refinement is needed, the output from this run can be used as a starting model for a model with NLTE treatment of continua and lines. The final output from TLUSDISK can be directed to the SYNSPEC (Hubeny & Lanz 1995a), which evaluates atmospheric opacity and emissivity and produces a synthetic spectrum. Those two programs are accompanied with a set of utility and shell programs, which simplify the process of preparing the initial input and processing the output to give

the final disc synthetic spectrum. In addition to that Semionaoff (1998) developed an utility program RINGRUN to simplify the production of a complete disc model.

5.6.1 Basic assumptions

Most of this section is adopted from the user guide of TLUSDISK version 187. The disc is assumed to be in a steady state, geometrically thin and in Keplerian rotation. The vertical structure is solved for a set of axially symmetric concentric rings where a plane-parallel 1-D atmosphere calculation is performed. The atmosphere at each disc radius R (specified in the disc mid plane) is in hydrostatic equilibrium, with depth-dependent gravity (g) that arises from the vertical component of the central star's gravitational force on the disc material. Neglecting the self-gravity of the disc and assuming that R is much larger than the distance from the central plane (z):

$$\frac{dP}{dz} = -g(z)\rho \tag{5.30}$$

$$g = \frac{GM_1 z}{R^3} \tag{5.31}$$

where P is the pressure, ρ is the mass density, M_1 is the central star mass and G is the gravitational constant. The mass surface density is given by the standard disc model (Shakura & Sunyaev 1973):

$$\Sigma = \frac{\dot{M}}{3\pi\bar{\omega}}\left[1 - \left(\frac{R_1}{R}\right)^{1/2}\right], \tag{5.32}$$

$$\bar{\omega} = \frac{\sqrt{GM_1R_1}}{Re}. \tag{5.33}$$

where $\dot{M}$ is the mass transfer rate through the disc, R_1 is the central star radius, and $\bar{\omega}$ is the depth-averaged kinematic viscosity, parameterized in terms of Reynolds number R_e of the flow (Lynden-Bell & Pringle 1974) and (Kriz & Hubeny 1986). The viscosity ω is allowed to vary as a power law of the mass column density above a certain physical depth m(z):

$$\omega(m) = \bar{\omega}(\zeta + 1)\left(\frac{2m}{\Sigma}\right)^{\zeta} \tag{5.34}$$

The power law index ζ is usually set to a numerical value larger than zero to prevent the "thermal catastrophe" of the disc in the low optical depth regions where electron scattering is the dominant (only) opacity source (Hubeny 1989). The disc radiates

all the mechanical energy dissipated by the viscous shearing between the Keplerian orbits. According to the standard formulae this quantity may be written as follows:

$$D_{mech}(z) = \frac{9GM_1\omega(z)\rho(z)}{4R_1^3} \tag{5.35}$$

where $\omega(z)$ is the viscosity. The energy balance equation then becomes:

$$\int_0^\infty (\kappa_\nu J_\nu - \eta_\nu) d\nu = D_{mech}(z) \tag{5.36}$$

where κ_ν and η_ν are the absorption and emission coefficients, and J_ν is the mean intensity of the radiation, at frequency ν.

As is customary in the stellar atmosphere theory, one expresses the total energy dissipated (and therefore radiated away) from the unit disc face as $D(R) = \int D_{mech}(z)dz$, through the effective temperature, T_{eff} as $\sigma T_{eff}^4 = D(r)$, where σ is Stefan-Boltzmann constant. Assuming further a stationary, Keplerian disc, the effective temperature is given by:

$$T_{eff} = \left(\frac{3GM_1\dot{M}}{8\pi\sigma R^3}\left[1 - \left(\frac{R_1}{R}\right)^{1/2}\right]\right)^{1/4} \tag{5.37}$$

Here is a summary of the basic assumptions:

• Disc is divided into a set of concentric rings, each behaving as an independent plane parallel radiating slab; no assumptions about optical thickness are made. One run of TLUSDISK calculates the vertical structure of one ring.

• Hydrostatic equilibrium in the vertical z-direction.

• The energy balance is considered as a balance between the net radiation loss (calculated without invoking neither optically thin, nor optically thick approximations) and the dissipated mechanical energy.

• The dissipated energy is proportional to viscosity, which is given through Reynolds number (not by means of α).

• The effect of illumination of the disc by the central star can be taken into account using the formalism described in Hubeny (1990b).

• The total radiative flux is not constant, but increases upwards (from the central plane of the disc to it's surface), it's value being determined through the energy balance equation.

• Analogously, the gravity acceleration is not constant and depends on the distance from the central plane.

• The vertical structure of the disc (temperature, density, radiation field etc.) follows from the appropriate model calculations.

The program solves the basic equations (radiative transfer, hydrostatic equilibrium, energy balance, statistical equilibrium, charge and particle conservation) by the use of the hybrid CL/ALI (Complete Linearization/Accelerated Lambda Iteration) method (Hubeny & Lanz 1995b).

The thermal structure of the atmosphere, which is determined by the mass accretion rate and the radial distance from the central star, plays a crucial role in the convergence of the models, which consists of a set of concentric rings with variable T_{eff}, between the limits shown in table 5.1.

Both the TLUSDISK and SYNSPEC programs perform input and output using logical units. Those are usually files with default name `fort` and an extension, corresponding to appropriate logical unit number, like `fort.5` and `fort.9`. In the following the file name will be ommited most of the time.

TLUSDISK usually expects to exist two input units, 5 and 7. Unit 5 is the primary model description, containing physical parameters like the mass and the radius of the central star, the mass accretion rate, chemical species to be used and their abundances, as well as switches for computational options. Unit 7 contains an initial estimate of disc atmosphere structure, namely the effective temperature, mass and electron densities and energy level populations in case of NLTE model, for each mass depth point. Usually this is a converged model from the previous TLUSDISK run, but it may also be taken from literature or constructed by other means. If unit 7 does not exist a LTE-gray model is calculated for the initial estimate. Structure of those units will be described in some details in the following subsection.

SYNSPEC needs at least four input units, 5, 7, 19 and 55, to run. Unit 55 is a set of control switches, describing the spectra to be computed. Units 5 and 7 are atmosphere model files, used by TLUSTY or TLUSDISK. Unit 19 contains a linelist. Also, depending on the parameters, set in unit 55, there might be needed a multitude of other input units, describing exact line profiles, transition cross-sections, superlevels, and possibly change of chemical composition relative to the model. The program solves the radiative transfer equation in a given wavelength range with a given resolution, controlled by the input from the unit 55. Wavelength point spacing also can be prescribed by the user. The output from SYNSPEC can contain a complete synthetic spectrum, detailed profiles of a few lines, emergent continuum with hydrogen Balmer lines, and a linelist for a given spectral range. It is possible to calculate a synthetic spectrum, containing more chemical elements, than the initial model, or having a different abundances, thus allowing the calculation of a simpler model, with only principal opacity sources included.

There are also shell programs, that also employ few other package programs, such as program for rotational convolution of spectra `ROTIN`. Usually this shell is provided

by SYNPLOT. This program is written in IDL command language, and provides a user friendly interface to SYNSPEC, allowing creation of input files using IDL command line parameters. SYNPLOT also has means of manipulating the produced spectra and plotting it using a variety of options. Unfortunately, it does not cover all possible SYNSPEC parameter combinations and, while making most common uses of SYNSPEC easy, has to be bypassed when more sophisticated calculations of spectra are needed.

5.6.2 How to build a model to obtain a disc spectrum

The process of calculation of the synthetic spectrum of an accretion disc model starts from preparation of the main input, unit 5, for the TLUSDISK, version 187. The file consists of eight principal blocks of the following structure:

Block 1: Contains the main parameters of the disc annulus like the radial distance, the mass and radius of the central star, Reynolds number, viscosity power law index ζ, and main parameters for calculations, the number of iterations and the convergence criterium. Also in this block is described the structure of the rest of the input file: number of depth points, explicit chemical species, transitions, etc..

Block 2: Contains a set of frequency points, at which radiative transfer equations are solved. For each frequency there can be specified a number of treatment options, such as integration scheme and CL/ALI switch. This block can be automatically generated using `SETFRE` utility program, included with the package.

Block 3: Provides a turbulent velocity, which can be specified as depth-dependent, or depth-independent value.

Block 4: List of chemical species has to be included in model calculations and give their abundances and treatment options. Each element can be considered explicitly (energy levels are given, and statistical equilibrium equations will be solved for their populations), non-explicitly (element affects total number of particles and charge via LTE equations, but not the opacity) or ommited altogether.

Block 5: Contains data describing the exciplicit ions. The most important parameters are the indices of the first and last exciplicit levels for each exciplicit ion, the effective charge and the models of evaluation of populations of non-exciplicit levels and of free-free opacity.

Block 6: This block contains data for exciplicit levels and defines the ionisation energy, statistical weight and principal quantum number for each exciplicit level as well as various parameters, which determine how the levels are treated.

Block 7: Describes transitions between levels. Transitions are specified for each ion by naming starting and ending level indexes and parameters controlling the

calculation of collisional and radiative rates, line profiles and cross-sections. Lines can be allowed to contribute to equilibrium equations as well as to the opacity and emissivity of the material. In this case addition treatment options are required, such as depth dependence of the profile, number of points describing the profile, and their distribution.

Block 8: Contains remaining parameters for model calculation. For our purpose the most important are switches, controlling LTE/NLTE mode, options for complete linearization solution (to solve some of the systems equations out of the CL loop, thus keeping corresponding quantities, such as temperature, electron density or particle density, fixed during the CL loop and recalculating them after its completion) and acceleration parameters.

This input structure will be used for all disc rings to be computed, with appropriate changes. In our treatment we split the disc into 8 rings, placed at distances of 1.4, 2.0, 2.8, 4.0, 5.56, 8.0, 11.3 and 15.0 R_1 from the central star described as circles shown in Fig. 5.1. In the figure the line of each circle assumed to lie in the center of the ring. The choice of the inner disc edge distance was based on the observational properties of the AM CVn systems, which will be discussed more while setting the model grid. As possible mechanisms, disrupting the disc close to the stellar surface, a weak magnetic field of a rotating white dwarf or irradiation by the central star together with the boundary layer can be named. The first run of TLUSDISK produces an LTE model. If further refinement is needed, the output from this run can be used as a starting point for a model with NLTE treatment of continua and lines. Later on we will discuss the necessity of the NLTE treatment in more detail. The following simple calculations show how does the area of one ring can be calculated. We will also show how to calculate the area of all the rings one by one, and then show how to calculate the total area of the disc. There are two cases to be considered: first, in case we have only one ring with a radial distance R_{i+1} where i denotes the ring number and $R_i = R_1$, where R_1 is the radius of the star, and $i + 1$ means the first ring after the surface of the star. Then the area of this ring can be calculated as:

$$A_i = \pi R_i (R_{i+1} - R_i)$$

In case we have more than one ring, then the area of an arbitrary ring j at a radial distance R_j from the central star, can be calculated using the following formula:

$$A_j = \pi R_j (R_{j+1} - R_{j-1}) \tag{5.38}$$

Finally, the total area of the disc 'A' can be calculated as:

$$A = \pi (R_{out}^2 - R_{in}^2) \tag{5.39}$$

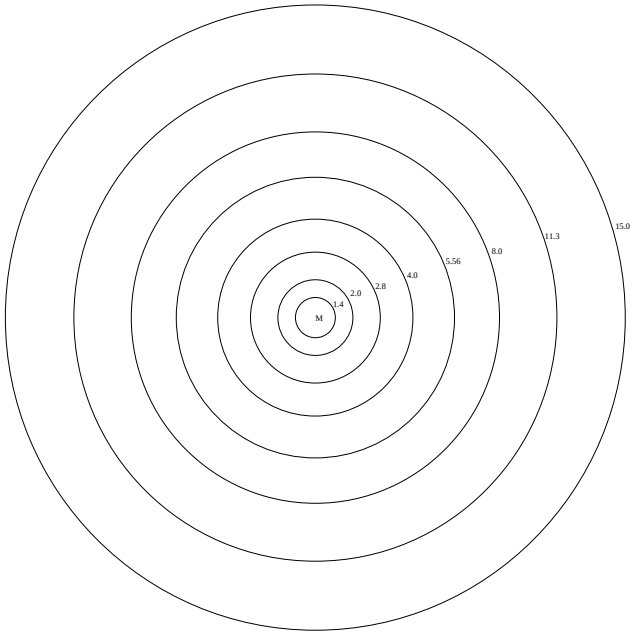

Figure 5.1: The disc consists of a set of concentric rings placed at distances of 1.4, 2.0, 2.8, 4.0, 5.56, 8.0, 11.3 and 15.0 R_* from the central star.

When a satisfying model is created, sometimes after a lengthy trial to convince it to converge, it is fed into the SYNSPEC/SYNPLOT programs to obtain an emergent intensity distribution for a chosen set of inclination angles. The intensity output, unit 18 in SYNSPEC notation, for each ring can then be combined into a complete disc spectrum using the DISKSYN program. This program takes intensity output from SYNSPEC and, if necessary, interpolates intensity to the desired disc inclination. Then it applies Doppler broadening to the spectrum, splitting each ring into a given number of azimuthal sectors and calculating Keplerian orbital velocity projection to the line of sight. The resulting ring spectra are then weighted by the area, occupied by a given ring in the projection to the plane perpendicular to the line of sight, and added together. The process of accretion disc synthetic spectrum calculation is graphically shown on Fig. 5.2 taken from Semionoff (1998).

The need for a minimal editing when calculating a disc model, prompted writing of yet another shell program, performing all steps necessary for creation of a complete disc emergent spectrum in a single run. This program, `RINGRUN`, takes a single input file, unit 5 for TLUSDISK, and several command line parameters, specifying number and position of disc rings, inclination angle(-s) and options for calculating synthetic spectra. It then prepares all necessary input files for TLUSDISK and SYNPLOT

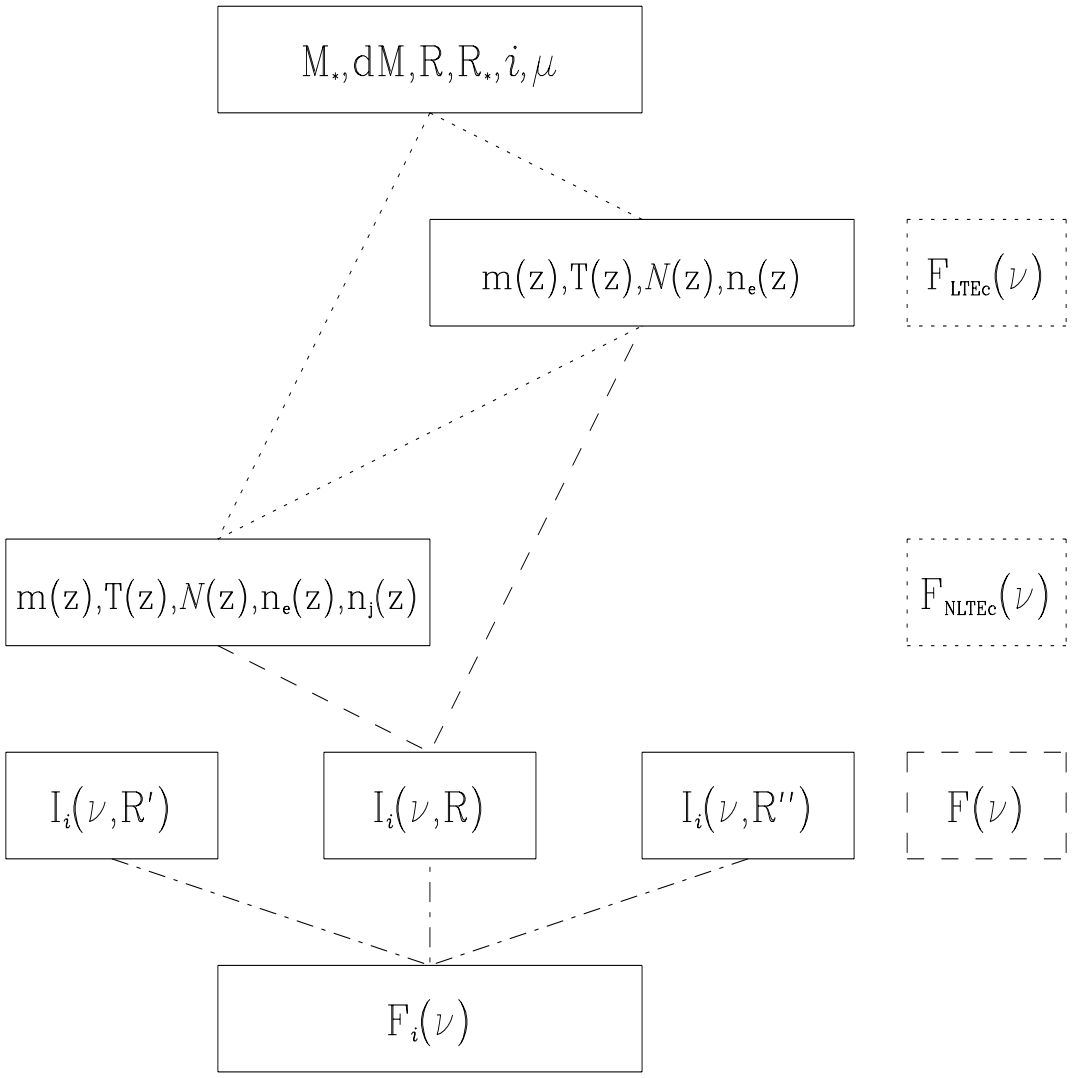

Figure 5.2: Model accretion disc theoretical spectra calculation flow chart. Parameters enclosed in the solid boxes (with their standard meaning) present various steps of the calculation (from top): an initial model ring parameters, LTE vertical structure of the ring atmosphere, NLTE vertical structure of a ring atmosphere, the specific intensity at given ring inclination and radius and the complete disc flux. Connecting lines represent processing of a specified parameter set by a program: dotted line – TLUSDISK, dashed line – SYNSPEC, dash-dotted line – DISKSYN. The boxes, drawn in line style, corresponding to one of the programs, are the given fluxes, produced by respective program as an auxiliary output. $\mathrm{F_{LTEc}}(\nu)$ and $\mathrm{F_{NLTEc}}(\nu)$ are continuum spectra of LTE and NLTE models, produced by TLUSDISK. $\mathrm{F}(\nu)$ is the total flux from a single ring perpendicularly to its surface, calculated by SYNSPEC.

and executes those programs. Also it serves the important task of keeping track of all calculated models and provides means of keeping all produced files separated without being mixed up with or overwritten by the output from subsequent runs. The `RINGRUN` program is written in IDL language by Semionoff (1998) and slightly modified by us, which allows to use simple means of controlling the amount of graphic and status log output, which is very important when searching for problematic points of a model, yet it can be overwhelming when calculation of a large ring set is performed with maximum verbose level. Other useful options include the possibility of recalculation of the whole disc with NLTE flag turned on or with different parameters for SYNPLOT, without the need to redo already performed often extremely time consuming steps.

5.6.3 Setting the model grid

Our goal of this modeling work is to find the best physical values for most of the disc parameters in the AM CVn systems discussed in chapter 3, such as the mass accretion rate $\dot{M}$, the inner and the outer radii of the disc R_{in}&R_{out}, the angle of inclination i and the abundance of elements. An additional free parameter is the distance to the systems. For our later investigations the assumptions and input parameters used in the calculations, are chosen in such a way that they should match the observational properties of the AM CVn systems.

The first step is to prepare the initial grid of the disc models by specifying the mass of the central star M_1 with radius R_1, the mass accretion rate $\dot{M}$, the angle of inclination i, the abundance and the size of the disc. We will also study the effects of departures from LTE in order to assess the necessity of computing more complicated and more time-consuming NLTE models.

In this approach, we concentrate most of our work on pure helium models in order to investigate the possibility that the AM CVn systems may have a pure helium accretion disc, and then we compare our final results with a H-He model of H/He$\approx$ 10^{-5} by number.

For this work we have computed models with mass transfer rates $\approx (2-9) \times 10^{-9} M_{\odot}$/yr, which is the range found to match the observed spectra of the AM CVn systems. We have used a model atom for helium with 14 levels of He I and one level of He II in the pure helium model. We also studied the spectra of the pure helium model when He II is included with 14 levels and He III as a highest one-level ion. Hydrogen, if considered, is represented by a 12-level model atom. We will discuss this matter in detail in sect.(5.7.2). All the atomic parameters (the photoionisation cross-section, oscillator strength, collisional rates) are taken as

default values provided by TLUSDISK.

Parameters used in the calculations have ranges found realistic based on other investigations. For the disc size we use $R_{out} = (0.4 - 0.5)a$ (where a is the distance between the two stars) which is about $15R_1$, as a reference radius for both AM CVn and HP Lib. This is the disc size found for AM CVn (Solheim et al. 1998). For unstable systems like V803 Cen and CR Boo, the disc size according to the thermal-tidal-instability model of Tsugawa & Osaki (1997) can oscillate within the three possibilities, the circularization radius (or the Lubow-Shu radius $R_{LS} = 0.29a$), the critical radius for the tidal instability $R_{cr} = 0.46a$ and the terminal disc radius $R_d = 0.36a$ at the end of a superoutburst. This also gives an average disc radius of $15R_1$, which we use as a reference radius for the discs of the AM CVn systems. A hole of $1.4R_1$ is assumed to be in the center of the discs, to make room for a boundary layer, since almost all the AM CVn systems are X-ray sources (Warner 1995a). We think that the He II line in emission at λ 4686 Å in the AM CVn systems is expected to appear due to the effect of the boundary layer in such systems. It is also possible that this line is generated in an optically thin layer at the top of the disc (Marsh et al. 1991).

The final parameter is the mass of the central star which is assumed to be a fixed value, calculated using the mass-radius relation for a semi-degenerate secondary filling its Roch lobe, presented by Savonije et al. (1986), and the computed value of $q = M_2/M_1$ from the superhump period observations, or from the predicted values of this ratio based on the Savonije et al. (1986) mass-radius relation. The final disc models can have different angles of inclination from $i = 0°$ to $90°$.

We are then left with only two varying parameters, the mass accretion rate $\dot{M}$ and the angle of inclination i, which are important for the physics and geometry of the systems.

As a result of our preliminary calculations we found that the pure helium model is the best model which matches the observed spectra of the AM CVn systems. As we will discuss later that both the pure helium model and the He-H model with H/He ratio found to be not more than 10^{-5} by number, are the best models to be used for comparing its theoretical spectra with the observed ones of the AM CVn systems. Thats why we concentrate all our investigations to study the spectra expected from the pure helium model or the He-H model with $H/He \leq 10^{-5}$. As mentioned before that our investigations were performed with certain range of mass accretion rate $(2 - 9) \times 10^{-9} M_\odot$/yr. Within this range we avoid the non-convergence problem of the outer rings, which might appear due to the low mass accretion rate $\dot{M}$ and as a consequence low effective temperature T_{eff}. The range of the effective temperature involved in our calculations is specified in Table. 5.1 and shown in Fig. 5.3. Within

Table 5.1: The effective temperature T_{eff} at the inner and outer radius of the disc with the variation of $\dot{M}$, while the mass of the central star being fixed at $M_1 = 1.1M_\odot$ and $M_1 = 1.2M_\odot$.

$M_1 =$	$1.1M_\odot$	$1.1M_\odot$	$1.2M_\odot$	$1.2M_\odot$
$\dot{M}(M_\odot/\mathrm{yr})$	R_{in}	R_{out}	R_{in}	R_{out}
2×10^{-9}	68 834	17 196	78 862	19 701
3×10^{-9}	76 177	19 030	87 275	21 803
4×10^{-9}	81 857	20 449	93 783	23 429
5×10^{-9}	86 554	21 623	99 164	24 773
6×10^{-9}	90 590	22 631	103 788	25 928
7×10^{-9}	94 149	23 520	107 866	26 947
8×10^{-9}	97 345	24 319	111 528	27 862
9×10^{-9}	100 254	25 045	114 861	28 694

this range all the disc rings are converged and we show this in Fig. 5.4, Fig. 5.5 and Fig. 5.6. These figures show that the rings at 1.4, 8.0 and 15 radial distances are all converged, but it is also seen that the number of iterations used in the calculation of the ring at $1.4R_1$ of a very high effective temperature, is much less than the number of iterations used in the calculations of the ring at $15R_1$, of a much lower effective temperature. This means that the number of iterations required for a certain ring to converge decreases with increasing effective temperature of the ring. Also the relative change in the temperature with depth is very different in the inner rings in comparation to the outer ones, which found to be much more stable for the inner rings compared to the outer ones.

We also show the temperature distribution in the disc with depth at different radial distances, and at a certain mass accretion $4 \times 10^{-9} M_\odot/\mathrm{yr}$, as seen in Fig. 5.7, Fig. 5.8 and Fig. 5.9. In such figures we see that the temperature distribution is not stable in the outer rings when compared to the inner ones, due to their low temperature. We found the same when we studied the density distribution in the disc with depth at different radial distances, as seen in Fig. 5.10, Fig. 5.11 and Fig. 5.12. The instability in the density distribution in the disc depends also on the temperature of the disc, which also depends on the disc mass accretion rate. The temperature and density found to be unstable at lower mass accretion rates.

The next step after securing the convergence problem for our calculations which is the most important, is to study the lines expected from each ring of the pure helium disc spectra. Fig. 5.13 and Fig. 5.14 show the identified He lines at two different wavelengths chosen as part of the 3500-7000 Å one ring spectrum of the pure helium accretion disc model. The lines shown in these figures are lines expected from the outer rings of the disc of a temperature $\approx$ 20 000K where He I lines are very strong. To study the strength of the He I lines at different parts of the disc, we plotted the synthetic spectra expected from the 8 considered rings in our model grid calculations as seen in Fig. 5.15. In this figure from top left to right bottom appear the spectra of the following rings $1.4, 2.0, 2.8, 4.0, 5.56, 8.0, 11.3$, and $15R_{\star}$. It is clearly seen that He I lines are very week in the spectra of the innermost rings of the high effective temperatures, while it is very strong for the outermost rings of a lower effective temperatures $\approx$ 20 000K. It is also seen in Fig. 5.16 that the continuum of the inner rings (of the high T_{eff}) is steeper than the continuum of the outer rings of the lower T_{eff}.

5.7 The influence of the disc parameters on the disc spectra

In this section we study the influence of some of the accretion disc parameters on both the continuua and the line profiles of the accretion disc spectra. The parameters which our investigation are focused on are the mass accretion rate $\dot{M}$, the angle of inclination i and the inner and outer radius of the disc R_{in} and R_{out}. There are two other important parameters, the abundance of elements and the number of azimuthal points assumed to obtain the total disc spectrum. We also include in this section table(5.1) which shows the values of the effective temperatures at the inner and outer radius of the disc, which varies with the mass accretion rate $\dot{M}$ and the mass of the central star M_1 .

5.7.1 Azimuthal points

We may think of the number of azimuthal points as a number of integration points, or a number of sectors which divide the disc as seen in Fig. 5.17. A small number of points seem to give a better resolution of the output spectra, but in fact it does not give any better resolution; it is only a much less accurate integration as seen in Fig. 5.18, where the spectra become smoother and smoother with increasing the number of azimuthal points 'integration points', which gives a better and

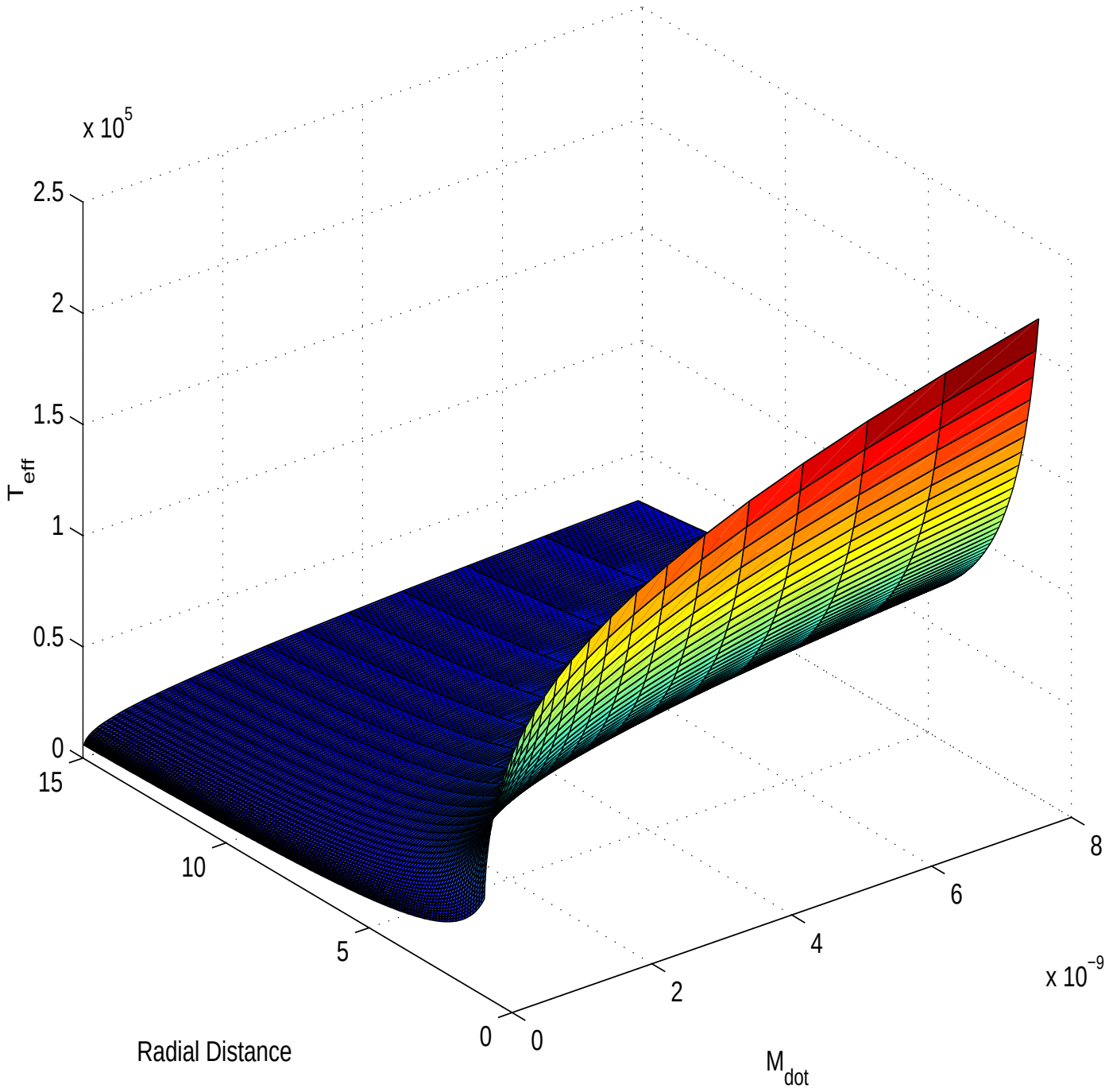

Figure 5.3: The radial temperature distribution in the accretion disc models when $M_1 = 1.1 M_\odot$.

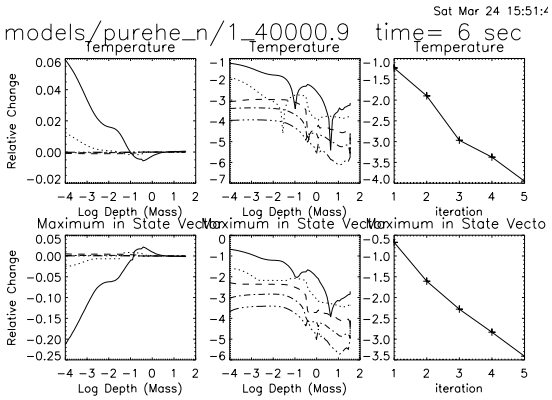

Figure 5.4: The right upper and lower boxes show the number of iterations performed for the ring of $R/R_\star = 1.4$. The upper two boxes to the left show the relative change in temperature with depth, which also affect how many iterations needed to make the model converge. The two lower boxes to the left show the relative change in the state vector with depth. The parameters used for this ring are $\dot{M} = 4 \times 10^{-9} M_\odot/\mathrm{yr}$, $M_1 = 1.1 M_\odot$.

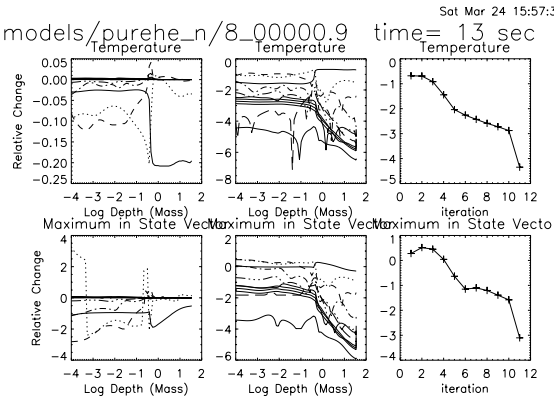

Figure 5.5: The right upper and lower boxes show the number of iterations performed for the ring of $R/R_\star = 8$. The upper two boxes to the left show the relative change in temperature with depth, which also affect how many iterations needed to make the model converge. The two lower boxes to the left show the relative change in the state vector with depth. The parameters used for this ring are $\dot{M} = 4 \times 10^{-9} M_\odot/\mathrm{yr}$, $M_1 = 1.1 M_\odot$.

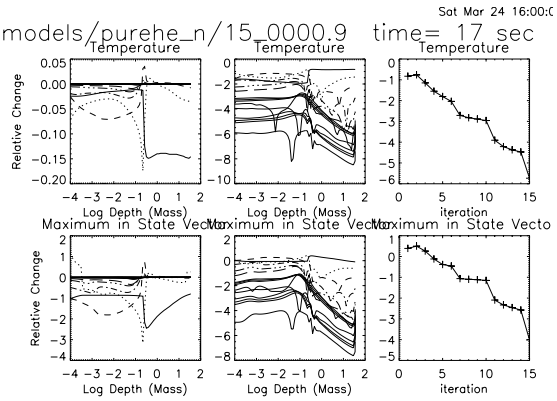

Figure 5.6: The right upper and lower boxes show the number of iterations performed for the ring of $R/R_\star = 15$. The upper two boxes to the left show the relative change in temperature with depth, which also affect how many iterations needed to make the model converge. The two lower boxes to the left show the relative change in the state vector with depth. The parameters used for this ring are $\dot{M} = 4 \times 10^{-9} M_\odot/\mathrm{yr}$, $M_1 = 1.1 M_\odot$.

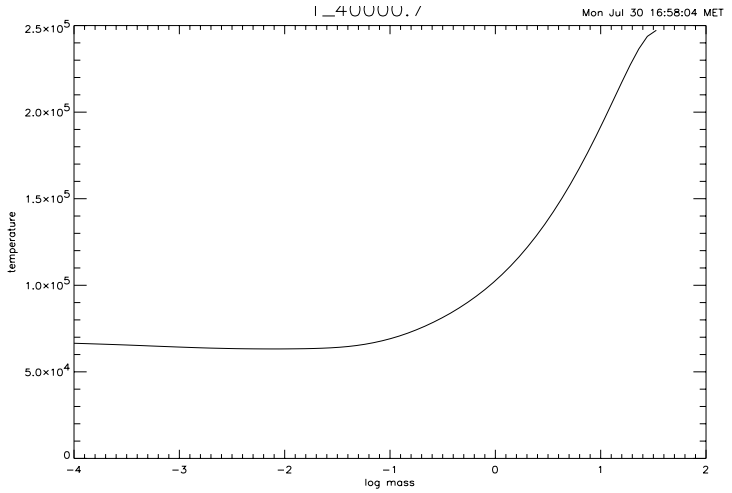

Figure 5.7: The disc temperature distribution with depth at $R = 1.4R_1$. The parameters used for this model are $\dot{M} = 4 \times 10^{-9} M_\odot/\mathrm{yr}$, $M_1 = 1.1 M_\odot$.

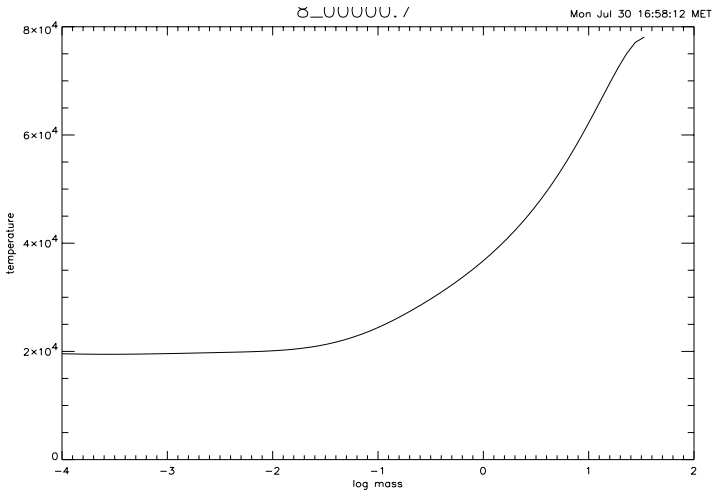

Figure 5.8: The disc temperature distribution with depth at $R = 8R_1$. The parameters used for this model are $\dot{M} = 4 \times 10^{-9} M_\odot/\mathrm{yr}$, $M_1 = 1.1 M_\odot$.

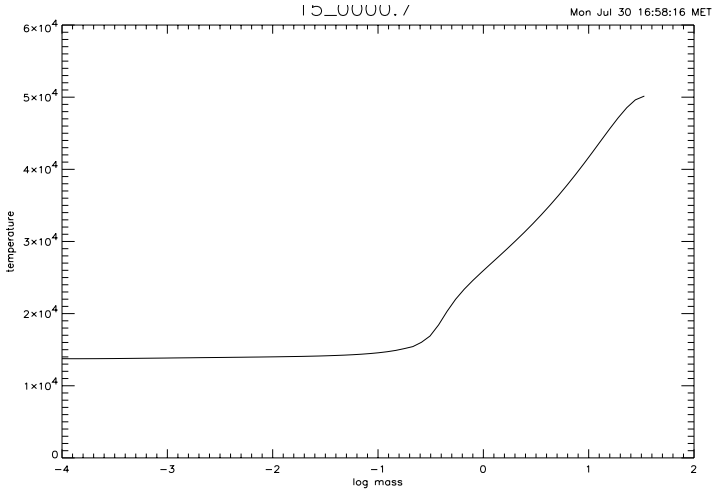

Figure 5.9: The disc temperature distribution with depth at $R = 15R_1$. The parameters used for this model are $\dot{M} = 4 \times 10^{-9} M_\odot/\mathrm{yr}$, $M_1 = 1.1 M_\odot$.

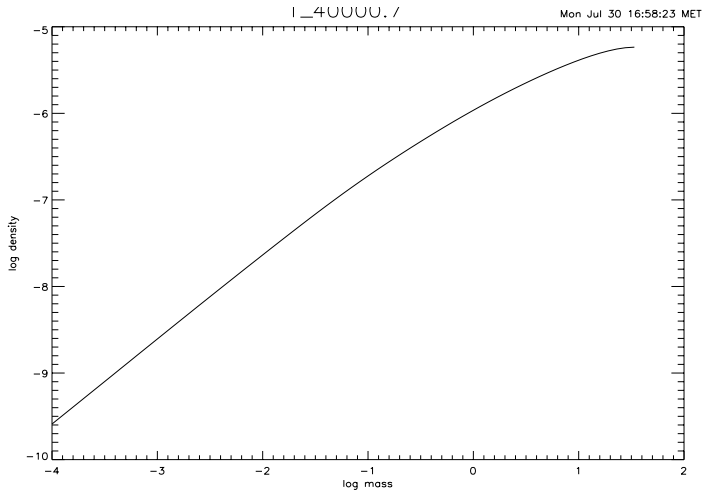

Figure 5.10: The disc density distribution with depth at $R = 1.4R_1$. The parameters used for this model are $\dot{M} = 4 \times 10^{-9} M_\odot/\mathrm{yr}$, $M_1 = 1.1 M_\odot$.

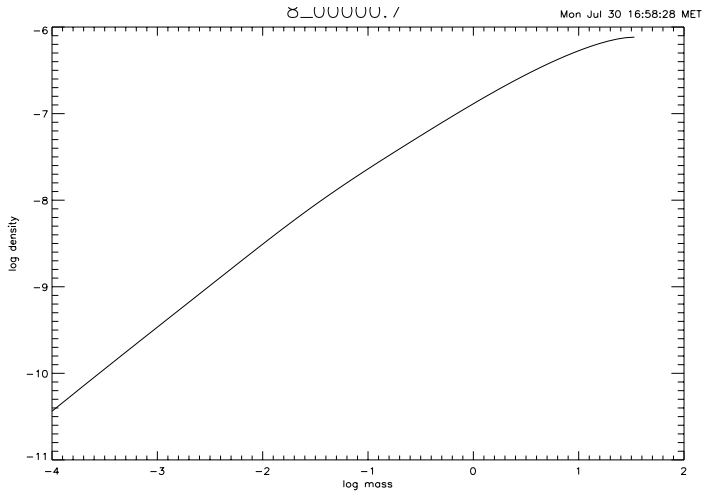

Figure 5.11: The disc density distribution with depth at $R = 8R_1$. The parameters used for this model are $\dot{M} = 4 \times 10^{-9} M_\odot/\mathrm{yr}$, $M_1 = 1.1 M_\odot$.

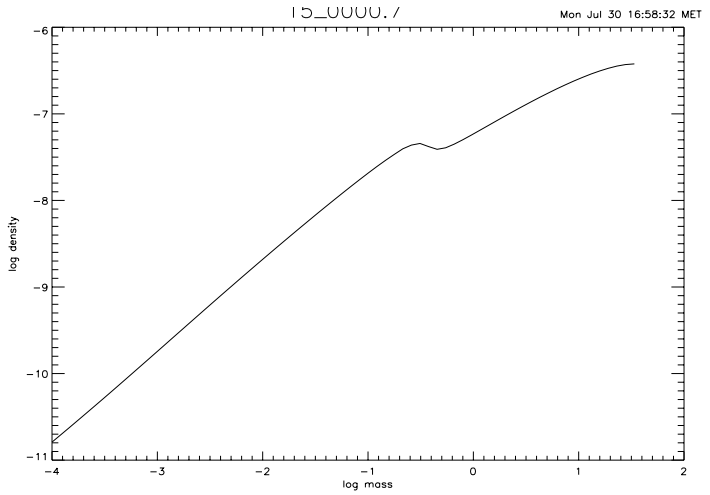

Figure 5.12: The disc density distribution with depth at $R = 15R_1$. The parameters used for this model are $\dot{M} = 4 \times 10^{-9} M_\odot/\mathrm{yr}$, $M_1 = 1.1 M_\odot$.

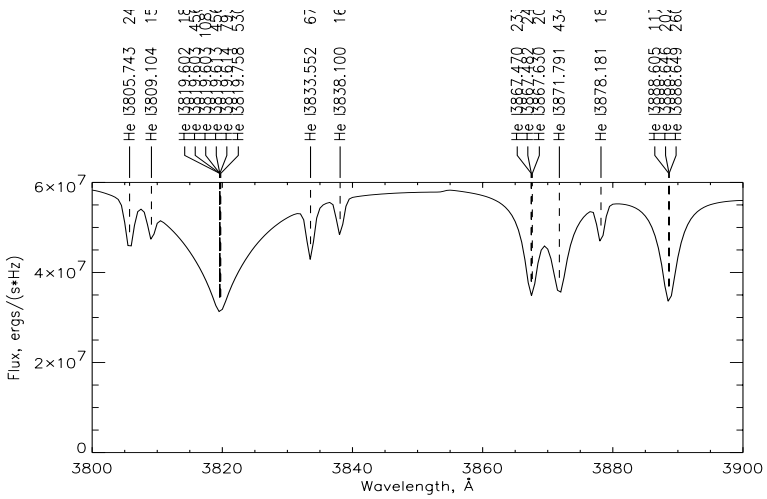

Figure 5.13: A sample part of the outermost ring λ 3500-7000 Å spectrum, showing strong He lines which appear in this region in the spectrum of the pure helium model. The numbers seen at the top of the figure specify the lines wavelengths and their equivalent widths (EW). The parameters used for this ring are $\dot{M} = 5 \times 10^{-9} M_\odot/\mathrm{yr}$, $M_1 = 1.1 M_\odot, R = 15R_1$.

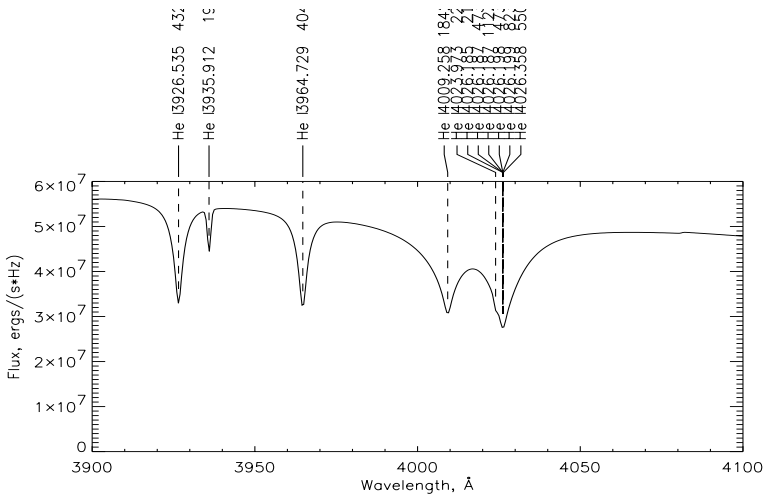

Figure 5.14: A sample part of the outermost ring λ 3500-7000 Å spectrum, showing strong He lines which appear in this region in the spectrum of the pure helium model. The numbers seen at the top of the figure specify the lines wavelengths and their equivalent widths (EW). The parameters used for this ring are $\dot{M} = 5 \times 10^{-9} M_{\odot}/\mathrm{yr}$, $M_1 = 1.1 M_{\odot}, R = 15 R_1$.

more accurate result. The reasonable number of azimuthal points can be found by increasing the number of points, until no changes seen in the output spectra, with further increase in the number of points. In our case we found that any number which ranges between 30 and 50 is very sufficient as seen Fig. 5.18.

5.7.2 Abundance

The abundance is one of the main parameters which influences the disc spectra. Since the AM CVn stars spectra can be explained with a pure helium model or maybe a pure helium model with small traces of hydrogen, we investigated the influence of an extra amount of hydrogen on the line profiles. We have used a model atom for helium with 14 levels of He I and one level of He II in the pure helium model. We also studied the spectra of the pure helium model when He II is included with 14 levels and He III as a highest one-level ion, and we found a small difference in the spectra of the very innermost rings of the disc, when compared to the spectra of the same rings expected from the pure helium model of He II as a one-level ion as seen in Fig. 5.19. We have also found that the differences decrease gradually with increasing radial distance from the central star as seen in Fig. 5.20, and become completely negligible in the final integrated disc spectra as seen in Fig. 5.21. This is

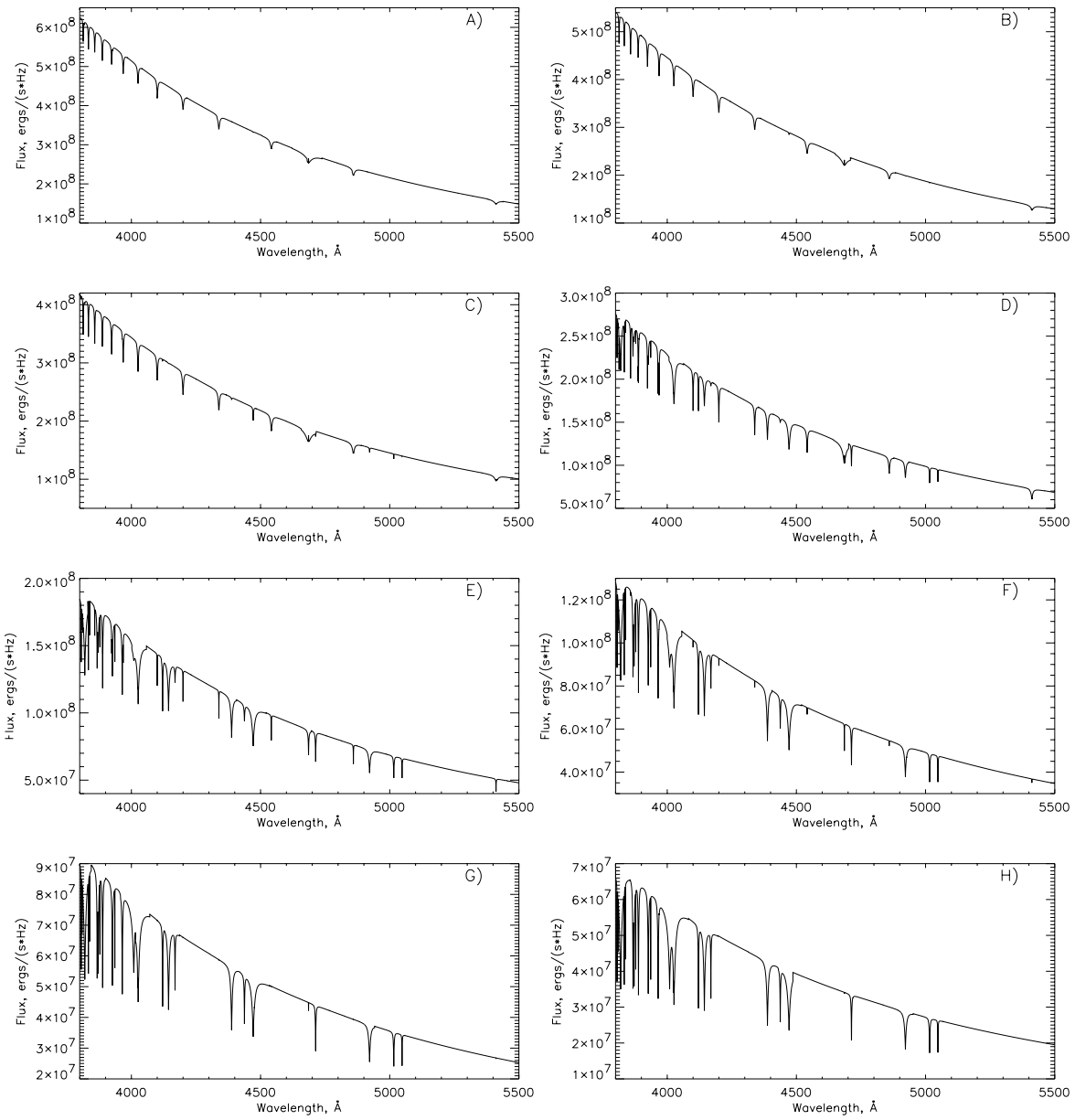

Figure 5.15: The total flux received from each ring in the pure helium accretion disc model with parameters: $\dot{M} = 4 \times 10^{-9} M_{\odot}/\mathrm{yr}$, $M_1 = 1.2 M_{\odot}, i = 15^{\circ}$ and the radial distance R assumed from top left to right bottom are 1.4, 2.0, 2.8, 4.0, 5.56, 8.0, 11.3 and 15.0 R_1, where R_1 is the radius of the central star. The effective temperature of the inner and outer ring is $\approx$ 93 700 and 23 400K, respectively.

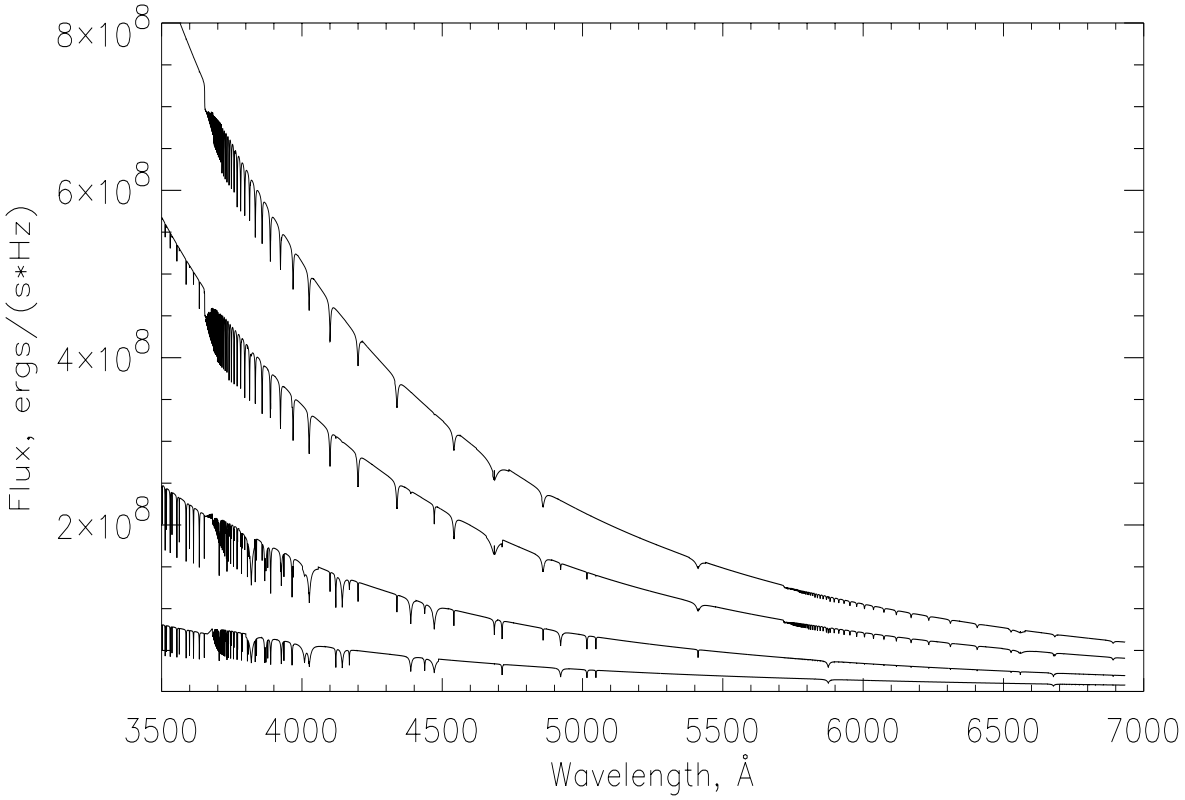

Figure 5.16: The total flux received from separate rings in the pure helium accretion disc model with parameters: $\dot{M} = 4 \times 10^{-9} M_{\odot}$/yr, $M_1 = 1.2 M_{\odot}, i = 15^{\circ}$ and the radial distance R assumed from top are 1.4, 2.8, 5.56 and 15.0 R_1, where R_1 is the radius of the central star. The effective temperature of the inner and outer ring is $\approx$ 93 700 and 23 400K respectively.

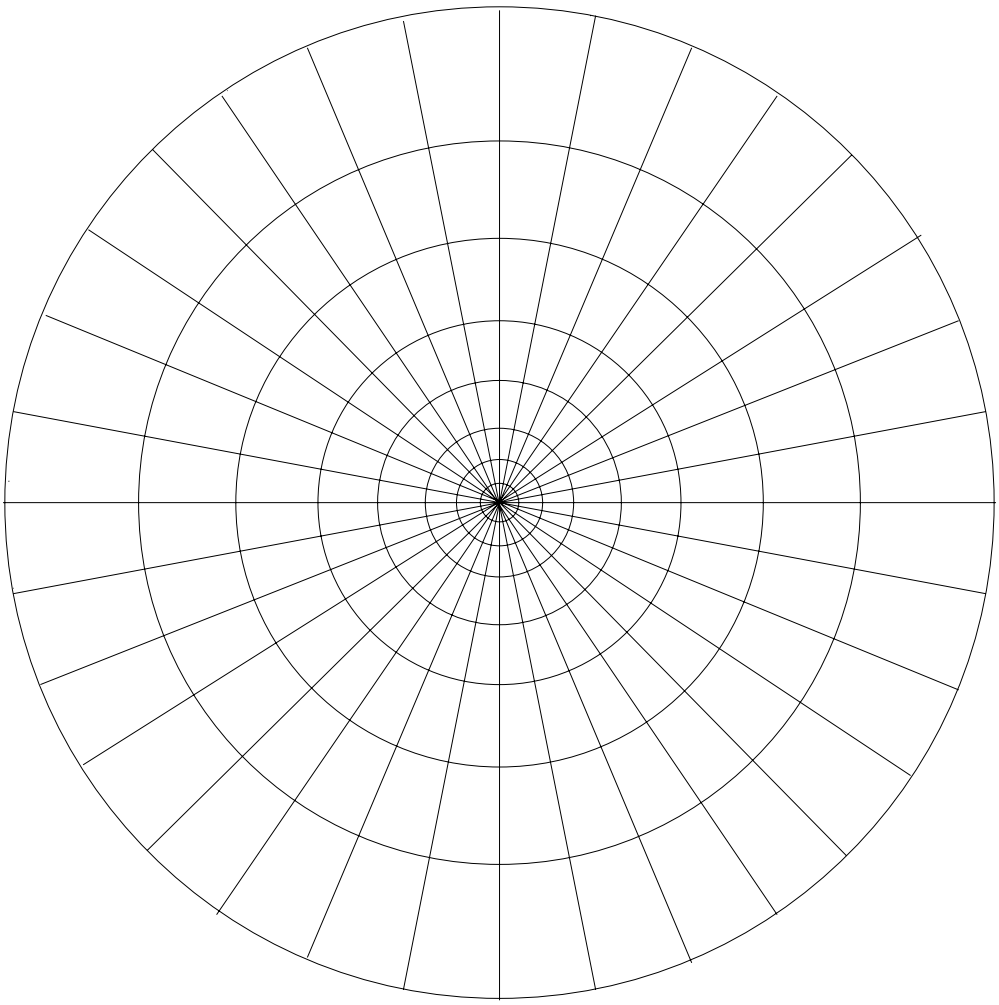

Figure 5.17: The disc structure with the rings and the number of sectors assumed.

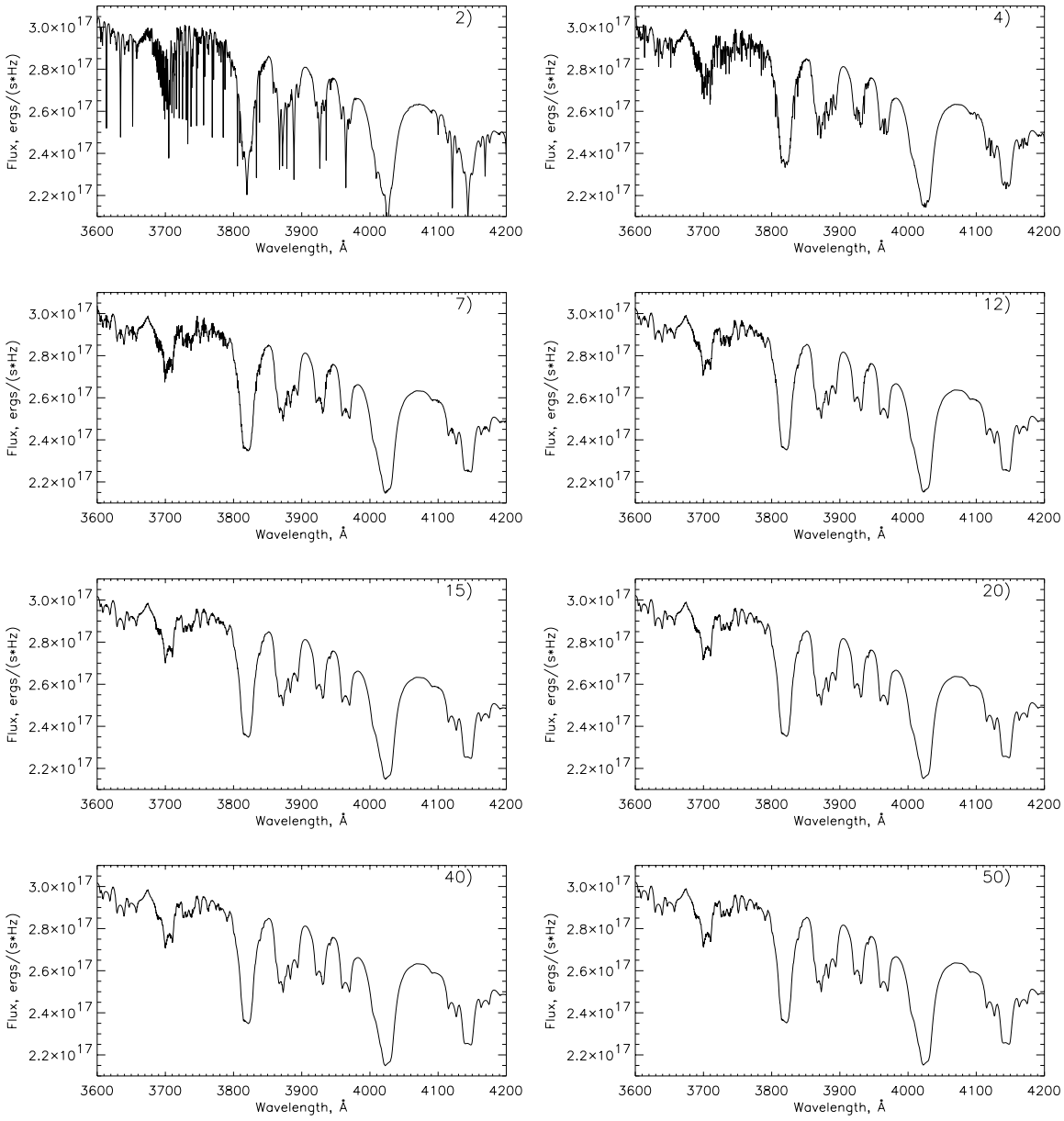

Figure 5.18: The influence of the number of azimuthal points considered for integrating the total disc spectrum. The parameters used for these models are $\dot{M} = 4 \times 10^{-9} M_{\odot}/\mathrm{yr}$, $M_1 = 1.2 M_{\odot}, R_{in} = 1.4 R_1, R_{out} = 15 R_1, i = 15^{\circ}$ while the number of azimuthal points assumed is written in the upper right corner of each panel.

because He II is important in the innermost rings which make a small contribution to the total spectrum, because of their small geometrical contribution (that is, 10% of the radial extent translates to only 1% of the total area). Moreover, He II lines that originate in the inner rings are smeared by Keplerian velocity which is largest there. The lines seen in the total disc spectrum of the pure helium model are identified in both Fig. 5.22 and Fig. 5.23.

We have added hydrogen into the helium model with 12 exciplicit levels, and we found that a very small amount of hydrogen easily appear in the spectra, and in some cases H_γ can be mistaken as He II lines as seen in Fig. 5.24. We demonstrate how the H_γ line at 4340 Å quickly becomes a deep line even with small amounts of hydrogen compared with helium. The H/He ratios by number are in Fig. 5.24 from panel a) to c) given as $10, 10^{-1}$ and 10^{-3} which demonstrate that H_γ can be mistaken as a He II line with such ratios. On the other hand we found that the H_γ will not be mistaken as a He II line when the H/He $\leq 10^{-5}$ by number as seen in Fig. 5.25 and Fig. 5.26. Fig. 5.25 shows that the disc of H/He = 10^{-5} is hotter than the pure helium model, which explains the difference in the lines seen in Fig. 5.26. The lines in panel (b) of Fig. 5.26 have been broadened with FWHM=20 Å to demonstrate the large sensitivity of the predicted spectrum on the hydrogen abundance, which makes it possible to estimate the upper limits of the H/He number density in the accretion disc, from the observed spectra of the AM CVn systems of a 20 Å resolution presented later in this work. Also in this figure we used $i = 20$ instead of 35 as in Fig. 5.24, because at smaller angles we can better estimate such an upper limit, due to the reasons which will be discussed later in sec. 5.7.4. Based on these conclusions, our major investigations will be done using the pure helium model with 14 levels of He I and He II is considered as a one level ion. We will only get a 'negative' effect from including He II exciplicitly in the model. It will only increase the computing time of the model, due to the high number of exciplicit levels considered in the model, which at the end will give the same result as if they were not included.

5.7.3 Mass accretion rate

Fig. 5.27 shows spectra of an accretion disc with different mass accretion rates ($\dot{M} = 9, 6$ and 3×10^{-9}) $M_\odot$/yr. The radial temperature is a function of $\dot{M}$ (eq. 5.37), and as a consequence the continuum becomes rapidly steeper with increasing $\dot{M}$. On the other hand the lines become less deep with increasing $\dot{M}$ as seen in Fig. 5.28, this is because for higher mass accretion rate like $\dot{M} = 9 \times 10^{-9} M_\odot$/yr the disc is hot everywhere (T_{eff} $\geq$25 000 K as shown in table(5.1)), so the He I lines, which are strongest around 20 000 K cannot contribute as much as for cooler discs where the

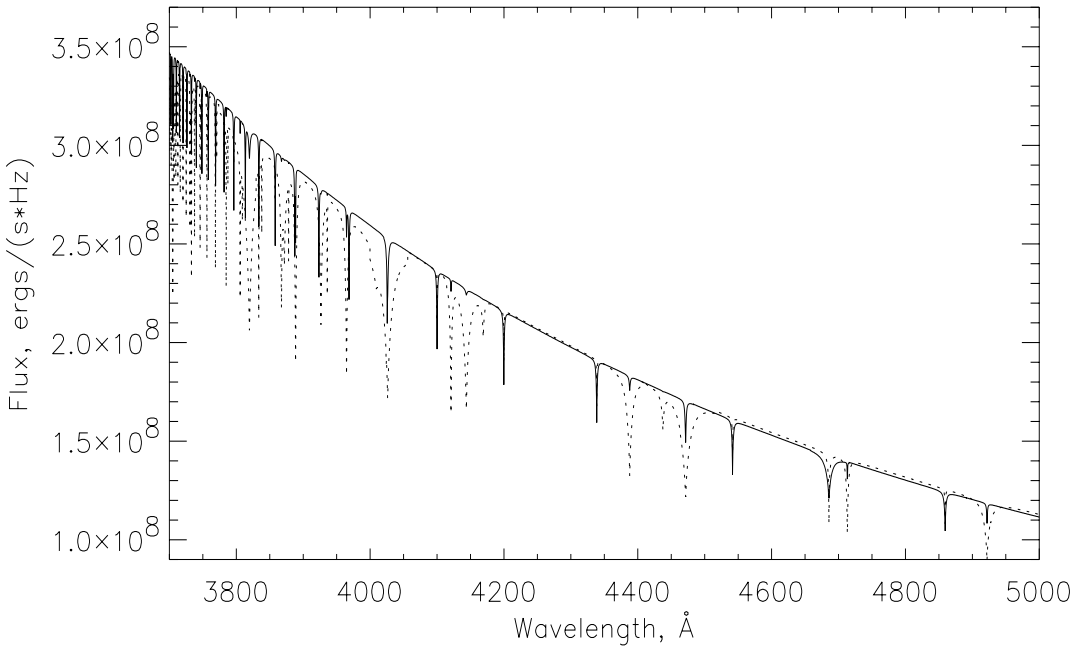

Figure 5.19: The influence of the He II consideration on the NLTE pure helium accretion disc spectra. 'Dotted line' shows the ring spectrum at $R/R_1 = 2.8$ of the pure helium model with He II considered as one level ion, while the 'solid line' shows the spectrum of the same ring but when He II is a 14 level atom and He III as a one level ion. The parameters used for these models are $\dot{M} = 4 \times 10^{-9} M_\odot/\mathrm{yr}$, $M_1 = 1.1 M_\odot, R_{in} = 1.4 R_1$, and $i = 20°$.

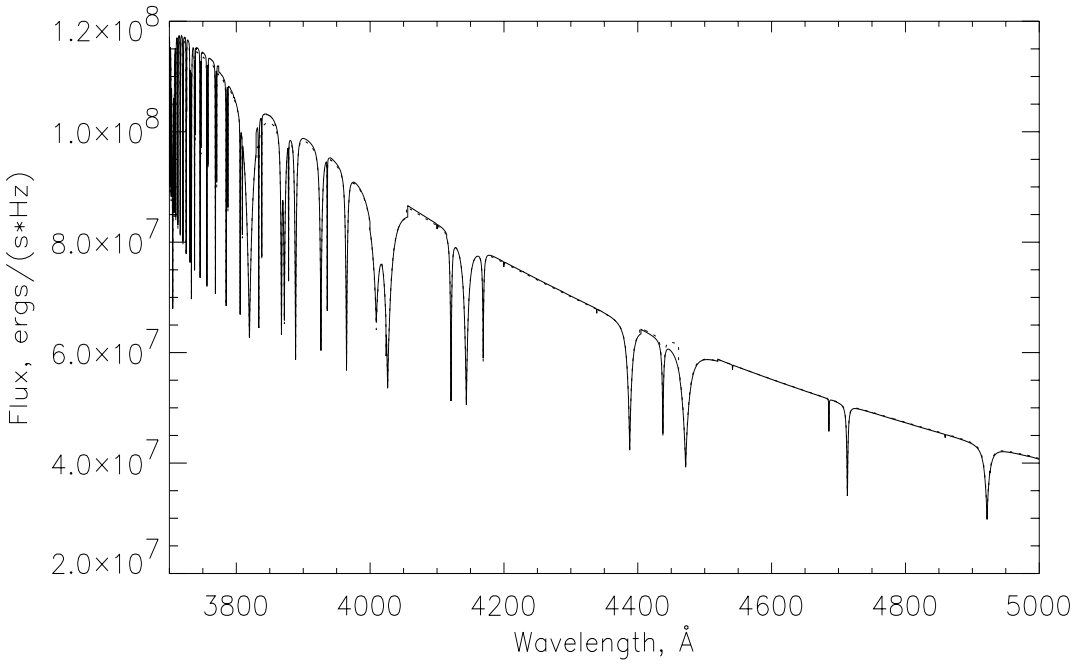

Figure 5.20: The influence of the He II consideration on the NLTE pure helium accretion disc spectra. 'Dotted line' shows the ring spectrum at $R/R_1 = 11.3$ of the pure helium model with He II considered as one level ion, while the 'solid line' shows spectrum of the same ring but when He II is a 14 level atom and He III as a one level ion. The parameters used for these models are $\dot{M} = 4 \times 10^{-9} M_\odot/\mathrm{yr}$, $M_1 = 1.1 M_\odot, R_{in} = 1.4 R_1$, and $i = 20^\circ$.

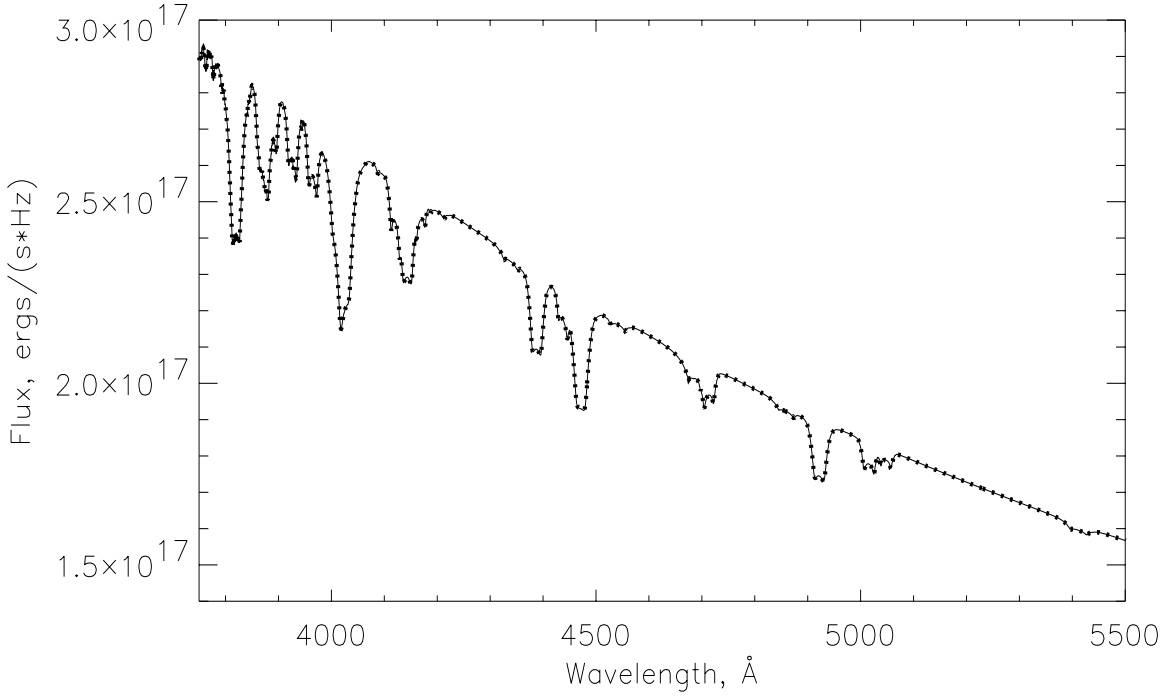

Figure 5.21: The influence of the He II consideration in the model on the continuum and the lines of the NLTE pure helium accretion disc spectra. 'Thick dotted line' shows the total disc spectrum of the pure helium model with He II considered as one level ion, while the 'solid thin line' shows the total disc spectrum but when He II is a 14 level atom and He III as a one level ion. The parameters used for these models are $\dot{M} = 4 \times 10^{-9} M_{\odot}$/yr, $M_1 = 1.1 M_{\odot}, R_{in} = 1.4 R_1, R_{out} = 15 R_1$, and $i = 20°$.

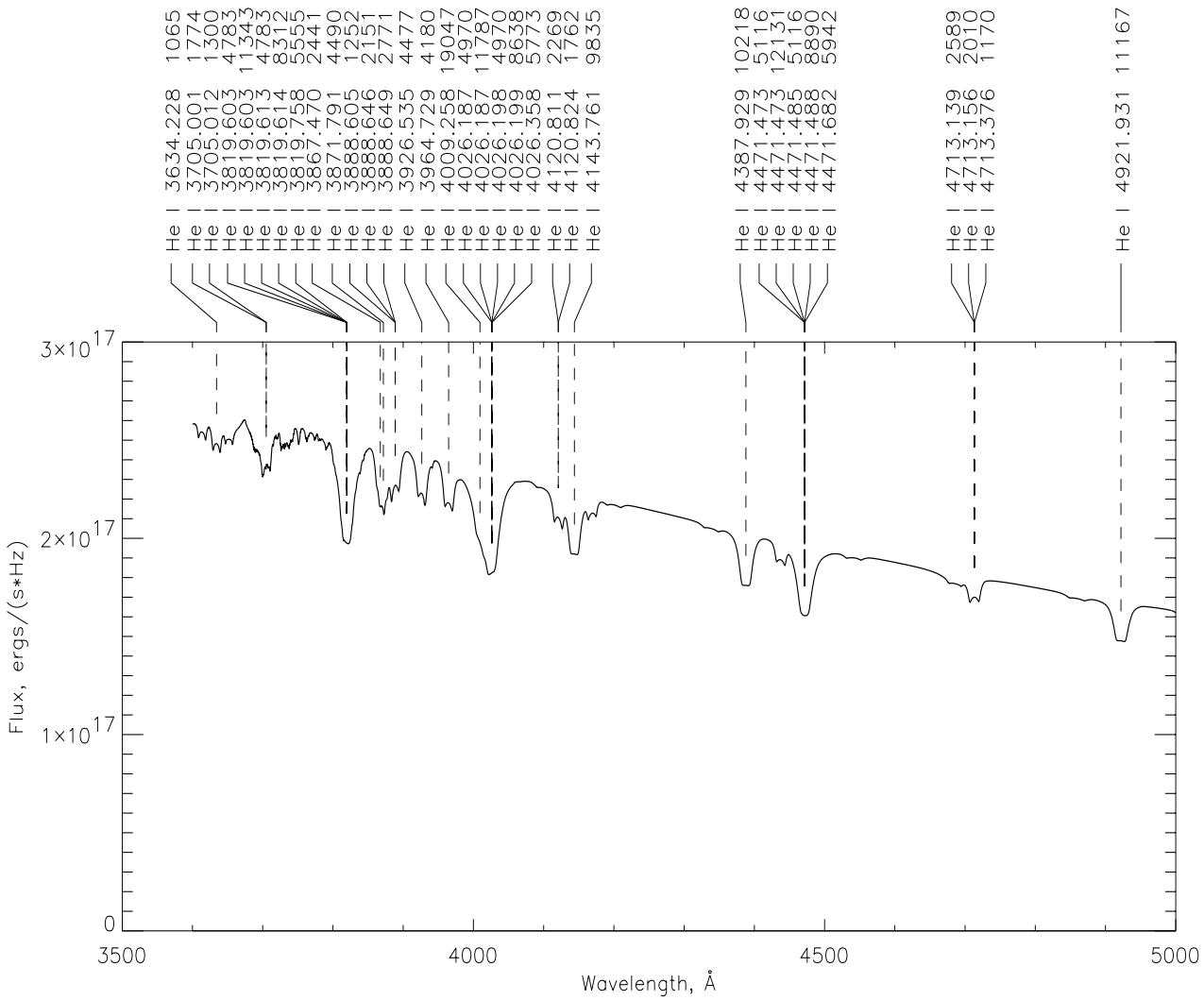

Figure 5.22: The identification of the helium lines in the total disc spectrum. The parameters used for these models are $\dot{M} = 3 \times 10^{-9} M_{\odot}/\mathrm{yr}$, $M_1 = 1.1 M_{\odot}, R_{in} = 1.4 R_1, R_{out} = 15 R_1$, and $i = 15°$.

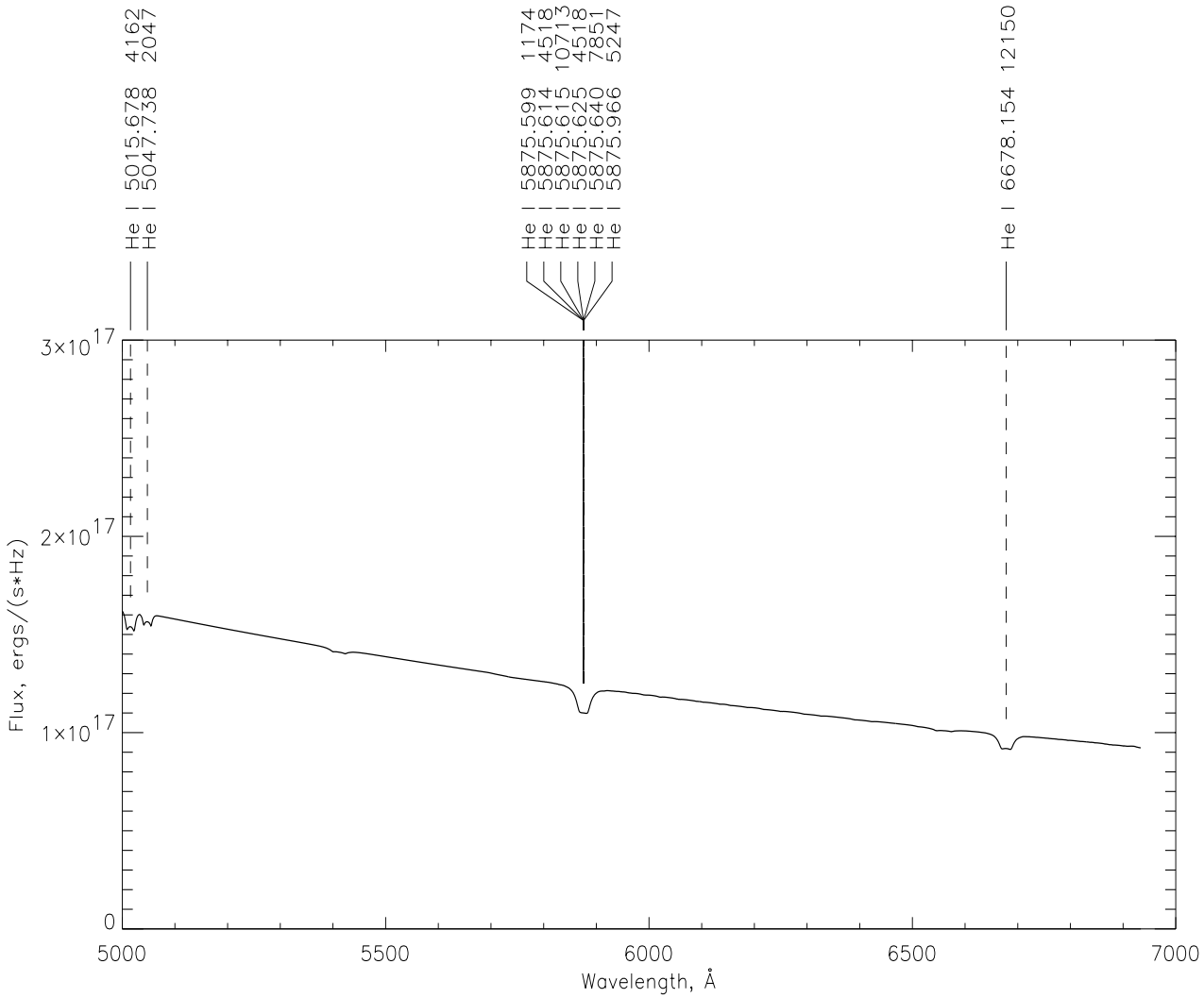

Figure 5.23: The identification of the helium lines in the total disc spectrum. The parameters used for these models are $\dot{M} = 3 \times 10^{-9} M_\odot/\mathrm{yr}$, $M_1 = 1.1 M_\odot, R_{in} = 1.4 R_1, R_{out} = 15 R_1$, and $i = 15°$.

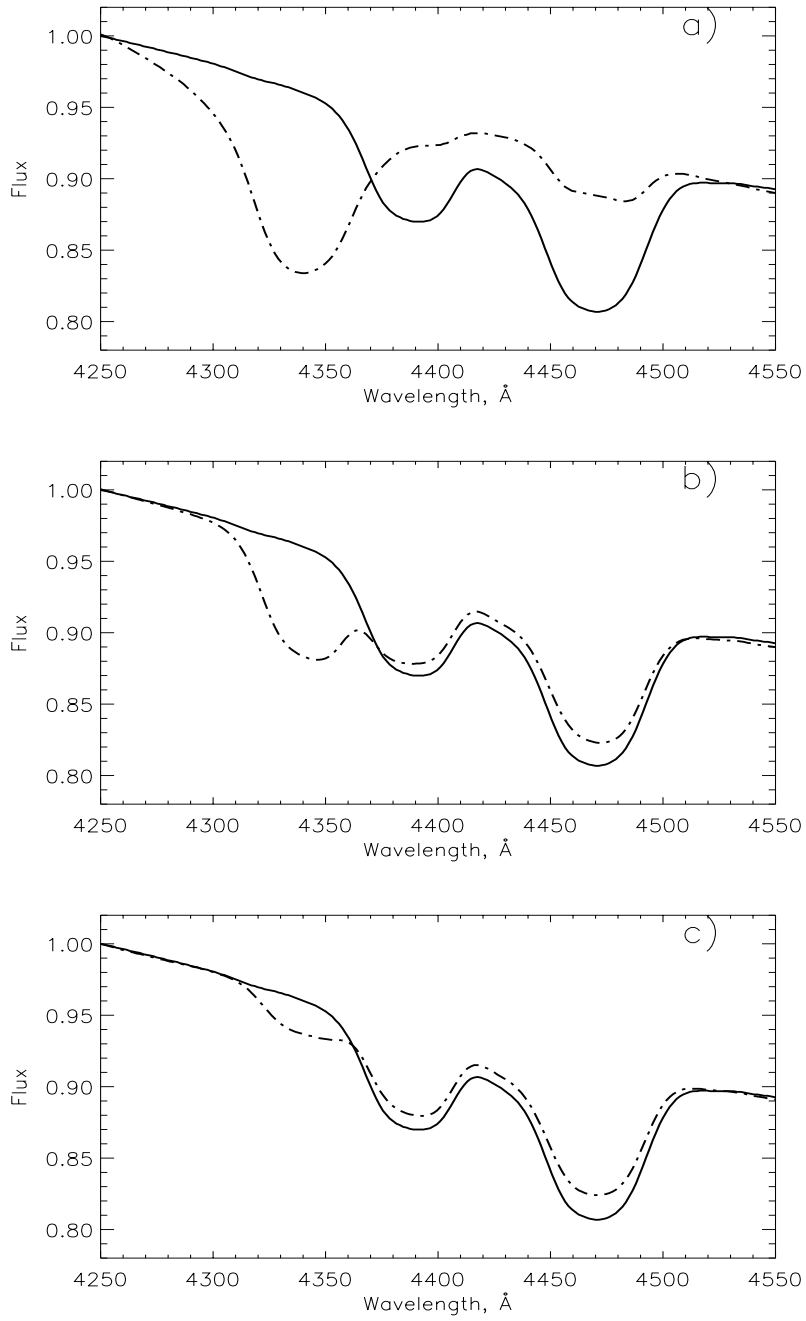

Figure 5.24: The influence of an extra amount of hydrogen on the line profiles of the NLTE hydrogen-helium accretion disc spectra (dashed dotted line), when compared with the spectra of the pure helium model (solid line). The parameters used for these models are $\dot{M} = 4 \times 10^{-9} M_{\odot}/\mathrm{yr}, M_1 = 1.1 M_{\odot}, R_{in} = 1.4 R_1, R_{out} = 15 R_1$, and $i = 35^{\circ}$ while the H/He ratio by number varies from panel a) to d) as $10, 10^{-1}$ and 10^{-3}, normalised to 1.0 at the left hand upper corner. The lines have been broadened with FWHM=20 Å.

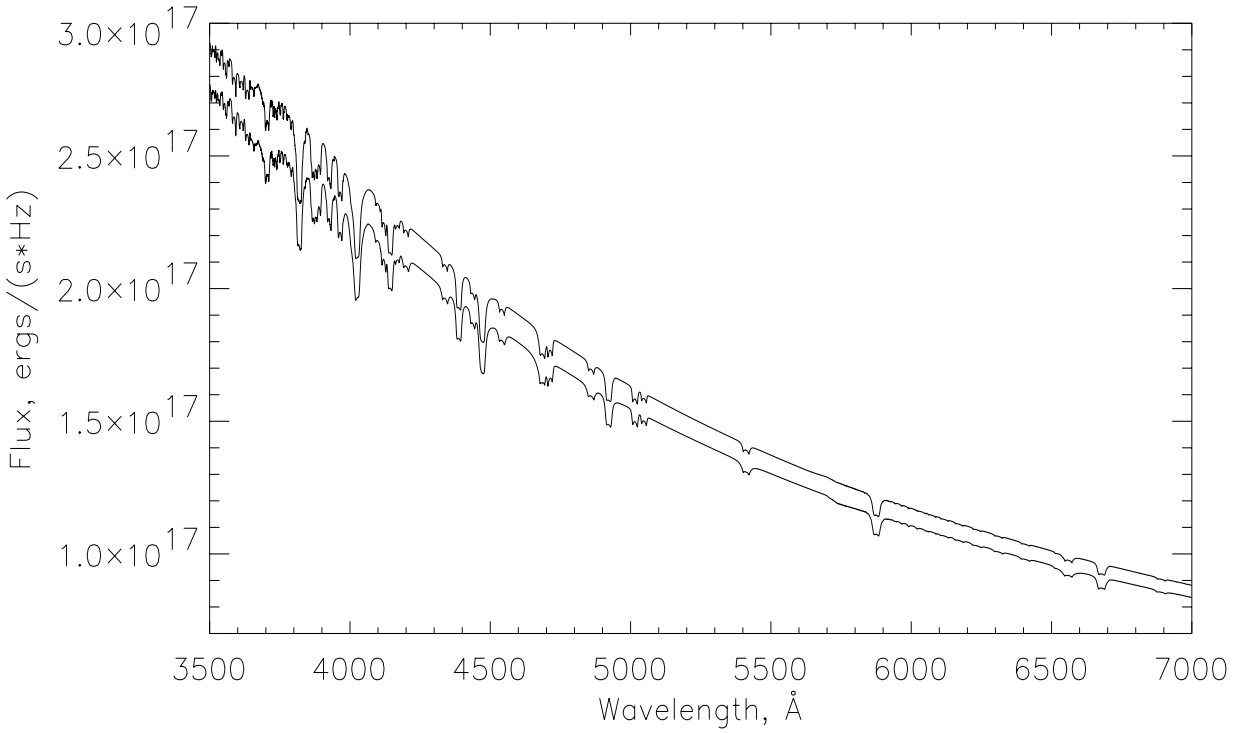

Figure 5.25: The influence of a small amount of hydrogen on the continuum and the line profile of the NLTE hydrogen-helium accretion disc spectra (upper line), when compared with the spectra of the pure helium model (lower line). The parameters used for these models are $\dot{M} = 3 \times 10^{-9} M_{\odot}$/yr, $M_1 = 1.0 M_{\odot}, R_{in} = 1.4 R_1, R_{out} = 15 R_1$, and $i = 20^{\circ}$ while H/He $= 10^{-5}$ by number.

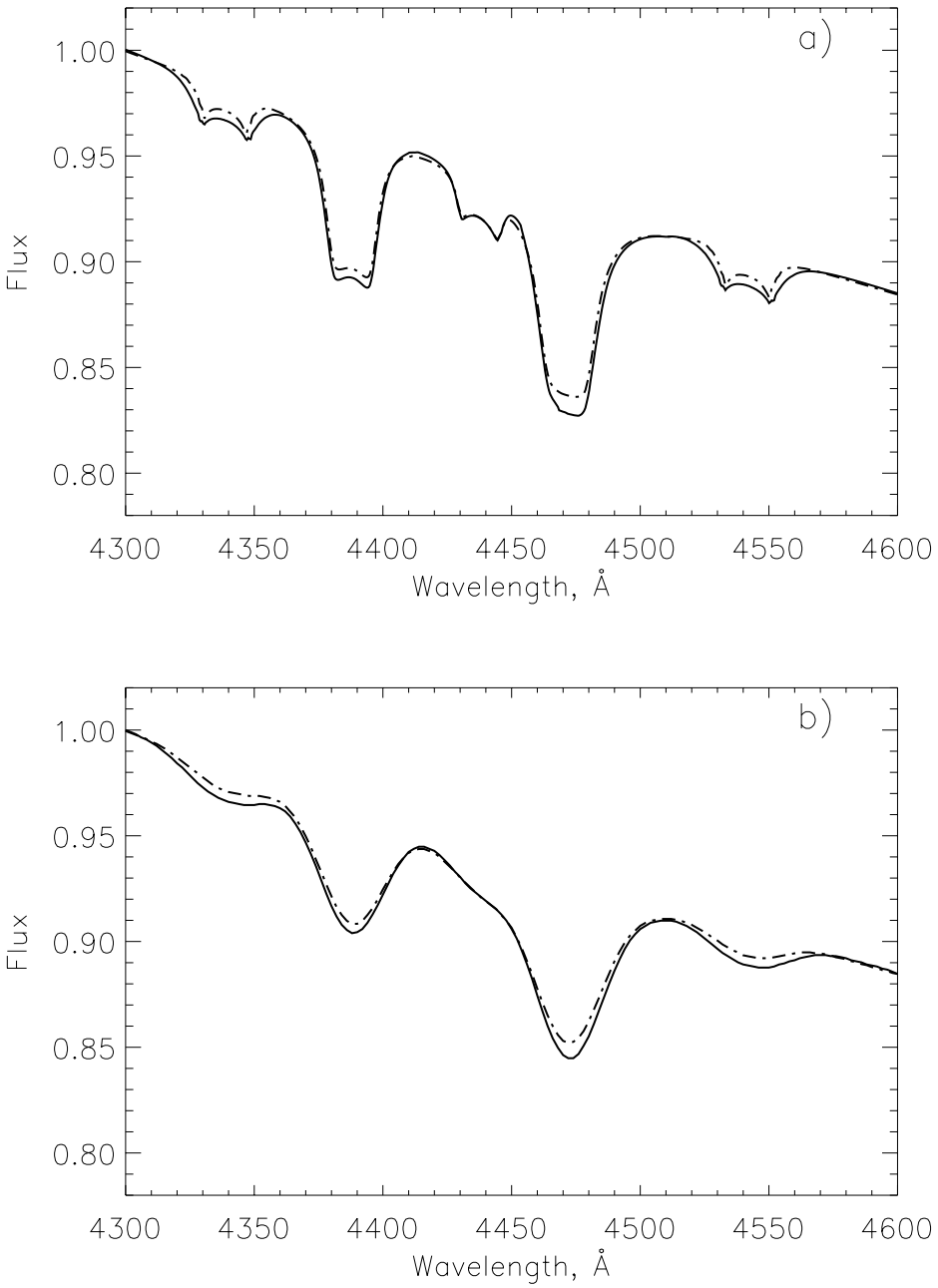

Figure 5.26: The influence of a small amount of hydrogen of the H/He = 10^{-5} by number on the line profiles of the NLTE hydrogen-helium accretion disc spectra (dashed dotted line), when compared with the spectra of the pure helium model (solid line). We show such influence on the lines in both high resolution spectra (panel a) and a spectra of FWHM=20 Å (panel b). The parameters used for these models are $\dot{M} = 3 \times 10^{-9} M_{\odot}$/yr, $M_1 = 1.0 M_{\odot}, R_{in} = 1.4 R_1, R_{out} = 15 R_1$, and $i = 20°$.

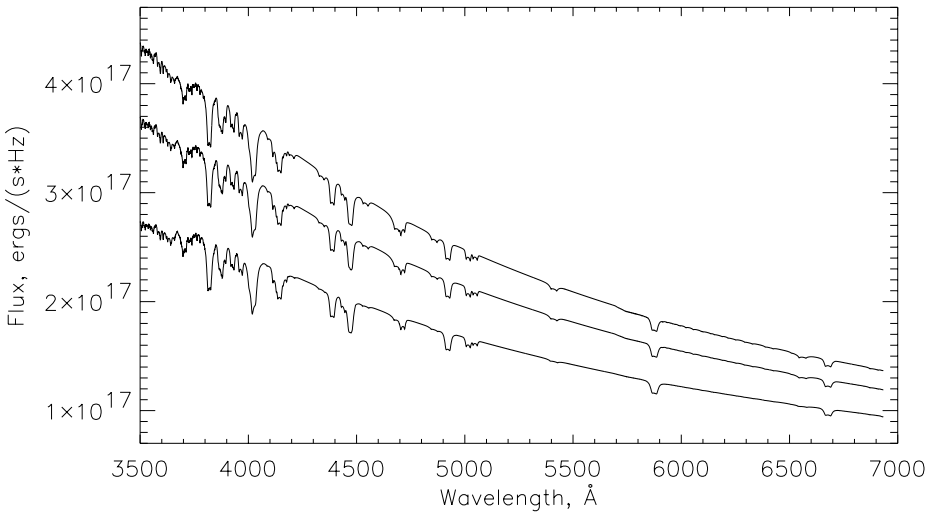

Figure 5.27: The influence of the mass accretion rate on the slope of the NLTE pure helium accretion disc spectra. The parameters used for these models are $M_1 = 1.1M_\odot, R_{in} = 1.4R_1, R_{out} = 15R_1, i = 20°$ while $\dot{M}$ from the top 9, 6 and $3{\times}10^{-9} M_\odot$/yr.

He I are stronger for all annuli. The lines also become narrower with increasing $\dot{M}$ because the He I lines are formed in a given temperature range and thus originate mostly in the radially distant part of the disc, where the Doppler broadening is very small. In Fig. 5.29 we show how the structure of the line profile remain unchanged with increasing the mass accretion rate, although the depth and the width of the line do change.

5.7.4 Angle of inclination i

Variations of the angle of inclination make significant changes in the slope of the continuum, as shown in Fig. 5.30. The reason is because the total flux received from the disc increases with increasing $\cos(i)$. In addition to that the lines are influenced in a more serious way as sharp, deep and narrow absorption lines are formed at smaller angles of inclinations. On the other hand, the line profiles become wider and filled with emission-like cores with even more narrow central absorption lines at higher inclinations as seen in Fig. 5.31 where the angles considered are from the top 75°,45° and 15°. We also investigated the influence of the angle of inclination variations on the structure of the line profile of the pure helium accretion

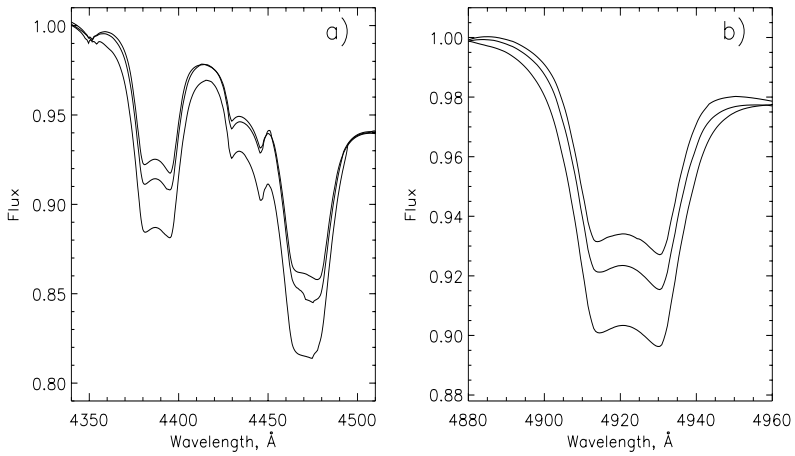

Figure 5.28: The influence of the mass accretion rate on the line profile of the NLTE pure helium accretion disc spectra. The parameters used for these models are $M_1 = 1.1M_\odot, R_{in} = 1.4R_1, R_{out} = 15R_1, i = 20^\circ$ while $\dot{M}$ from the top is 9, 6 and $3{\times}10^{-9}M_\odot$/yr. The flux is normalised to 1.0 at the left upper corner.

disc spectra, and we found that the structure of the line is dramatically influenced by the variations of i as seen in both Fig. 5.32 and Fig. 5.33. In these two figures we show the level of influence on the line with a step of 5° from $5^\circ - 87^\circ$. It is clearly seen that there is a huge difference in the line structure when $i = 5^\circ$ compared to $i = 87^\circ$.

5.7.5 Inner radius of the disc

We have studied the spectra of three different discs with R_{in} varied between 1.4, 4 and $6R_1$ while the rest of the system parameters remain the same: $\dot{M} = 4 \times 10^{-9}M_\odot$/yr, $M_1 = 1.1M_\odot, R_{out} = 15R_1$ and $i = 20^\circ$. It is clearly seen in Fig. 5.34 that the slopes of the spectra become somewhat steeper with smaller R_{in} of the disc, because of the added flux from the inner hot rings. On the other hand we found that the lines become deeper and with a slightly narrower wings with bigger R_{in} as seen in Fig. 5.35. This is due to the removal of the inner hot rings with higher Keplerian velocities.

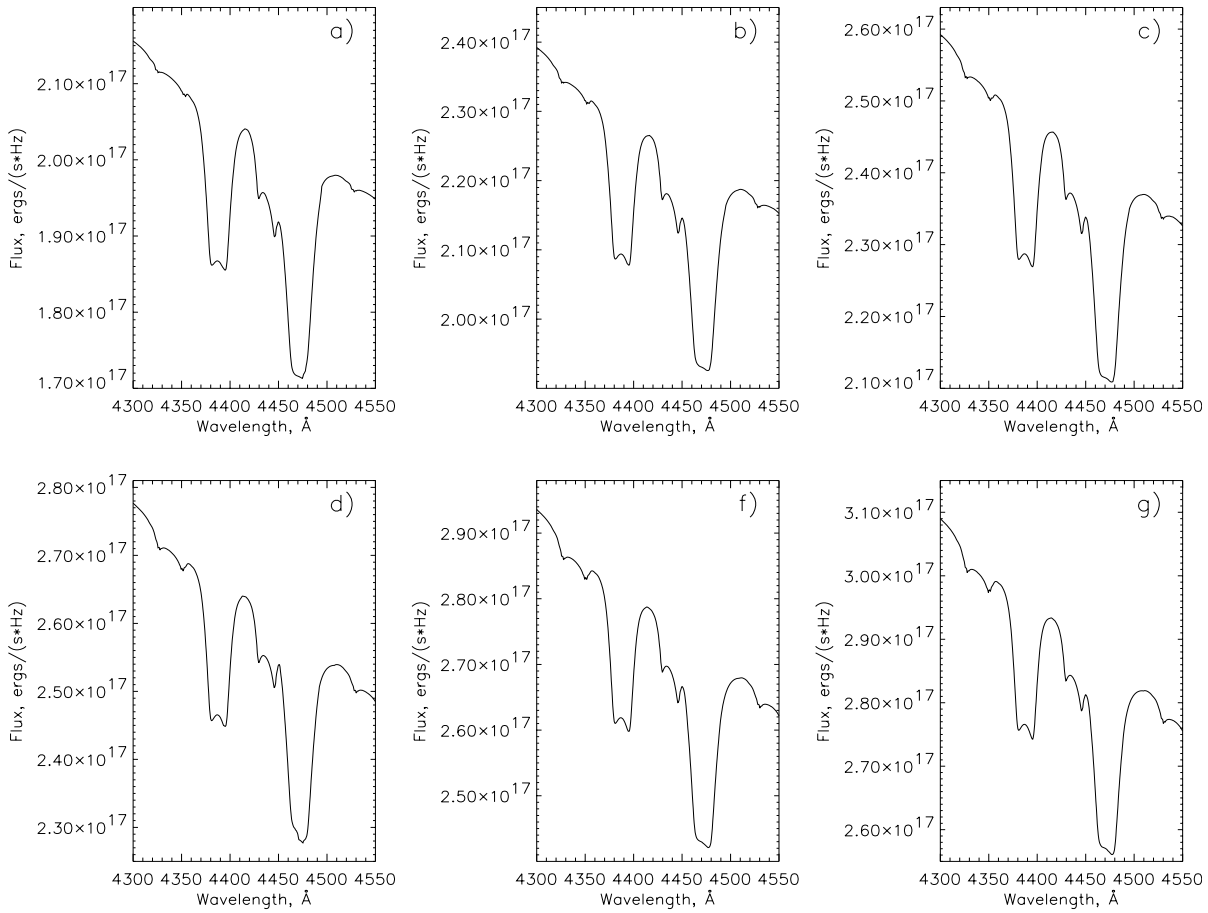

Figure 5.29: The influence of the mass accretion rate on the structure of the line profile of the pure helium accretion disc spectra. The figure shows that the line keeps its structure with increasing or decreasing $\dot{M}$ although the width and the depth of the line change. The parameters used for these models are $M_1 = 1.1M_\odot, R_{in} = 1.4R_1, R_{out} = 15R_1$ and $\dot{M}$ from the left top to the right bottom are (3, 4, 5, 6, 7 and 8 $\times 10^{-9} M_\odot$/yr)

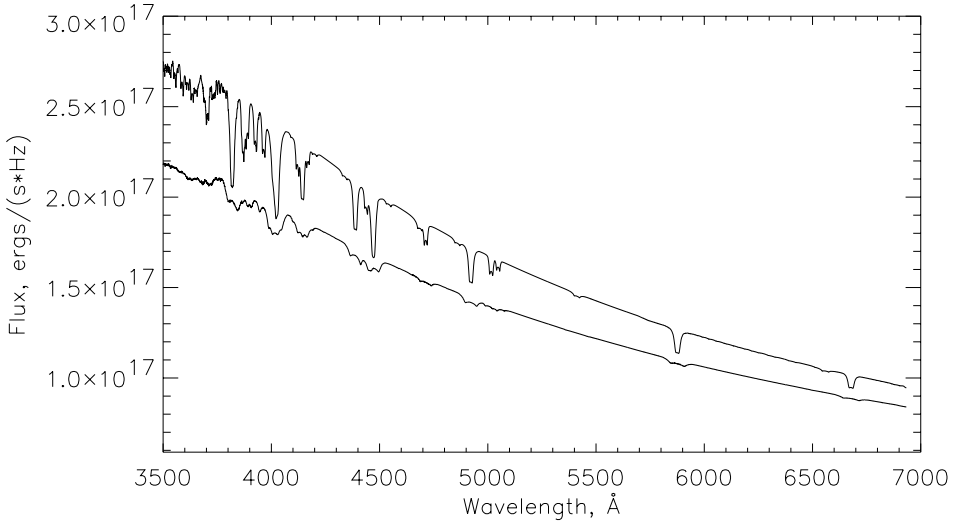

Figure 5.30: The influence of the angle of inclination i on the continuum of the NLTE pure helium accretion disc spectra. The parameters used for these models are $\dot{M} = 3 \times 10^{-9} M_{\odot}/\mathrm{yr}$, $M_1 = 1.1 M_{\odot}, R_{in} = 1.4 R_1, R_{out} = 15 R_1$, while i from the top 15° and 75°.

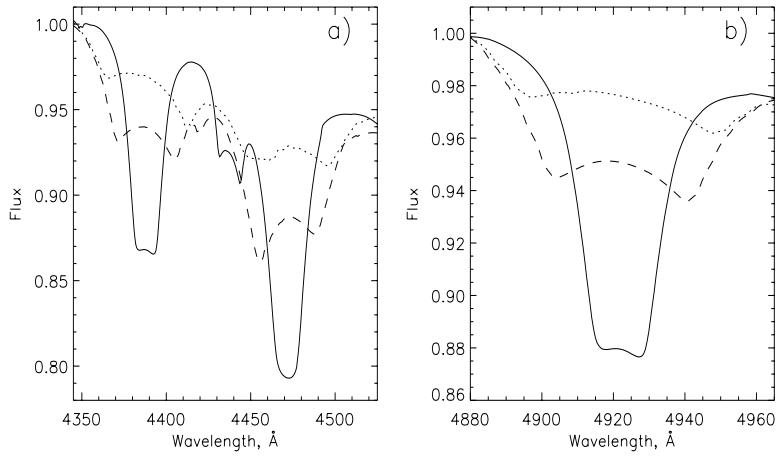

Figure 5.31: The influence of the angle of inclination i on the line profile of the NLTE pure helium accretion disc spectra. The parameters used for these models are $\dot{M} = 3 \times 10^{-9} M_{\odot}/\mathrm{yr}$, $M_1 = 1.1 M_{\odot}, R_{in} = 1.4 R_1, R_{out} = 15 R_1$, while the angles represented by the (dotted line), (dashed line) and (solid line) are $75°, 45°$ and 15° respectively The flux is normalised to 1.0 at the left upper corner.

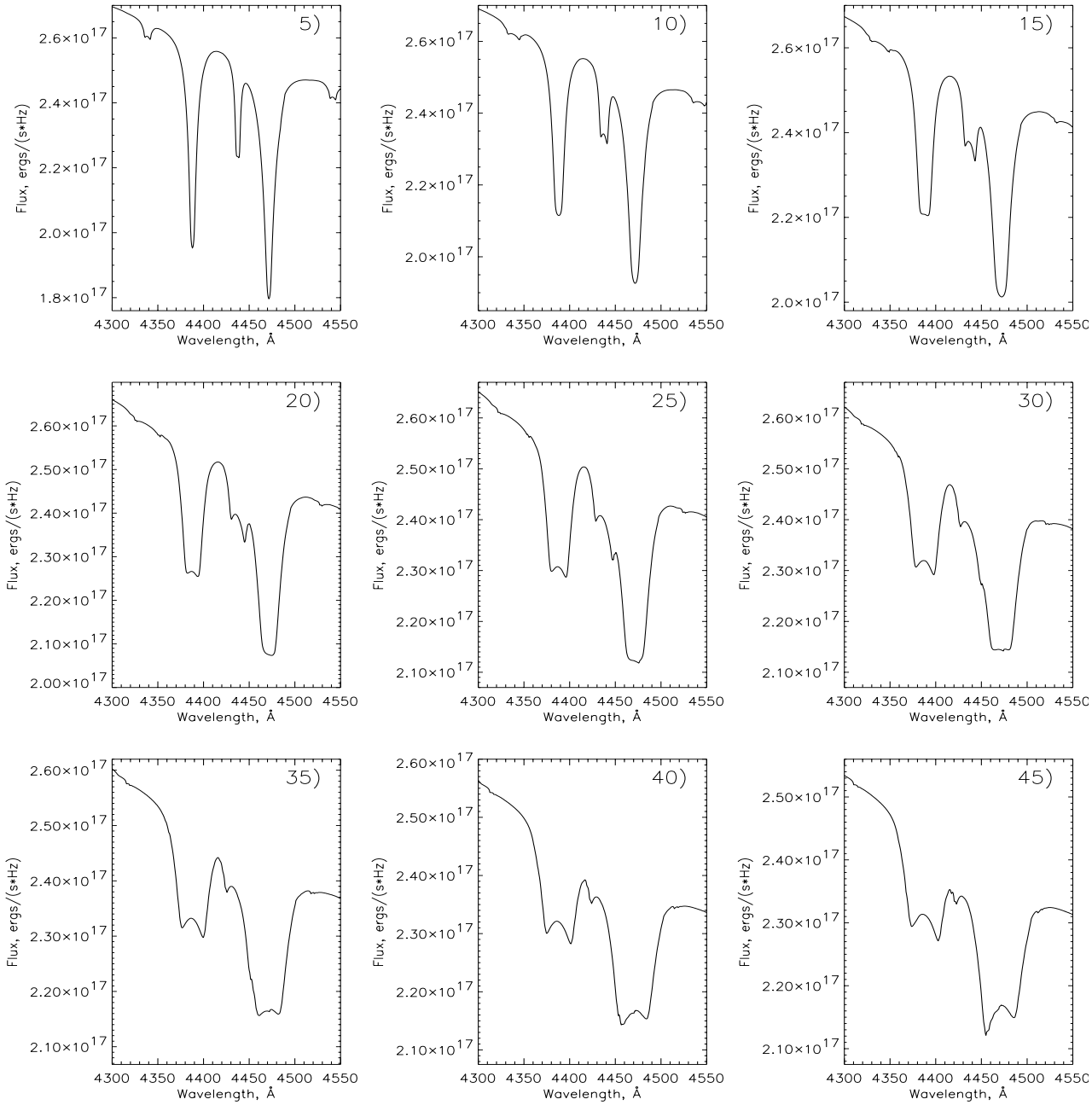

Figure 5.32: The influence of the angle of inclination variations on the structure of the line profile of the pure helium accretion disc spectra. The parameters used for these models are $\dot{M} = 4 \times 10^{-9} M_{\odot}/\mathrm{yr}$, $M_1 = 1.1 M_{\odot}, R_{in} = 1.4 R_1, R_{out} = 15 R_1$ while the value of the angle i is written at the upper right corner of each panel.

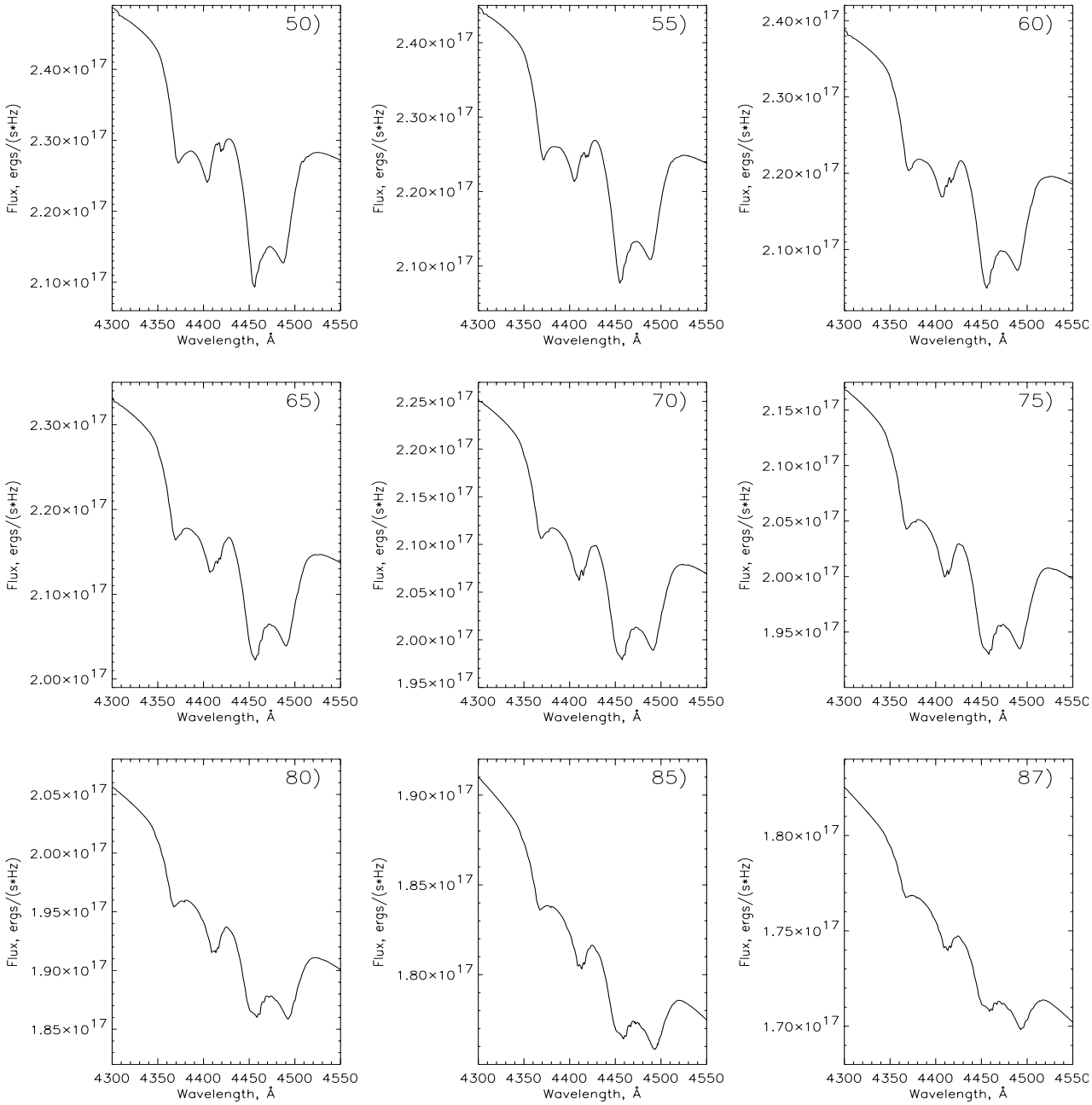

Figure 5.33: The influence of the angle of inclination variations on the structure of the line profile of the pure helium accretion disc spectra. The parameters used for these models are $\dot{M} = 4 \times 10^{-9} M_{\odot}/\mathrm{yr}$, $M_1 = 1.1 M_{\odot}, R_{in} = 1.4 R_1, R_{out} = 15 R_1$ while the value of the angle i is written at the upper right corner of each panel.

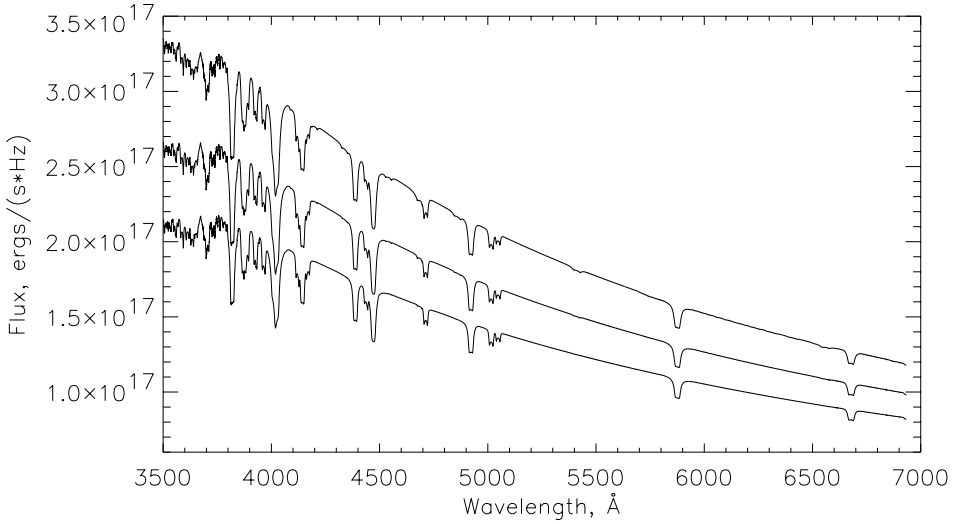

Figure 5.34: The influence of the inner radius on the continuum of the NLTE pure helium accretion disc spectra. The parameters used for these models are $\dot{M} = 4 \times 10^{-9} M_{\odot}/\mathrm{yr}$, $M_1 = 1.1 M_{\odot}, R_{out} = 15 R_1$, and $i = 20^{\circ}$ while the inner radius is from the top 1.4, 4 and $6 R_1$.

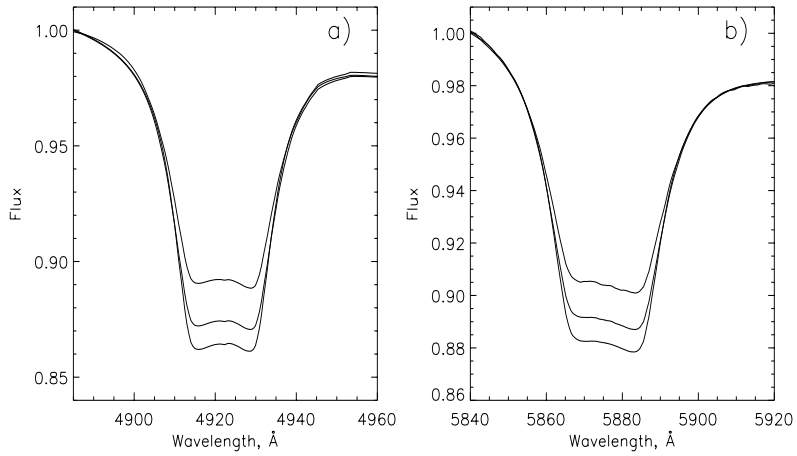

Figure 5.35: The influence of the inner radius variation on the line profile of the NLTE pure helium accretion disc spectra. The parameters used for these models are $\dot{M} = 4 \times 10^{-9} M_{\odot}/\mathrm{yr}$, $M_1 = 1.1 M_{\odot}, R_{out} = 15 R_1$, and $i = 20^{\circ}$ while the inner radius is from the top 1.4, 4, and $6 R_1$. The flux is normalised to 1.0 at the left hand upper corner.

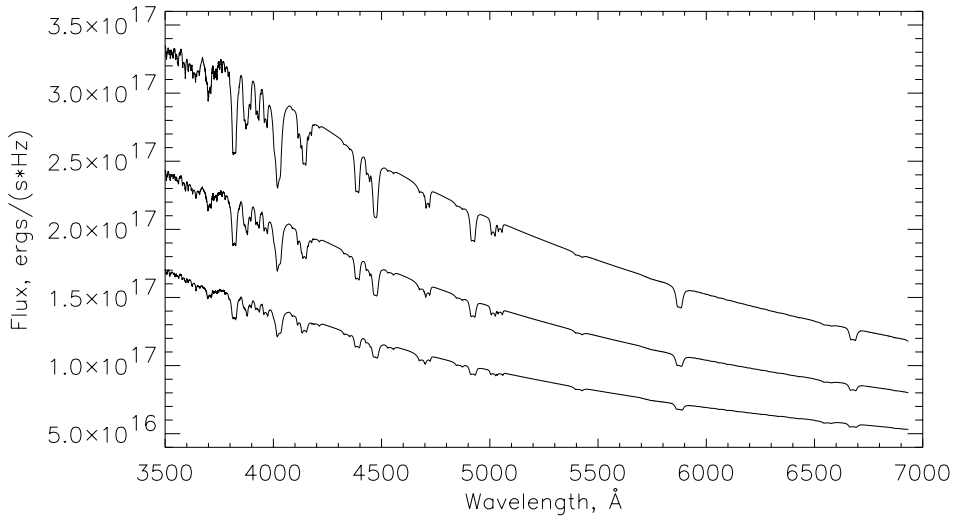

Figure 5.36: The influence of the outer radius on the continuum of the NLTE pure helium accretion disc spectra. The parameters used for these models are $\dot{M} = 4 \times 10^{-9} M_{\odot}$/yr, $M_1 = 1.1 M_{\odot}, R_{in} = 1.4 R_1$, and $i = 20^{\circ}$ while the outer radius is from the top 15, 11 and $8 R_1$.

5.7.6 Outer radius of the disc

We have studied the influence of the outer radius variations on the disc spectra, where we varied R_{out} between 8, 11 and $15 R_1$ while the inner radius at $1.4 R_1$ remain unchanged like the rest of the system parameters. Fig. 5.36 shows that the slopes of the spectra become steeper with smaller R_{out} due to the higher flux received from the hot smaller discs compared a cooler discs with a larger surface area. As in the R_{in} variations case, the lines become slightly deeper and with a narrower core with bigger R_{out} as in Fig. 5.37. This is because of adding the outer cold rings with larger surface areas and less effective temperatures, and lines less affected by Keplerian broadening. We also studied the effect of the outer radius variations on the line structure of the spectra of the pure helium accretion disc model, we found that the effect is almost similar to the $\dot{M}$ case, but very little changes in the structure of the line can be noticed in such case as seen in Fig. 5.38 when compared to the case of $\dot{M}$ variations.

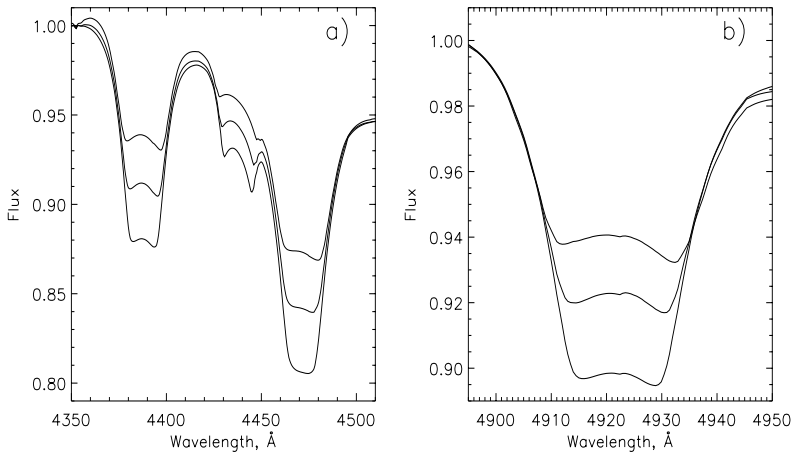

Figure 5.37: The influence of the outer radius variation on the line profile of the NLTE pure helium accretion disc spectra. The parameters used for these models are $\dot{M} = 4 \times 10^{-9} M_{\odot}/\mathrm{yr}$, $M_1 = 1.1 M_{\odot}, R_{in} = 1.4 R_1$, and $i = 20^{\circ}$ while the outer radius from the top $8, 11$ and $15 R_1$. The flux is normalised to 1.0 at the left upper corner.

5.8 Departures from LTE

For more than two decades computing NLTE model stellar atmosphere, it has been demonstrated that NLTE effects play an important, even crucial role in atmospheres of virtually all types of hot stars (effective temperature around 10 000 K and hotter), for a summary see (Mihalas 1978; Kudritzki & Hummer 1990; Crivellari et al. 1991).

We have studied the effect of the LTE and NLTE treatment on the continuua and the line profiles of the pure helium disc spectra, and we found that the overall shape of the LTE and NLTE continua are very similar as seen in Fig. 5.39 while the He I lines, which are always in absorption in our models, are weaker in the NLTE compared to the LTE case, as can be seen in Fig. 5.40. Generally speaking the reason can be as follows: In the LTE case the source function S_ν is equal to the Planck function B_ν, which means the occupation numbers can be described by the Boltzmann formula for the kinetic temperature. This condition can be valid specially in the case of lower temperatures. On the other hand at higher effective temperature, $S_\nu > B_\nu$, there is a breakdown in the validity of the LTE approximation, and so, the LTE assumption, however, fails to take into account the relative temperature dependence of the radiative and collisional rates. The importance of NLTE effects is a reflection of the relative importance of these two kinds of processes. Roughly speaking, the

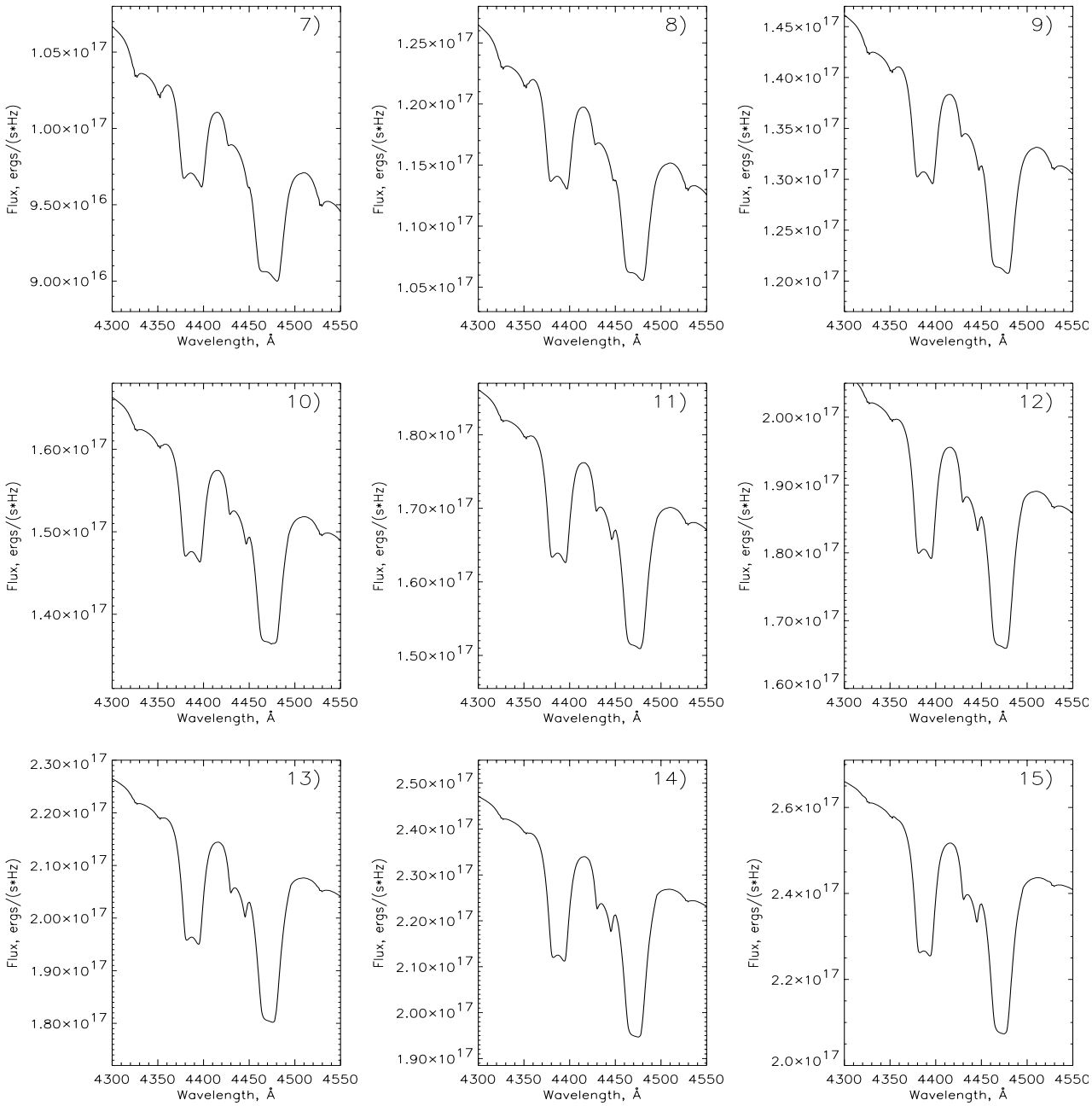

Figure 5.38: The influence of the outer radius variation on the structure of the line profile of the pure helium accretion disc spectra. The parameters used for these models are $\dot{M} = 4 \times 10^{-9} M_{\odot}/\mathrm{yr}$, $M_1 = 1.1 M_{\odot}, R_{in} = 1.4 R_1, i = 15^{\circ}$ while the outer radius varies from (7-15 R_1) as see at the upper right corner of each panel.

upward collisional rates depend on temperature as $T^{1/2}\exp(-E_{ij}/kT)$ where E_{ij} is the energy separation between the two levels i and j. At high temperatures, $kT > E_{ij}$ for the excited states of He; thus, the collisional rates become a very weak functions of temperature. On the other hand the continuum radiative rates, however become a strong functions of temperature. Thus, with rising effective temperature the continuum radiative rates become the dominant terms in the rate equations, and in such case the temperature in the atmosphere is not described by the kinetic temperature anymore and it becomes so much higher. This means that the level populations are described differently from the LTE case.

We found that the equivalent width of He I lines in the NLTE case increase with decreasing mass accretion rate, which means with decreasing temperature and become comparable to the equivalent width of the LTE lines at low temperatures. We expect that the He I lines may become even deeper in the NLTE than in the LTE case at very low temperatures, as obtained for the O stars by Auer & Mihalas (1971). This was impossible to prove in our case, because at lower average temperature than presented in table (5.1), the test models did not converge because they were convectively unstable due to low T_{eff}, and the current version of TLUSDISK does not treat convection properly. In order to get an idea of the difference in lines for models computed with LTE and NLTE, we have for a model grid calculated the difference in equivalent width of the He I line at 4388 Å . Denoting the line equivalent width in the LTE and NLTE case as W_{LTE} and W_{NLTE}, respectively, we can define the relative difference between the two quantities as:

$$\delta_{EW} = \mid \frac{W_{LTE} - W_{NLTE}}{W_{NLTE}} \mid \tag{5.40}$$

Based on the value of δ_{EW}, we may explore differences between LTE and NLTE in any parameter space as seen in Fig. 5.41 to Fig. 5.45, where contour lines correspond to the appropriate values of δ_{EW} of the converged models, while shaded areas show the parameter space where the test models did not converge, most likely because they were convectively unstable due to low T_{eff}.

From such figures we conclude that the difference in equivalent width for the line selected, can vary from less than 10 percent to more than 40 percent between LTE and NLTE models. We also conclude that disc models with pure helium composition must be treated as NLTE, in order to avoid discrepancies from 0.1 up to 0.4 in line equivalent width which may arise from LTE only considerations.

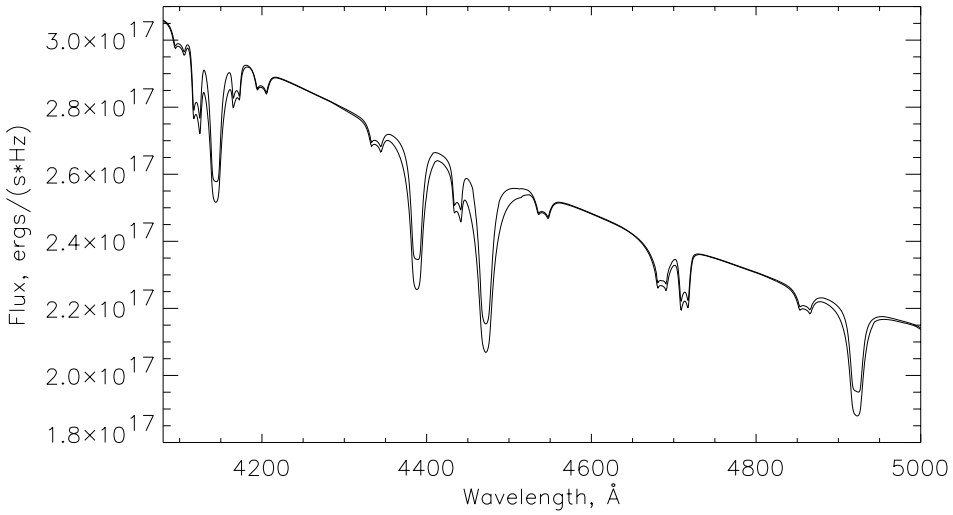

Figure 5.39: The influence of the LTE and NLTE consideration on the continuum of the pure helium accretion disc spectra. Upper and lower lines represent the NLTE and LTE models respectively. The parameters used for these models are $\dot{M} = 6 \times 10^{-9} M_\odot/\mathrm{yr}$, $M_1 = 1.2 M_\odot, R_{in} = 1.4 R_1, R_{out} = 15 R_1$, and $i = 10°$.

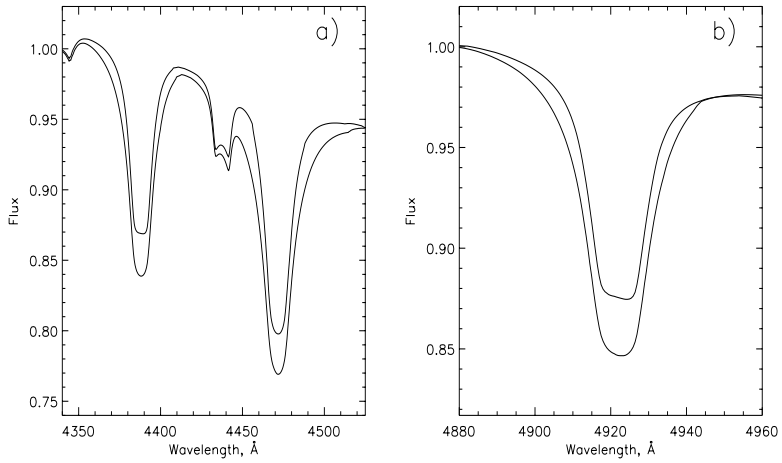

Figure 5.40: The influence of the LTE and NLTE consideration on the line profile of the pure helium accretion disc spectra. Upper and lower lines represent the NLTE and LTE models respectively. The parameters used for these models are $\dot{M} = 6 \times 10^{-9} M_\odot/\mathrm{yr}$, $M_1 = 1.2 M_\odot, R_{in} = 1.4 R_1, R_{out} = 15 R_1$, and $i = 10°$, normalised to 1.0 at the left upper corner.

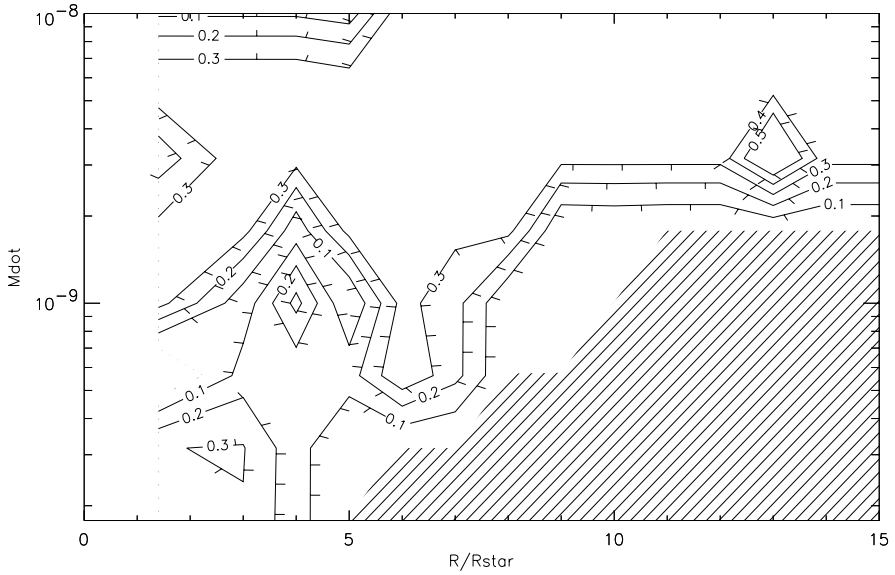

Figure 5.41: Relative difference between the line equivalent width of the He I line at λ 4388 Å for LTE and NLTE calculations as a function of $\dot{M}$ and R.

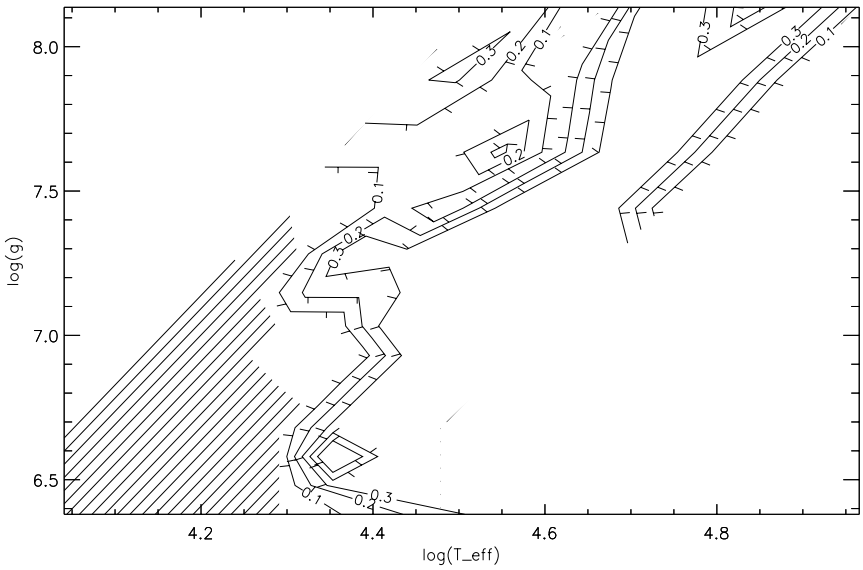

Figure 5.42: Relative difference between the line equivalent width of the He I line at λ 4388 Å for LTE and NLTE calculations as a function of $\log(g)$ and $\log(T_{eff})$.

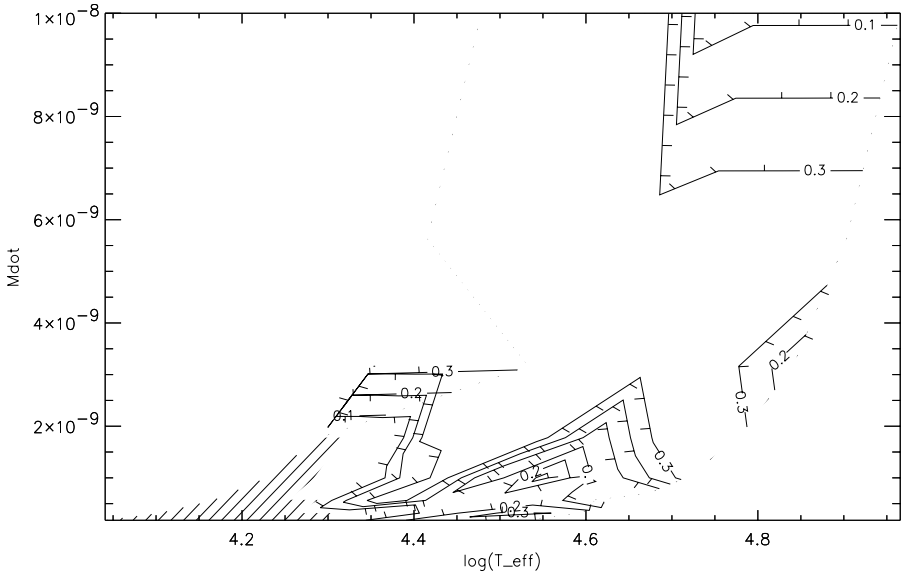

Figure 5.43: Relative difference between the line equivalent width of the He I line at λ 4388 Å for LTE and NLTE calculations as a function of $\dot{M}$ and $\log(T_{eff})$.

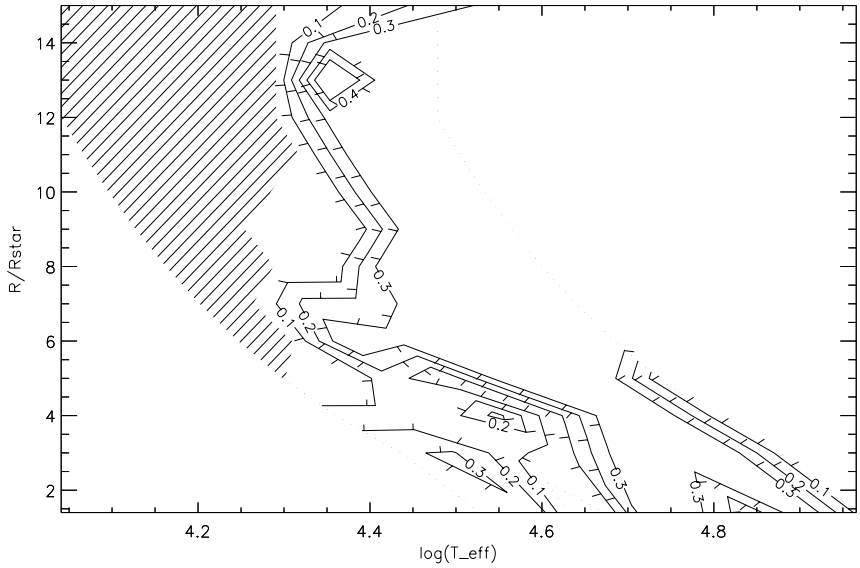

Figure 5.44: Relative difference between the line equivalent width of the He I line at λ 4388 Å for LTE and NLTE calculations as a function of R and $\log(T_{eff})$.

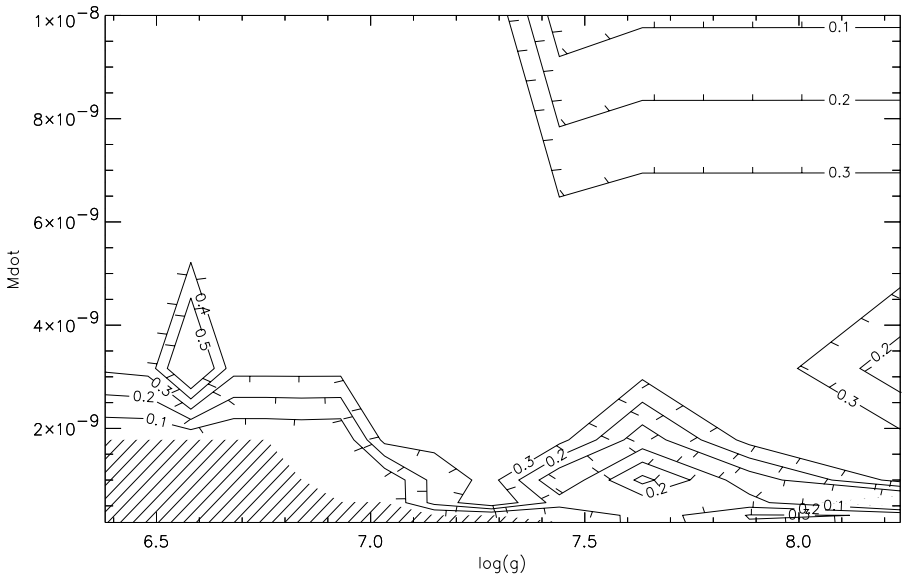

Figure 5.45: Relative difference between the line equivalent width of the He I line at λ 4388 Å for LTE and NLTE calculations as a function of $\dot{M}$ and $\log(g)$.

5.9 Summary

In this chapter we mainly discussed the effects of some of the disc parameters on both the line profiles and the continua of the pure helium accretion disc spectra. Our concern was to focus on the effect of such parameters on the slope of the continuum and the width and depth of the lines. We have seen that some of the parameters have a significant effect on the slop of the continuua and less effect on the lines, such as the mass accretion rate and the inner and outer radius of the disc. The opposite was found in the case of the angle of inclination variations, where the lines were seriously influenced compared to the continuua. The determination of the hydrogen abundance with respect to helium in the AM CVn accretion discs found to be H/He=10^{-5} by number, came as a breakthrough in the history of the systems. Departures from LTE were also investigated in order to assess the necessity of computing NLTE models. Differences between the predicted LTE and NLTE equivalent widths of helium lines varied between 10 to 40%, a non-trivial value which demonstrates that NLTE effects are important and must be taken into account in accurate analysis of the observed spectra of the AM CVn systems. In the the next chapter we will use such theoretical investigations as a base to fit the observed spectra of the AM CVn systems taken with the Nordic Optical Telescope.

Chapter 6

Fitting of observations with NLTE pure helium models

6.1 Introduction

The only way to test the efficiency of our theoretical models, is by fitting it to the observations. In this chapter we fit the pure helium accretion disc models to the observed optical spectra of four of the AM CVn systems. These spectra were obtained in three different years: starting with 1997, 1999 and 2001. We will see in the next sections that the 1997 observations gave us a solid base to understand the accretion disc of the AM CVn systems, while the 1999 and 2001 observations were intended to complete the whole picture of the systems parameters, and to build a global understanding to the helium discs of the AM CVn family members.

6.2 The 1997 observations

In this section we fit only the pure helium accretion disc models to the observed spectra of the AM CVn systems, conducted at the Nordic Optical Telescope in 1997. In the next subsections we will discuss the best fit to each system separately, and discuss for one system (V803 Cen) the reasons for obtaining these good fits. We will also discuss possible errors in our results. Table 6.1 includes the observed and predicted values for some of the parameters of the AM CVn systems (Warner 1995b; Tsugawa & Osaki 1997; Nelemans et al. 2001a; Nasser et al. 2001).

Table 6.1: The list of parameters for some of AM CVn systems.

Object Name	P_{orb} (s)	*Mass Ratio* M_2/M_1	M_1 $M_\odot$	*Disc Size* R_1
AM CVn	1028.27	0.084	1.1	15
HP Lib	1119	≥ 0.075	> 1.13	$(15-18)$
CR Boo	1471	0.057	1.035	$(10-17)$
V803 Cen	1611	≤ 0.043	< 1.2	$(15-27)$

6.2.1 V803 Cen

V803 Cen was discovered by Elvius (1975) to be an unusually blue object in which the spectrum shows only broad, shallow absorption lines of He I with complete absence of H lines. The He I features were found to vary strongly, fading to invisibility at times. It was classified as a rapid variable with a dominating period of 1611 s with a complex harmonic structure and a member of the AM CVn family by O'Donoghue et al. (1987). Fig. 6.1 shows the combination of parameters of the NLTE model which gives the best fit by the eye to the observed spectrum 'gc030014' of V803 Cen. The values of the parameters are $M_1 = 1.2M_\odot, \dot{M} = 3 \times 10^{-9} M_\odot/\mathrm{yr}, R_{in} = 1.4R_1, R_{out} = 17R_1$ and $i = 5^\circ$. The fit obtained with these values indicates that the distance of V803 Cen from the Earth is ≈ 405 pc if we assume the absence of interstellar absorption.

This is not the only set of parameters which can give a fit similar to the one in Fig. 6.1, other combinations of parameters can also give a fit which is close to this one. We found that by varying one parameter such as the mass accretion rate $\dot{M}$ within the range of $(3-5) \times 10^{-9} M_\odot/\mathrm{yr}$ as seen in Fig. 6.2 we get a similar but not a better fit than the one presented in Fig. 6.1. The same was noticed when we vary the angle of inclination and the size of the disc as seen in both Fig. 6.3 and Fig. 6.4 respectively. Changing one of these parameters only and leaving the rest fixed, will absolutely not give a better fit than the one presented in Fig. 6.1, but changing two or even may be three parameters at the same time might give a comparable fit to the one in Fig. 6.1. After this conclusion we found that, we can get a similar fit to the one obtained in Fig. 6.1 only if we change the parameters within the following ranges, $\dot{M} = (4 \pm 1) \times 10^{-9} M_\odot/\mathrm{yr}$, $R_{out} = (17 \pm 3)R_1$ and $i = 5^\circ \pm 3^\circ$ while the mass of the central star being fixed at 1.2 $M_\odot$. From these possible variations we

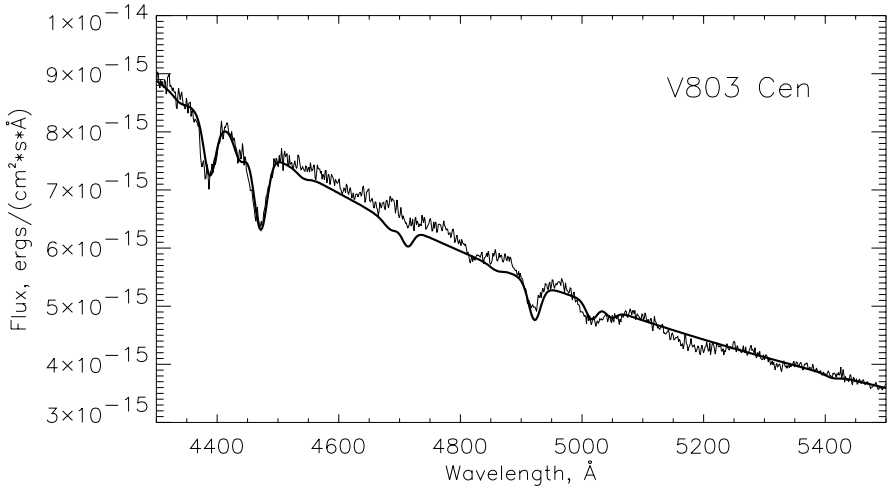

Figure 6.1: The best NLTE model (solid line) which fits the observed spectrum 'gc030014' (thick line) of V803 Cen with parameters $M_1 = 1.2M_\odot, \dot{M} = 3 \times 10^{-9} M_\odot$/yr, $R_{in} = 1.4R_1, R_{out} = 17R_1, i = 5^\circ$ and d=405 pc.

found that the distance to V803 Cen can vary within the range of 405 $\pm$ 50 pc if no interstellar absorption is assumed.

From such combinations of parameters for this system, we conclude that the size of the accretion disc of V803 Cen was (15-20) R_1 at the time of observations, which means the disc was within the range of the circularization and the tidal radius. We also found that the fit which we obtained for the disc size is closer to the circularization radius than the tidal radius, which confirm what has been found during the observation that the system was stable or may be towards a rising phase. More well flux calibrated spectra is certainly needed to study the system instability in more detail.

The excess of flux in the spectrum of V803 Cen between λ4500-4800Å might be due to the flux reflected from the secondary object or some dynamical effects in the disc such as shocks and flares. Such behavior can not be predicted, which is also part of the system's instability. This might be the reason for the lack of fit to the He I line at λ 4713Å, because our models are assumed to be stationary 'steady state' with no consideration to any dynamical effects.

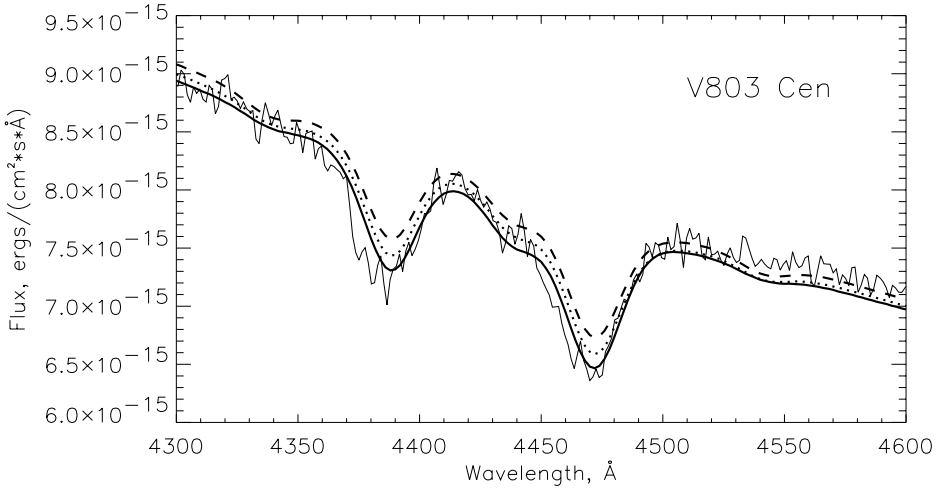

Figure 6.2: The possible variations of the mass accretion rate, which can also give a satisfactory fit to the spectrum 'gc030014' compared to the one presented in Fig. 6.1, with the rest of the system parameters being fixed. Dashed, dotted and solid lines represent the model spectra with the mass accretion rate of 5, 4 and $3 \times 10^{-9} M_{\odot}$/yr respectively, when they are normalised at λ 5500 Å.

6.2.2 CR Boo

CR Boo (= PG 1346-082) is a blue star classified as an AM CVn object by Wood et al. (1987) who presented spectroscopy and high-speed photometry and demonstrated that the star is a short-period cataclysmic binary in which the mass transferred through the accretion disc was predominantly helium rather than hydrogen. A WET campaign identified a coherent period of 1471 s, which is most likely the orbital period (Provencal et al. 1997).

Fig. 6.5 shows the NLTE model which best fits the observed spectrum 'gc040020' of CR Boo when the system was in the state of rising brightness, other possible similar fits can be obtained within the following range of parameters : $\dot{M} = (4 \pm 1) \times 10^{-9} M_{\odot}$/yr, $R_{out} = (15 \pm 2) R_1$ and $i = (30^{\circ} \pm 3^{\circ})$ with the mass of the central star being fixed at $1.0 M_{\odot}$ and $R_{in} = 1.4 R_1$. The fit obtained with these values indicates that the distance of CR Boo from the Earth is 469 ± 50 pc if no interstellar absorption is assumed. The excess of the flux in the region λ4550–5200Å may be due to flux reflected from the secondary object or due to some dynamical effects like shocks or flares. The best fit is obtained with the disc radius of $\approx 15 R_1$ which indicates that, at the time of the observations, the disc radius was closer to the tidal

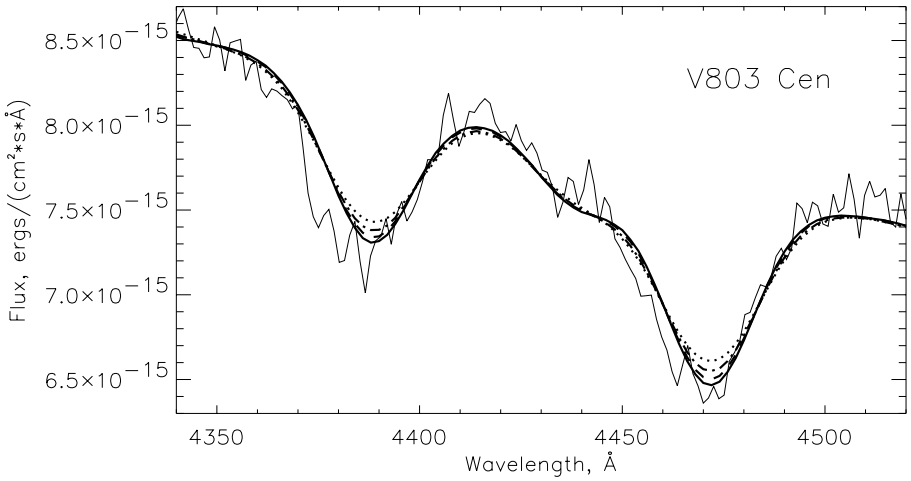

Figure 6.3: The possible variations of the angle of inclination, which can also give a satisfactory fit to the spectrum 'gc030014' compared to the one presented in Fig. 6.1, with the rest of the system parameters being fixed. Dotted, dashed dotted, dashed and solid lines represent the model spectra with the angle of inclination of $15°, 11°, 8°$ and $5°$ respectively, when they are normalised at λ 5500 Å.

radius than the critical radius. This means that at the time of the observation, the system was in a rising state.

6.2.3 HP Lib

This star was identified as an AM CVn star by O'Donoghue et al. (1994). Its fundamental period found to be 1119 s is close to the fundamental period of AM CVn itself, and its lack of change, in addition to a spectrum with similar broad absorption features, indicate that this is also an object stuck in its high state. A superhump period is not yet detected (Aminzade et al. 1999).

Fig. 6.6 shows the pure helium NLTE model which best fits the observed spectrum 'gc030024' of HP Lib. Other combinations of parameters which give similar fits are: $\dot{M} = (4 \pm 1) \times 10^{-9} M_{\odot}$/yr, $R_{out} = (14 \pm 3) R_1, i = (28° \pm 3°)$, with the mass of the central star being fixed at $1.1 M_{\odot}$ and $R_{in} = 1.4 R_1$. The fits obtained with these values indicate that the distance to HP Lib is 188± 50 pc if no interstellar absorption is assumed. The lack of fit at λ 4713Å can be due to the same reasons discussed before for CR Boo and V803 Cen for the same case.

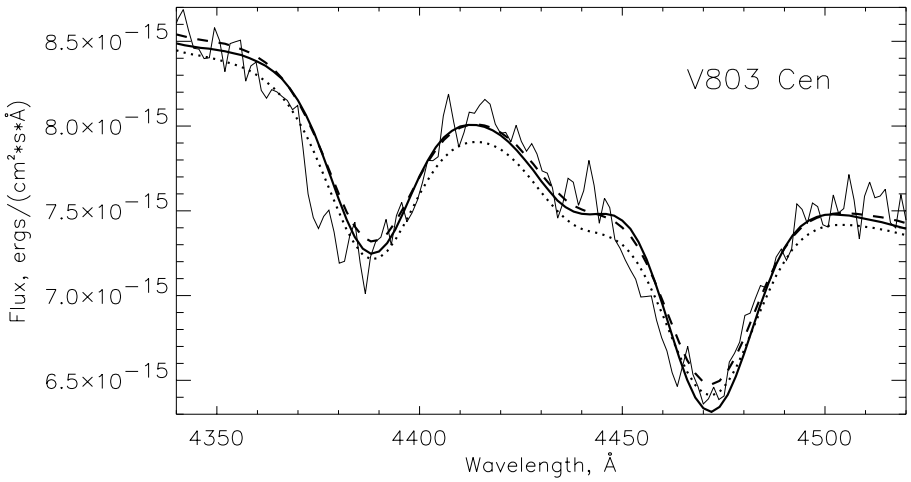

Figure 6.4: The possible variations of the disc outer radius, which can also give a satisfactory fit to the spectrum 'gc030014' compared to the one presented in Fig. 6.1, with the rest of the system parameters being fixed. Dashed, solid and dotted lines represent the model spectra with the disc outer radius of 15, 17 and $19R_1$ respectively, when they are normalised at λ 5500 Å.

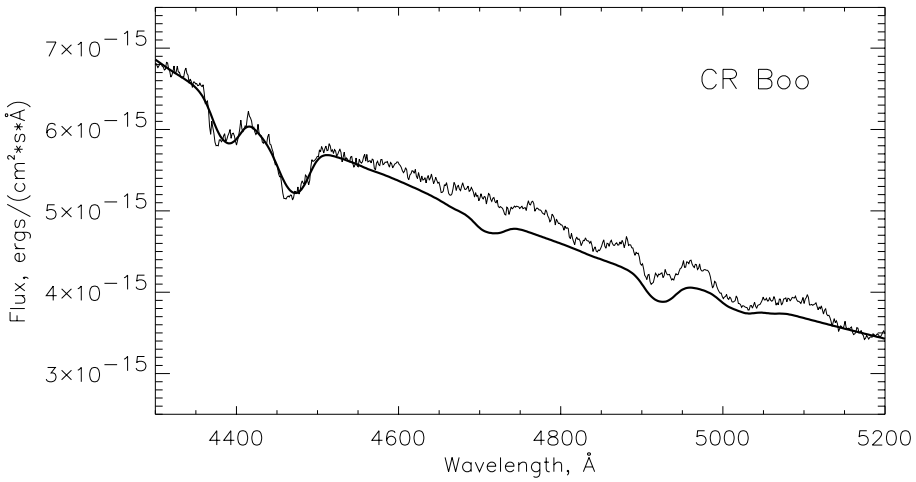

Figure 6.5: The best NLTE model (solid line) which fits the observed spectrum 'gc040020' (thick line) of CR Boo with parameters expected: $M_1 = 1.0M_\odot, \dot{M} = 4 \times 10^{-9} M_\odot/\mathrm{yr}, R_{in} = 1.4R_1, R_{out} = 15R_1, i = 30^\circ$ and d=469 pc.

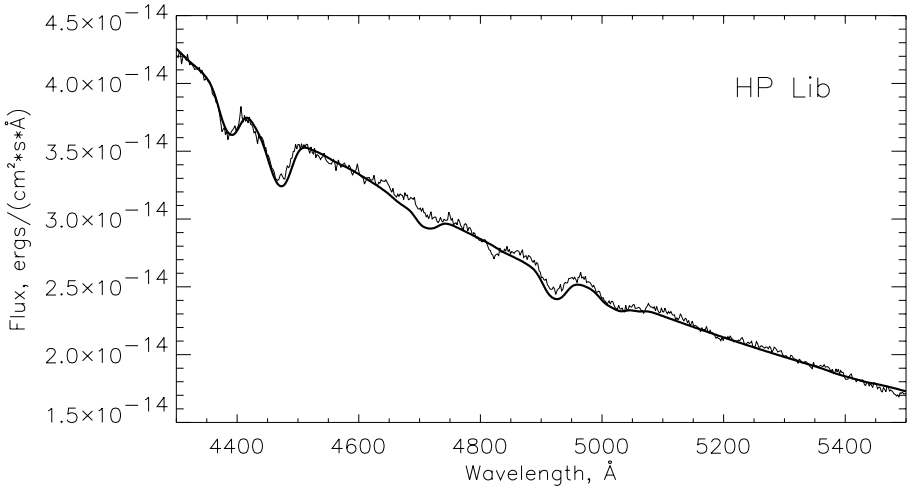

Figure 6.6: The best NLTE model (solid line) which fits the observed spectrum 'gc030024' (thick line) of HP Lib with parameters: $M_1 = 1.1 M_\odot, \dot{M} = 4 \times 10^{-9} M_\odot$/yr,$R_{in} = 1.4 R_1, R_{out} = 14 R_1, i = 28^\circ$ and d=188 pc.

6.2.4 AM CVn

AM CVn was found to have broad, shallow absorption He I lines and no traces of hydrogen, and was first classified as a DB white dwarf (Greenstein & Matthews 1957). Five years later photometric variability with a period of 17.5 min was discovered, Smak (1967) and Paczyński (1967) suggested that it could be a semi-detached pair of degenerate objects in which mass transfer is driven by loss of angular momentum due to gravitational wave radiation. Flickering, which is typical for cataclysmic variables was found by Warner & Robinson (1972), and this inspired Faulkner, Flannery & Warner (1972) to propose the double-degenerate white dwarf model, which has been the main accepted explanation for the AM CVn systems since then. The dominant photometric period is 525 s, which is a first harmonic of the fundamental period of 1051s (Solheim et al. 1998). A precession period of 13.38 hr is detected by Patterson et al. (1993). Doppler tomography has established 1028.73 s as the binary period (Nelemans et al. 2001b).

Fig. 6.7 shows the NLTE pure helium model which best fits the observed spectrum 'gc010043' of the AM CVn system. Other possible combinations of parameters which can also give a possible fit are: $\dot{M} = (3 \pm 1) \times 10^{-9} M_\odot$/yr, $R_{out} = (15 \pm 2) R_1$ and $i = 45^\circ \pm 3^\circ$, with the mass of the central star being fixed at $1.1 M_\odot$ and $R_{in} = 1.4 R_1$. The fit obtained with these values indicates that the distance to the AM CVn system

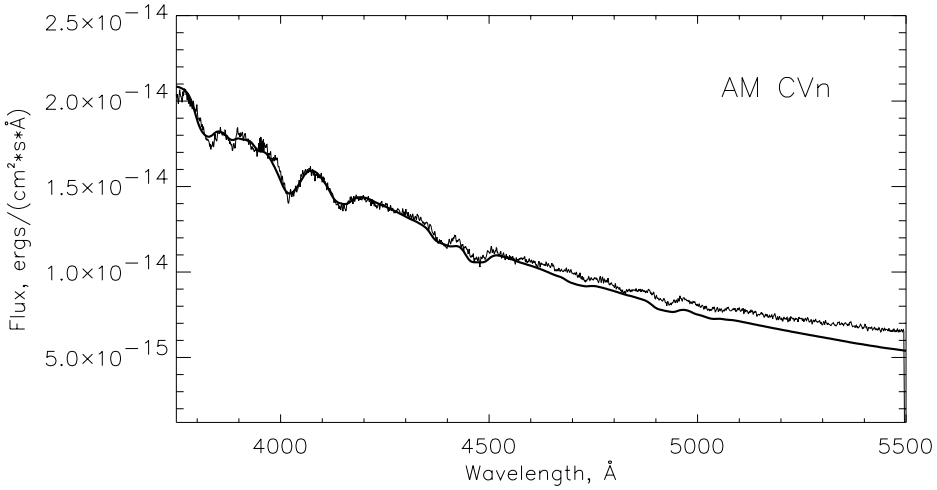

Figure 6.7: The best NLTE model (solid line) which fits the observed spectrum 'gc010043' (thick line) of AM CVn with parameters expected for the system to be $M_1 = 1.1M_\odot, \dot{M} = 3 \times 10^{-9} M_\odot/yr, R_{in} = 1.4R_1, R_{out} = 15R_1, i = 45°$ and $d = 288$pc.

is 288 $\pm$ 50 pc if no interstellar absorption assumed. This distance is close to the distance determined from the trigonometric parallax of the U.S. Naval Observatory; (235 $\pm$ 26)pc (Dahn, private communication). The model fits the observed spectrum well in the region $\lambda\lambda$(3700-4800) Å while it diverges gradually when approaching the IR part. This means that a source of energy with a temperature 7 000-10 000 K may be present. The secondary star with mass $\sim 0.084M_\odot$ is the only source of energy which may contribute in this region of the spectrum of AM CVn. The contribution from the secondary star has never been definitely detected, although indications of its presence have been found in the spectrum. The secondary star is believed to be sub-luminous, maybe only a few hundreds of K effective temperature (Savonije et al. 1986), but must be irradiated to a much higher temperature (Nymark & Solheim, 1995) because of its closeness to the central white dwarf and the disc.

Since our disc spectra are quite close to blackbody disc spectra, we used the blackbody-disc spectra calculations to find as a first approximation, the temperature of the secondary star in the AM CVn system. We constructed a spectrum consisting of a primary star surrounded by a disc of $15R_1$ having the same values of parameters, as used to fit the observed spectrum of the AM CVn in Fig. 6.7. We compared this with the IUE spectrum of Solheim (1992) as shown in Fig. 6.8 extended to the optical and IR regions by U, B, V, R and I photometric points (Massacand &

Solheim 1995) which represents the most complete wavelength coverage published up to date of the AM CVn system.

In Fig. 6.8 dotted lines show the flux of a set of rings forming the disc. Dashed-dotted line shows the spectrum of the central star with temperature of 1.0×10^5K, while the upper two dashed lines represent from the bottom the total disc spectrum and the spectrum of both the disc and the white dwarf, respectively. The squares in the figure are the photometric points. In the figure it is easy to see that the disc spectrum does not fit the observed spectrum in the UV and in the IR parts. This confirms the need for adding a hot (central) star to fit the UV part, and a secondary star in the IR part.

We have added the flux of the secondary star of a Roche lobe radius, to the spectra of both the disc and the central star, with the same values of parameters stated under Fig. 6.8, and we found that the best fit in the IR part to the total spectrum can be found with $T_{eff} = 10\,000$ K for the secondary star as seen in Fig. 6.9. In this figure the dotted line represents the flux of the secondary star with T_{eff} =10 000 K while the dark solid line represents the flux of the central star with $T_{eff} = 1.0 \times 10^5$ K. The dashed line represents the combined flux of both the central star and the secondary star. The lower dashed-dotted line represents the flux of the disc while the upper dashed-dotted line represents the total combined flux of the central star, the accretion disc, and the secondary star fitted with the observed spectrum of the system and the photometric points.

The T_{eff} we obtained for the secondary star is close to the T_{eff} obtained by Nymark & Solheim (1995) but different for the central star. They obtained $T_{eff} = 1.5 \times 10^5$K for the central star and $T_{eff} = 12\,000$K for the secondary, because they have used different values for the physical parameters of the disc like $\dot{M} = 1 \times 10^{-9} M_\odot$, $i = 40^\circ$ with disc size of $\approx 15 R_1$ and a distance of 125 pc while we used the values presented under Fig. 6.7. The present results for the parameters of the secondary star are only preliminary. If the object is substantially irradiated by the primary star and by the disc, there would be a wide distribution of T_{eff} over the stellar surface. The spectrum of the secondary star may thus be quite different from the single black-body flux distribution.

6.3 The 1999 observations

In March 1999, we were scheduled to observe the AM CVn systems for three nights at the Nordic Optical Telescope, using the spectrograph 'ALFOSC'. We had a clear weather only in the last night of observations, but unfortunately a small mistake occurred in choosing the proper combinations of grisms and slits. This mistake

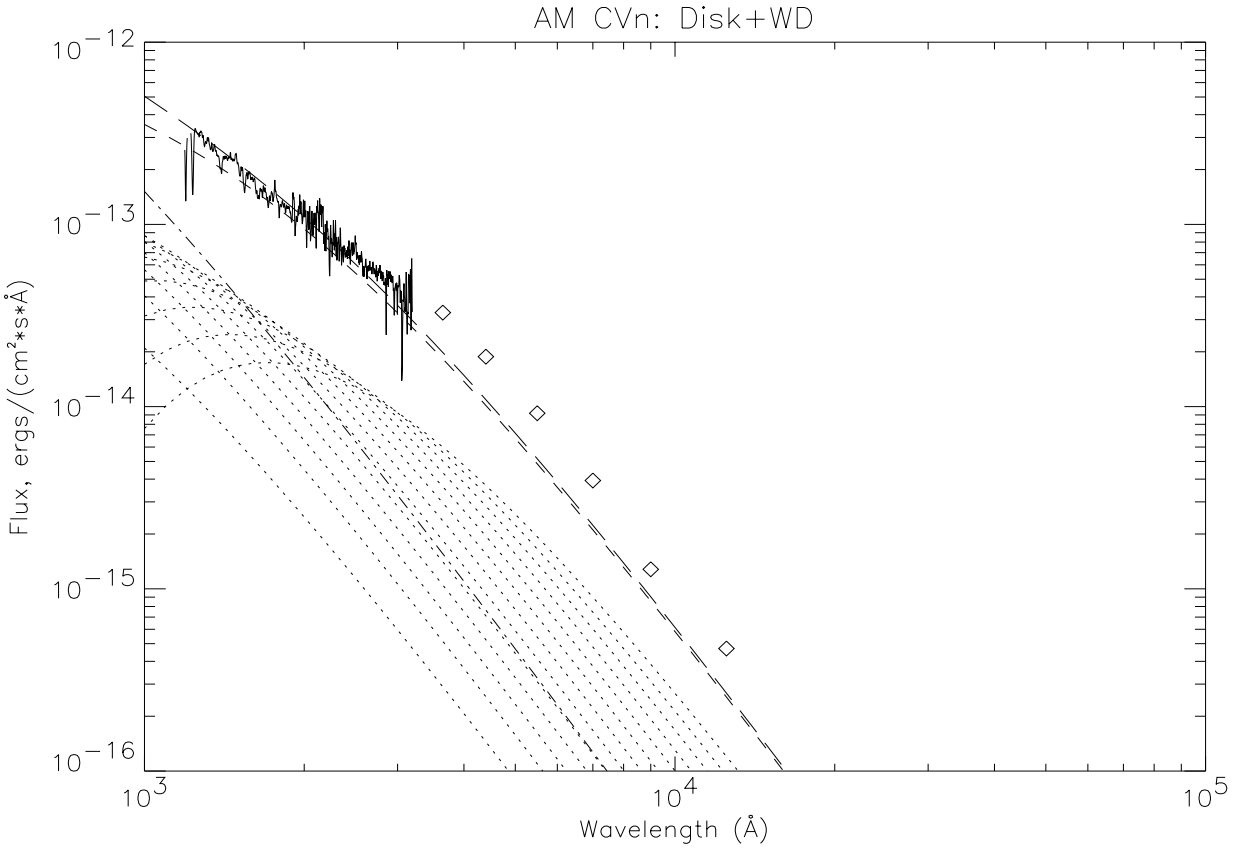

Figure 6.8: The best model (upper dashed line) of the "disc + the central star" which fits the observed IUE spectrum and photometric observations (thick line + squares) of AM CVn with parameters: $M_1 = 1.1 M_\odot, \dot{M} = 3 \times 10^{-9} M_\odot$/yr,$R_{in} = 1.4 R_1, R_{out} = 15 R_1, i = 45^\circ$ and the $T_{eff} = 1 \times 10^5$ K for the central star. The other lines are explained in the text.

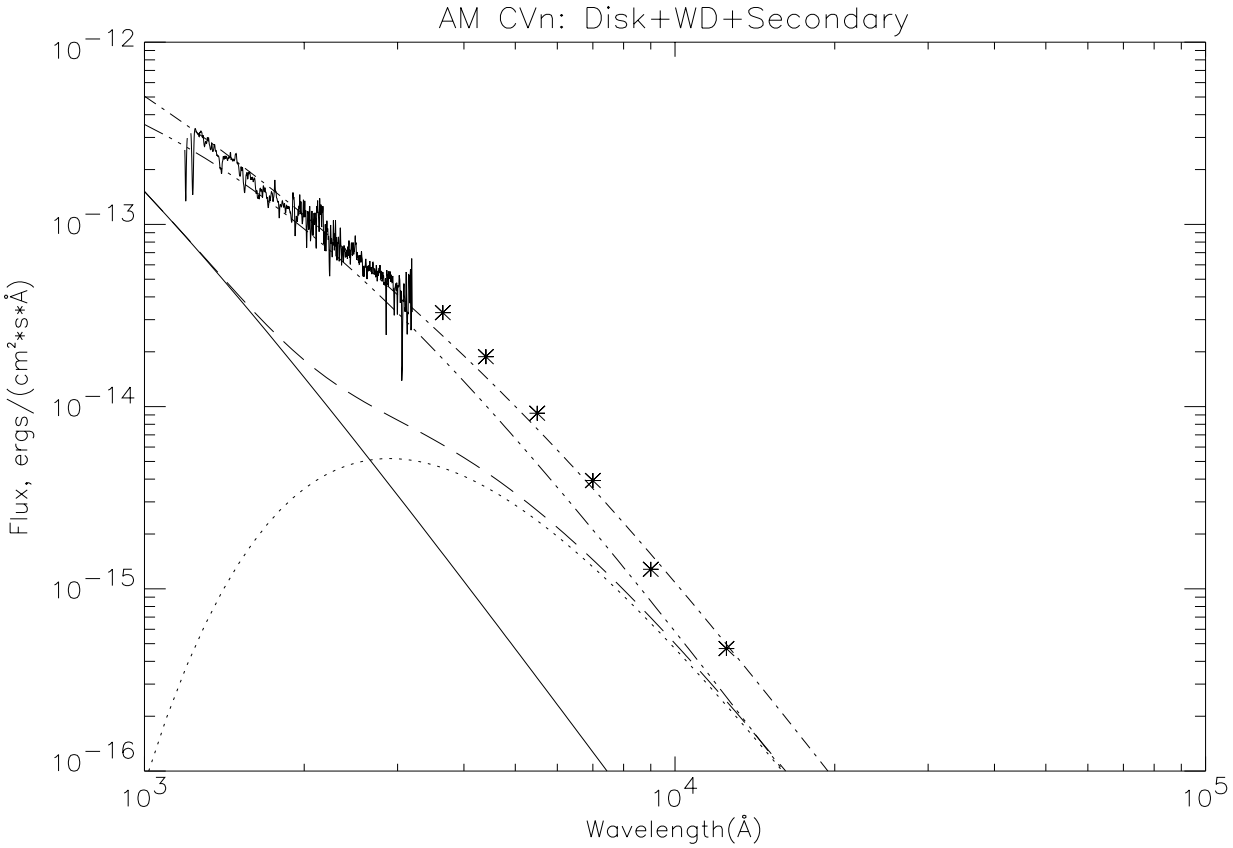

Figure 6.9: The best model (upper dashed dotted line) which fits the observed IUE spectrum (thick lines + stars) of AM CVn with parameters expected for the system to be $M_1 = 1.1 M_\odot, \dot{M} = 3 \times 10^{-9} M_\odot$/yr, $R_{in} = 1.4 R_1, R_{out} = 15 R_1, i = 45°, d = 288$ pc, T_{eff} =10 000K for the secondary star while for the central star $T_{eff} = 1.0 \times 10^5$ K. The rest of the lines are explained in the text.

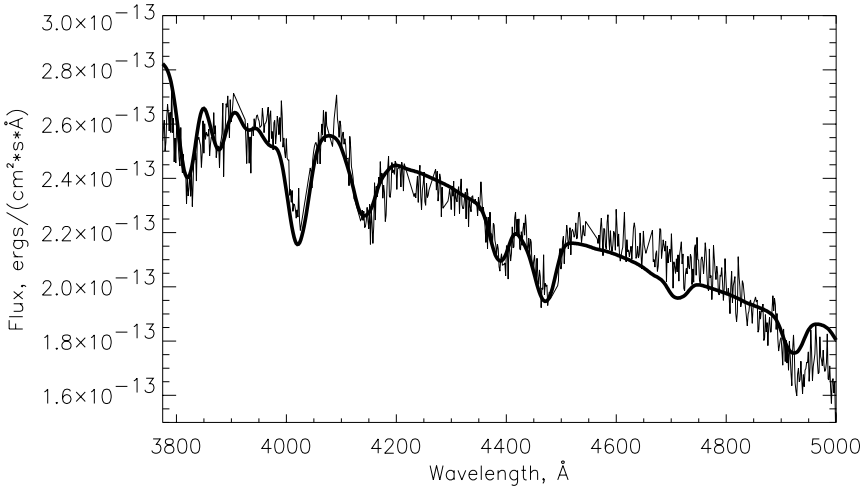

Figure 6.10: The best NLTE model (solid line) which fits the observed non-well flux calibrated spectrum taken in 1999 (thick line) of CR Boo with parameters expected: $M_1 = 1.0 M_\odot, \dot{M} = 1 \times 10^{-9} M_\odot/\mathrm{yr}, R_{in} = 1.4 R_1, R_{out} = 11 R_1$ and $i = 30°$.

made a major damage to the flat-field frames, which made the observed data become useless and impossible to reduce. Although we knew that the output of the reduction process will be far from being scientific, we reduced part of the data without using flat-field frames. This produced a relatively flux-calibrated spectrum which can be fitted with the model. Fig. 6.10 shows the best model which is fitted to the best relatively flux calibrated spectrum of CR Boo with parameters $M_1 = 1.0 M_\odot, \dot{M} = 1 \times 10^{-9} M_\odot/\mathrm{yr}, R_{in} = 1.4 R_1, R_{out} = 11 R_1$ and $i = 30°$. This was the only spectrum which seemed to be good enough to be presented in this thesis work. Fig. 6.11 and Fig. 6.12 represent a high resolution non-flux calibrated spectrum of the AM CVn system taken with the WHT at La-Palama. This spectrum has been given to us by Nelemans in (2001) to fit it with a higher resolution model. To fit our models to the spectrum, we had to divide it into two regions of about 200 Å because the spectrum is not flux calibrated. We obtained the best fit with the set of parameters stated under the two figures.

6.4 The 2001 observations

The need for a new observing campaign for both V803 Cen and CR Boo came after the results published by Nasser, Solheim and Semionoff (2001), hereinafter NSS,

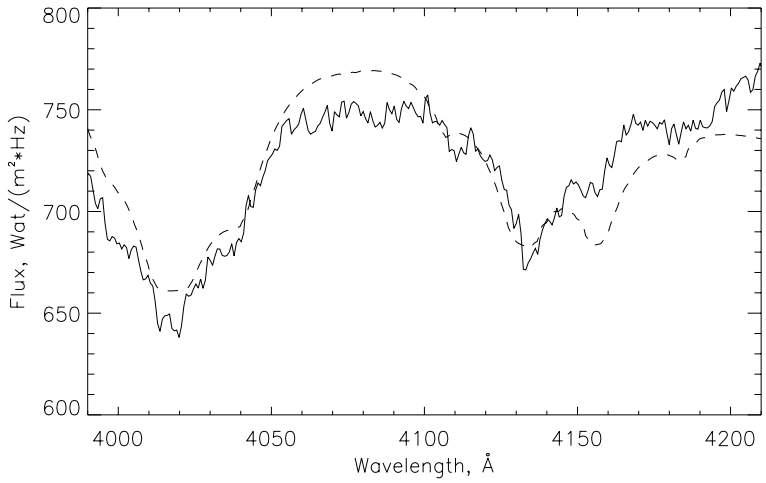

Figure 6.11: The best NLTE model (dashed line) which fits the observed spectrum (thin line) of AM CVn taken with the WHT (Nelemans 2001b), with parameters expected for the system to be $M_1 = 1.1 M_\odot, \dot{M} = 3 \times 10^{-9} M_\odot/yr, R_{in} = 1.4 R_1, R_{out} = 15 R_1, i = 45°$.

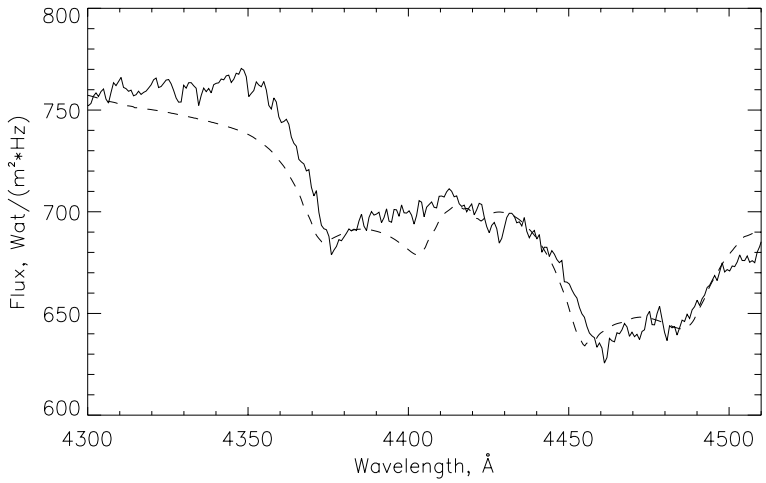

Figure 6.12: The best NLTE model (dashed line) which fits the observed spectrum (thin line) of AM CVn taken with the WHT (Nelemans 2001b), with parameters expected for the system to be $M_1 = 1.1 M_\odot, \dot{M} = 3 \times 10^{-9} M_\odot/yr, R_{in} = 1.4 R_1, R_{out} = 15 R_1, i = 45°$.

and also after our misfortune in the 1999 observations. In the work by NSS, a wide range of parameters has been determined for the AM CVn family members, such as $\dot{M}, i, R_{in}$ and R_{out}. The two very important parameters which has also been determined are both the abundance of elements in the disc and the distance to the systems. One parameter which is $\dot{M}$ has been determined with a certain accuracy for both systems AM CVn and HP Lib, which represents the todays accepted mass accretion rate for such systems. The reason is because they are both stuck in the high state, and their mass accretion rates is almost constant, and do not vary with time. On the other hand the mass accretion rate found for both V803 Cen and CR Boo, cannot really describe the final average value of $\dot{M}$, due to their instability. We expect that such systems have different mass accretion rates, which correspond to different magnitudes of the systems. We also think that there might be a relation between the variable mass accretion rate of the systems and their variable magnitude. The disc luminosity $L = \sigma T_{eff}^4$, is the fact we used to determine the relation between the mass accretion rate in the disc (which is also proportional to T_{eff}^4 from equation(5.37)) and its variable magnitude, using the following relation:

$$\triangle m = -2.5 \log \frac{\dot{M}_1}{\dot{M}_2} \tag{6.1}$$

where $\triangle m = m2 - m1$, where m_1 and m_2 are the lower and higher magnitudes respectively. The use of equation (6.1) is based on the blackbody accretion disc spectra, which shows that there is almost a linear relation between the system's U, B and V magnitudes and its mass accretion rate. This means that equation (6.1) can still be valid in the AM CVn case, and will be used as an approximation to find the magnitude-$\dot{M}$ relation. More investigations will be done in the future to confirm this, and to study the brightness of the system over the entire electromagnetic spectrum using the bolometric magnitude, to find the exact magnitude-$\dot{M}$ relation for such systems. The result of such investigations will be submitted as part of our publication in A&A later this year. The 1997 observations represent only the $\dot{M}$ of one state of each system, and do not at all describe the global picture of the mass accretion rate in such systems. The 2001 observations were intended to complete the picture of all parameters of both V803 Cen and CR Boo, and to give a global understanding for the accretion through their discs.

6.4.1 V803 Cen

During the 2001 observation, V803 Cen resisted us and refused to cooperate with us to solve its $\dot{M}$ mystery. The system remained keeping itself in the high state during

all the observing nights. Although the status of the system did not change during the observing run, we remained optimistic and hoping that when we reduce the data, we might find that the status of the system in 2001 observations was different from the 1997 one. Unfortunately, we were very disappointed when we discovered after reducing the data that the system was in the same state as in 1999 observations, but with a small variations in the the value of the magnitude. The question now is : what can we learn from the 2001 observed spectra of V803 Cen? Thanks to the photometric images which after reducing it using the aperture photometry techniques, helped us to determine the very small changes in the system magnitude during the three nights of observations. This certainly can help us to determine the changes in $\dot{M}$ with such tiny variations, by also using the lower and upper values of the magnitude. The B-magnitude of V803 Cen can in general change form 13.4 - 17 and the B-magnitude of the system was varying between 14.3 - 14.8 during the three nights of observations. As seen in Fig. 6.13, Fig. 6.14 and Fig. 6.15, we fitted the observed spectra of the system taken in three successive nights (April 12th-14th), respectively, with the same theoretical pure helium model. We found that we were able to fit the spectra of the three nights with the models of the following parameters : $\dot{M} = (4 \pm 1) \times 10^{-9} M_{\odot}$/yr, $R_{out} = (17 \pm 3) R_1$ and $i = 5^{\circ} \pm 5^{\circ}$ and d $\approx 370 \pm 70$ pc, with the mass of the central star being fixed at 1.2 $M_{\odot}$, which are almost the same parameters as the model fitted to the spectra of the same system, taken in 1997 (NSS) and of the following parameters : $\dot{M} = (4 \pm 1) \times 10^{-9} M_{\odot}$/yr, $R_{out} = (17 \pm 3) R_1$ and $i = 5^{\circ} \pm 5^{\circ}$, with the mass of the central star being fixed at 1.2 $M_{\odot}$. The uncertainty is estimated by eye. The B-magnitude of the system varied in the range 14.3 - 14.8 during the three nights of observations, correspond to the mass accretion rate $(4 \pm 1) \times 10^{-9} M_{\odot}$/yr. If $\dot{M} \propto L(B)$, we estimate that the $\dot{M} = (2 \pm 2 \times 10^{-8} - 4 \pm 2 \times 10^{-10}) M_{\odot}$/y will correspond to the B-magnitude of (13.4 - 17), which can possibly be the predicted mass accretion rate of the system in relation to its magnitude. The disc radius found to vary within the range of (15 - 20)R_1 at the time of observations, which indicates that the disc was within the range of the circularization and the tidal radius. Within such range it is hard to decide whether the system was stable or unstable, but probably in the oscillating 'cyclic' state as defined by Patterson et al. (2000).

Much can be said at this point about the fit in Fig. 6.13, Fig. 6.14 and Fig. 6.15. As we can see that the helium models fit most of the observed spectra very well. In some regions the fit was not quite satisfactory as seen in Fig. 6.13 with 'kd120029', where the fit was very bad specially within the region of λ 4100 - 4800Å, which might be due to many different reasons. Some of these reasons were discussed before for the 1997 observations, such as the flux reflected from the secondary object, shocks and flares. Other possible reasons can also make problems with the fit, such as the

noise in the spectra or a mistake during the reduction process. It can also be due to the time evolution of the spectra maintainence, where the exposure time was about 1800s for each spectrum. This can very much influence the spectra due to the instability of a system like V803 Cen. In the spectrum 'kd120027', possible lines other than helium expected to be from Carbon, Oxygen and Nitrogen might be detected in the region λ 4550 - 4750Å. The same was noticed in the spectra of V803 Cen shown in Fig. 6.14 and Fig. 6.15. Lines from heavy elements will be discussed in more details later in this chapter. The He I line at λ 4143Å is seen in all the spectra taken on 2001 for both V803 Cen and CR Boo is much stronger than it should be. The exact reason is not clear to us, but we think that it might simply be due to a problem with the flux calibration only in this region for some reason! It can also be due to the atmospheric effects, because we observed V803 Cen when it was very low 'close to the horizon' and almost hidden behind the dust in the atmosphere coming from west Africa 'the Sahara' (Abbott, private communications).

6.4.2 CR Boo

During the three nights of observations, CR Boo was also stuck in the high state, but fortunately its variability was higher than V803 Cen. On April 12th, the system was in a rising state and continued rising also on the 13th. On the 14th, the system went down but remained within the high state and higher than the state it had on the 13th. During the three nights of observations, the B-magnitude of the system changes within the range of 13.9 - 14.7, and in general the system changes its B-magnitude within the range of 13.6 - 17.4. We fitted the observed spectra of CR Boo taken on three successive nights with the spectra of the pure helium accretion disc model, and as a result we found the following: For the 12th of April spectra of B-mag 14.7, the models which gave the best fit shown in Fig. 6.16 has the parameters: $\dot{M} = (4 \pm 1) \times 10^{-9} M_{\odot}$/yr, $R_{in} = 1.4 R_1, R_{out} = (16 \pm 2) R_1, i = 30 \pm 5^{\circ}$ and d $\approx 320 \pm 100$ pc. For the 14th of April spectra of B-mag 13.9, the model which gave the best fit shown in Fig. 6.17 has the parameters $\dot{M} = (7 \pm 1) \times 10^{-9} M_{\odot}$/yr, $R_{in} = 1.4 R_1, R_{out} = (15 \pm 3) R_1, i = 30 \pm 5^{\circ}$ and d $\approx 330 \pm 100$ pc, with the mass of the central star being fixed at $1.0 M_{\odot}$ for the two models used to fit the spectra. From such results we found that the B- magnitude variations of 14.7 - 13.9 correspond to $\dot{M}$ variations of $(4 - 7) \times 10^{-9} M_{\odot}$/yr. Uncertainty is estimated by eye. The fits seen in both Fig. 6.16 and Fig. 6.17 are not very accurate simply because the observed spectra are very noisy.

The outer radius found with the best fit for CR Boo is about $15 R_1$. This indicates that at the time of observation, the disc radius was closer to the tidal radius than the critical radius. This means that the system was in a rising state during the

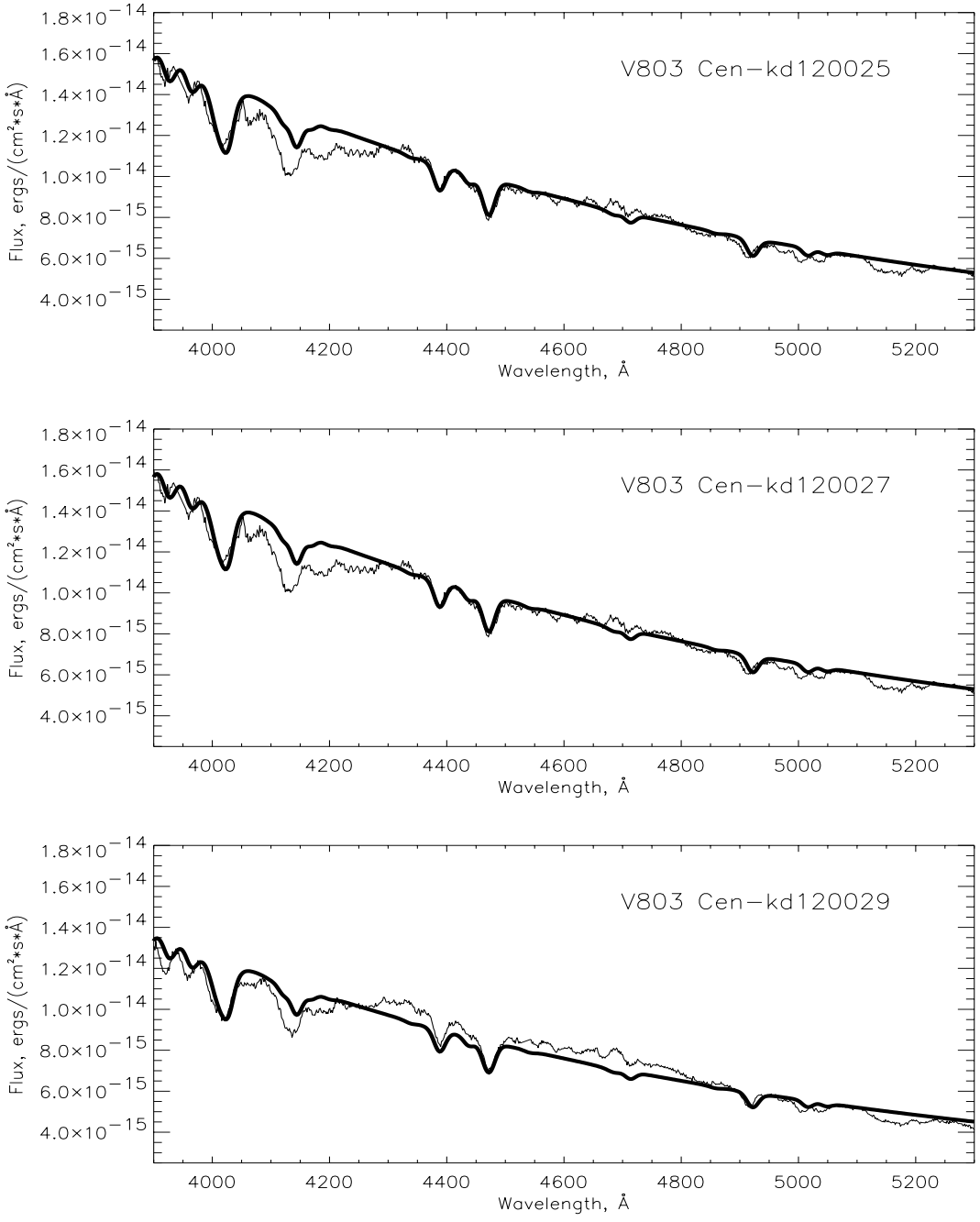

Figure 6.13: The best NLTE model (solid line) which fits the observed spectra (thin line) of V803 Cen taken with the NOT on the 12th of April 2001, with parameters $M_1 = 1.2M_\odot, \dot{M} = 3 \times 10^{-9} M_\odot/\mathrm{yr}$, $R_{in} = 1.4R_1, R_{out} = 17R_1, i = 5^\circ$ and d=390 pc.

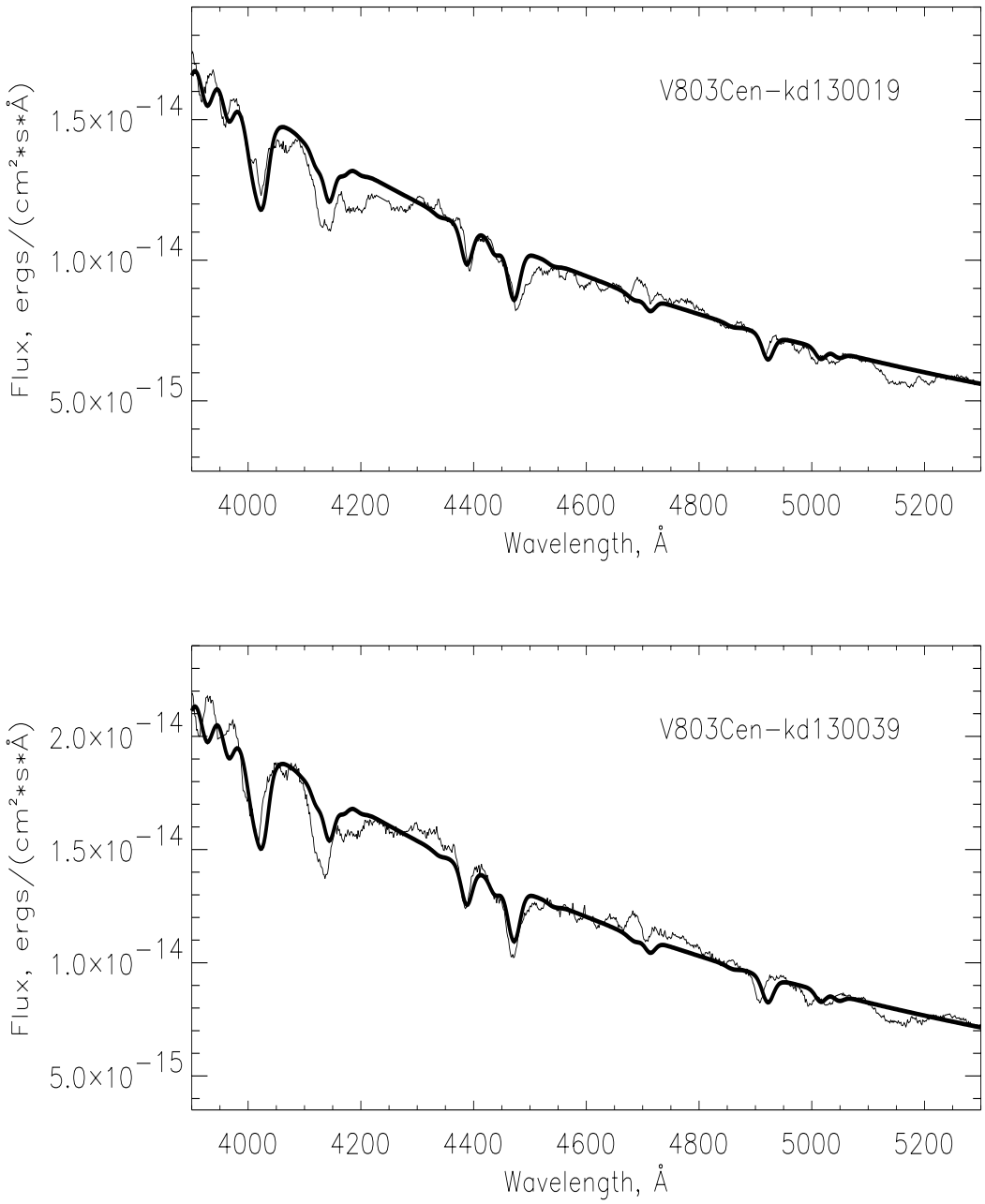

Figure 6.14: The best NLTE model (solid line) which fits the observed spectra (thin line) of V803 Cen taken with the NOT on the 13th of April 2001, with parameters $M_1 = 1.2M_\odot, \dot{M} = 3 \times 10^{-9} M_\odot/\mathrm{yr}$, $R_{in} = 1.4R_1, R_{out} = 17R_1, i = 5^\circ$ and d=360 pc.

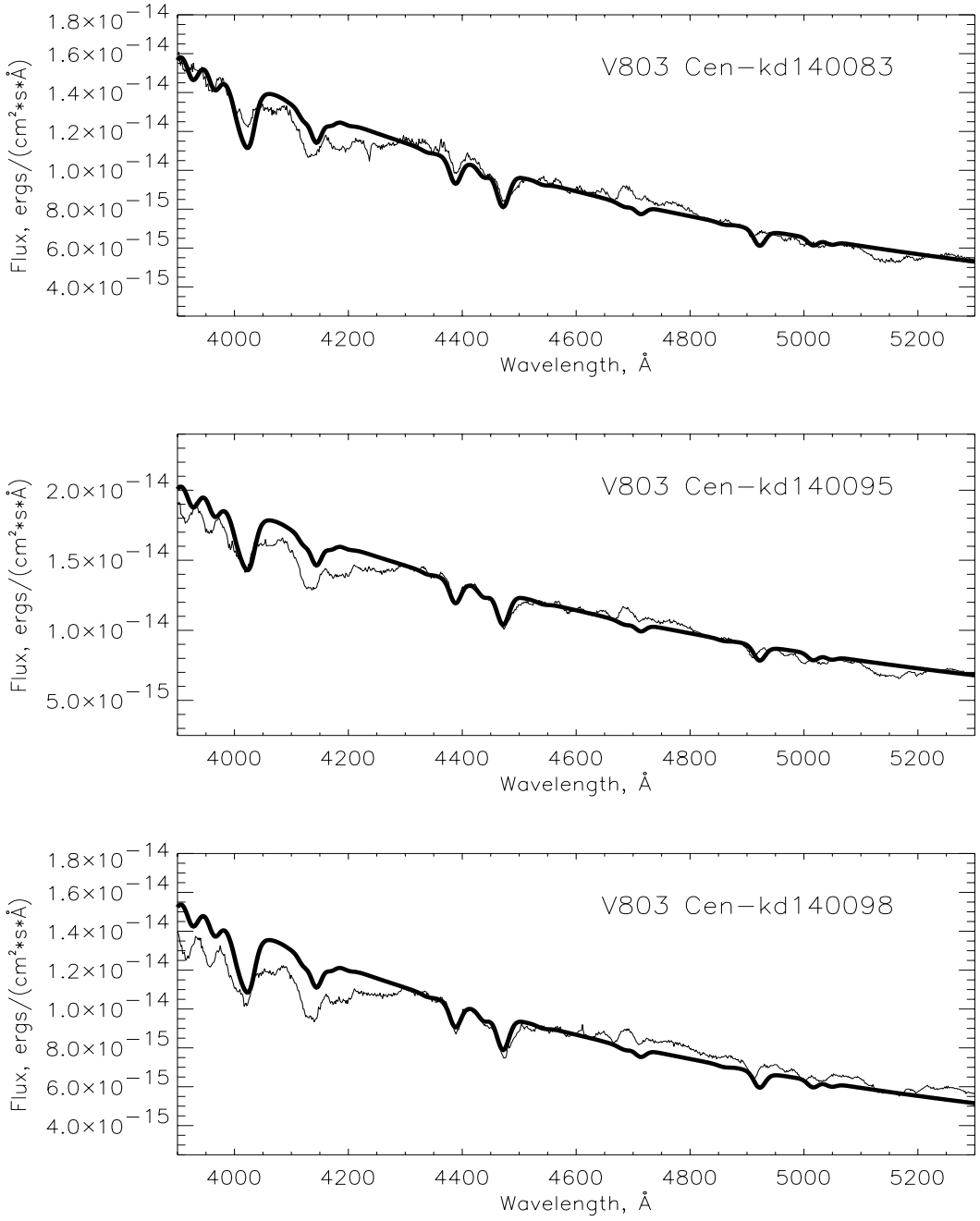

Figure 6.15: The best NLTE model (solid line) which fits the observed spectra (thin line) of V803 Cen taken with the NOT on the 14th of April 2001, with parameters $M_1 = 1.2M_\odot, \dot{M} = 3 \times 10^{-9} M_\odot/\mathrm{yr}$, $R_{in} = 1.4R_1, R_{out} = 17R_1, i = 5^\circ$ and d=380 pc.

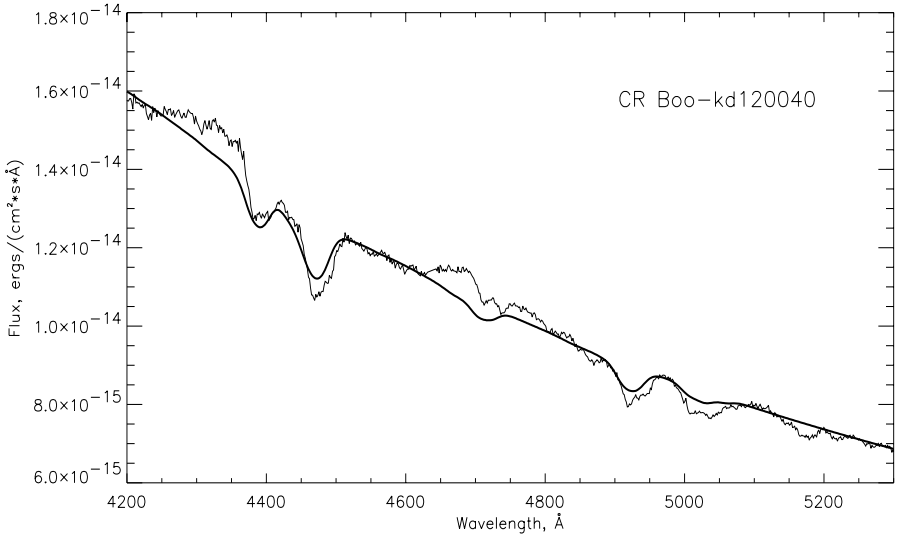

Figure 6.16: The best NLTE model (solid line) which fits the observed spectrum (thin line) of CR Boo taken with the NOT on the 12th of April 2001 with parameters: $M_1 = 1.0 M_\odot, \dot{M} = 4 \times 10^{-9} M_\odot/\mathrm{yr}, R_{in} = 1.4 R_1, R_{out} = 16 R_1, i = 30^\circ$ and d $\approx$ 320 pc.

observation, which was also found from the magnitude calculations.

6.5 CNO abundances

The first good analysis of optical spectra of AM CVn stars was done by Voikhanskaya (1982) based on spectra with resolution 4 - 5.5Å taken in the prime focus of the six-meter telescope in USSR, at that time the worlds largest telescope. She noticed the wide absorption lines which seemed to change shape, and the emission cores which seemed to move from the red to the blue part of the absorption profile and then back. Both these observations have later been confirmed as the 13.38 h precession (Patterson et al. 1993) and the S-wave (Nelemans et al. 2001).

Voikhanskaya also noted the broad emission detail, which she identified with the well known C III - N II at λ 4660 Å blend, which is observed in the spectra of many X-ray sources. This may be the first detection of heavier elements in the optical spectrum of the AM CVn system. The UV spectra of the AM CVn systems have many lines from heavy elements such as C IV, N IV, N V, Si III and Si IV (Wood et al. 1987), which most of it are believed to be generated in the atmosphere of the

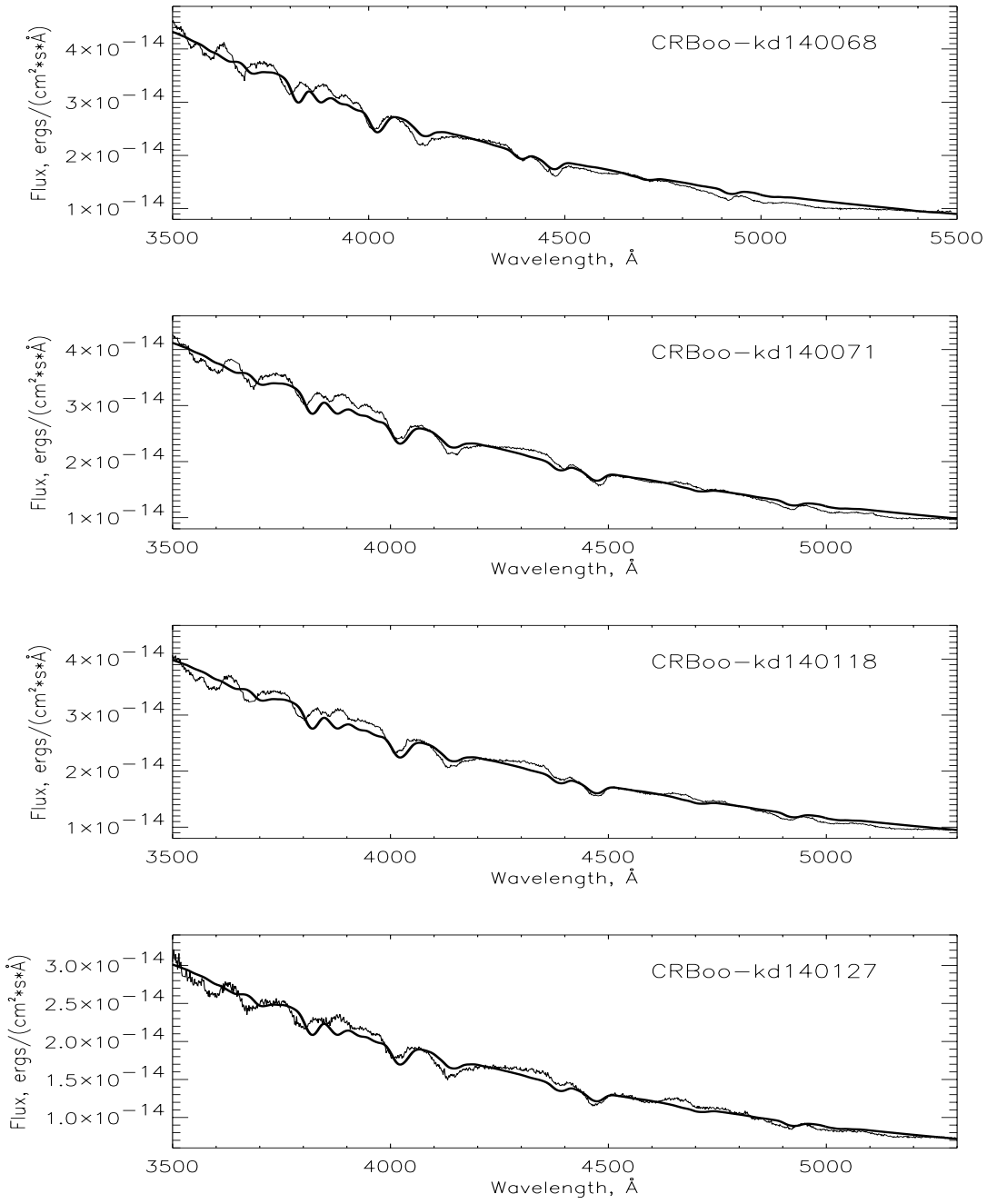

Figure 6.17: The best NLTE model (solid line) which fits the observed spectrum (thin line) of CR Boo taken with the NOT on the 14th of April 2001 with parameters: $M_1 = 1.0 M_\odot, \dot{M} = 7 \times 10^{-9} M_\odot/\mathrm{yr}, R_{in} = 1.4 R_1, R_{out} = 15 R_1, i = 30^\circ$ and d $\approx$ 330 pc.

central star.

In this work we consider the possibility that lines from heavy elements might exist in the optical spectra of the AM CVn systems as discussed by Voikhanskaya (1982), but they are hidden under the noise. In addition to that some of the evolutionary models describing the AM CVn systems, predicted the appearance of lines from heavy elements especially carbon at a certain evolutionary stage (Savonije 1986). In this section we want to investigate which lines will appear in the optical spectra of the AM CVn systems, and determine the upper limit for such elements. This can be done by adding heavy elements into the helium model, and determine when and at which upper limit 'ratio by number with respect to helium' these lines will start to appear in the spectra. This will make it easier for us to identify such lines in the available low resolution spectra we have and in the higher resolution spectra when available. We will also use such investigations to differentiate between the disc and the central star lines, specially we can still assume that the C III - N II lines at λ 4660 Å detected by Voikhanskaya (1982) are not from the disc but from the central star. Such lines in emission might also be generated from an optically thin layer of a hot gas at the top of the disc, and strongly irradiated by the central star, which might also be the same reason for the detection of the He II line in emission at λ 4668 Å in the spectra of the AM CVn systems.

No one so far has predicted an upper limit for the heavy elements in the accretion disc of the AM CVn systems, except in the work done by Tsugawa & Osaki (1997), to investigate the instability of the AM CVn systems. They proposed a disc model with a certain amount of heavy elements varied between (0.03 - 0.0004) by mass, while the rest is considered to be helium. We have used such an upper limit to investigate lines from heavy elements in the optical spectra of the AM CVn systems. We study only lines from the CNO abundances considered implicitly in the model, which means the atom is assumed not to contribute to the opacity; but is allowed to contribute to the total number of particles and to the total charge. Surprisingly we discovered that the upper limit proposed by Tsugawa & Osaki (1997), found to be far too high to be in the accretion disc of the AM CVn systems, because with such an upper limit, many lines appeared in the model spectra, but have never been detected in the observed spectra of the AM CVn systems.

In Fig. 6.18 we compare the spectrum of the pure helium model with the spectrum of the helium model but with C/He=O/He=N/He=10^{-3} by number, and as seen in this high resolution spectrum that many C, N and O lines have appeared in this wavelength range in the spectrum of the helium model with the CNO abundances. We have also looked at these lines in the model spectra of FWHM=20Å as seen in Fig. 6.19, to be able to compare with the observed spectra of the AM CVn systems presented in this thesis. We discovered that many lines appeared in the model

spectra of the CNO abundances, which do not exist in the observed ones. The strongest lines are C II lines at both λ 3920 and λ 4267 Å, N II line at λ 5679 Å and O II lines at λ 4414.8, 4641 and 4649Å. The C II line at λ 4267 Å was the strongest of all the carbon lines, but this line has not been detected in the observed spectra of the AM CVn systems. We will use this line as a reference line to determine the upper limit of carbon in the accretion disc of the AM CVn systems, which can also give us a clue if there will be any carbon lines left in the model spectra, when we decrease carbon into a limit where this line will disappear as in the observed spectra. In the same way we will use the strongest oxygen and nitrogen lines as references to determine the upper limits of oxygen and nitrogen in the accretion disc of the AM CVn systems. This will help us to give an explanation to the fluctuations 'lines or maybe noise' seen in the observed spectra of the AM CVn systems obtained in 2001.

6.5.1 Upper limits

We decreased the amount of carbon in the model to vary as follows: C/He=$10^{-3}, 5\times 10^{-4}, 10^{-4}$ and 10^{-5} by number, represented by the solid, dotted, dashed dotted and dashed lines respectively as seen in Fig. 6.20 for the spectra of FWHM=20Å. This demonstrates that carbon cannot be more than 10^{-5} by number with respect to helium in the accretion disc of the AM CVn systems.

Weak oxygen lines were detected in the high resolution model spectra, but were blended and not well detected in the model spectra of FWHM=20Å when O/He=10^{-3} by number. The oxygen lines appeared clearly in the spectra of FWHM=20Å when O/He number density was 10^{-2}. O II lines at λ 4414.8, 4641 and 4649Å were the strongest of all which appeared in the spectra of FWHM=20Å, but were not detected in the observed spectra. O II line at 4649Å is used as a reference line to determine the upper limit of oxygen in the accretion disc of the AM CVn systems. In Fig. 6.21 we demonstrate that by decreasing the amount of oxygen in the model into 10^{-5} by number with respect to helium, the O II line at λ 4649Å will disappear, which also demonstrates that the upper limit for oxygen in the accretion disc of the AM CVn systems is $\leq 10^{-5}$ by number with respect to helium.

The same demonstration has been done for the N II line at λ 5679 Å as seen in Fig. 6.22 for the model spectra of FWHM=20Å, but not detected in the observed spectra of the AM CVn systems. This also demonstrates that the upper limit for nitrogen in the accretion disc of the AM CVn systems is $\leq 10^{-5}$ by number with respect to helium. With such upper limits the helium model of C/He=O/He=N/He $\leq 10^{-5}$ by number, behave in exactly the same way as the pure helium model.

Even after such investigations, we still did not detect or even suspect any lines from such elements in the observed optical spectra of the AM CVn systems, of FWHM=20Å presented in this work. This is because with the upper limits found for the CNO abundances in the accretion disc of the AM CVn systems, no lines from such elements remained in the model spectra which can be detected in the observed ones. Based on that we conclude that carbon, oxygen and nitrogen if exist in the accretion disc of the AM CVn systems, will not have number density ratios with respect to helium more than 10^{-5}, which is the upper limit found as a result of our calculations. We also conclude that the fluctuation seen in the observed spectra of both V803 Cen and CR Boo taken on 2001, which were not fitted with the model are not real. It must be noise in the spectra due to the dust in the atmosphere during the observations (Abbott, private communications), because we observed V803 Cen at the NOT when it was very low (close to the horizon) and almost hidden behind the dust in the atmosphere.

6.5.2 Evolution

One thing is worth mentioning in this section is the helium ignition in the donor star of the AM CVn systems, based on our determination for the upper limits of the CNO abundances, in the accretion disc of such systems. Since the disc matter is accreted from the secondary star, we could indirectly see the core of it and investigate if it has exhausted hydrogen but not ignited helium or if it has ignited helium and developed a carbon-oxygen core. Since a star expands after it has left the main-sequence, such two cases are likely to occur most often. The evolutionary path of a systems like AM CVn which can end up with a double degenerate binary or a degenerate primary and a semi-degenerate secondary has been discussed in many papers (Zapolsky & Salpeter (1969); Iben & Tutukov 1984, 1986; Savonije et al. (1986); Iben & Webbink 1988; Tutukov & Federova et al. (1989); Nelemans 2001a; Schenker 2001). After the first common envelope is ejected from the systems, the binary orbit is smaller, the primary evolves to a carbon-oxygen white dwarf, and the secondary star continues to burn hydrogen, but now with a very different abundance and possibly a much larger mass as well. Eventually the secondary fills its Roche lobe, and with its core exhausted of hydrogen, a helium matter mass transfer event ensues. This mass transfer episode produces a second common envelope, since the compact primary star can only accrete matter at a low rate. Once the envelope is expelled , the secondary star emerges as a helium degenerate or semi-degenerate star, of a lower mass than the primary star.

In our investigations for the model optical spectra of the AM CVn systems, we found the following upper limits for the CNO abundances in the accretion disc

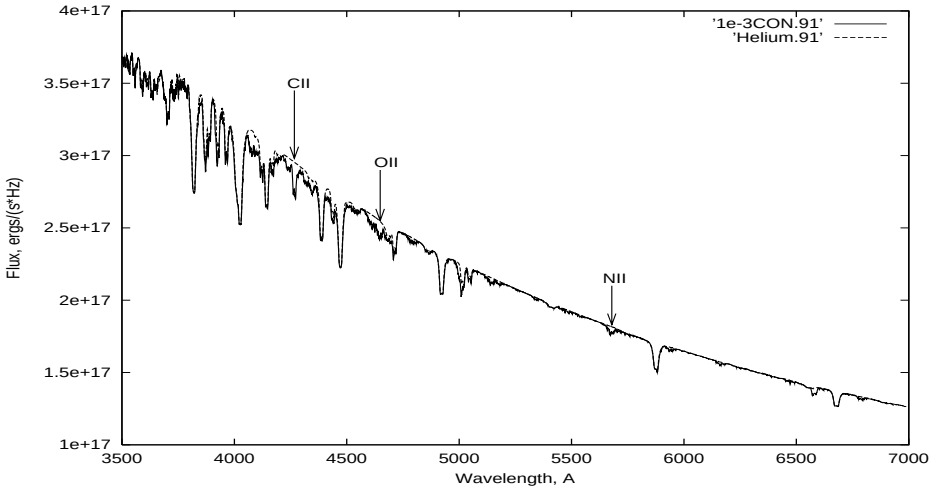

Figure 6.18: The high resolution spectrum of the helium model with C/He=N/He=O/He=10^{-3} by number 'solid line' compared with the pure helium model 'dashed line'. The parameters used in this model are $M_1 = 1.1 M_\odot, \dot{M} = 5 \times 10^{-9} M_\odot$/yr, $R_{in} = 1.4 R_1, R_{out} = 15 R_1$ and $= 15^\circ$.

of such systems: C/He=O/He=N/He $\leq 10^{-5}$ by number, which reflect the same abundances in the donor star. Such upper limits reflects two different possibilities about what the donor star might be: the first one is, if C/He=O/He=N/He $\approx 10^{-5}$ by number, then this means that the (C + O + N)/He $\approx$ 3000 times by number than the CNO abundances in the Sun, but still it is not enough to be detected in the observed spectra, according to Savonije et al. (1986). Such ratios of CNO abundances in the donor star with respect to the CNO abundances in the Sun, indicate that the donor star has ignited helium and developed a carbon-oxygen core, the theory which has been proposed by Savonije et al. (1986). The second case if C/He = O/He = N/He $\ll 10^{-5}$ by number, then this is an indication that the donor has exhausted hydrogen and maybe ignited helium, but no carbon-oxygen core developed yet. Analysis of a high resolution optical spectra, in addition to the existing UV spectra may answer this question.

6.6 Summary

Many important parameters such as the mass accretion rate, the angle of inclination, the abundance of elements and the distance to the AM CVn systems have been investigated. We fitted the observed spectra with the model as a tool to estimate

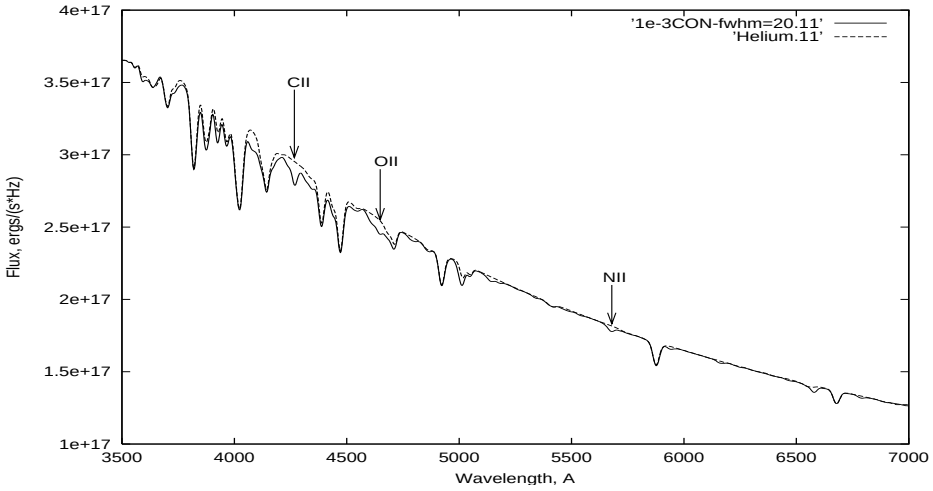

Figure 6.19: The spectrum of the helium model broadened with FWHM=20Å with C/He=N/He=O/He=10^{-3} by number 'solid line' compared with the pure helium model 'dashed line' which fitted well the observed spectra of the AM CVn systems. The parameters used in this model are $M_1 = 1.1M_\odot, \dot{M} = 5 \times 10^{-9} M_\odot$/yr, $R_{in} = 1.4R_1, R_{out} = 15R_1$ and $i = 15°$.

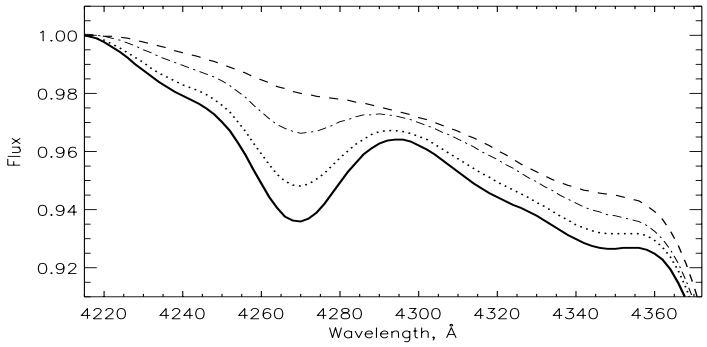

Figure 6.20: The influence of an extra amount of carbon on the C II line at λ 4267Å of the NLTE helium accretion disc spectra broadened with FWHM=20Å. C/He number density ratios assumed are $10^{-3}, 5 \times 10^{-4}, 10^{-4}$ and 10^{-5} represented by the solid, dotted, dashed dotted and dashed lines respectively. The parameters used in this model are $M_1 = 1.1M_\odot, \dot{M} = 5 \times 10^{-9} M_\odot$/yr, $R_{in} = 1.4R_1, R_{out} = 15R_1$ and $i = 15°$.

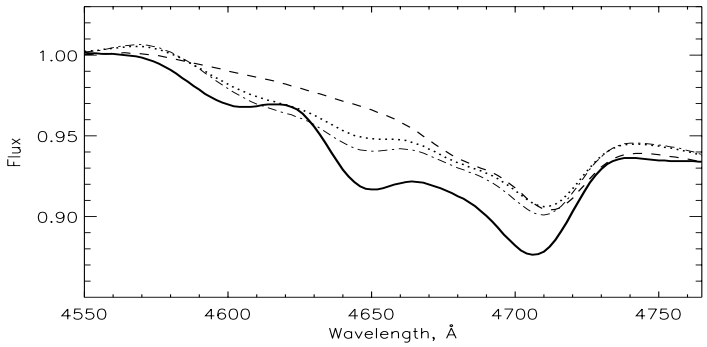

Figure 6.21: The influence of an extra amount of oxygen on the O II line at λ 4649Å of the NLTE helium accretion disc spectra broadened with FWHM=20Å. O/He number density ratios assumed are $10^{-2}, 10^{-3}, 5 \times 10^{-4}$ and 10^{-5} represented by the solid, dashed dotted, dotted and dashed lines respectively. The parameters used in this model are $M_1 = 1.1 M_\odot$, $\dot{M} = 5 \times 10^{-9} M_\odot$/yr, $R_{in} = 1.4 R_1, R_{out} = 15 R_1$ and $i = 15°$.

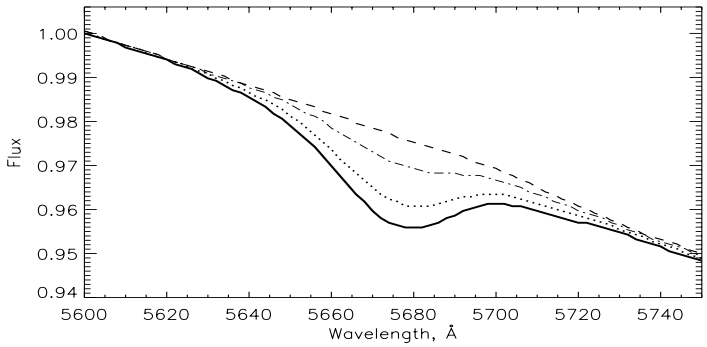

Figure 6.22: The influence of an extra amount of nitrogen on the N II line at λ 5679Å of the NLTE helium accretion disc spectra broadened with FWHM=20Å. N/He number density ratios assumed are $10^{-3}, 5 \times 10^{-4}, 10^{-4}$ and 10^{-5} represented by the solid, dotted, dashed dotted and dashed lines respectively. The parameters used in this model are $M_1 = 1.1 M_\odot$, $\dot{M} = 5 \times 10^{-9} M_\odot$/yr, $R_{in} = 1.4 R_1, R_{out} = 15 R_1$ and $i = 15°$.

such parameters with a certain accuracy and in particular the abundance of elements. Such investigations can give us a better idea about the evolution of these systems which is our main goal in this work. We will discuss our results in more detail in the next chapter.

Chapter 7

Discussion and conclusions

7.1 Introduction

In this chapter we will discuss our results presented in the previous chapters in details. Several points will be taken into account in our discussion, most important of all are the obtained values for the systems parameters, and how far such values can be scientifically accepted. This can be deduced based on the results obtained for the same or similar systems by other people using different methods than ours. At the end we will state our conclusions based on our summary and comparation of our results with the ones obtained by the previous investigations.

7.2 Summary

Spectra of stationary geometrically thin, optically thick pure helium accretion discs in the AM CVn systems have been investigated. Computations of synthetic spectra were done for both LTE and NLTE cases. A similar work by La Dous (1989) for solar composition discs has been used as the main reference for our work. Input parameters were chosen in such a way that we let the parameters which had largest influence on the spectrum vary, while the others were kept almost constant. As concluded by La Dous (1989) we found that the parameters M_1 and $\dot{M}$ have much the same effect on the spectrum, as is obvious from eq. 5.37. The angle of inclination has a determining effect on the character of the observable continuous spectrum as well as the line profile. Two out of five parameters in the spectrum computation, the mass of the central star and the outer radius of the disc, cannot be determined directly from the spectroscopic observations. On the other hand, three other parameters,

the mass accretion rate $\dot{M}$, the angle of inclination i and the inner radius of the disc can be determined from spectroscopic observations. As also concluded by La Dous (1989), we found that the first two parameters can be determined from the optical part of the spectrum, while the last one has a very small effect in this region, and may only be determined from the UV part of the spectrum.

Based on these conclusions, we have decreased the number of free parameters in the model calculations as much as possible to be able to obtain a good fit to the observed spectra of the AM CVn systems. As mentioned in the previous sections, the mass of the central star was set in the model as a fixed parameter. The variations of the outer radius were very limited and determined based on the thermal-tidal-instability model of Tsugawa & Osaki (1997) for the unstable objects, while for the stable objects we used the work done by Solheim et al. (1998). Finally we ended up with only two varying parameters, the mass accretion rate and the angle of inclination, which are considered as the only two parameters which can be determined from the optical spectroscopic observations, and our good fits for the observed spectra confirm that.

The blue shifted edges noticed in the observed spectra of V803 Cen and CR Boo at λ 4370 Å and λ 4470 Å are due to the precession of the disc, which makes the line profile vary with the phase of the precession of the system and depend on the exposure time used during the observations. The exposure time used in almost all the 2001 spectra is 1800 s which is slightly longer than the orbital period of the systems. The same has been noticed in the set of observed spectra of the AM CVn system presented by Nelemans et al. (2001b).

In our calculations we found that both the H-He model of the number density ratio $H/He \leq 10^{-5}$, and the pure helium models gave a similar satisfactory fit to the observed spectra. The C,N,O elements may also exist in the disc, and according to our investigations found to be $\leq 10^{-5}$ by number with respect to helium. This lead us to the conclusion that the accretion discs of the AM CVn systems most likely consist of almost pure helium, and the hydrogen has left the system (via stellar wind in the common envelope phase or another mechanism). With such ratio we are able to set the upper limit of the C, N and O abundance in the disc and the secondary star, but we are not able to decide if the donor star has ignited helium and developed a carbon-oxygen core. High resolution spectra in the optical region or an analysis of the existing UV spectra may answer this question.

Similar work has been done by El-Khoury & Wickramasinghe (2000) for some of the AM CVn systems, but only with LTE models. They applied a χ^2- minimization technique to estimate several system parameters for the two systems, AM CVn and CR Boo. In their work they let almost all the disc parameters be free, ignoring the limits from other observations which may be considered while setting the model

grid. Leaving all the parameters free will certainly increase the level of uncertainty in the final results, especially when leaving both the mass of the central star and the outer radius of the disc free. For example, they considered the mass of the central star as a free parameter for the AM CVn system and determined it to be 0.84 $M_{\odot}$. In contrast, we have used a fixed value of mass, $\approx 1.1 M_{\odot}$, based on independent evidence, such as the mass-radius relation for a semi-degenerate secondary and the estimated mass ratio q from photometric observations.

This difference in the mass can change the entire calculation quite significantly and give different values for the parameters than we obtained above. The close agreement between our calculated spectroscopic distance and the parallactic distance of AM CVn gives additional support for our procedure and the accuracy of the derived parameters of the studied systems. The values of both the mass accretion rate $\dot{M}$ and the angle of inclination i, obtained as a result of our calculations, are also different from that obtained by El-Khoury & Wickramasinghe (2000), likely because we have used different masses and consequently different disc sizes. The difference in the values obtained for CR Boo can also be due to different reasons, most likely due to the instability of the system and because of the different disc radius assumed in both our and their calculations, which will certainly affect the values of both $\dot{M}$ and i. The assumption of LTE for their calculations and NLTE for our calculations can also give slightly different results.

Warner (1995a) predicted angles of inclination for some of the AM CVn systems, using the maximum observed velocity v_{max} in the disc, if the disc reaches down to the surface of the primary star, while in our calculation we used $R_{in} = 1.4 R_1$. The formula for v_{max} given in Warner (1995a) is:

$$v_{max}^2 = \frac{GM_1}{R_1} sin^2 i$$

The angles we found as a result of our calculations are closed to his estimated angles but not the same, because he didn't include any assumptions about the inner and outer radius of the disc. Patterson et al. (1993) have also studied the relation between the mass of the primary star and the angle of inclination in the AM CVn system itself, assuming a range of (1-3)R_1 as the inner radius of the disc, and without any assumptions about the disc outer radius. The angle $\approx 45^{\circ}$ we found for the AM CVn system agree with his range of angle estimates, within the boundary conditions considered for R_{in}.

The mass transfer rate we have determined is related to particular spectra and may not represent the real transfer rate for the objects. We should therefore increase the errors when necessary. For AM CVn we have considerable variations in the line profiles during the P=13.32 hr period of precession, and we therefore increase the

error by 50 percent. For HP Lib we have not found any sign of precession, so we keep the errors as they are. For V803 Cen we found the magnitude variations of 14.8 - 14.3 correspond to $\dot{M}$ variations of $(5-3)\times10^{-9}M_{\odot}$/yr. This leads us to the conclusion that if $\dot{M}\propto L_{(B)}$ as found from the blackbody approximations, then the magnitude variations of the system in the range 13.4 - 17 correspond to $\dot{M}$ variations of $7\times10^{-9}M_{\odot}$/yr - $6\times10^{-10}M_{\odot}$/yr. For the case of CR Boo we found the magnitude variations of 13.9 - 14.7 correspond to $\dot{M}$ variations of $(7-4)\times10^{-9}M_{\odot}$/yr. From this we conclude that if $\dot{M}\propto L_{(B)}$ then the magnitude variations of the system in the range 13.6 - 17.4 correspond to $\dot{M}$ variations of $1\times10^{-8}M_{\odot}$/yr - $3\times10^{-10}M_{\odot}$/yr. For V803 Cen the disc radius found to vary within the range of (15 - 20)R_1 at the time of observations, which indicates that the disc was between the range of the circularization and the tidal radius. Within such range it is hard to decide whether the system was stable or unstable during the observations, but from the magnitude calculations and the mass accretion rate we found for the system indicates that the system was in or towards a stable phase. The outer radius found with the best fit for CR Boo is about $15R_1$. This indicate that at the time of observations, the disc radius was closer to the tidal radius than the critical radius. This confirm that the system was in a rising state during the observation, which we found also from the magnitude calculations. In table 7.1 we show the calculated and estimated values for $\dot{M}$ and i, including systematic errors. For the inclination we use the errors from the fitting by eye, except for AM CVn, where the error is increased by 50 percent due to the precession period changes. Our mass estimate, with ranges reflecting the mass variations possible from the spectral fitting, is found to be very similar to the values presented in table 6.1, with possible variations in M_1 found to be $\approx \pm\ 0.05$ $M_{\odot}$ in either system.

Since the interacting binary model was first proposed by Faulkner et al. (1972), many studies of the evolution and stability of these system have taken place. It is now commonly agreed that the orbital period will increase with time due to mass transfer, which again will decrease with time as in VY Scl systems. Depending on the nature of the secondary star, i.e. if it has a C-O core or is a pure helium object, we will get different values of the $\log\dot{M}$ versus $\log P$ relation. In Fig. 7.1 we show two such relations taken from Nelemans et al. (2001a), the dashed line showing the evolution if the secondary is a fully degenerate white dwarf, and the dotted line if the secondary is a semi-degenerate pure helium star. Our results support the semi-degenerate helium star model but do not fully agree with it. This is because the mass-radius relation for a semi-degenerate helium secondary given by Nelemans et al. (2001a), gives a higher mass for the primary star in some systems than the ones we used in our calculations. This as a consequence will give higher $\dot{M}$ for the stable

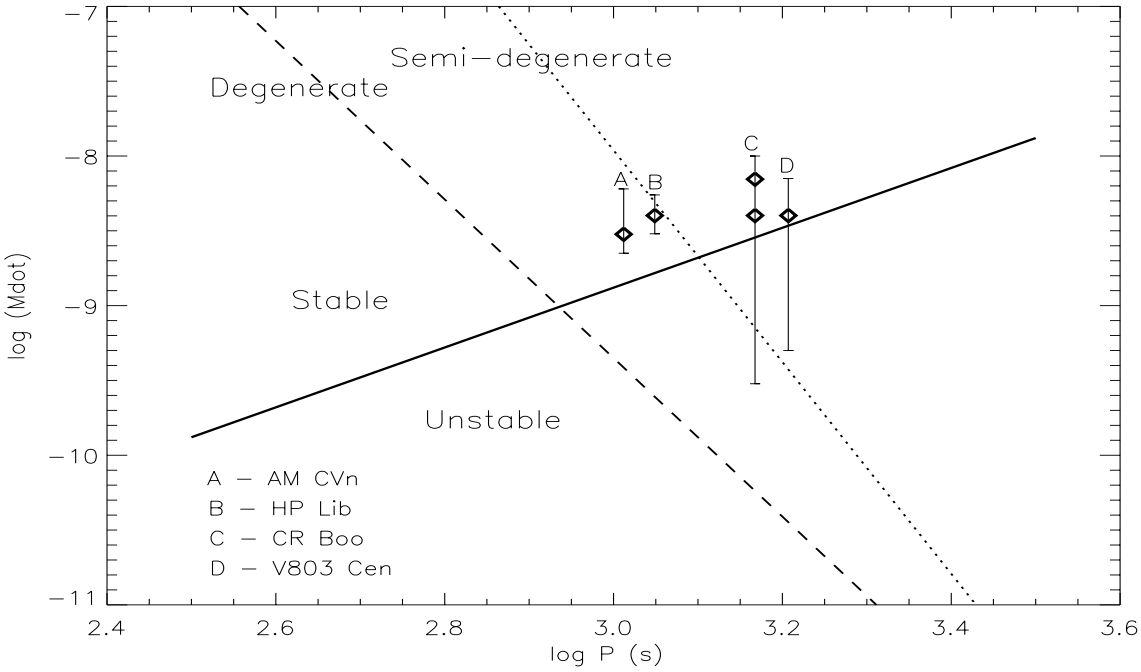

Figure 7.1: The mass transfer rate versus period for the AM CVn objects. The error bars represent the systematic errors, due to the observations done at a particular phase. The solid line is the border between the thermally stable (upper part) and unstable discs (lower part) (Tsugawa & Osaki 1997). The dashed line is the evolution calculated for a system with a white dwarf secondary and the dotted line for a system with a semi-degenerate pure helium atmosphere secondary with a C-O core (Nelemans et al. 2001a).

systems as seen in Fig. 7.1 (dotted line), as also found that $\dot{M}$ is proportional to $M_1^{8/3}$ for a stable system like AM CVn itself, as in equation (10) given in Warner (1995a). The masses of the primary stars in the AM CVn systems in the range of (1.0 - 1.2) $M_\odot$ used in our calculations found to be the reasonable masses, which can give an acceptable fit to the observed spectra of the AM CVn systems. This must be taken into account by the evolutionary models.

In Fig. 7.1 we have also drawn the border between the thermally stable and unstable mass transfer rates, as calculated by Tsugawa & Osaki (1997). We find that AM CVn and HP Lib are stable as expected, and that the mass transfer rate of CR Boo and V803 Cen also belong to the stable part, but on average they must belong to the unstable regime. The mass transfer rate found for V803 Cen lies in the stable part of Fig. 7.1, while with the magnitude found for the system during the 2001 observations, it must lie in the unstable part according to Patterson et al. (2000), which claimed that V803 Cen spend 50 percent of its time in the cyclic state, and the same is probably applied to CR Boo. Also from Fig. 7.1 we should notice the diminishing of $\dot{M}$ with the increase of P_{orb}. The reason for such cases and according to Warner (1995a) is eventually be augmented by an irradiation-induced component. When this dominates, the same VY Scl behavior as seen in the H-rich systems would be expected also for the AM CVn systems. As the irradiative flux F_{irr} on the surface of the secondary is proportional to $L(1)/a^2$, where L(1) is the luminosity of the primary star and the disc while a is the orbital separation, it follows from Kepler's Third Law, $L(1) \propto M_1\dot{M}/R_1$ and R_1 is approximately $\propto M_1$ that

$$F_{irr} \propto \frac{M_1^{2/3}\dot{M}}{(1+q)^{2/3}} P_{orb}^{-4/3} \tag{7.1}$$

Since AM CVn systems of $q \sim 0.05$, behave in exactly the same way as VY Scl stars of $q \sim 0.03 - 0.4$, Warner (1995a) expected that the AM CVn systems should therefore experience the same F_{irr} as the VY Scl stars when their periods are in the range 1280 s $\leq P_{orb} \leq$ 1520 s. The VY Scl stars evolve through their instability range and continue through their semi-detached state always in the direction of decreasing P_{orb}, while the AM CVn systems evolve through their $\dot{M}$ instability range with increasing P_{orb}, but if they become detached they will evolve back to shorter P_{orb} to be recycled. When the orbital separation is sufficiently large to prevent irradiation lifting $\dot{M}$ into a quasi-stable high state, the system will settle down to a very low $\dot{M}$ state like that of GP Com.

Table 7.1: Parameters for four of the AM CVn systems, as a result of our calculations, with no interstellar absorption assumed.

Object Name	$\log(\dot{M})$ $M_\odot/yr$	i $degrees$	R_{disc} R_1	d pc
AM CVn	-8.5 ± 0.3	45 ± 5	(15 ± 2)	288 ± 50
HP Lib	-8.4 ± 0.13	28 ± 5	(14 ± 3)	188 ± 50
CR Boo	$[(-8.0) - (-9.52)]$	30 ± 5	(15 ± 3)	469 ± 50
V803 Cen	$[(-8.15) - (-9.3)]$	5 ± 5	(17 ± 3)	405 ± 50

7.3 Conclusions

Our main conclusions are the the following:

1 – The NLTE pure helium accretion disc model is a good model to compare with the observed spectra of the AM CVn systems. At the same time, small traces of hydrogen, with a hydrogen to helium number density ratio should be $\leq 10^{-5}$, can also be introduced into the pure helium model without being detected in our low resolution spectra. We found that these traces of hydrogen don't improve the final fit to the observed spectra when compared to the fit from the pure helium model. The same was found for C, O and N, where their number density ratios should be $\leq 10^{-5}$ with respect to helium, in order not see lines from such elements as in the observed optical spectra. This means that the accretion disc of the AM CVn systems can be a pure helium or a helium disc with some traces of hydrogen, carbon, oxygen and nitrogen of not more than 10^{-5} by number with respect to helium. We also include the possibility that all the hydrogen was removed from the system at earlier evolutionary stages, leaving a pure helium disc.

2 – We have found that differences between the predicted LTE and NLTE equivalent widths of helium lines are between 10 and 40 % in certain rings. Thus, we have demonstrated that NLTE effects are important, and should be taken into account in accurate analyses of the observed spectra of the AM CVn systems.

3 – Our results correspond with the result obtained for the H-He abundance by Iben

& Tutukov (1986) and totally agree with the the upper limit found by Marsh et al. (1991) to fit the observed spectra of GP Com. It is also to a certain extent agree with the results obtained by El-Khoury & Wickramasinghe (2000) for the rest of the parameters, given that we have different assumptions and considerations.

4 – The slope of the continua of the pure helium models is influenced by the mass accretion rate, inner and outer radius variations while less affected by the variations of the angle of inclination, and the opposite is found for the influence of such parameters on the line profile. However, while taking the line depth and width variations into account, the line profile in the spectra of the pure helium model, preserves its structure when varying both the mass accretion rate and the outer radius of the disc. On the other hand the line fails to preserve its structure with the angle of inclination variations, due to the reasons discussed above.

5 – From the obtained values for $\dot{M}$ which correspond to a certain B-magnitude, we found that V803 Cen had a mass transfer rate as if it was in a stable state during the 2001 observations, with disc radius variations between the circularization and tidal radii, while CR Boo was climbing from intermediate to high state with a disc radius closer to the tidal than the critical radius .

6 – The magnitude variations of V803 Cen in the range 13.4 - 17 corresponds to the mass accretion rate variations $7 \times 10^{-9} - 6 \times 10^{-10} M_{\odot}$/yr. The same is applied to CR Boo, where the magnitude variations of 13.4 - 17 corresponds the mass accretion rate of $1 \times 10^{-8} - 3 \times 10^{-10} M_{\odot}$/yr.

7 – Our final estimates for the mass accretion rate of the AM CVn systems agree with the evolution of a semi-degenerate secondary of Nelemans et al.(2001a). Parameters for four of the AM CVn systems as a result of our observations and calculations are presented in table 7.1.

8 – Our angle estimates found for the AM CVn system itself agree with the estimates of Patterson et al. (1993), derived by the relation between the mass of the primary star M_1 and the system angle of inclination.

9 – The secondary star in the AM CVn systems has ignited helium, but we still do not know if it has developed a C-O core or not yet. Analysis of higher resolution spectra in the optical, in addition to the existing UV spectra is necessary to settle this matter.

7.4 What is left for the future?

Despite the fact that our results presented in this thesis have solved many of the longstanding problems about the accretion discs of AM CVn systems, much is still left to be done. Our models calculations represents only a steady state 'stationary' accretion disc with the absence of any dynamical or time dependent phenomena. Such case needs to be included in the future and in particular the eccentricity of the accretion disc, specially in the unstable systems like V803 Cen, CR Boo and CP Eri. Convection was not included in our modeling work, which will have a considerable effect on the line forming regions if it has been considered. In our work the mass accretion rate was limited within the range $2 \times 10^{-9} - 1 \times 10^{-8} M_{\odot}$/yr, with the possibility of making models with $\dot{M} > 1 \times 10^{-8} M_{\odot}$/yr. On the other hand we were not able to calculate a model below $1 \times 10^{-9} M_{\odot}$/yr, because the outer rings didn't converge below such value due to the low effective temperatures of such rings. Discs with mass accretion rate $\approx 1 \times 10^{-11} M_{\odot}$/yr are certainly needed to compare with the spectra of the low state objects in the AM CVn family, such as GP Com.

Most of the observed spectra used in this work are low resolution (FWHM = 20Å), which are good enough to be fitted with our models, but only with the broad strong lines besides the continua. This spectra were not very useful to use for the determination of the upper limits of the C, O and N abundances in the disc, which can answer some of the questions about the evolution of the AM CVn systems. Higher resolution spectra are certainly highly desired for this task.

He II in emission at 4686Å is seen in most of the AM CVn systems spectra. One of the explanations for the appearance of this line in emission in the spectra of the optically thick disc systems, is that the line is generated in a hot layer of an optically thin material located on the surface of the disc. This cannot be taken into account in our model calculations, the reason why we do not see the He II line at 4686Å in emission in our model spectra.

Much is also left to be done for the other components of the systems. For example, there is an evidence of hot winds in the UV part of the AM CVn spectra (Solheim & Kjeldseth-Moe 1987; Solheim & Sion 1994), which need to be investigated. Studying the wind lines is not an easy task but a very interesting one. The role of the primary and secondary stars in producing the observed spectra of the AM CVn systems has not been thoroughly investigated. More investigations are certainly needed to be done for the UV and the IR regions of the spectra, to have a complete and global picture about such peculiar and particular systems.

7.5 Appendix & definition of important quantities

In the appendix we list all the constants and the definition of the important quantities used in this work.

Appendix

speed of light in vacuum: c = 2.99792458 $\times 10^{10}$ cm s^{-1}
Newtonian constant of gravitation: G = 6.6726 $\times 10^{-8}$ g^{-1} cm^3 s^{-1}
Planck's constant: h = 6.6260755 $\times 10^{-27}$ ergs s
Boltzmann's constant: k = 1.380658 $\times 10^{-16}$ ergs K^{-1}
gas constant: $R_{gas} = N_A k$ = 8.314511 $\times 10^7$ erg $K^{-1}mole^{-1}$
Stefan-Boltzmann constant: σ = 5.67051 $\times 10^{-5}$ erg cm^{-2} K^{-4} s^{-1}
Solar mass: $M_\odot = (1.9891 \pm 0.0004) \times 10^{33}$ g
Solar luminosity: $L_\odot = (3.847 \pm 0.003) \times 10^{33}$ erg s^{-1}
Solar radius: $R_\odot$ = 6.96 $\times 10^{10}$ cm
Solar effective temperature: $T_{eff}(\odot)$ = 5780 K
astronomical unit (AU): 1 AU = 1.496 $\times 10^{13}$ cm
parsec (pc): 1 pc = 3.086 $\times 10^{18}$ cm

See index for references to definitions of important quantities	
binary separation	a
Planck function	B_ν
speed of light	c
sound speed	c_s
distance	d
mechanical energy	D_{mech}
specific energy	e
force per unit volume	f
flux of radiation	F
energy emission per unit surface	Q
advective cooling per unit surface	Q_{adv}
radiative cooling per unit surface	Q_{rad}
gravitational constant	G
Planck constant	h
disc thickness	H
angle of inclination	i
specific intensity	I_ν
angular momentum of binary systems	J
mean intensity	J_ν
Boltzmann constant	k
luminosity	L
Eddington luminosity	L_{Edd}
inner Lagrangian point	L_1
solar mass	$M_\odot$
mass of the primary star	M_1
mass of the seconday star	M_2
mass column density	m
mass accretion rate	$\dot{M}$
Eddington accretion limit	$\dot{M}_{Edd}$
critical accretion rate	$\dot{M}_{crit}$
particle number density	N

See index for references to definitions of important quantities	
binary orbital period	P_{orb}
superhump period	P_s
beat period	P_b
gas pressure	P_{gas}, P
radiation pressure	P_{rad}
mass ratio	q
radius of the primary star	$R_1, R_\star$
radial distance in the disc	R
inner radius of the disc	R_{in}
outer radius of the disc	R_{out}
Reynolds number	R_e
Roche radius	R_L
solar radius	$R_\odot$
circular radius	R_{circ}
critical radius	R_{crit}
tidal radius	R_{tidal}
specific entropy	S
source function	S_ν
gas temperature	T
effective temperature	T_{eff}
central temperature	T_c
time	t
nuclear timescale	t_{nuc}
cooling timescale	t_{rad}
dynamical timescale	t_{dyn}
boundary layer extent	t_b
shear stress	W
vertical structure of the disc	z
adiabatic index	γ
opacity	κ_ν
Rosseland mean	κ_R

See index for references to definitions of important quantities	
mean molecular weight	μ
frequency	ν
wavelength	λ
kinematic viscosity	ν
velocity	v
parallel velocity	$v_{\|\|}$
perpendicular velocity	$v_{\perp}$
orbital velocity	v_{ϕ}
Keplerian velocity	v_K
mean density of a lobe filling star	$\bar{\rho}$
Sefan-Boltzmann constant	σ
surface density	Σ
optical depth	τ
solid angle	Ω
Kepler angular velocity	Ω_k
specific angular momentum	ℓ
angular velocity	ω
depth-averaged kinematic viscosity	$\bar{\omega}$
gravitational force	Φ

Bibliography

[1] Abramowicz M., Czerny B., Lasota J. P. & Szuszkiewicz E. 1988, ApJ, 332, 646

[2] Abramowicz M., Lasota J. P., Xu C., Proceedings of the IAU Symposium, Bangalore, India, 1985, Dordrecht, D. Reidel Publishing Co. 1986, p. 371-380; Discussion, p. 381.

[3] Abbott T. C., Robinson E. L., Hill G. J., Haswell C. A. 1992, ApJ, 399, 680

[4] Aminzade R. et al. 1999, in ASP conf. ser 169, 11th European Workshop on White Dwarfs, ed. J.-E. Solheim & E. G. Meistas (San Francisco: ASP), 305

[5] Auer L. H. & Mihalas D. 1969, ApJ, 158, 641

[6] Bard S. 1995 Master thesis, The University of Tromsø

[7] Balbus S. A. & Hawley J. F. 1991, ApJ, 376, 214

[8] Burbidge E. M. & Strittmatter P. A. 1971, ApJ, 170, L39

[9] Cannizzo J. K. 1984, Nat, 311, 443

[10] Cannizzo J. K. 1993, in Accretion Disks in Compact Stellar Systems, ed. J. C. Wheeler (World Scientific), 6

[11] Cannon C. 1973, ApJ, 185

[12] Chandrasekhar S. 1961, Proc. Nat. Acad. Sci., 46, 53

[13] Chen X. & Taam R. E. 1993, ApJ, 412, 254

[14] Elvius A. 1975, A&A, 44, 117

[15] El-Khoury W. & Wickramasinghe D. 2000, A&A, 358, 154

[16] Eggleton P. 1983, ApJ, 268, 368

[17] Faulkner J., Flannery B. P. & Warner B. 1972, ApJ, 175, L79

[18] Frank J., King A. & Raine D. 1992, Accretion Power in Astrophysics. Cambridge Astrophysics Series, Cambridge University Press

[19] Gammie C. F. & Menou K. 1998, ApJL, 492, 75

[20] Giclas H. L., Burnham R. & Thomas N. G. 1961, Lowell Obs. Bull. No. 112, 61

[21] Greenstein J. L. 1979, in 'White Dwarfs and Variable Degenerate Stars', ed. H. M. Van Horn and V. Weideman, Proc IAU Colloq. 53, p. 374

[22] Greenstein J. L. & Mathews M. S. 1957, ApJ, 126,14

[23] Hansen C. J. & kawaler S. D. 1994, Stellar Interiors, Physical Principles, Structure, and Evolution, Springer Verlag.

[24] Hawley J. F. & Balbus S. A. 1991, ApJ, 376, 223

[25] Hiros M & Osaki Y. 1990, PASJ, 42

[26] Hubeny I. 1988, Computer Physics Communications, 52, 103, 132

[27] Hubeny I. 1989, in Theory of accertion disks, ed. F. Meyer W., Duschl J., Frank and E. Meyer-Hofmeister (Dordrecht:Kluwer), p. 455

[28] Hubeny I. 1990a, ApJ, 315, 632

[29] Hubeny I. 1990b, IAU Coll, 129, ed. C. Bertout et al. (Gif Sur Yvette: Edition Frontieres), 227

[30] Hubeny I. 1992, The Atmospheres of Early Type Stars, in Lecture Notes in Physics, 401, ed. U. Heber and C. Jeffery, Springer Verlage, Berlin, p. 377

[31] Hubeny I. & Lanz T. 1992, A&A, 262, 501

[32] Hubeny I. 1994, Vertical Structure and Theoretical Spectra of Accretion Disks, in Proceedings of the Symposium on Interacting Binary Stars in Conjunction with the 105 meeting of the Astronomical Society of the Pacific, p. 3

[33] Hubeny I. & Lanz T. 1995a, User's guides for TLUSTY, TLUSDISK and SYNSPEC, Distributed in electronic form with the appropriate program.

[34] Hubeny I. & Lanz T. 1995b, ApJ, 439, 875

[35] Iben I. & Tutukov A. 1984, ApJ Suppl., 54, 335

[36] Iben I. & Tutukov A. 1986, ApJ, 742, 752

[37] Iben I. & Webbink R. 1988, in IAU Colloquium 114, White Dwarfs, ed. G. Wegner (Berlin : Springer), p.477

[38] Kato et al. 1999, Disk Instabilities in Close Binary Systems, p. 45, eds. Mineshige S., Wheeler J. C., (Universal Academy Press, Tokyo)

[39] Kato et al. 2000, MNRAS, 315, 140

[40] Kepler S. O. 1989, Lecture Notes in Physics, White Dwarf, G. Wegner (Ed.), 443

[41] Kholopov P. N. 1985, Gen. Cat. Var. Stars, 4th edn, Astr. Council of Acad. Sci., USSR, Moscow

[42] Kriz S., & Hubeny I. 1986, Bull. Astron. Inst. Czechosl. 37, 129

[43] Kudritzki R. P. & Hummer D. G. 1990 ARA&A, 28, 303

[44] Kurucz R. L. 1970, SAO Special Report, 309

[45] Kusunose M. & Mineshige S. 1992, ApJ, 392,653

[46] La Dous C. 1989, A&A 211, 131

[47] Lasota J. P. & Pelat D. 1991, A&A, 249, 574

[48] Lubow S. H. 1994, Theory of Accretion Disks - 2, Proceedings of the NATO Advanced Research Workshop, held in Garching, Germany, edited by Wolfgang D., Frank J., Meyer F., Meyer-Hofmeister E., and Werner T., NATO Advanced Science Institutes (ASI) Series C, 417, 109

[49] Luyten W. J. 1933, MNRS, 93, 197

[50] Luu C. & Liang E. P. 1994, MNRAS, 266

[51] Lynden-Bell D. & Pringle J. E. 1974, MNRAS, 168, 603

[52] Marsh T. R., Keith H. & Simon R. 1991, ApJ, 366, 535

[53] Massacand C. & Solheim J.-E. 1995, Baltic Astronomy 4, 378

[54] Mihalas D., Stellar Atmospheres, W. H. Freeman and Co. 1978, second edition.

[55] Narayan R. & Yi L. 1994, ApJ, 428, L13

[56] Nasser M. 1998, Master Thesis, The International Centre for Theoretical Physics, Trieste, Italy.

[57] Nasser M. 2000, A User's Guide, 'The Reduction Steps of Long Slit Spectra Using IRAF', The University of Tromsø

[58] Nasser M., Solheim J.-E. & Semionoff. D. 2001, A&A, 373, 222 (NSS)

[59] Nather R. E., Robinson E. L. & Stover R. J. 1981 ApJ, 244, 269

[60] Nauenberg M. 1972, ApJ, 175, 417

[61] Nelemans G., Portegies Zwart, S. F.,Verbunt F., Yungelson L. R. 2001a, A&A, 368, 939

[62] Nelemans G., Steeghs D. & Groot P. J. 2001b MNRAS, 326, 621

[63] Nymark T. K. & Solheim J.-E. 1995, BA, 386,395

[64] Marsh T. R., Janet H. W., Keith H., Lambert D. 1995, MNRAS, 274, 452-460

[65] O'Donoghue D., Menzies, J. W. & Hill, P. W. 1987, MNRAS, 227, 347

[66] O'Donoghue D., Kilkenny D., Chen A., Stobie R. S., Koen C., Warner B., Lawson W. A. 1994, MNRS, 271, 910

[67] Oke J. 1974, ApJ Suppl. Ser., 72, 21

[68] Osaki Y. 1989, PASJ, 41, 1005

[69] Osaki Y. 1996, Proceedings of the 158th Colloquium of the International Astronomical Union (IAU); held at Keele; United Kingdom, edited by A. Evans and Janet H. Wood, 127

[70] Paczyński B. 1967, Acta Astron., 17, 287

[71] Patterson J., Stener E., Halpern J. & Raymond J. C. 1992, ApJ, 384,234

[72] Patterson J., Halpern J. & Shambrok A. 1993, ApJ, 419, 803

[73] Patterson et al. 2000, PASP, 112, 625

[74] Probst R. G. 1983, An Infrared Search for Very Low Mass Stars - JHK Photometry and Results for Composit Systems ApJ Suppl, 53, 335 - 349

[75] Provencal J. L. et al. 1997, ApJ, 480, 383P

[76] Rutten R. J. 1999, Radiative Transfere in Stellar Atmospheres, lecture notes Utrecht Univ,. 6th WWW edition

[77] Savonije G. J., M. de Kool, E. P. J. Van Heuvel 1986, A&A, 155, 51

[78] Schenker K. 2001, Conf. Proc., Göttingen, Germany, 'in press'

[79] Semionoff D. 1998, Master Thesis, The University Of Tromsø

[80] Sensson R. 1982, ApJ, 258,335

[81] Shakura N. I. & Sunyaev R. 1973, A&A, 24, pp. 337

[82] Smak J. I. 1967, AcA, 17, 255

[83] Smak J. I. 1983, Acta Astron., 33, 333

[84] Solheim J.-E. & Kjeldseth-Moe O. 1987, Ap&SS, 131, 785

[85] Solheim J.-E. 1992, Evolutionary Processes in Interacting Binary Stars, ed. Y. Kondo

[86] Solheim J.-E. & Sion E. M. 1994, A&A, 287, 503

[87] Solheim J.-E. et al. 1998, A&A, 332, 939

[88] Szkody P., Howell, S. B., Mateo M., Kreidle T. J. 1989, PASP, 899

[89] Tsugawa M. & Osaki Y. 1997, PASJ, 49, 75-84

[90] Taam R. E. & Lin D. N.C. 1984, ApJ, 287, 761

[91] Tutukov A. V. & Fedorova A. V. 1989, SvA, 33,606

[92] Ulla A. 1994, SSRV, 67, 241

[93] Voikhanskaya N. F. 1982, Sov. Astron. 16, 558

[94] Wandel A. & Liang E. P. 1991, ApJ, 380, 84

[95] Wampler E. J. 1967, ApJ, 149, L101

[96] Warner B. & Robinson E. L. 1972, MNRAS, 159, 101

[97] Warner B. 1995a, ApSS, 225, 249

[98] Warner B. 1995b, in Cataclysmic Variables Stars (Cambridge U. Press)

[99] Westin B. M. 1980, A&A, 81, 74

[100] Whitehurst R. 1988, MNRAS, 232, 35

[101] Wood M. A., Winget D. E., Nather R. E., Hessman F. V. 1987, ApJ, 313, 757

[102] Zapolsky H. S. & Salpeter E. E. 1969, ApJ, 158, 809